Title: Advanced Cuttings Transport Study

Type of Report: Final Technical
Reporting Period Start Date: July14, 1999
Reporting Period End Date: July 13, 2004

Principal Authors:
Stefan Miska, Principal Investigator (2003-2004)
Troy Reed, Principal Investigator (2000-2003)
Ergun Kuru, Principal Investigator (1999-2000)
Nicholas Takach, Co-Principal Investigator
Kaveh Ashenayi, Co-Principal Investigator
Ramadan Ahmed, Research Associate
Mengjiao Yu, Research Associate
Mark Pickell, Project Engineer
Len Volk, Research Associate
Mike Volk, Project Manager
Barkim Demirdal
Affonso Lourenco
Evren Ozbayoglu
Paco Vieira
Lei Zhou
Zhu Chen
Aimee Washington
Crystal Redden
Sameer Nene
Jagruthi Godugu
Ameen Al-hosani

Date of Issue: September 30, 2004
DOE Award Number: DE-FG26-99BC15178

The University of Tulsa
600 South College Avenue
Tulsa, Oklahoma 74104

DISCLAIMER

This report was prepared as an account of work sponsored by and agency of the United States Government, Neither the United States Government nor any agency thereof, nor any of their employees, makes any warranty, express or implied, or assumes any legal liability or responsibility for the accuracy, completeness, or usefulness of any information, apparatus, product, or process disclosed, or represents that its use would not infringe privately owned rights. Reference herein to any specific commercial product, process, or service by trade name, trademark, manufacturer, or otherwise does not necessarily constitute or imply, its endorsement, recommendation, or favoring, by the United States Government or agency thereof. The views and opinions of authors expressed herein do not necessarily state or reflect those of the United States Government or any agency thereof.

Abstract

The Advanced Cuttings Transport Study (ACTS) was a 5-year JIP project undertaken at the University of Tulsa (TU). The project was sponsored by the U.S. Department of Energy (DOE) and JIP member companies. The objectives of the project were: i) to develop and construct a new research facility that would allow three-phase (gas, liquid and cuttings) flow experiments under ambient and EPET (elevated pressure and temperature) conditions, and at different angle of inclinations and drill pipe rotation speeds; ii) to conduct experiments and develop a data base for the industry and academia; and iii) to develop mechanistic models for optimization of drilling hydraulics and cuttings transport. This project consisted of research studies, flow loop construction and instrumentation development.

Following a one-year period for basic flow loop construction, a proposal was submitted by TU to the DOE for a five-year project that was organized in such a manner as to provide a logical progression of research experiments as well as additions to the basic flow loop. The flow loop additions and improvements included: i) elevated temperature capability; ii) two-phase (gas and liquid, foam etc.) capability; iii) cuttings injection and removal system; iv) drill pipe rotation system; and v) drilling section elevation system.

In parallel with the flow loop construction, hydraulics and cuttings transport studies were preformed using drilling foams and aerated muds. In addition, hydraulics and rheology of synthetic drilling fluids were investigated. The studies were performed under ambient and EPET conditions. The effects of temperature and pressure on the hydraulics and cuttings transport were investigated. Mechanistic models were developed to predict frictional pressure loss and cuttings transport in horizontal and near-horizontal configurations. Model predictions were compared with the measured data. Predominately, model predictions show satisfactory agreements with the measured data.

As a part of this project, instrumentation was developed to monitor cuttings beds and characterize foams in the flow loop. An ultrasonic-based monitoring system was developed to measure cuttings bed thickness in the flow loop. Data acquisition software controls the system and processes the data.

Two foam generating devices were designed and developed to produce foams with specified quality and texture. The devices are equipped with a bubble recognition system and an in-line viscometer to measure bubble size distribution and foam rheology, respectively.

The 5-year project is completed. Future research activities will be under the umbrella of Tulsa University Drilling Research Projects. Currently the flow loop is being used for testing cuttings transport capacity of aqueous and polymer-based foams under elevated pressure and temperature conditions. Subsequently, the effect of viscous sweeps on cuttings transport under elevated pressure and temperature conditions will be investigated using the flow loop. Other projects will follow now that the “steady state” phase of the project has been achieved.

Acknowledgment

We wish to express our appreciation to the U.S. Department of Energy, our industry partners and The University of Tulsa. Without the support, financial and technical, of each of these groups successful completion of this project would not have been possible.

Special thanks go to Rhonda Lindsey Jacobs and Mr. Jim Barnes of the DOE. Ms. Lindsey who facilitated moving this research to the University from former Federal Laboratory in Bartlesville and Mr. Barnes, as our technical contact, provided input and advice throughout the life of the project.

While individuals at each of the sponsoring companies of the JIP played prominent support roles, two individuals deserve special mention: Dr. Peter Bern of British Petroleum and Mr. Phil Harris of Halliburton. In addition to technical advice, Dr. Bern wrote one of the requisite letters of support from industry; his letter served as a model for others to follow. Mr. Harris was always eager to help with his expertise on foam systems. He also hosted on us on several occasions when we requested visits to discuss difficult issues with him and his colleagues.

This study would not have been possible without several donations of equipment and chemicals. We wish to thank Halliburton for their donation of an HT-400 fracturing pump. This is the primary pump for the ACTF and we simply could not have functioned without it. We greatly appreciate the efforts of Halliburton's Mr. Paul Padgett for arranging the donation, and Paul Mendenall and David Stribling for their ongoing assistance. Andre Leibsohn Martins made our study of synthetic fluids (Task # 8) possible by providing, through Petrobras, over 100 bbl of their paraffin-based synthetic drilling fluid, including its shipment from Brazil to the U.S. Mr. Les Robertson was our contact at Bachman Services for numerous drums of their surfactant and foam breaking chemicals. These chemicals made it possible to conduct two of our foam research projects, even though Bachman was not a member of TUDRP or the ACTS-JIP. Also donations by Alan Wild of Moyno Industrial Product, Kent Van Valkenburg of VANCO Engineering, and Charles Alworth have been very important to us. We also must recognize the special efforts of the contractors who have been on the project many times over the last five years especially Mike Poston of Weamco and Kevin Smith of K & L Mechanical. Finally, Mr. Garth Shewchuk, formerly of Weatherford International Ltd. was instrumental in Weatherford's donation of their polymer-blend surfactant / foam breaker system, currently being used in Task 13. Both he and Mr. Robertson also provided expertise in how to make best use of their systems during personal visits to our facilities.

At the University of Tulsa Office, Dr. Alan Soltow, Ms. Lisa Thompson and Ms. Leah Bevin, of the Office of Research, handled administrative and contractual issues, and were our liaisons with the DOE. Dr. Jim Sorem was responsible for support from the university's College of Engineering and Natural Sciences. We also benefited greatly from his experience with mechanical systems.

Finally, we would like to extend our appreciation to Ms. Paula Udwin for helping with the budget and many other administrative issues and Steve Turpin for making things work on the flow loop.

Table of Contents

List of Tables

List of Figures

1. Introduction

The concept for the project we now call the Advanced Cuttings Transport Study (ACTS) began with BDM and the United States Department of Energy (DOE). BDM was a private company that managed operations of the National Institute for Petroleum Energy Research (NIPER) in Bartlesville, OK. At about this same time, officials of PDVSA (the Venezuelan National Oil Company), expressed to DOE their interest in research studies of compressible fluids. At the May, 1997, Advisory Board Meeting (ABM) of Tulsa University Drilling Research Projects (TUDRP), a project involving the hydraulics of underbalanced drilling operations (UBD) was jointly proposed by INTEVEP (the research arm of PDVSA) and JNOC (the Japanese National Oil Company). Later in May, 1997, officials of DOE's newly formed National Petroleum Technology Office (NPTO), located in Tulsa, OK, approached TUDRP to inquire if they would be interested in undertaking a major study that included the construction of a new flow loop with advanced capabilities for studies of cuttings transport, hydraulics and fluid properties such as rheology. The loop would be capable of investigating both conventional (incompressible) and compressible fluids of the type involved in UBD. TUDRP researchers agreed to undertake the study and design of the new flow loop, later named the Advanced Cuttings Transport Facility (ACTF), was soon to begin.

TUDRP already possessed a powerful research facility for studying cuttings transport called the LPAT (Low Pressure Ambient Temperature) flow loop. The LPAT loop, with a 100-ft test section that allows tests to be conducted at any inclination angle between horizontal and vertical, is the largest of its kind in the world. The new ACTF loop would complement the LPAT loop with the ability to study fluid properties and cuttings transport at elevated temperatures and pressures; hence the new loop would serve as a "wellbore simulator" and would be the only test facility of its kind in the world. The ACTF was to be constructed adjacent to the LPAT.

A "brainstorming session" was organized by TUDRP in September, 1997, to discuss the design, capabilities and dimensions of the new facility. Members of several companies and the DOE attended the brainstorming session. In 1998 the DOE awarded TUDRP a grant of almost $600,000 to design and construct the basic loop. The basic loop would include a large concrete base onto which a loop of steel piping capable of flowing water at flow rates up to 250 gpm and pressures up to 700 psi would be placed. This initial loop was completed slightly ahead of schedule and TUDRP was invited to submit a five-year proposal, including statement of work, to the DOE. After inviting input from TUDRP industry partners in the form of loop design, research directions, design of the test matrix, etc., the proposal was submitted and later approved by the DOE. Industry participation was required at a rate of 20% of the DOE funding. Several companies agreed to help fund the project and the ACTS-JIP formally commenced on July 14, 1999.

The original Statement of Work consisted of 12 tasks, divided among three major categories: construction, research and instrumentation. The original tasks consisted of:

Task 1 Construction of Elevated Temperature Facility;
Task 2 Construction of Aeration System;
Task 3 Construction of Cuttings Injection/Separation Facility;

Task 4 Construction of Drill Pipe Rotating Facility;
Task 5 Construction of Loop Inclination Facility;
Task 6 Research on Cuttings Transport with Foam at LPAT Conditions;
Task 7 Research on Cuttings Transport with Aerated Mud at LPAT conditions;
Task 8 Research on Synthetic Drilling Fluids at EPET Conditions;
Task 9 Research on Foam Flow under EPET Conditions;
Task 10 Research on Cuttings Transport with Aerated Mud at EPET Conditions;
Task 11 Development of Cuttings Monitoring System;
Task 12 Development of Foam Bubble Size and Distribution Monitoring System.

Results obtained during the course of the project made it apparent that the goals of the study would benefit from the addition of one research subtask, one new major research task and a safety task. The newly added tasks were:

Task 9b Study on Foam Rheology Using a Rotational Viscometer and Development of a Foam Generator/Viscometer for EPET Conditions;
Task 13 Research on Cuttings Transport with Foam at EPET Conditions;
Task S1 Development of a Safety Program.

The research tasks in the original plan were selected so that results could be obtained during each phase of construction. With this goal in mind, two of the research tasks were jointly conducted with, and jointly funded by, TUDRP. The joint tasks also afforded experience and knowledge that would assist in the implementation of subsequent ACTS-JIP tasks.

Although the ACTF is capable of investigating any type of drilling fluid, a major focus of the ACTS-JIP was to study compressible fluids. As mentioned, underbalanced drilling or UBD, in its simplest definition, involves the use of compressible drilling fluids. Compressible fluids can range from gas used alone (air drilling) to a system in which gas is introduced into a liquid system (foam, aerated mud, or mist) to obtain a variable range of low-density fluids. UBD has been experiencing growth at an increasing rate. In 1999 UBD was estimated to represent 20-30% of all drilling projects. At TUDRP'S May, 2004, ABM, a high-ranking official at Weatherford International, a major global service company, stated that UBD operations have been experiencing about 8% growth per year in his company. Drilling with compressible fluids (in the case of underbalanced drilling) has been shown to provide significant benefits, including:

- Increased drilling rate (rate of drill bit penetration);
- Minimization or elimination of lost circulation while drilling;
- Reduction or elimination of differential pipe sticking;
- Increased productivity by reducing formation damage;
- Improved formation evaluation while drilling;
- Reduced stimulation requirements;
- Earlier production.

Despite these advantages, information on successful UBD methodology has often been fragmented and difficult to assess. Low-head compressible drilling fluid technologies offer real promise for mitigating or altogether avoiding many types of productivity impairment phenomena. Meeting the world's increasing hydrocarbon demand will also require improved exploitation of existing, but heretofore economically and technically unapproachable, reserves in reservoirs with reduced pressures because of prior production. Significant reserve additions or 'reclamation' may be realized if the hazards associated with drilling in sub-normally pressured environments (e.g., lost-circulation and differentially stuck pipe) can be effectively managed. Low-head compressible fluid drilling technologies are one of the keys to unlocking these resources. Where UBD is applicable, it can add millions of dollars in value over the remaining life of a well.

Based on the current level of understanding of UBD, it can still be considered an emerging technology, roughly comparable to where horizontal drilling was 15 yrs ago, or multilateral drilling 10 years ago. Drilling with compressible fluids is done mainly on land. This is because of safety concerns and the extra compressors and other equipment that are required. However, in June, 2002, 116 drilling engineers attended the Drilling Engineering Association's deepwater workshop in Galveston, Texas. The meeting included breakout sessions for identifying potential JIPs with the aim of finding solutions to various problems. One JIP candidate was for determining the capability of UBD operations in 12,000 feet of water. Developments such as these demonstrate that UBD operations offshore could be the next new development in drilling technology.

Mixing of gas and liquid phases is a way to achieve the desired drilling fluid density, which in turn controls the "static" component of the borehole pressure. Gas can be injected into the liquid stream through the drill string or via some special purpose annulus injection device.
Depending upon the structure and relative volumes of gas and liquid phases, we can distinguish among gas, mist, foam, and aerated mud. Usually, air or nitrogen is used as the gas phase. The liquid phase is usually water with surfactant and corrosion inhibitor. Polymers (or other chemicals) may be added to inhibit interaction with water-sensitive formations. Foam is generated by adding a surfactant to the liquid phase that surrounds gas bubbles.

Characteristically, foam viscosity is greater than that of the liquid and gas components that comprise it. Although viscosity may improve cuttings transport, it also results in greater pressure losses. Designing proper fractions of gas and liquid phases, volumetric flow rates, and types of polymers and surfactants is critical for achieving the desired flowing bottom hole pressure and cuttings transport.

The performance of compressible drilling fluids is rather unpredictable. As mentioned, this is because, compared to conventional (incompressible) drilling fluids, very little is known about the hydraulic and rheological properties of aerated drilling fluids. Even less is known about their cuttings transport capabilities. The complex flow mechanisms involved in compressible drilling fluid circulation make determination of the optimum combination of liquid and gas injection rates very difficult. Other questions remain, such as how to predict the bottom-hole pressure and how to combine different controllable variables in order to obtain optimum cutting transport performance and bit hydraulics.

For all of the above reasons, the overall objective of the ACTF wellbore simulator is to determine non-Newtonian fluid characteristics and cuttings transport performance of compressible fluids (aerated mud and foam) and of conventional (incompressible) drilling fluids under elevated temperature and pressure in a large-scale experimental facility.

During the 5-year project period, faculty members, staff and graduate students of the University of Tulsa participated in completion of the project. The project delivered: i) cuttings transport testing facility (Flow Loop); ii) two PhD and six MS theses, iii) 10 JIP reports; iv) 20 DOE quarterly reports; and v) DOE final report.

In addition, several individuals at the U.S. Dept. of Energy and in private industry contributed to the project. Below is a list of key individuals, categorized by affiliation.

U.S. Department of Energy

Ms. Rhonda Lindsey, who facilitated moving this research to the University from former Federal Laboratory in Bartlesville.
Mr. Jim Barnes, Technical Contact during the project.

University of Tulsa

Dr. Stefan Miska, Executive Director of Drilling Research at TU; Principal Investigator (PI) during Year 5.
Mr. Mark Pickell, Manager of Engineering and Design, responsible for design of the flow loop.
Dr. Nicholas Takach, Co-PI; Project Manager during construction of the basic flow loop (1998)
Dr. Ergun Kuru, PI for Year 1
Dr. Troy Reed, PI for Years 2-4
Dr. Kaveh Ashenayi, Co-PI
Dr. Michael Volk, Project Manager
Dr. Ramadan Ahmed, Research Associate
Dr. Mengjiao Yu, Research Associate
Mr. Steve Turpin, Research Technician
Ms. Paula Brooks Udwin, Project Assistant
Dr. Al Soltow, Executive Director of Research and Sponsored Programs
Ms. Lisa Thompson, Director of Research and Sponsored Programs
Dr. James Sorem, Senior Associate Dean, College of Engineering and Natural Sciences

Industry

Dr. Peter Bern, British Petroleum
Dr. Mayela Rivero, formerly with PDVSA

In addition to the individuals listed above, several others from the University of Tulsa, the U.S. DOE and our industry partners made valuable contributions.

This report presents the construction of a cuttings transport testing facility, development of related instrumentations and results of cuttings transport studies conducted at the University of Tulsa. This project was sponsored by the United State Department of Energy (DOE) and 10 JIP member companies. The information provided in this report is divided into fourteen main sections.

As discussed at the last ABM of ACTS JIP, future research activities will be under the umbrella of Tulsa University Drilling Research Project (TUDRP), which consists of 15 member companies and the US DOE. Advisory board meetings will continue to be held in November and May of each year.

2. Executive Summary

Flow Loop Design and Construction (Task 1-5)

The flow loop project we now call Advanced Cuttings Transport Study (ACTS) is complete. The concept for the flow loop began with BDM and The Unites States Department of Energy (DOE). The University of Tulsa (TU) was chosen as a most logical place to locate the test loop. In the summer of 1997 a contract was entered into between TU and BDM, funded by the DOE, to develop designs and a project plan.

A number of interested industry representatives including those from AMOCO, ARCO, Canadian FracMaster, Schlumberger-Dowell, Halliburton, Mobil, as well as the DOE, BDM, and TU met to address the basic objectives of the Cuttings Transport Facility, as it was called then, and the physical dimensions and capabilities that should be included.

Following this initial contract for loop design, a subsequent contract was entered into by TU with BDM, again funded by the DOE, for an initial construction phase which was to build a basic test loop and flow water up to 250 gpm at pressures up to 700 psi. In May of 1998 construction began and equipment was moved in.

Subsequent to completion of a basic flow loop a proposal was submitted by TU to the DOE for a five-year project which would be structured in such a manner as to provide for a logical progression of research experiments as well as additions to the flow loop itself. The flow loop construction sequence was defined as:

Year 1 – Addition of elevated temperature capability;
Year 2 – Addition of two-phase (air, liquid, and foam) capability;
Year 3 – Addition of cuttings transport;
Year 4 – Addition of drill pipe rotation;
Year 5 – Addition of drilling section elevation.

On July 14, 1999, the ACTS JIP was officially formed. In the interim between initial loop construction and the 5 Year Proposal, a number of tests were performed using water only. During this time, a pulsation dampener downstream of the Halliburton pump was installed and the rheology section was modified to allow for either parallel or series flow. A Micro Motion flow meter was added replacing the sonic Doppler meters. Other required instrumentations were also installed in the system.

During Year 1, a 2-MM BTU indirect fired natural gas boiler, two plate-style heat exchangers and water cascade cooling tower were purchased and installed. Additionally a second 100 bbl mud storage tank and a small 5 bbl tank with mixer and transfer pump were purchased and installed. A considerable amount of piping was installed in order to make the new tanks, heat exchangers, and cooling tower functional. A new gas supply line was laid from some distance away to the test loop in order to supply the boiler. A canopy was constructed over the boiler. And, lastly, an insulation contractor was hired to insulate the flow loop piping and the storage tanks to minimize heat loss during elevated temperature experiments.

Subsequent to Year 1 construction a series of experiments utilizing a synthetic drilling mud supplied by Petrobras was conducted at temperatures up to 180°F and pressures up to 1200 psig. This was the first scheduled series of experiments for the test loop. Year 2 construction began after these experiments. A diesel powered air compressor, air accumulator tank, air/liquid separator tower, and injection pumps for water, surfactant, and foam breaker were purchased and installed. In addition, the Moyno Tri-Phaze pump and Coriolis flow meters were installed in the system.

As the Task 9 experiments were being conducted in the summer of 2001, plans for Year 3 constructions were rapidly taking shape. A cuttings injection location was chosen downstream of the Moyno pump. With the design criteria finalized, the air/liquid separator was dismantled and shipped off to the contractor who was building the injection and removal towers. The new towers were fabricated and installed. During this time a completely new control and data acquisition system was installed. We also installed an emergency stop system that is manually operated from the control cabin. It utilizes relays that return electronically controlled valves and motors to the default position when activated.

The scheduled addition for Year 4 was drill pipe rotation. A series of support spiders was conceived which would use a conventional internally upset drill pipe thread form that is relieved to include high density polyethylene bushings, a dirt seal, and a pressure seal. Separate sets of spiders were made to accommodate concentric operation and two different levels of eccentricity. A blind flange was machined to accept a drive shaft which connected to the drill pipe. Two additional blind flanges were also machined for different degrees of eccentricity. A hydraulic motor and chain drive were installed to provide the rotation. The system proved to work very well. During this time a drilling choke was received from SWACO. This choke was installed upstream of the cuttings removal tower to provide a secondary back pressure control. Basket strainers were also installed in the return line to trap fine cuttings. An extension to the existing canopy was also made.

Year 5 construction was the addition of drill string elevation. The new I-beam style mast was designed, fabricated and installed. The hydraulic cylinders were assembled. We raised the mast using the hydraulic cylinders to approximately 25 to 30 degrees inclination. While lowering the mast, it moved laterally a couple of degrees. Upon visual inspection, severe spalling of the concrete on the face of the support pillar, and deformation of the steel support structure was observed. The support structure is still capable to provide support to the mast for all future experiments in the horizontal configuration. However, the support structure needs rebuilding to operate the mast in elevated configuration. Chiksan joints and flexible hoses have been installed. Also, piping has been installed which will allow closed-loop operations. A new air compressor has been purchased and installed. A satellite laboratory has been constructed behind the existing Control Building to serve on-going test loop experiments with auxiliary laboratory equipment.

Study of Cuttings Transport with Foam under LPAT Conditions (Task 6)

Cuttings transport experiments with water and foam were performed at ambient temperature and pressure in horizontal and highly-inclined configurations. The results indicated that cuttings bed thickness increases as foam quality increases, and decreases with the increase in flow rate and foam density. The effect of inclination angle on cuttings transport is found to be negligible at high inclination angles.

As a part of this investigation, rheological and hydraulic behaviors of aqueous foams were also studied. Rheological models are developed for estimating generalized consistency index (K’) and generalized flow behavior index (N) for laminar foam flows in pipes and annular geometries. Rheology experiments were conducted to determine foam rheological properties as a function of foam quality. Analysis of the flow curves of the foam used in this study indicated that foam behaves like a pseudo-plastic fluid with a negligible yield stress. Wall slip was also observed.

A mathematical model was developed for predicting frictional pressure losses and cuttings transport in foam drilling. Model predictions were compared with experimentally measured data. Model predicted results are in good agreement with experimental measurements.

Cuttings Transport with Aerated Muds under LPAT Conditions (Task 7)

This study was conducted to gain more in depth understanding of cuttings transport in horizontal and highly-inclined wells with aerated fluids. Experiments were carried out in a field-scale low-pressure flow loop which has a 90 ft annular test section (8" X 4.5"). The tests were performed at horizontal and inclination (80° from vertical) configurations. Pressure drop, cuttings accumulation, pressure and temperature in the test section were recorded in each experiment through a data acquisition system. The effects of gas and liquid flow rates, drilling rate, inclination angle, pressure drop and flow patterns on cuttings transport were analyzed. In order to reduce the test matrix, the effects of drill pipe rotation, drill pipe eccentricity and liquid phase viscosity on cuttings transport were not investigated. Gas and liquid injection rates were set in the range of 200 to 700 GPM. Drilling rates (ROP) of 30, 50 and 70 ft/hr were used in the experiments. For each total flow rate, different combinations of gas and liquid were chosen to maintain a constant total flow rate.

The results indicated the possibility of defining a boundary for the minimum air and water velocities required to avoid the formation of a stationary cuttings bed. The minimum required air and water injection rates for cuttings transport were found to be a function of the cuttings injection rate. Similarly the minimum energy required for solids transport was found to be constant for a given solids injection rate. The inclination effect was negligible for angles close to horizontal.

Study of Synthetic Drilling Fluids under EPET Conditions (Task 8)

Rheological and volumetric properties of synthetic based drilling fluids are sensitive to downhole conditions. As a result, there is a discrepancy between calculated and measured frictional pressure losses. In this study the effects of pressure and temperature on rheological and volumetric properties of synthetic drilling fluids were investigated. Elevated pressure and elevated temperature flow tests were conducted in a flow loop that has pipe and annular test sections. Rheology measurements and PVT analyses were made using a HPHT rotational viscometer (Fann 70) and PVT cell, respectively. Rheological parameters were determined for Bingham Plastic, Power Law and Yield Power Law fluid models.

Pressure loss predictions were made using different hydraulic models. In laminar pipe flow, predictions of hydraulic models vary significantly, particularly for high yield stress and high viscosity fluids. Bingham Plastic model estimations are the highest among the three models. In turbulent flow, predictions of the models are comparable. However, in laminar annular flows, model predictions are higher than the measured data. Discrepancy between model predictions and the measured data decreases as temperature increases. In almost all cases, model predictions are higher than the measured data. Therefore, a more accurate hydraulic model should be developed to determine pressure losses of non-Newtonian fluids in annuli.

Study of Foam Flow under Elevated Pressure and Temperature Conditions (Task 9)

An extensive experimental study on the flow behavior of foam in pipe and annular geometries was conducted using a full-scale flow loop. The tests were conducted at pressures up to 700 psig and temperatures up to 185 °F. The objective of this research is development of an improved mathematical model for hydraulics of foam drilling. At the same time, flow properties of foam, its stability and compressibility were also investigated. A conventional drilling fluids hydraulic model, based on the Herschel-Bulkley rheological model, was adopted for foams using the principle of "Volume Equalization". A detailed discussion on the effects of foam generation, foam quality, pressure, temperature and geometry on foam flow behavior is presented. Results indicated that foam texture and quality significantly affect foam rheology. Pressure and temperature appear to have secondary effects. The importance of accounting for wall slippage in foam flow is highlighted and a new concept to evaluate the slip velocity in annuli is proposed. Results have shown that foam rheology can be characterized by a Power-Law model. A computer code was written based on the modified hydraulic model. Satisfactory agreement with experimental data in frictional pressure loss predictions was obtained for the flow of foams through pipes and annuli.

Experimental Study of Foam Rheology Using Rotational Viscometer and Development of Foam Generator/Viscometer (Task 9b)

One of the important findings from research Task 9 is that foam texture (i.e., bubble size, shape & size distribution) has a considerable effect on the rheology of foam. This identified the need to have an instrument that can generate foam with a controlled bubble size and is able to measure simultaneously its rheological properties. Hence a foam generator/viscometer was designed and built as a part of a new research task (Task 9b). The instrument generates foam with desired properties and measures its rheological properties. It is capable of controlling the following six variables independently: i) foam quality, ii) pressure, iii) temperature, iv) surfactants and other additives, v) bubble size, and vi) surface roughness inside the viscometer.

In addition to instrumentation development, Task 9b includes an experimental study of foam rheology. This investigation is more focused on the phenomenon of "wall slip". In order to quantify the wall slip, a variety of roughnesses were applied to the surfaces that the foam is in contact with while rheology measurements are being made. Foam rheology tests were performed using a Couette-type rotational viscometer with different cup-rotor assemblies that have different surface roughnesses. Foams with varying qualities were generated using the foam generator/viscometer system and the Dynamic Testing Facility (see Section 11) and tested under ambient temperature and low pressure conditions. Experimental results indicated that foams behave as non-Newtonian fluids with shear-thinning properties. Rheological measurements obtained using different cup-rotor assemblies showed significant differences suggest that the possibility of wall slip.

Study of Cuttings Transport with Aerated Mud under EPET Conditions (Task 10)

Flow and cuttings transport experiments were conducted with aerated mud at elevated pressures and elevated temperatures. During flow test runs, water and air flow rates were in the range of 50-250 gal/min (0.19-0.95 m3/min) and 50-150 scf/min (1.42-4.25 m3/min); and measurements of frictional pressure drop and mixture density over the entire annular section were carried out. Stratified and slug flow were the two flow patterns observed over the range of the chosen test matrix. The experimental results indicate that temperature influences the two phase flow patterns and frictional pressure losses.

The cuttings transport experiments were carried out at elevated pressures and temperatures ranging from 185 to 500 psi and 80 to 175°F. The following test parameters were measured: i) cuttings weight in the annulus (the volumetric cuttings concentration); ii) mixture density; and iii) frictional pressure losses. The results clearly show that, in addition to the liquid and gas flow rates, temperature considerably affects the cuttings transport efficiency of aerated muds. The volume of cuttings which accumulated in the annulus was very sensitive to the liquid flow rate. Predominately, elevated temperature was found to cause a significant increase in the cuttings volumetric concentration at given flow conditions. The injection of air has both negative and positive effects on cuttings transport, depending on other flow parameters. The effect of pressure on cuttings concentration and frictional pressure loss is insignificant.

A mechanistic model for cuttings transport with aerated mud was developed by combining two-phase hydraulic equations, turbulent boundary layer theory and a particle transport mechanism. The model can be useful for predicting the cuttings volumetric concentration in the annulus and critical pressure drop for preventing cuttings from deposition. Predictions of the mechanistic model are in agreement with measured data.

Development of Cuttings Monitoring System (Task 11)

The objective of this task is to develop a non-intrusive cuttings bed monitoring system. Four possible approaches were considered to tackle this problem. After evaluating the possibilities, we decided to develop an ultrasound measurement system that monitors the cuttings bed in the test section. Cost and safety issues mainly drove this decision. Therefore, a circuit board was designed and developed to collect data from ultrasound sensors and control the functions of individual sensors that are in groups of four. The board communicates with the PC via a RS232 link. A PC is used to control the functions of the entire system and to process the collected data. After several revisions the board is now functioning with acceptable noise level. Hence, we were able to conduct several tests.

Data acquisition software was developed to obtain and manipulate measurements. The software was further modified to improve the accuracy. To account for the nonlinear nature of the fluid flow we are using neural network to analyze the data being collected. We have identified and purchased a commercial neural network development package. The neural network system is trained and tested. The data gathered from various static and dynamic tests is used for the purpose of training the neural network system.

We tested the system with clear plastic on one end of the test cell to verify that we could distinguish between different depths of sand in a static bed of sand. The results indicated that we could distinguish different sand levels. We also have devised a way to secure the sensors in the caps in exactly the same manner to achieve consistency of performance. Additionally, dynamic tests were performed using the Dynamic Testing Facility (DTF). Finally, a preliminary test was conducted on the main flow loop at 100 gpm flow rate and 20 lb/min cuttings injection rate. The measured bed thickness using the ultrasonic method showed a satisfactory agreement with nuclear densitometer readings. Thirty different data points were collected after the test section was put into liquid holdup mode. Readings indicated 2.5 to 2.7 inches of sand. The corresponding nuclear densitometers readings were between 2.5 and 3.1 inch.

Development of Instrumentation for Foam Bubble Characterization (Task 12)

Foam bubble size and size distribution can influence the rheology and the cuttings transport ability of foams. Bubbles in a shear field (flowing) may tend to be ellipsoidal, which might alter both the rheology and transport characteristics. The objective of this task is to develop the methodology and apparatus needed to measure the bubble size, size distribution and shape during cuttings transport experiments.

In order to develop bubble characterization techniques, and test instrumentation being design for cuttings tomography under dynamic conditions, a facility referred to as the Dynamic Testing Facility (DTF) was designed during Year 1 and completed during Year 2. The DTF was constructed on a 16’ x 2-½’ skid with a Unistrut cage for supporting the pipe and other components.

A Bubble Characterization Cart was designed and constructed to analyze bubble size distribution of foam in the ACTS flow loop using a stop-flow technique. The stop-flow technique was developed to allow the capture of foam images while foam is flowing. In this technique the flow rate is sufficiently rapid to give a relatively short residence time between the ACTS flow loop and the visualization cell (5-10s). A microscope equipped with a digital camera is mounted over the view port to capture foam images. After evaluation of several image processing software packages, a package was selected and tested.

Furthermore, to remotely monitor the test section through the view ports, a wireless on-line monitoring system with a Client Server control was developed and tested. Sharp images were obtained through a CCD camera with the use of a ring light or fiber light. The results indicated that up to 15 frames per second videos can be captured and transmitted with this system.

Study of Cuttings Transport with Foam under Elevated Pressure and Elevated Temperature Conditions (Task 13)

This research task was not in the original proposal. It is a continuation of two other research tasks (Task #6 and Task #9) on foam rheology and cuttings transport. A literature survey, mathematical modeling, and preliminary rheology and cuttings transport tests have been conducted. The objectives of this research are: i) to investigate experimentally foam rheology under EPET conditions using pipe viscometers; ii) to determine experimentally volumetric requirements for effective cuttings transport with foam in horizontal wellbores without pipe rotation; iii) to develop a mechanistic cuttings-transport model; and iv) to verify the cuttings transport predictions of the model with experimental data.

After successful completion of the first trial foam test, two sets of rheological tests were conducted at different foam flow rates while keeping other test parameters constant. A preliminary cuttings transport test was also conducted to evaluate the new cuttings injection auger, densitometers response and carrying capacity of foam. In addition to this, laboratory foam stability tests were performed with 100-ml liquid phase samples.

Safety Program (Task 1S)

The objective of this task is to identify problems (findings) that might result in injury, property damage or the release of environmentally damaging materials, to provide recommendations to minimize the findings, and to develop an action plan based on these recommendations.

This project was initiated during the fourth quarter of 2000 to assess the hazards associated with the Advanced Cuttings Transport Facility (ACTF) and develop an Action Plan to address problems discovered during a Hazards Review. The Hazards Review is used to improve the overall safety characteristics and reduce the possibilities of accidents. Each individual component of the ACTF is examined for the effect and consequences on safety, health, and the environment, of the component in all possible operational modes.

3. Flow Loop Design and Construction (Tasks 1-5)

3.1 INTRODUCTION

The flow loop project we now call Advanced Cuttings Transport Study (ACTS) is complete. This report is intended to recap the evolution of the flow loop from a design and construction perspective from its conception.

The concept for the flow loop began with BDM and The Unites States Department of Energy (DOE). The University of Tulsa (TU) was chosen as a most logical place to locate the test loop. In the summer of 1997 a contract was entered into between TU and BDM, funded by the DOE, to develop designs and a project plan.

A number of interested industry representatives including those from AMOCO, ARCO, Canadian FracMaster, Schlumberger-Dowell, Halliburton, Mobil, as well as the DOE, BDM, and TU met to address the basic objectives of the Cuttings Transport Facility, as it was called then, and the physical dimensions and capabilities that should be included.

A site at TU's "North Campus" research facility was chosen as the location (Fig. 3.1).

Fig. 3.1 Construction site at TU's "North Campus"

Basic designs were discussed with the industry participants and developed into the flow loop concepts for the initial construction and future phases which would ultimately include aerated fluids and foam, cuttings transport, drill string rotation, and test section elevation.

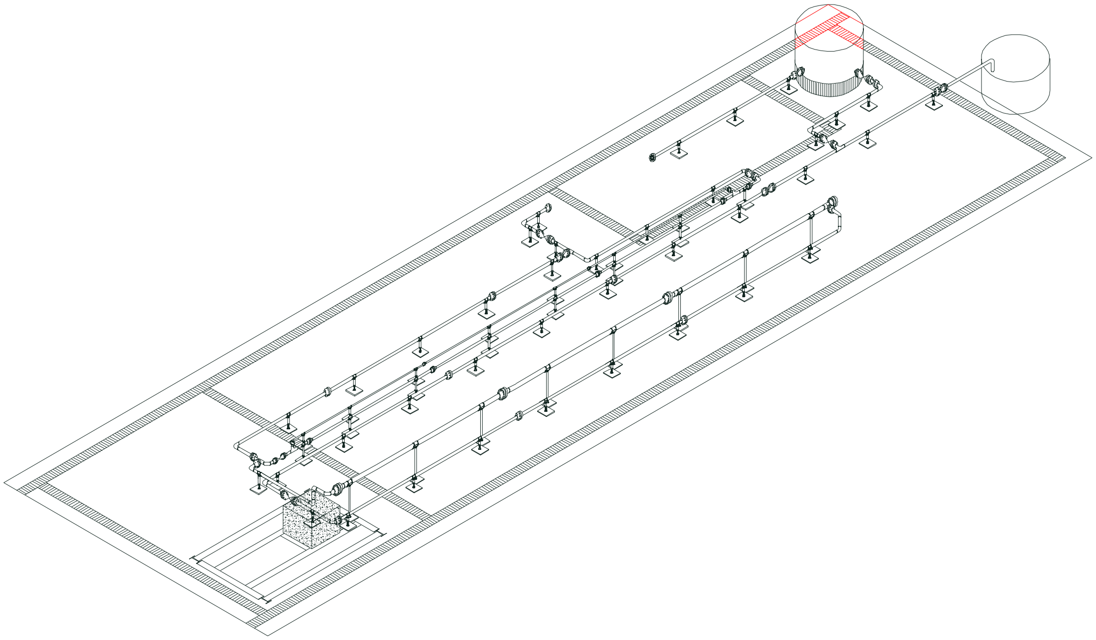

Fig. 3.2 Basic piping configuration

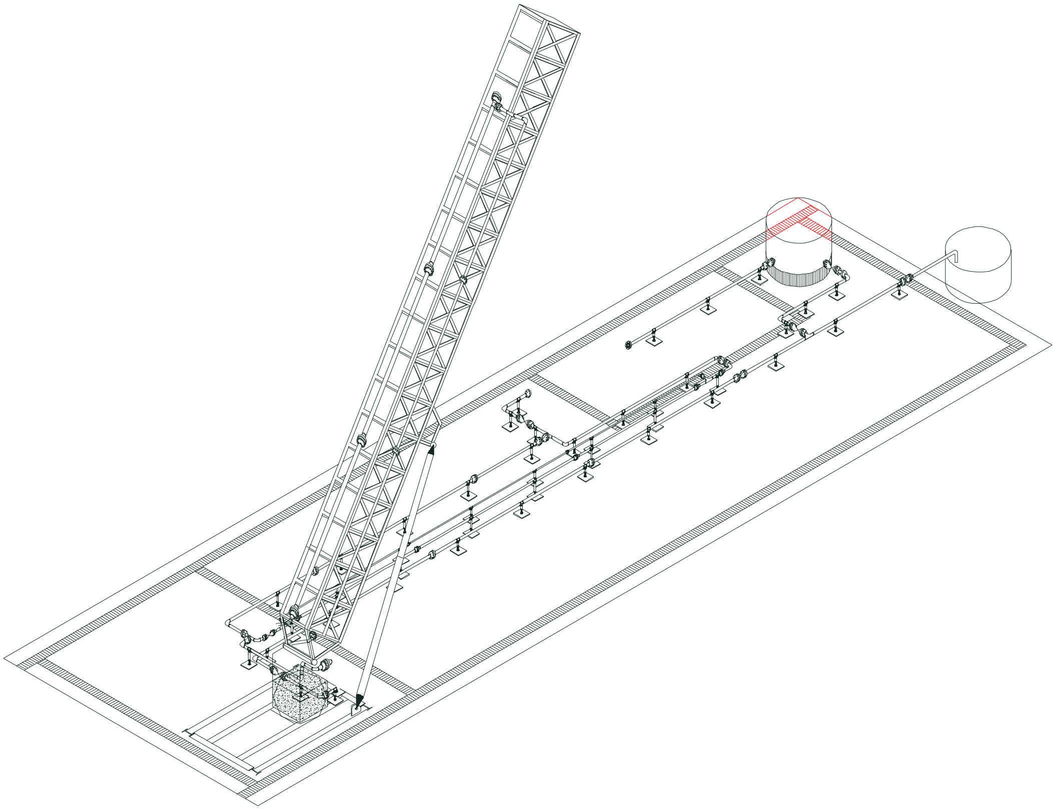

Fig. 3.3 Mast elevation

Following this initial contract for loop design, a subsequent contract was entered into by TU with BDM, again funded by the DOE, for an initial construction phase that was to build a basic test loop and flow water up to 250 gpm at pressures up to 700 psi.

In May of 1998 construction began. Equipment was moved in:

Fig. 3.4 Construction site (May of 1998)

The foundation was prepared (Fig. 3.5):

Fig. 3.5 Foundation work

Trenches, forms, and reinforcing steel were placed (Fig. 3.6):

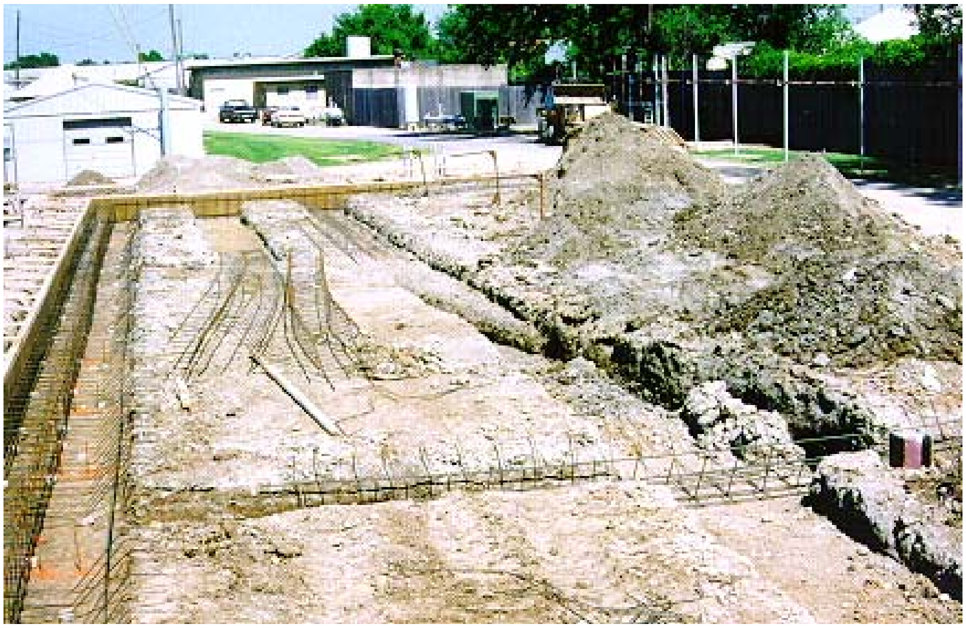

Fig. 3.6 Reinforcing steel

Concrete was poured (Fig. 3.7):

Fig. 3.7 Concrete pouring

Piping was fabricated off site and brought in (Fig. 3.8):

Fig. 3.8 Fabricated pipes

The piping was assembled (3.9):

Fig. 3.9 Prefabricated piping

Halliburton donated a mud pump (3.10):

Fig. 3.10 Donated mud pump (Halliburton Frac Pump)

And, on September 24, 1998, the new test loop was dedicated (Fig. 3.11):

Fig. 3.11 When the test loop was dedicated (September 24, 1998)

Subsequent to completion of the basic flow loop a proposal was submitted by TU to the DOE for a five-year project which would be structured in such a manner as to provide for a logical progression of research experiments as well as additions to the flow loop itself. BDM was not involved with this new proposal. The flow loop construction sequence was defined as:

Year 1 – Addition of elevated temperature capability;
Year 2 – Addition of two-phase (air, liquid, and foam) capability;
Year 3 – Addition of cuttings injection and separation facilities;
Year 4 – Addition of drill pipe rotation;
Year 5 – Addition of drilling section elevation.

Because of the timing of the new proposal, fiscal Year 1 began on July 14, 1999 and so for each subsequent year:

Year 1 – July 14, 1999 thru July 13, 2000
Year 2 – July 14, 2000 thru July 13, 2001
Year 3 – July 14, 2001 thru July 13, 2002
Year 4 – July 14, 2002 thru July 13, 2003
Year 5 – July 14, 2003 thru July 13, 2004

3.2. ADDITION OF ELEVATED TEMPERATURE CAPABILITY

On July 14, 1999, the ACTS JIP was officially formed. In the interim between initial loop construction and the 5 Year Proposal, a number of tests were performed using water only. These tests were performed for the purpose of calibrating the instruments. Considerable problems were being had with the differential pressure meters. After several months of work it was discovered that the three differential meters that we purchased had sequential serial numbers; that is, they were manufactured at the same time and all three had a faulty component in their electronics. Once they were repaired our results dramatically improved.

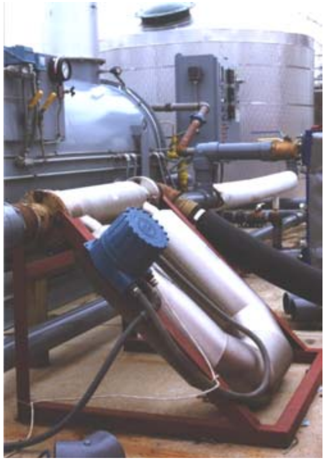

Fig. 3.12 Flow meter (Micro Motion)

Fig. 3.13 Indirect fired boiler (2 mm BTU)

Also during this time we installed a pulsation dampener downstream of the Halliburton pump. This is a great improvement. The rheology section was modified to allow for either parallel or series flow. A Micro Motion flow meter (Fig. 3.12) was added replacing the sonic doppler meters that we had purchased the previous year. Temperature transmitters were added in anticipation of the Year-1 (Task 1) construction. And, instrumentation was added to the 4-inch return line in order that it, too, could be used for rheology measurements.

During Year 1 construction a 2-MM BTU indirect fired natural gas boiler (Fig. 3.13) was purchased and installed, two plate-style heat exchangers were installed, and a water cascade cooling tower was installed. Additionally a second 100-bbl mud storage tank was purchased and installed, as well as a small 5-bbl tank (Fig. 3.14) with mixer and transfer pump to mix drilling muds and transfer them to one of the larger tanks.

Fig. 3.14 Mud mixing tank

A considerable amount of piping (Fig. 3.15) was installed to make the new tanks, heat exchangers, and cooling tower functional, and a new gas supply line was laid from some distance away to the test loop in order to supply the boiler. A canopy was constructed over the boiler (Fig. 3.16). And, lastly, an insulation contractor was hired to insulate the flow loop piping (Fig. 3.17) and the tanks (Fig. 3.16) to minimize heat loss during elevated temperature experiments.

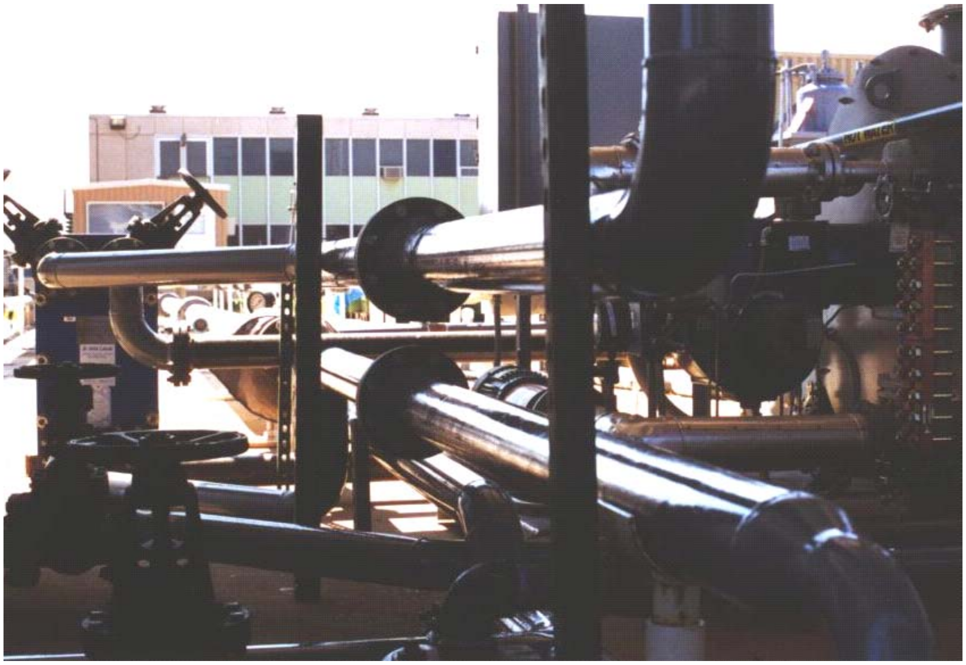

Fig. 3.15 New piping

Fig. 3.16 Tank insulation

Fig. 3.17 Piping insulation

Fig. 3.18 Canopy cover over the boiler

3.3 ADDITION OF TWO-PHASE CAPABILITY

Subsequent to Year-1 construction and before Year-2 construction began, a series of experiments utilizing a synthetic drilling mud supplied by Petrobras was conducted at temperatures up to 180°F and pressures up to 1200 psig. This was the first scheduled series of experiments for the new test loop (Task 8).

During the progression of the tests it was discovered that the synthetic mud would flash to steam on the downstream side of the pressure control choke valves. These valves were bladder style chokes and operated by applying compressed nitrogen gas on the outside surface of the bladder to create a constriction on the inside of the bladder. The velocity and temperature extremes created when the mud flashed were outside the capabilities of the bladder material. After several, sometimes dramatic, failures of the chokes, they were replaced with a Fisher cage and bean-style choke.

The new Fisher choke proved to work very well; however, after very little use it was discovered that fine abrasives in the Petrobras mud were quickly eroding the valve cage (Fig. 3.19):

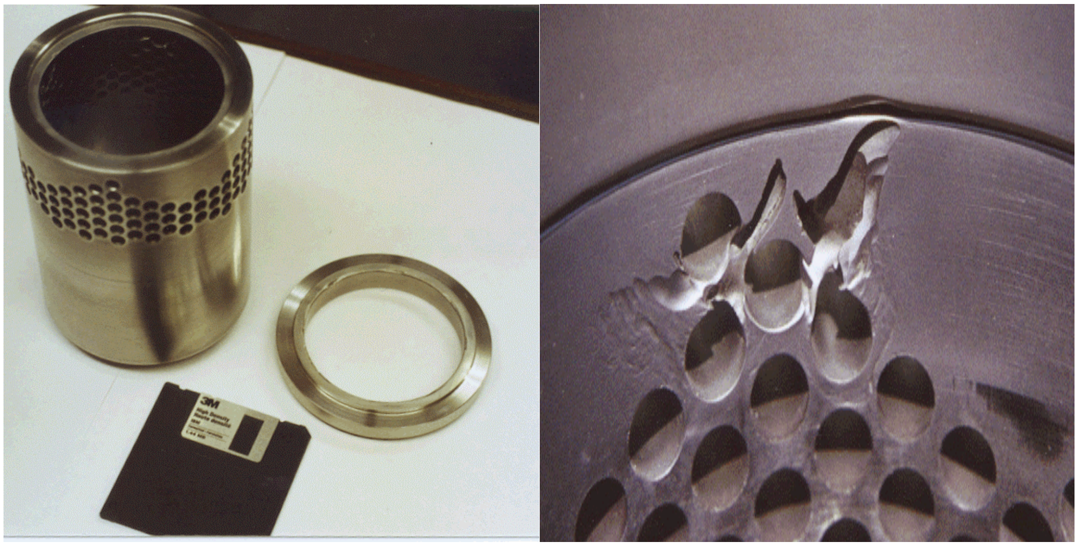

Fig. 3.19 Fisher choke

At this point, Fisher Control Valves donated two small angle chokes (Fig. 3.20) to the project. We installed these in parallel with the result that we could achieve any desired back pressure and had very good control of the process:

In summary, Test loop construction for year-two (Task 2) consisted of:

1. A diesel powered air compressor capable of 400 cfm at 200 psig (Fig. 3.21);
2. An air accumulator tank (Fig. 3.21);
3. An air/liquid separator tower (Fig. 3.22);

4. Injection pumps for water, surfactant, and foam breaker (Fig. 3.23, 3.24, and 3.25);
5. Variable Frequency Drivers for each injection pump;
6. Tanks for surfactant and foam breaker;
7. The Moyno Tri-Phaze pump and Variable Frequency Driver (Fig. 3.26);
8. Pressure relief valves;
9. A static mixer;
10. Micro Motion meters for the air system and the water injection system;
11. An air pressure control valve;
12. A pressure control valve for the separation tower;
13. A mist eliminator pad for the separation tower (Fig. 3.27);
14. Many miscellaneous pipe and instrument fittings to hook it all up;
15. Wiring for power and instrumentation.

Fig. 3.20 Angle chokes

Fig. 3.21 Air compressor and air accumulator tank

Fig. 3.22 Separator tower

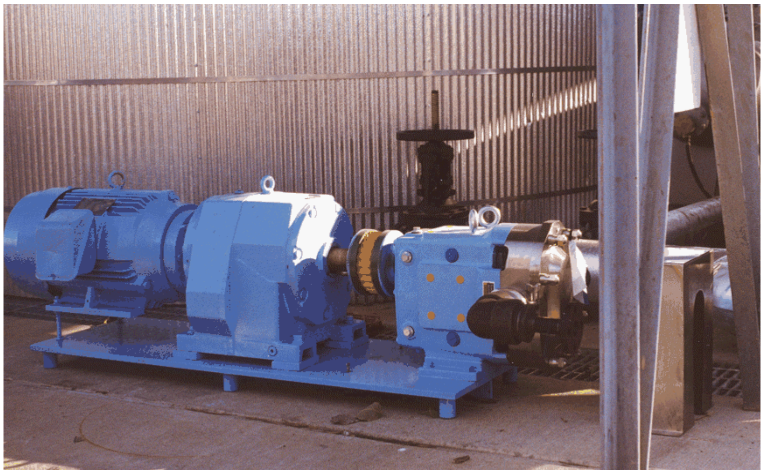

Fig. 3.23 Liquid injection pump

Fig. 3.24 Surfactant injection pump

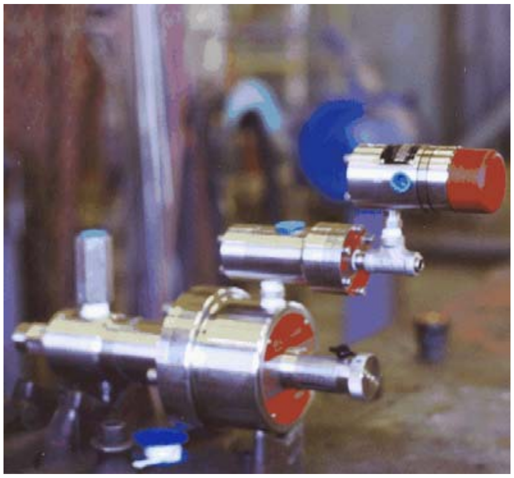

Fig. 3.25 Foam breaker injection pump

During this season's construction phase, considerable effort was put into cleaning out the Petrobras synthetic drilling mud used in experimentation last year. To say the least, cleaning up the synthetic mud was a challenge.

The new experiments (Task 9) were studies on foam flow in simulated down-hole conditions. The synergy of the newly installed component parts to create, control, and to break foam was unique. The technique used was called "air on demand". The air component is introduced to the suction side of the Moyno pump (Fig. 3.26) at any pressure up to 200 psig. Liquid is pumped into the Moyno pump suction at any flow rate up to 75 gpm. The liquid injection pump is a positive displacement lobe pump with a VFD controller and its own Micro Motion flow meter. Whatever flow rate the computer called for, it deliveries at whatever pressure it encounters. The air supply also has its own Micro Motion flow meter. The operator determine ahead of time what volumetric flow rate of air is needed for the experiment and what volumetric flow rate of liquid. Once the liquid volume is set into the computer, the speed of the Moyno pump and/or the air supply pressure is manually adjusted until the air volumetric flow rate is satisfied.

Foam is generated by injecting surfactant immediately downstream from the Moyno pump where it would be well mixed with the air and water flowing there and then the mixture is sheared through a partially closed ball valve.

The technique of adding energy to the foam mixture with the ball valve was not the initial plan. During construction, a static mixer was installed in the piping downstream of the Moyno pump. It was planned that this would provide not only sufficient mixing to fully form the foam but, by injecting surfactant at different locations along the length of the static mixer, different bubble characteristics might be achieved.

During the course of the experiments, however, it was observed that the foam was not fully formed (equilibrated) and that more energy was required to do so. By partially closing the ball valve located immediately upstream of the static mixer it was discovered that the differential pressure drop in the rheology section piping would cease to change, indicating that the foam was equilibrated and its rheological properties had stabilized.

Fig. 3.26 Moyno Tri-Phaze pump

Fig. 3.27 Demister pads

It was decided that the bean and cage Fisher choke valve that had originally been purchased in replacement of the bladder chokes should be refurbished and installed in order to automate future foam experiments.

The Separator Tower (Fig. 3.22) however was the key component in the year's research. The basic operation is simply that of a common vertical liquid/gas separator but its functions in foam breaking and back pressure control are unique. The tower performs three basic functions:

1. <u>Liquid/Gas Separation</u>. Liquid/gas separators are more commonly thought of as horizontal vessels where liquids are collected over a series of baffles and drained through one or more outlets along the bottom of the vessel. Gas is vented through an outlet on the top of the vessel. In our case, because of the foam and because of the tower's future application as part of cuttings separation, a vertical design is needed. The liquid/gas separation function however, is the same in a vertical design as it is in the more traditional horizontal separators.

2. <u>Foam Breaking.</u> The Separator Tower includes three chemical injection ports along the incoming piping. Injection quills at each of these ports spray defoamer into the foam stream to break the foam bubbles. In practice this has proved to be a good first step in foam breaking. The second step in foam breaking comes by way of holding a liquid level inside the tower. A differential pressure transmitter monitors the liquid level inside the tower and communicates that information to the computer. Down stream control valves (the aforementioned angle choke valves operating in parallel) open and close to maintain the liquid level at the desired height. This plays a role in breaking the foam because the collected liquid is rich in defoamer chemical. Contact between remaining bubbles from the initial defoamer spray and the defoamer-rich liquid provides additional foam breaking. It is important to maintain a liquid level near the point where foam entered the tower. Additional foam breaking occurs at the de-mister pads (Fig. 3.27).

3. Demister pads. These pads, located near the top of the tower, provide a coalescing point where gas is allowed to continue to the vent point and the liquids drain back down inside the tower. The system works well. Those occasions when foam is not completely broken and bubbles vent with the gas appear to be explainable by way of having the proper ratio of defoamer for the situation and maintaining a constant gas velocity at the vent. Experimentation showed that the amount of defoamer required can vary considerably by conditions other than flow rate. Temperature, foam composition, and pressure all play a part. Also, if the computer program for the vent control valve does not provide for an even vented gas flow rate and flow surges occur, then unbroken foam is picked up in the flow surge and vented before it is completely broken. It requires a finely-tuned process and is not simple, but the system functions well when all parts are working as designed.

4. Back Pressure Control. During foam or any liquid/gas experiment, the gas vent on top of the tower actually controls the back pressure. Liquid is maintained at a desired level inside the tower by bleeding the liquid off via down stream control valves (Fig. 20) while the gas pressure inside the tower (and therefore back pressure in the test loop) is maintained by the gas vent control valve.

3.4 ADDITION OF CUTTINGS INJECTION AND REMOVAL FACILITIES

As experiments were being conducted in the summer of 2001, plans for Year -3 (Task 3) constructions of cuttings injection and removal facilities were rapidly taking shape. A number of considerations were made as to location of the injection point and the volume of cuttings needed to maintain high cuttings injection rate experiments. A location was chosen downstream of the Moyno pump. It was recognized that it would mean that the injection hopper would have to have a 2000 psig (was 275 psig) operating pressure but it was noted that this would have a number of advantages:

1. Injection of rock downstream of the Moyno Pump and the static mixer helps minimize rock breakage and changes in particle size during tests. One of the objectives is to obtain as many tests as possible from a given load of rock.

2. Placement of the rock hopper closer to the annular test section helps optimize the use of the available rock capacity for cuttings-transport tests, and thereby make the loop more productive. i.e., more testing is possible in less time.

3. By injecting the cuttings downstream of the Moyno Pump, this extends the useful life of this very expensive pump.

4. Since it was now known that the static mixer did not always provide the desired foam rheology / texture, there was a need to use other devices to accomplish this task. Placing the injection hopper downstream of the Moyno pump and not passing cuttings through the “foam generator”, allows the selection of a wider range of choices for foam generation devices

5. The location avoids possible plugging of the static mixer with cuttings.

6. Since the basic design generates foam downstream of the Moyno Pump, it is difficult to achieve a uniform feed of cuttings through the pump when there are small liquid flow rates, such as occur with high-quality foams. By injecting cuttings downstream of the static mixer, after the foam is generated, this problem is avoided. This allows a more uniform feed of cuttings into the Loop and avoids introducing slugs at the injection point.

7. The location avoids passing of cuttings through the elbows and turns in the pipe at the discharge end of the Moyno Pump. This has the effect of reducing erosion in those areas of the Flow Loop.

8. By placing the hopper downstream of the pumps, it allows cuttings-transport tests with either the Moyno Pump (for foams and compressible fluids) or the Halliburton Frac Pump (for single-phase drilling fluids). A high-pressure (2,000 psi) rock hopper enables tests with either pump.

9. This location provides the potential to conduct future tests with compressible fluids at higher pressures; i.e., greater than 650 psi. Otherwise it would require the installation of another pump like the Moyno pump that could handle two-phase gas/liquid fluids and discharge pressures up to 2,000 psi.

With the design criteria finalized a dramatic change took place in the appearance of the test loop. The air/liquid separator (Fig. 3.28) was dismantled and shipped to the contractor who was building the injection and removal towers. The new towers were fabricated (Fig. 3.29), brought on site (Fig. 3.30) and installed (Fig. 3.31).

Fig. 3.28 Dismantled separator tower

Fig. 3.29 Fabrication of the towers

Fig. 3.30 Towers brought on site

Fig. 3.31 Towers installed

Fig. 3.32 Injection and removal towers after installation

Fig. 3.33 Johnson Screen placed in the separation tower

During this time a completely new control and data acquisition system was installed. Up to this time each instrument was hard-wired into the control building where the data was sequenced and fed to the computer. The massive numbers of wires traveling to and from the control building had grown unmanageable with the original system. A new field point data system was adopted. This system gathers all of the instrumentation and control wires on the test loop into one of two central locations. These locations (nodes) (Fig. 3.34) sequence the data on-site and feed it to the control room (Fig. 3.35) over one set of wires. In the control room the data is received, sorted, and fed into the computer in a similar manner as it was before, but now it is prioritized, scheduled, and, most importantly, sequenced on-site rather than hard-wired all the way to the control room. There are three Nodes that consist of a FP-2000 real-time-capable Ethernet controller. Each node is configured with input and output modules that support the wide array of transmitter, control and valve requirements needed to operate our test facility. There are analog 4-20 mA outputs, analog 4-20 mA inputs and digital output modules. Each of these can be swapped easily to aid in trouble shooting of technical problems. The FP-2000 modules are connected via Ethernet to a Net gear Switch with a Gigabyte uplink port to ensure plenty of bandwidth to the main CPU. We currently operate the system at 2 scans per second.

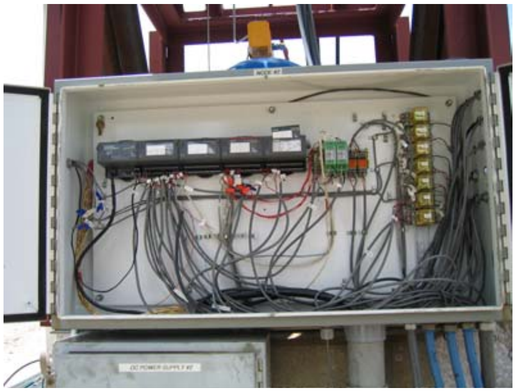

Fig. 3.34 Field point node

Fig. 3.35 Control room

We also installed an emergency stop system that is manually operated from the control cabin. It utilizes relays that return electronically controlled valves and motors to the default position when activated. We have separate controllers for the Hardy Load Cells and the Ronan Density Meters. They provide a 4-20 mA output signal that interfaces with our DAQ system. The data is then recorded for later use by the student. The new system immediately added over 17 new data points being received and is expandable to handle virtually any number of points that may be desired in the future.

As with anything in the field of experimentation there comes the opportunity for everything to work perfectly as intended and there is the opportunity for “working out the bugs.” With the new towers there were many things that worked perfectly. Two things were not as perfect as we had hoped. The cuttings injection rate was acceptable, but still not as precisely controllable as we had hoped. Also, the system to weigh the cuttings over time as they are being injected and weighing them over time as they are being collected, proved to be neither consistent nor sufficiently accurate. The injection rate problem was not serious enough to require immediate attention although an upgrade to the procedure was budgeted for Year 5. The cuttings weight measurement problem was too serious to use as designed. An alternative method consisting of flushing the cuttings to a separate container and then weighing them proved adequate. An upgrade to the system was budgeted for Year 5.

3.5 ADDITION OF DRILL PIPE ROTATION SYSTEM

Year-4 (Task 4) construction proved however that sometimes things work the first time even better than you hoped for. The scheduled addition for Year 4 was drill pipe rotation. A series of support spiders (Fig. 3.36 & 3.37) was conceived which would use a conventional internally upset drill pipe thread form that is relieved to include high density polyethylene bushings, a dirt seal, and a pressure seal. Separate sets of spiders were made to accommodate concentric operation and two different levels of eccentricity.

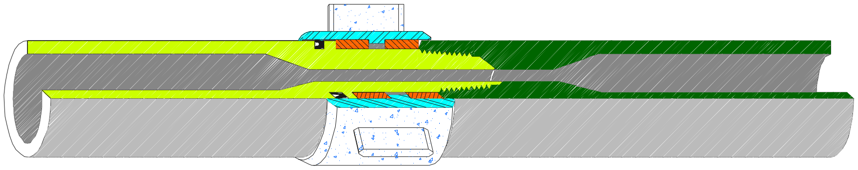

Fig. 3.36 Support spiders

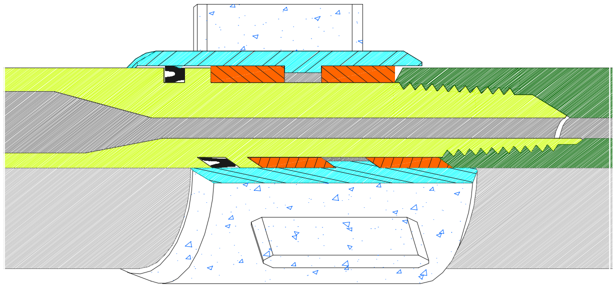

Fig. 3.37 Details of support spiders

A blind flange was machined (Fig. 3.38) to accept a drive shaft that connected to the drill pipe. Two additional blind flanges were also machined for different degrees of eccentricity. A hydraulic motor and chain drive complete the rotary head and provide the rotation (Fig. 3.39):

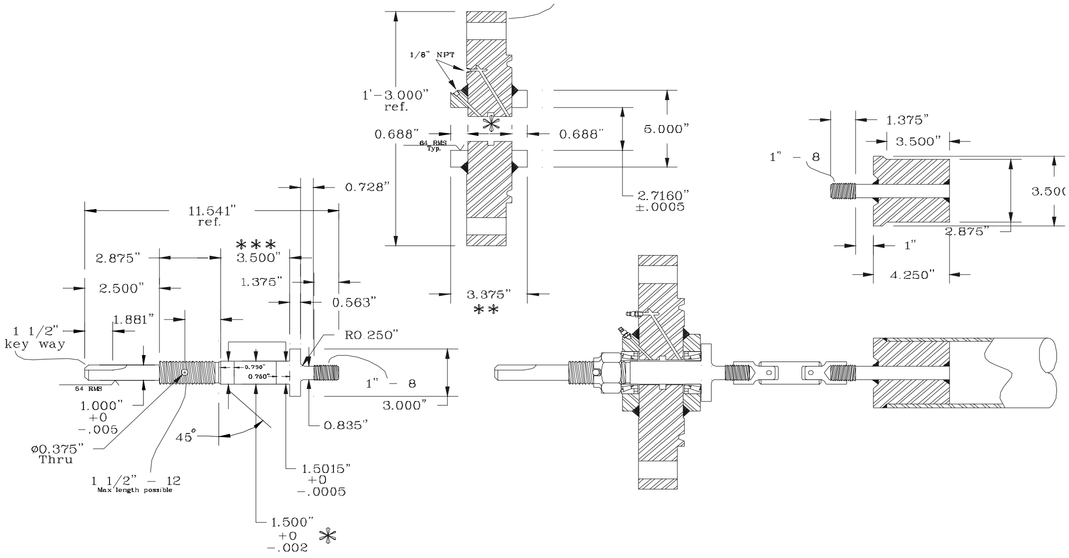

Fig. 3.38 Machined blind flange

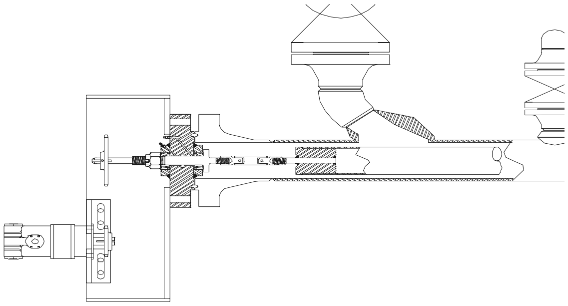

Fig. 3.39 Rotary head

Fig. 3.40 Rotating head

The system works very well. During this time a drilling choke was received from SWACO. This choke (Fig. 3.41) was installed upstream of the cuttings removal tower and will give us a secondary location to control back pressure. This is advantageous, especially with two-phase and foam experiments because the extra velocity created by the expanding gas helps sweep cuttings from the piping and is also thought to be beneficial in breaking foam.

Also added during this time were basket strainers (Fig. 3.42) to help trap fine particulates from the cuttings. During normal operation the cuttings rub against each other and bang into the pipe wall breaking off small pieces that ultimately are small enough to pass through the .0600" gap in the Johnson screen (Fig. 3.33). These small pieces are very abrasive and can be damaging to other components of the test loop if allowed to freely circulate.

Fig. 3.41 SWACO choke

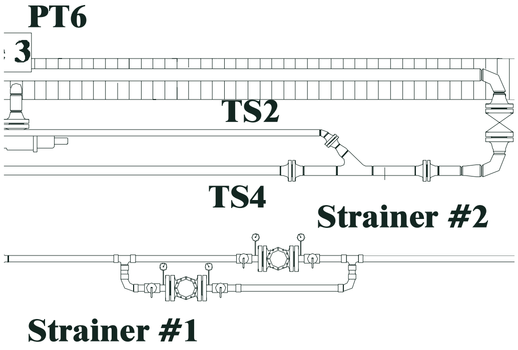

Fig. 3.42 Strainers

An extension to the existing canopy (Fig. 3.43) was also made. This helps protect the equipment and also improves the working environment during hot summer days or inclement weather:

Fig. 3.43 Extension to the existing canopy

3.6 ADDITION OF DRILLING SECTION ELEVATION

Year-5 (Task 5) construction is the addition of drill string elevation. It was planned that surplus mast sections (Fig. 3.44), known to be available from time to time in the industry, would be used for the mast component of the construction. In fact, some excellent looking mast sections were located.

Unfortunately, due to liability concerns, we were not able to secure any design information on these. We learned that we would have to design our own mast (Fig. 3.45 and 3.46) and have it fabricated. The new mast was fabricated locally (Fig. 3.47) and delivered to the site in two pieces (Fig. 3.48); and installed (Fig. 3.49 and 3.50).

Fig. 3.44 Surplus mast sections

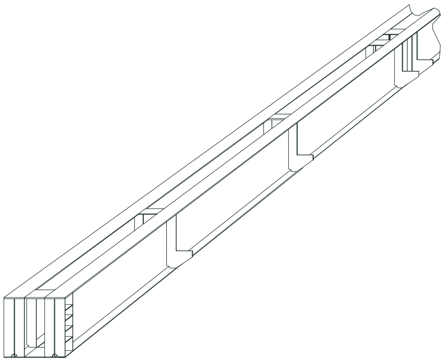

Fig. 3.45 I-beam style mast

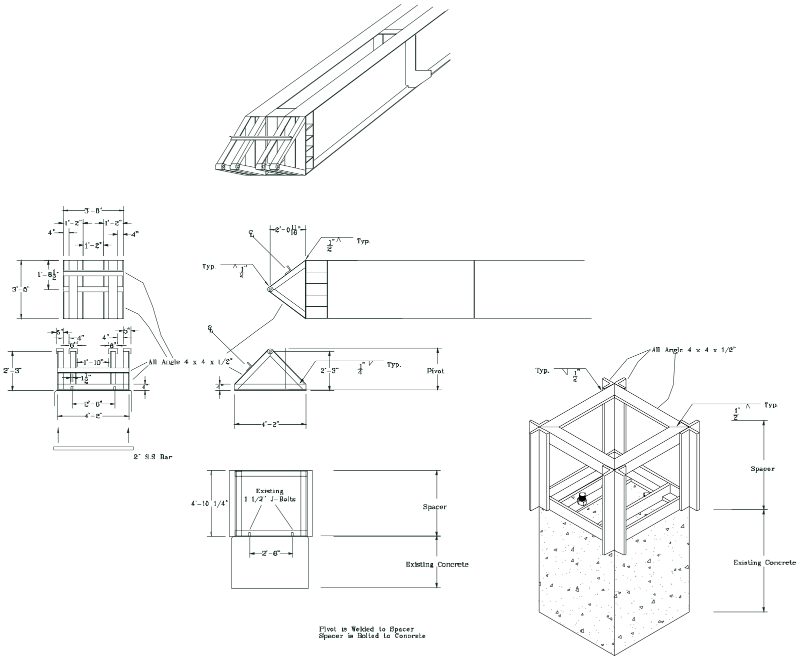

Fig. 3.46 Design of twin I-beam style mast

Fig. 3.47 Fabricated new mast

Fig. 3.48 Delivered mast pieces

Fig. 3.49 Assembling of a hinged joint

Fig. 3.50 Assembling of mast pieces

During installation, hard piping make-ups using Chiksan joints connect the Drilling Section and 4-inch return line and allow for full movement of the mast from horizontal to vertical.

Additionally, flexible hoses (Fig. 3.51) have been installed to isolate both towers from piping loads that have been blamed for inconsistent readings in the tower load cells.

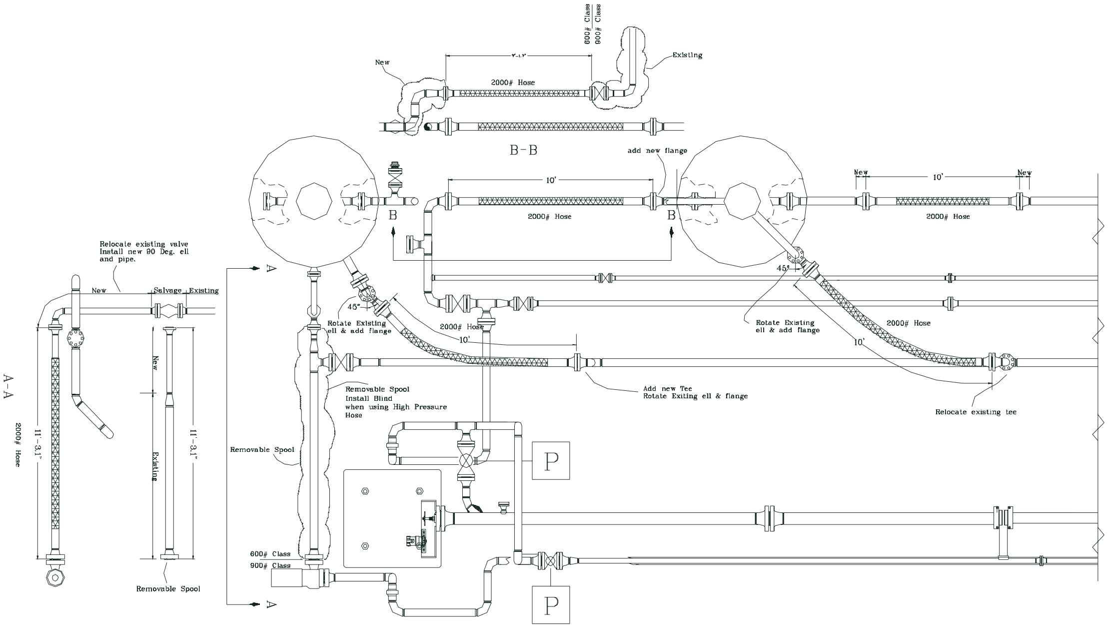

Fig. 3.51 Flexible hoses

Also, piping has been installed which will allow closed-loop operations. It was decided that the option to be able to recirculate continuously within the test loop would be advantageous.

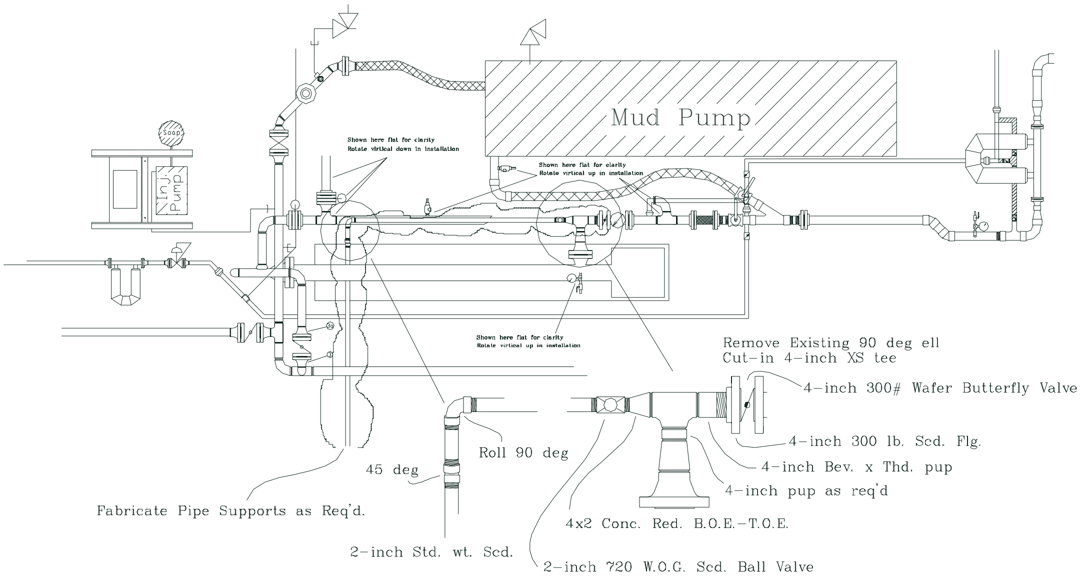

Fig. 3.52 Closed loop piping details

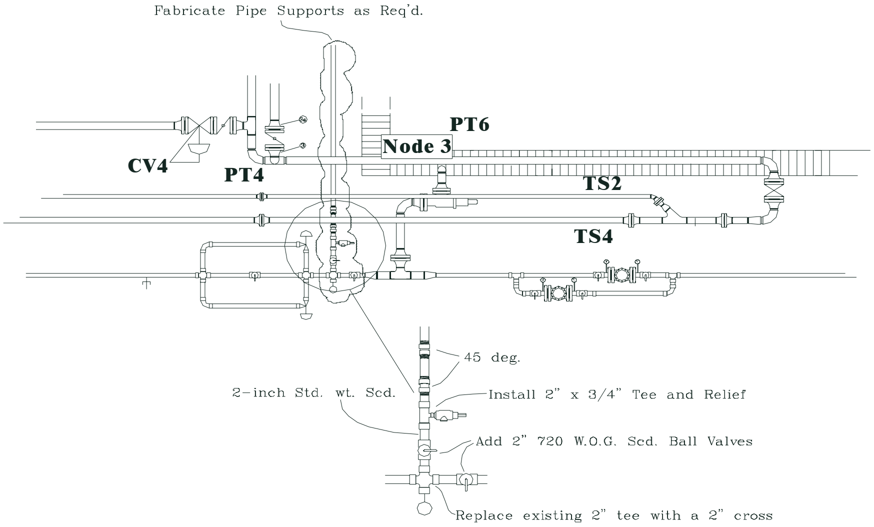

Fig. 3.53 Closed loop piping

At horizontal, the mast centerline is approximately 10-feet above ground (Fig 3.54).

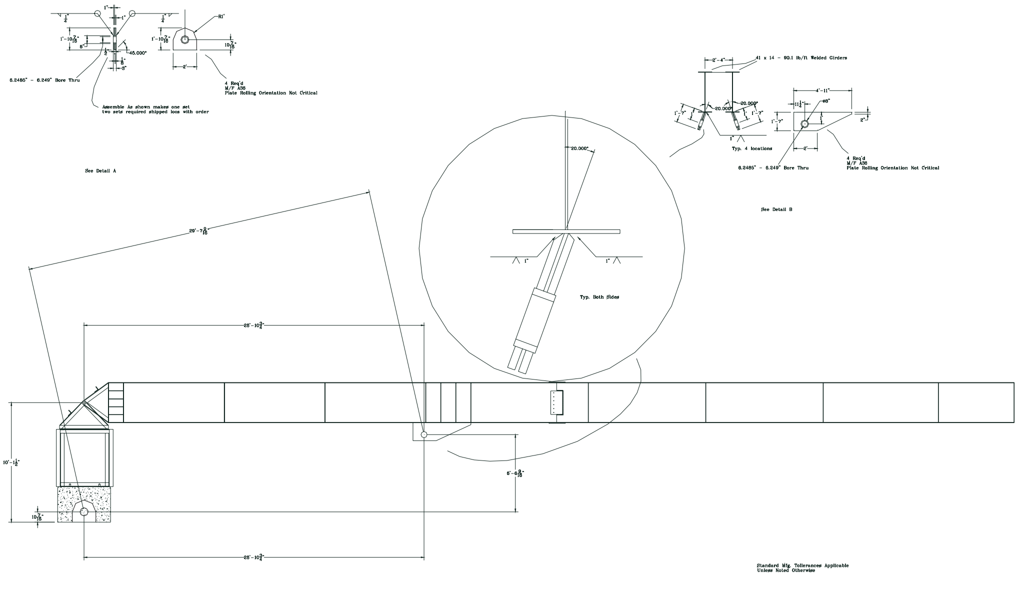

Fig. 3.54 Mast centerline

The hydraulic cylinders are splayed out for lateral support (Fig. 3.55).

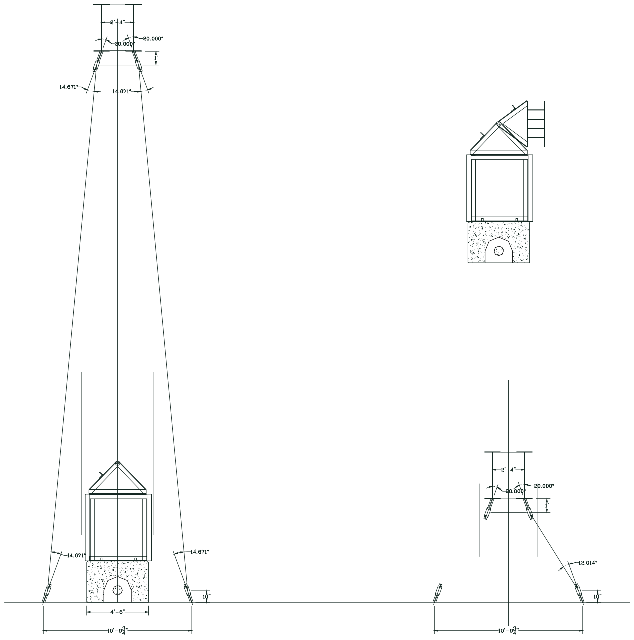

Fig. 3.55 Hydraulic cylinders

Because the hydraulic cylinders are splayed out nearly 11-feet wide at the base but only 2'-4" at the mast, the heim joint end connection points for the hydraulic cylinders are angled 20 degrees. This complicates the hydraulic cylinder design and requires 30 degrees of rotation at the end connections. The heim joints are capable of 40 degrees of rotation but when the cylinders were first received we discovered we had not specified the width of the clevis ends and that they were so closely spaced together as to restrict the angle of rotation. The cylinders were returned to the manufacture for re-work.

On Wednesday June 23rd we raised the mast (Fig. 3.56) on the ACTS flow loop for the first time. The initial lift worked well. For the sake of safety we used a large fork lift in conjunction with the hydraulic cylinders. With the assist of the fork lift, we raised the mast approximately 10 degrees. We then continued upward using only the hydraulic cylinders to approximately 25 to 30 degrees inclination (Fig 3.57). All went very well.

Fig. 3.56 Hydraulic cylinders at approximately 10 degrees inclination

Fig. 3.57 Hydraulic cylinders at approximately 25 to 30 degrees inclination (side view)

Fig. 3.58 Hydraulic cylinders at approximately 25 to 30 degrees inclination (front view)

We decided next to lower the mast and lift from horizontal without the assist of the fork lift. While lowering the mast, it moved laterally several degrees. Upon visual inspection, severe spalling of the concrete on the face of the support pillar, and deformation of the steel support structure was observed. With the aid of a crane, the mast was then lowered to its original horizontal position. At this time, the facility is ready for testing in the horizontal position. No damage appears to have occurred in the mast itself, the hydraulic cylinders, attachment points for the hydraulic cylinders, the concrete base, the steel I-beam sub-structure, the attachment j-bolts the concrete pillar other than superficial spalling on two corners of the pillar. The support structure is still capable to provide support to the mast for all future experiments in the horizontal configuration. The support structure will, however, have to be re-built before operating the mast in any elevated configuration.

There is not one single component or action that stands out as the definitive explanation of failure of the support structure. Certainly in the higher stress condition created during the initial lift of the mast from horizontal, and through continued lifting, no problems were evidenced at all. Quite the contrary, knowing we were past the critical stress stage it was a moment of congratulation that all was going flawlessly. When the mast was begun to be lowered, however, one cylinder obviously favored the other and torsion was imposed to such a degree that the support structure became deformed (Fig. 3.59). The design of the support structure is shown in Fig. 3.60.

Fig. 3.59 Deformed mast support structure

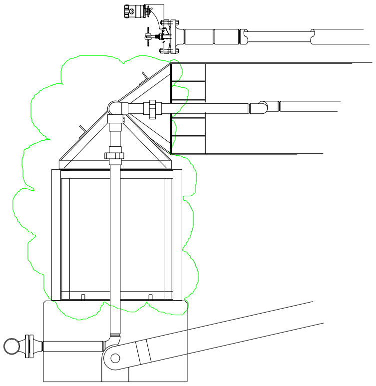

Fig. 3.60 Design of mast support

As it became deformed, the front corners (those corners closest to the hydraulic cylinders and resting on the concrete) imposed a point load onto the concrete and caused it to spall off in those areas. As the mast continued to be lowered, the support structure further deformed and the mast rotated.

The mechanism which caused one cylinder to be favored is complex beyond our means to understand at this juncture. Perhaps when we are able to disassemble the support structure we will learn more. Without any instrumentation on the cylinders to monitor the pressure on each side of each cylinder's piston we can't say absolutely that, for example, one cylinder received more pressure than the other and that caused the torsion. We do know how the hydraulic pump and the valves and lines that go to the cylinders work and we can see that it should not be possible for one cylinder to see more pressure than the other.

It is reasonable to assume that the hydraulic cylinders are not perfectly matched and therefore, even when pressurized the same amount, there would be some minor differences in their resulting force. But this should be negligible and no difference was apparent when the mast was being raised. Also, it is reasonable to assume that the cylinders were not installed with such precision as to be perfectly complimentary to each other and not have any tendency whatsoever to want to push the mast either left or right, but this too should be negligible and no difference was apparent when the mast was being raised.

The same could be said for friction in the pivot pin, alignment of the pivot pin to the axis of rotation, friction in the clevis ends of the cylinders and the alignment of those ends. However, due to the length of the mast there is an opportunity to magnify any tendencies toward misalignment. Also, there was no overt effort to design the support structure for strength against torsion. Therefore, it is our hypothesis that the hydraulic cylinders did not push at the same rate and that was the primary causative problem. Repairs, of course, are dependant on the availability of sufficient budget, however we anticipate that the repairs we will look strongly at will include a support structure resistant to torsion and a means by which the cylinders can be collectively monitored and individually controlled. We will be consulting with others who have experience with hydraulic systems similar to this to help us.

The exact nature of all repairs and modifications are yet to be decided, and ideas continue to come forth almost daily, however some of the ideas have included:

1) Rebuild the support structure with such appropriate changes as to avoid repeating the current damage;

2) Add controls and instrumentation to the hydraulic cylinders to assure that they act in unison;

3) Re-design the lift system to utilize a tower and winch system rather than hydraulic cylinders;

4) Re-design the lift system to utilize a single hydraulic cylinder;

5) Rebuild the mast to result in a lighter lifting load requirement;

6) Re-design the lift system such that the base-end connection of the hydraulic cylinder(s) would operate from a point more directly underneath the mast-end connection, thus minimizing tension loads in the mast;

7) Add provisions for crane attachment in the event that whatever lifting system is utilized happened to fail a crane could assist the mast back to horizontal;

8) Redesign to allow no more than a limited amount of elevation (example: 30 degrees, 45 degrees);

9) Some combination of two or more of the above.

Pluses and minuses of each of these could be seen as following:

1) Rebuild the support structure with such appropriate changes as to avoid repeating the current damage:

Pluses:
- Returns the mast to operational status;
- Avoids previous weaknesses;
- Relatively inexpensive.

Minuses:
- Does not correct any tendencies that the hydraulic cylinders may have for wanting to extend or retract at different rates from each other, beyond brute strength of the support structure to prevent it.

2) Add controls and instrumentation to the hydraulic cylinders to assure that they act in unison:

Pluses:
- Removes problems with the cylinders operating at independent rates.

Minuses:
- Additional expense.

3) Re-design the lift system to utilize a tower and winch system rather than hydraulic cylinders:

<u>Pluses:</u>

- Could provide a greater angle-of-attachment which would reduce loading in the mast.

<u>Minuses:</u>

- Such a mast would be subject to very large forces tending to pull it over, it would require a very massive design;
- Would probably require a large foot-print;
- Would probably require guy-wires which would be in the way of existing structures;
- Would probably limit the angle to which the mast could be raised;
- Would involve several costly expenditures, including the tower, winch, associated tackle, mast modifications for attachment, dead men for cable stays;
- Inherently less safe than the hydraulic cylinder method because there is no back-up in case a cable breaks.

4) Re-design the lift system to utilize a single hydraulic cylinder:

<u>Pluses:</u>

- Avoids the two hydraulic cylinder method that has already shown a tendency to impose torsion;
- Reasonably easy to do with materials at hand.

<u>Minuses:</u>

- Using only one of the hydraulic cylinders is marginally sufficient to raise the mast;
- Using only one hydraulic cylinder defeats the benefits of lateral support intended with the two cylinder design;
- Using only one hydraulic cylinder removes the safety factor of having a second cylinder back-up.

5) Rebuild the mast to result in a lighter lifting load requirement:

<u>Pluses:</u>

- Reduces the amount of stress on the support structure;
- Lowers the required hydraulic pressure;

<u>Minuses:</u>

- Of the total weight lifted, the piping is approximately 16,000 lbs. and the mast approximately 16,000 lbs. Even if the mast could be lightened by 25% (doubtful) the overall result would only be a 12.5% reduction in total weight;
- If lowering the weight of the existing mast, cuttings lightning holes would have a minimal affect;
- If building a new mast from scratch, the process would be costly for a small amount of benefit.

6) Re-design the lift system such that the base-end connection of the hydraulic cylinder(s) would operate from a point more directly underneath the mast-end connection, thus minimizing tension loads in the mast:

Pluses:

- Provides a more favorable angle to push the mast up, resulting in greater vertical force and less horizontal force.

Minuses:

- Would not be able to use existing hydraulic cylinders;
- New expensive multi-stage cylinder(s) would be required;
- Could possibly result in limited angles of elevation;
- Would require a large attachment plate on a relatively thin area of the concrete floor.

7) Add provisions for crane attachment in the event that whatever lifting system is utilized happened to fail a crane could assist the mast back to horizontal:

Pluses:

- Provides an extra level of safety in the event the hydraulic cylinders become inoperable.

Minuses:

- None.

8) Redesign to allow no more than a limited amount of elevation (example: 30 degrees, 45 degrees):

Pluses:

- Makes it easier to justify partial solutions;
- Allows for smaller, least expensive components to be used.

Minuses:

- Goes against the original design premise.

9) Some combination of two or more of the above:

Not applicable for an individual response.

At this time, the facility is ready for testing in the horizontal position. Elevation capabilities will be available again as soon as repairs are made.

In addition to the above items, accomplishments in Year-5 (Task 5) construction also include:

- relocating electrical panels;
- piping revisions to allow use of the SWACO choke during liquid hold-up;
- relocating the air expansion tank;
- installation of clean-out hatches in each of the 100-bbl storage tanks;
- installation of a second 6-inch view port;
- significant renovation of the operating software;

- relocating Field Point cabinet Node 2;
- significant instrument re-wiring;
- repair of missing and damaged piping insulation (victim of two years of piping revisions without repair or replacement of insulation;
- replacement of valve seats in the liquid hold-up valves;
- replacement of the liquid injection pump head;
- replacement of the jockey pump impeller;
- addition of a new fork lift;
- addition of a new scissor lift;
- refurbish the Fisher bean and cage choke valve to use in foam experiments.

Also, a new air compressor has been purchased for the ACTS test loop. The intent at the time when the budget was developed was to add to the capacity by simply increasing the quantity of compressed air that was currently being used in like and kind. From prior years expenditures the existing air compressor is capable of 400 scfm at 200 psig. Planned for Year-5, and approved by DOE in the year-5 Continuation Proposal, was $72,500 for an additional 750 scfm, also at 200 psig.

It was discovered, that for this plan to be effective all of the compressed air had to pass through the Moyno Tri-Phase pump for additional compression, but the capacity of the Moyno pump was already at maximum level.

Since the Moyno pump could not handle any additional volume, plans shifted from using the Moyno for additional compression to directly injecting the air into the flow loop. This meant that the 750 scfm at 200 psig compressor would not longer be useful and that a different compressor with greater pressure capability was needed. After extensive research into the availability of both new and used compressors, the best options became:

1) A used natural gas compression unit for approx. $80,000;
2) A 500 scfm at 650 psi system for approx. $122,000;
3) A new diesel powered Sullair compressor for approx. $110,000.

We decided that our best course of action was to purchase the new Sullair air compressor (Fig. 3.61) option #3. A new quotation was obtained at a lower price of $101,500 with a 3% discount available for payment in advance. Although more expensive, we believe that we were better served with a new unit, even though it may be of lower capacity than the other options.

We believe that this compressor will reliably serve our needs and allow us the option at some time in the future, if needs arise, to set a booster to increase the pressures. Such a booster might be loaned by a member company interested in the work, or rented. The location for the new air compressor is on a skid approximately 177.1” x 87.5” as shown in Fig. 3.61.

Fig. 3.61 New Sullair air compressor

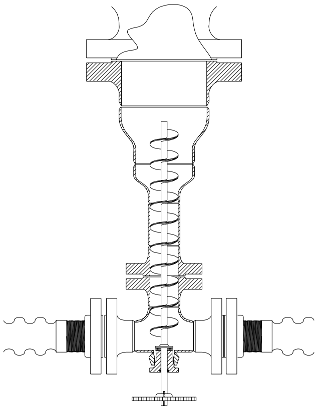

Fig. 3.62 Screw auger

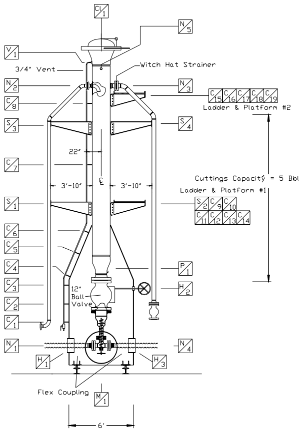

Fig. 3.63 Injection tower

The cuttings injection auger (Fig. 3.62) has been retro-fitted with a Moyno rotor and stator to improve the precision of cuttings injection. The original design consisted of a screw auger located vertically beneath the injection tower (Fig 3.63). This system proved to work adequately but room was left for improvement. The screw auger was shown to self-feed under certain circumstances. Therefore, a rotor / stator design (Fig. 3.64) such as that used by Moyno is expected to give superior results without any tendency to self-feed.

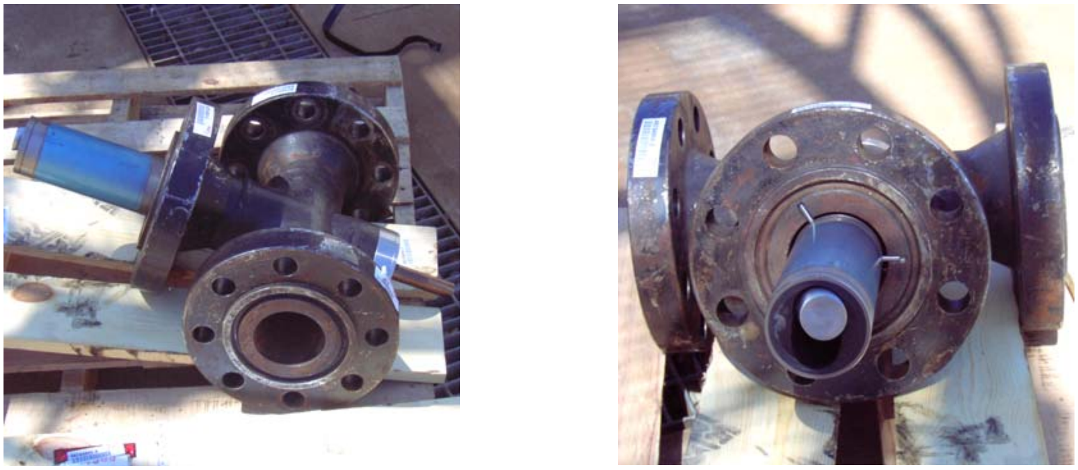

Fig. 3.64 Cuttings injection system (Moyno rotor/stator design)

Lastly, a new laboratory has been built near the ACTS test loop. The floor plan of the laboratory is presented in Fig. 3.65. It is located immediately behind the existing Control Building to serve on-going test loop experiments with auxiliary laboratory equipments such as the Fann 75 viscometer, the Foam Generator/Viscometer, and the DTF flow loop. The proximity to the existing ACTS flow loop will provide important support to the work being done there. Figures 3.66 and 3.67 show pictures of the lab.

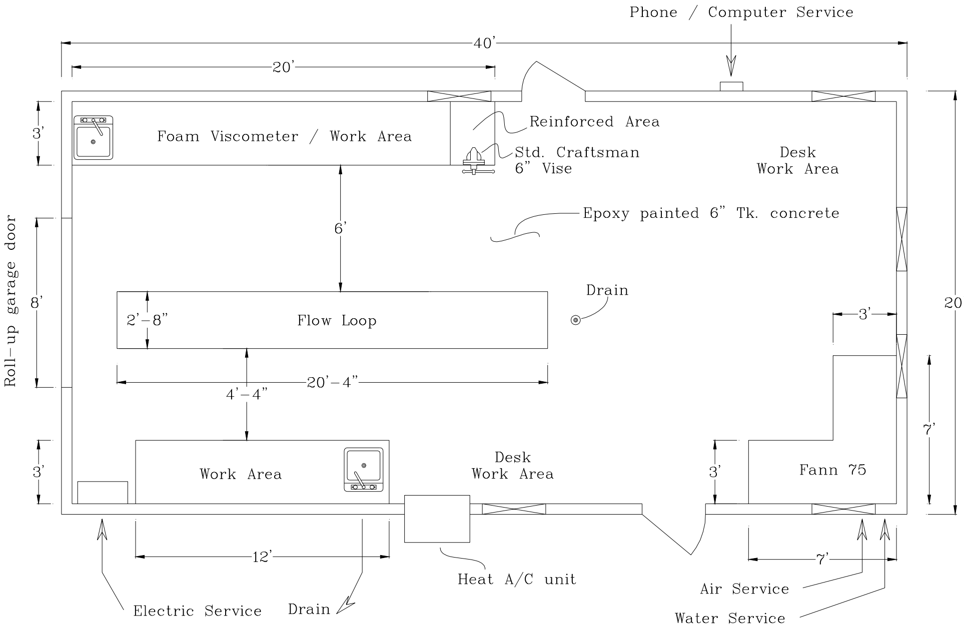

Fig. 3.65 Floor plan of new laboratory

Fig. 3.66 New laboratory (outside)

Fig. 3.67 New laboratory (inside)

3.7 ACTF EQUIPMENT SUMMARY

Following is a brief list of major equipment on the ACTF test loop.

Concrete Slab

- 40’ x 125’ x 8 ½” tk. (some areas thicker)
- Concrete minimum compressive strength 3000 psi

Piping

- 2-inch high pressure = 0.218” w.t. (sch. 80) A-36
- 3-inch high pressure = 0.300” w.t. (sch. 80) A-36
- 4-inch high pressure = 0.337” w.t. (sch. 80) A-36
- 6-inch high pressure = 0.432” w.t. (sch. 80) A-36
- 1-inch low pressure = 0.133” w.t. (sch. 40) A-36
- 1 ½-inch low pressure = 0.145” w.t. (sch. 40) A-36
- 2-inch low pressure = 0.154” w.t. (sch. 40) A-36
- high pressure flanges = ANSI 900# class RTJ
- low pressure flanges = ANSI 150# class RF
- medium pressure flanges = ANSI 600# class RF
- low pressure piping is defined as suction piping, MWP = 285 psi @ 100°F or 260 psi @ 200°F
- medium pressure piping is defined as the removal tower area, MWP = 1480 psi @ 100°F or 1350 psi @ 200°F (by project definition however the value is simply given as 1000 psi MWP)
- high pressure piping is defined as the test loop piping between the pumps and the chokes with the exception of the removal tower area, MWP = 2220 psi @ 100°F or 2025 psi @ 200°F (by project definition however the value is simply give as 2000 psi MWP)

Flexible Hoses

- 2000 psi MWP
- -40°F to +175°F
- 6000 psi burst pressure

Storage Tanks

- 10-ft. dia. x 7-ft high
- Fiberglass
- 100-bbl Capacity

Buried Storm Water Sump Tank

- 10-ft. dia. x 7-ft high
- Fiberglass
- 100-bbl Capacity

Mixing Tank

- 4 ft. dia. x 3 ft. high
- Fiberglass

Air Accumulator (Compressor storage Tank)

- 500 psi MWP
- 750 psi test pressure
- head tks. 5/8”
- shell tks. ¾”
- A516-70 material
- designed per ASME Boiler Pressure Vessel Code

Air Receiver (Liquid Hold-up)

- 2160 psi MWP
- 3250 psi test pressure
- head tks = 1 3/16”
- shell tks = 1.031”
- A-36 mat’l
- Designed per ASME Boiler Pressure Vessel Code

Boiler

- Indirect natural gas fired
- Glycol circulation system
- Maximum 225°F
- Approx. 2,000,000 Btu

Cooling Tower

- Water cascade with cooling fan
- Approx. 1,500,000 Btu

Heat Exchangers

- 4-inch 150 # RF suction
- 4-inch 150# RF discharge
- 275 psi MWP

Jockey Pump

- 25 HP
- 3600 rpm
- Centrifugal
- 500 gpm
- 125 ft. head

Liquid Injection Pump

- 0.5 to 100 gpm
- 10 – 200 psi
- Positive displacement
- 20 HP 460v

Surfactant Injection Pump

- Max 60 gph
- Max 2000 psi

Moyno Pump

- 8”-300# RF suction
- 8”-900# RTJ discharge
- 6-stage
- 70 durometer stator
- 75 HP motor
- 500 gpm maximum
- 500 psi maximum differential

Halliburton HT-400 Frac. Pump

- 4-inch quick couple suction
- 4-inch hammer-union discharge
- Diesel Engine power
- Approx. 500 gpm maximum liquid pumping rate
- Approx. 10,000 psi maximum differential

Small Air Compressor

- Ingersol-Rand
- Diesel Engine power
- 200 psi maximum discharge pressure
- 400 cfm maximum discharge rate

Large Air Compressor

- Sullair
- Diesel Engine power
- 500 psi maximum discharge pressure
- 900 cfm maximum discharge rate

Drill Pipe Rotation

- Specification 250 rpm
- 3 ½” drill pipe
- System constructed for concentric / 0.541” offset / 0.881” offset

Injection Towers

- 42-ft high
- 2000 psi MWP
- 200°F

Separator Towers

- 30-ft high
- 1000 psi MWP
- 200°F

Liquid / Gas Separator (Foam Breaker)

- 2000 psi MWP
- 200°F
- 20” Sch 80 (1.031” tk) pipe

Cuttings Injection System

- Hydraulic motor powered
- Moyno progressive cavity pump internals
- Approximately 0.3 cu ft. per minute at 20 rpm

Liquid Hold-up Valves

- Orbit 4”-900# RTJ Reduced port ball valves
- -20F to +500°F
- 2160 psig MWP

Mast

- Net weight mast 16,000 lbs.
- Net weight piping 17,000 lbs
- Net weight fluid 1,300 lbs (based on 5.761” I.D. w/ 1.43 gravity fluid x 968.8”)
- X-sec 42” wide x 41” high
- Made from 2 ea. 41 x 14 90.1 #/ft. welded girder
- Designed per AISC design formulae
- Wind load based on 70 mph

Hydraulic Cylinders

- 8” ID
- 349” long retracted
- 465” long extended
- 3000 psi MWP
- 4500 psi test pressure

Hydraulic Power Unit

- 460v 3 phase 40 Hp electric motor
- 100 gal capacity
- 0-20 gpm
- 0-3000 psi

Differential Pressure Transmitters

- Rosemount Model 3051
- Measurement range adjustable
- Maximum working pressure 3626 psi
- Output 4-20 mA

Static Pressure Transmitters

- Rosemount Model 3051
- Measurement range adjustable
- Maximum working pressure 4000 psi
- Output 4-20 mA

Temperature Transmitters

- Rosemount Model 3144
- Measurement range fixed 0-200°F
- Output 4-20 mA

Fluid Characterization Lab

- 20 ft x 40 ft x 10 ft high clearance inside

4. Study of Cuttings Transport with Foam under LPAT Conditions (Task 6)

ABSTRACT

A hydraulic equation relating pressure drop with average flow velocity, hydraulic diameter and other rheological properties is presented for foam flow in conduits. Rheological parameters for foam qualities ranging from 70% to 90% were experimentally determined using a flow loop. In this range of quality the foam behaves like a pseudo-plastic fluid. A three-layer mechanistic model and associated computer simulator were developed to describe cuttings transport. The simulator is capable of estimating bed thickness and pressure drop mostly with an error of less than 25%. Data from cuttings transport experiments with foam were compared with results from the simulator. The experimental parameters included: 70 to 90 angles of inclination; 1 ft/s to 16 ft/s average annular velocities; 20 ft/hr to 90 ft/hr rates of penetration; and 70% to 90% foam qualities. As the foam quality increases at a given flow rate and rate of penetration, bed thickness also increases. Inclination angles greater than 70 degrees do not have a significant effect on bed thickness. Empirical equations and Artificial Neural Networks (ANN) were also developed and compared with the simulator for estimating the bed thickness. ANN provides a more accurate estimation of bed thickness than the empirical equations or the proposed model, especially when the bed thickness is small.

4.1 INTRODUCTION

Inefficient cleaning of wellbore may cause severe problems, such as stuck pipe, lost circulation, high torque and drag, loose control on density, poor cement jobs, etc. A solution to solve this problem is to increase the annular drilling fluid velocity to decrease cuttings concentration in the annular space. But the increment of the annular fluid velocity is limited because of the erosion of open hole section and higher bottomhole equivalent circulating density (ECD) applied to the formations. Studies indicated that if the flow rate is high enough, the cuttings can be transported easily with any kind of fluid. However, it is frequently impossible to use such pumps continuously because of physical limitations, and wellbore erosion and formation damage.

Foam has been used as a drilling fluid in many drilling operations and the results from various field cases are well documented in the literature. In many cases, drilling with foam has shown to provide significant benefits, including increased productivity (by reducing formation damage), increased drilling rate, reduced operational difficulties associated with drilling in low pressure reservoirs (e.g., lost-circulation and differentially stuck pipe), and improved formation evaluation while drilling. Although viscosity may improve cuttings transport, it also results in higher pressure losses. Selecting appropriate foam quality, volumetric flow rates, and types of polymers and surfactants is critical for achieving the desired flowing bottomhole pressure and cuttings transport.

Foams consist of a continuous liquid phase, forming a cellular structure that surrounds and entraps a gas phase as shown in Fig. 4.1. Foams are considered to be dry or wet, depending on the gas content. Wet foams have spherical bubbles with large amount of liquid between the bubbles, and dry foam bubbles are polyhedral in shape with very thin liquid film between the bubbles. In between these two extremes, geometrical figures having both curved and flat faces can exist.

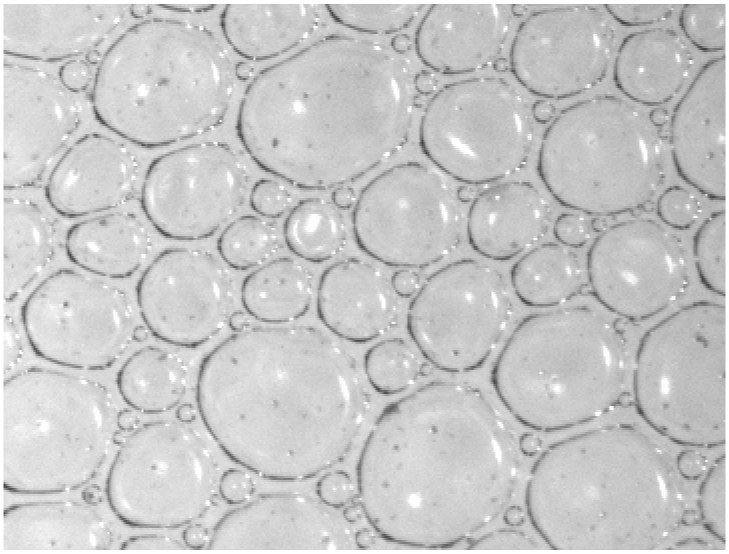

Fig. 4.1 Structure of foam

Foams can have extremely high viscosity. Mostly their viscosity is greater than either the liquid or the gas that they contain. At the same time, their densities are much lower than the density of water. Therefore, by using foam as a drilling fluid, efficient cuttings transport and underbalanced conditions can be achieved simultaneously. Foams are also preferred when water influx is a problem because they can handle large amounts of water. However, foams lead to corrosion on the drillstring and other equipment, especially when air is used as the gas phase. Foams should not be used if wellbore instability is a problem. Additional costs are associated with the use of foams due to special equipment requirements and expensive chemicals.

The use of foam as a drilling fluid was developed to meet a special set of conditions under which other drilling fluids had failed[1]. Foams are usually used for removing formation fluid that enters the borehole while drilling, removing solid particles, when completing or working over wells in depleted reservoirs, or for being a very successful insulating medium when lost circulation is a problem.

Foams are usually characterized by the quality (Γ), the ratio of the volume of gas and the total foam volume:

$$\Gamma = \frac{V_g}{V_g + V_L} \tag{4.1}$$

where V_g and V_L are gas and liquid volumes. In the present research studies, foams are referred to as aqueous foams with quality ranging from 52% to 96%.

Although foam rheology has been studied for many years, still foam rheology is not well understood. Even less is known about cuttings transport with foam. Therefore, this study undertakes a comprehensive analysis of cuttings transport with foam in inclined and horizontal wells.

4.2 LITERATURE REVIEW

Rheological characterization of foam can be categorized under two major groups; conventional (quality based) approach[1-5], and volume equalized approach[6-8]. In the first group, foam quality is thought to be the major variable on foam rheological properties. A set of rheological model parameters are developed for different foam qualities. Thus, as the foam quality changes, the parameters used in the models need to be changed as well. In the second group, invariance property of the Reynolds number is used, i.e., friction factor is assumed to be constant along the flow direction. A new variable is introduced, called "specific volume expansion ratio" which is the ratio of liquid phase density to the foam density, and this variable is used instead of "foam quality" for the characterization of the foams. All density-dependent parameters are normalized with respect to liquid density by using this variable. The principle states that if we plot volume-equalized shear stress vs. volume-equalized shear rate, points obtained at different qualities and different geometries lie on one curve in isothermal conditions.

Studies on cuttings transport have been in progress since the 1940's. Initial investigations focused on terminal velocity determination for single-phase drilling fluids. Since most of the wells were vertical, terminal velocity was enough to address most of the problems. As interest in directional and horizontal wells increased, studies were shifted to experimental approaches[9-11] and mathematical modeling (mechanistic models) to explain the cuttings transport phenomenon at different inclination angles. Gavignet and Sobey[12] introduced a two-layer mechanistic model for explaining the cuttings transport phenomenon in inclined wellbores. Their model consists of a stationary bed and pure fluid flow in the upper layer.

Clark and Bickham[13] developed a mechanistic model based on forces acting on a single bed particle. The model predicts the critical flow velocity required to initiate the movement protruding cuttings bed particles. Three modes for cuttings bed particle transport were suggested: rolling, lifting and settling.

Nguyen and Rahman[14] developed a three-layer mechanistic model. Their model considers three layers: stationary bed layer, dispersed layer and fluid flow layer. The model is applicable for different modes of transport, ranging from a stationary bed condition to a fully suspended flow.

Recently underbalanced drilling has become an economical, viable and safe drilling technique. However, studies conducted on cuttings transport in highly inclined wells with aerated fluids, especially with foams, are very limited. Saintpere, et al.[15] analyzed hole cleaning with foam in inclined wells using a mechanistic approach and ignoring inertial effects. They introduce a few dimensionless parameters for describing the fluid rheology, foam properties, flowing time, etc. They observed the worst hole cleaning performance at angles 40°-60°.

Martins, et al.[16] experimentally studied effective hole cleaning with foam. They developed empirical equations to predict the bed erosion capacity in horizontal wells as a function of foam quality and Reynolds number. Krug and Mitchell[17] developed charts for estimating the required flow rates for foam drilling as a function of penetration rate, depth and bottomhole pressure. Foam was assumed to be a Bingham Plastic fluid and the effect of solids on rheology of foam was neglected in the development of the chart.

Okpobiri and Ikoku[18] developed a semi-empirical correlation to determine frictional pressure loss due to the solid phase in foam flow. They predicted the minimum volumetric requirements for foam drilling operations. For a constant flow Reynolds number, they observed an increase in frictional pressure loss with increase in solid mass flow rate. They assumed that all foam drilling operations are performed in the laminar flow region and foam qualities vary between 55 % and 96 %.

Guo, et al.[19] addressed the determination of bottomhole pressure when foam is used as a drilling fluid. They used an equation of state for foam and calculated hydrostatic head and frictional losses along the annulus by using an iterative procedure. Foam was considered to be a Power-Law fluid. Model predictions were compare with other calculation procedures. The study was one of the first studies conducted on modeling of cuttings transport with foam in horizontal and highly-inclined wells.

4.3 STATEMENT OF THE PROBLEM

As the need for directional and horizontal wells increased, the interest in cuttings transport problems has shifted from vertical wells to inclined and horizontal wells. Although cuttings transport in horizontal and inclined wells has been studied for many years, the focus has been mostly on single-phase fluids, i.e., liquids. Even with single-phase fluids, there is still a lack of understanding of the complex mechanism of cuttings transport. Some researchers have tried to develop empirical equations based on experimental data and others attempted to develop mathematical models. However, the problem is getting more difficult as drilling fluids become more complex.

In order to better understand the issues related to cuttings transport problems, the rheology of the fluid has to be studied extensively. In the literature, there has been no attempt to describe cuttings transport with foam in horizontal and inclined wellbores. Although there are field applications of foam drilling for directional and horizontal wells reported to be successful, there is a lack of understanding of what is really happening in the wellbore. Since well costs increase drastically for directional and horizontal drilling operations, a proper understanding of such problems may decrease the drilling costs significantly. The most extensive study about foam drilling was conducted only for vertical wells[18]. Since then no other research has been conducted on cuttings transport with foam. Therefore, the aim of this study is to fill this gap by investigating cuttings transport with foam in horizontal and highly-inclined wellbores.

4.4 THEORY

In order to model cuttings transport with foam, the rheological and hydraulic characterizations of foam have to be properly determined.

4.4.1 FOAM RHEOLOGY

Foam is known to be a compressible non-Newtonian fluid. Ozbayoglu et al.[20] concluded that there is no “best” model to explain the rheological behavior of foam for all quality ranges. However, the rheology can be better characterized by the Power Law model for 70% to 80% quality foams. Therefore, generalized rheological model parameters, N and K’, are preferred to explain foam behavior in this study. N and K’ are functions of foam quality. Thus, wall shear stress in terms of generalized rheological parameters can be defined as:

$$\tau_W = K'\left(\frac{8U}{d_{hyd}}\right)^N \tag{4.2}$$

Wall shear stress can also be expressed as:

$$\tau_w = f\,\frac{\rho U^2}{2} \tag{4.3}$$

Therefore, if friction factor is determined properly, wall shear stress and frictional pressure loss can be calculated. The friction factor is determined using the Generalized Reynolds number given by:

$$N_{Re} = \frac{\rho U^{2-N} d_{hyd}^N}{8^{N-1}K'} \tag{4.4}$$

As seen in Eq. 4.4, the Reynolds number is a function of N and K’. Using generalized rheological parameters eliminates the limitation of depending on a single rheological model. If flow equations for circular pipe and concentric annuli are derived and compared, one can define the shear rate at the wall in a general form as[20]:

$$F(\tau_w) = \left(\frac{8U}{d_{hyd}}\right)\left[a + \frac{b}{N}\right] = \gamma_w \tag{4.5}$$

where

$$N = \frac{\partial \ln\left(\frac{d_{hyd}}{4}\frac{\Delta P}{\Delta L} - \frac{d_{hyd}}{2}\overline{\rho}U\frac{\partial U}{\partial L}\right)}{\partial \ln\left(\frac{8U}{d_{hyd}}\right)} \tag{4.6}$$

If Eq. 4.5 is expanded, integrated and solved for 8v/d_{hyd}, a generalized equation is obtained that is valid for any time-independent fluid for any kind of conduit if a and b are properly selected. This general equation is:

$$\frac{8U}{d_{hyd}} = \frac{1}{b}(\tau_w)^{-\frac{a}{b}}\int_0^{\tau_w} \tau^{\frac{a}{b}-1}F(\tau)\,d\tau \tag{4.7}$$

where a and b are only geometry dependent. Kozicki[21] conducted a study for defining proper a and b values for various shaped conduits. Using his data, empirical correlations are developed for determining a and b values as a function of a dimensionless diameter, which is defined as

$$d_{dim} = \frac{d_{hyd}}{d_{eq}} \tag{4.8}$$

where

$$d_{eq} = \sqrt{\frac{\text{Flow Area}}{\pi/4}} \tag{4.9}$$

The relations for geometric parameters a and b for various conduit types are determined after a regression analysis as

$$a = 1.012 + (-0.25)d_{dim}^{1.563} \tag{4.10}$$

and

$$b = 0.51 + (-0.242)d_{dim}^{1.366} \tag{4.11}$$

By using geometric parameters a and b, one can define the shape of a conduit.

If experimental data indicates the presence of a wall slip effect, measured flow rate values need to be corrected for an effective slip effect before they are used for the development of a flow curve, which is intended to portray the relationship between shear stress and shear rate at a given point in the fluid, without any extraneous effects such as may be introduced by the proximity of solid surfaces. The measured volumetric flow rate from the pipe flow experiments may be corrected to the value it would have in the absence of the "slip" by the following equation:

$$Q_c = Q_m - 0.5\pi\beta\tau_w R \tag{4.12}$$

The effective slip coefficient, β, needs to be determined to calculate the slip corrected flow rates. β can be estimated by using the Oldroyd-Jastrzebski correlation[22], which suggests a three-step procedure to determine the value of β: i) Obtain a plot of Newtonian wall shear rate, 8v/D, vs. $1/D^2$ at constant wall shear stress, τ_w; ii) The slope of the least–squares straight lines will be equal to $8\beta\tau_w$. Therefore, the value of β can be determined by dividing the slope of the least-squares line by $8\tau_w$, iii) A functional relationship between the effective slip coefficient and wall shear stress can be determined by curve fitting of the plot of β vs. τ_w.

4.4.2 LAYERED MODEL

Based on experimental observations, a layered model was proposed to describe the cuttings transport phenomenon in horizontal and highly-inclined wellbores. A set of equations are developed to solve for the unknowns, such as layer geometries, velocities in each layer, in-situ cuttings concentration and frictional pressure loss.

Major Assumptions

Three layers presented in Fig. 4.2 are considered in analyzing the problem. Hence, the following assumptions are made for each computational grid in the axial direction:

- Layer I: Fluid layer without cuttings and with uniform physical and chemical properties;
- Layer II: Moving mixture layer with cuttings and slip between the cuttings and the fluid;
- Layer III: Uniformly compacted stationary cuttings bed layer with constant porosity and negligible pore fluid flow;
- Cuttings are assumed to be uniform and spherical with constant diameter and density.

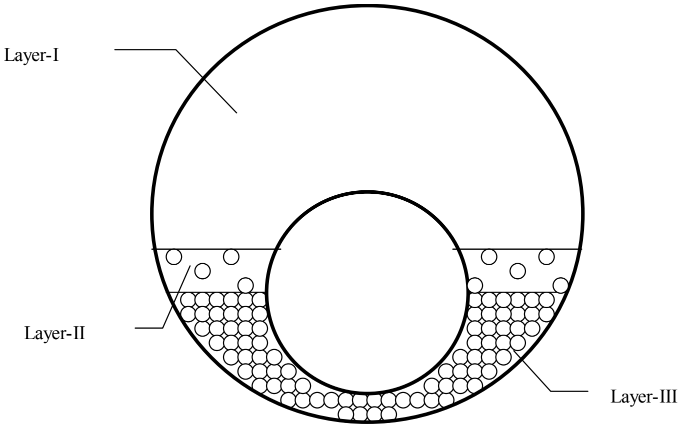

Fig. 4.2 Cross-section of the wellbore

In the proposed model, the wellbore is divided into longitudinal grids with a given length. Within one grid, the velocity, density and fluid properties are assumed to be constant. However, due to pressure change from one wellbore grid to the other, fluid velocity, density, fluid properties, etc. are re-calculated for the next grid by using the equation of state for gases modified for foam. In terms of foam quality, the volumetric expansion due to change in pressure and temperature can be determined as:

$$Q_2 = Q_1\left[(1-\Gamma_1)+\frac{P_1T_2}{P_2T_1}\Gamma_1\right] \tag{4.13}$$

where the indices 1 and 2 refer to the consecutive grid order.

Mass Balance

Assuming a constant ROP and fluid flow rate, mass balance in a control volume (a single grid) can be defined for fluid phase as:

$$v_I A_I \rho_f + v_{II} A_{II} \rho_f \left(1 - C_{C,II}\right) = \bar{v} A_w \left(1 - C_C\right) \rho_f \tag{4.14}$$

Similarly for solid phase:

$$v_{II} A_{II} C_{C,II} \rho_c = \bar{v} A_w C_C \rho_c \tag{4.15}$$

where v_{II} is the slurry velocity at the second layer, which is defined as:

$$v_{II} = v_{II,f} - \frac{v_{slip} \rho_c C_{C,II}}{\rho_s} \tag{4.16}$$

where in-situ slurry density, ρ_s is:

$$\rho_s = \rho_f \left(1 - C_{C,II}\right) + \rho_c C_{C,II} \tag{4.17}$$

Transport velocity of the solids, V_T, is defined as:

$$v_T = v_{II,f} - v_{slip} \tag{4.18}$$

On the right side of Eqs. 4.14 and 4.15, the terms $\bar{v}$ and C_C are the average velocity in the wellbore and the feed cuttings concentration, respectively, which are defined as:

$$\bar{v} = \frac{Q_f + A_{bit} ROP}{A_w} \tag{4.19}$$

and

$$C_C = \lambda \frac{ROP}{\bar{v}\left[1 - \left(\frac{d_i}{d_o}\right)^2\right]} \tag{4.20}$$

where λ is the correction factor,

$$\lambda = \frac{m_{total} - m^*_{bed}}{m_{total}} = \frac{A_{bit} - A^*_{bed}(1 - \varphi_{bed})}{A_{bit}} \tag{4.21}$$

As an important note, C_C is not the total cuttings concentration in the wellbore. It is the amount of cuttings in motion that are introduced to the wellbore. The total in-situ cuttings concentration present in the system is:

$$C_{C,total} = C_{C,II} + C_{C,bed} \tag{4.22}$$

Momentum Balance

The free body diagram of a wellbore section with the layers is presented in Fig. 4.3. In a given wellbore grid, the fluid density and velocity are assumed to be constant. From the free body diagram, the force balance for the first layer in steady state flow condition can be written as:

$$\Delta PA_{I} - \tau_{I-II}S_{I-II}\Delta L - \tau_{I-w}S_{I-w}\Delta L - \rho_{f}gA_{I}\Delta L\mathrm{Sin}\alpha = 0 \tag{4.23}$$

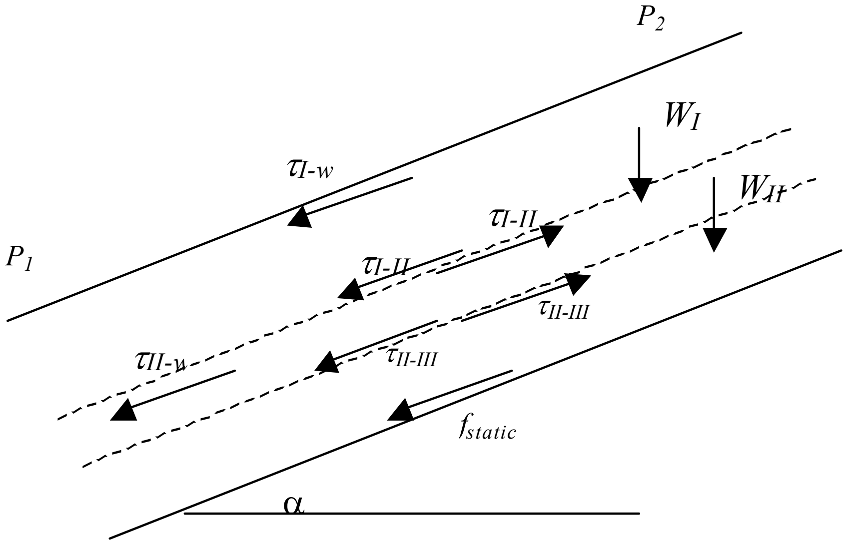

Fig. 4.3 Free body diagram of a wellbore grid with flow upward (left to right)

Similarly the force balance equation for the second layer becomes:

$$\Delta A_{II} + \tau_{I-II}S_{I-II}\Delta L - \tau_{II-III}S_{II-III}\Delta L - \tau_{II-w}S_{II-w}\Delta L - \rho_{s}gA_{II}\Delta L\mathrm{Sin}\alpha = 0 \tag{4.24}$$

Finally, force balance for the cuttings bed layer is:

$$\Delta PA_{III} + \tau_{II-III}S_{II-III}\Delta L - f_{III-w}\rho_{b}gA_{III}\Delta L\mathrm{Cos}\alpha = 0 \tag{4.25}$$

In Eq. 4.23, Eq. 4.24 and Eq. 4.25, shear stress terms, τ_{i-j}, are defined as:

$$\tau_{i-j} = f_{i-j}\frac{\rho_{i}(v_{i} - v_{j})^{2}}{2} \tag{4.26}$$

where indices i and j indicate the surfaces where the shear stress is acting. One of the key points for this model is determining the interfacial shear stress between the bed surface and the second layer. This shear stress defines whether the bed is under erosion, development or steady state. It is known that there is a critical interfacial shear stress at which the bed is neither built-up nor eroded. Thus, momentum equations are solved when interfacial shear stress is equal to the critical interfacial shear stress. The term f_{III-w} is the static friction factor between the bed and the wellbore, and it was determined experimentally as a function of the ratio of the bed cross section area to the annular area (dimensionless bed area), $\frac{A_{bed}}{A_w}$:

$$f_{III-w} = 0.617\left(\frac{A_{bed}}{A_w}\right)^{0.252} \tag{4.27}$$

The interfacial shear stress between the layer boundaries can be expressed in terms of a friction factor. In this study, the empirical correlation developed by Televantos is used:

$$\frac{1}{\sqrt{2f}} = -0.86\ln\left(\frac{d_c/d_{hyd}}{3.7} + \frac{2.51}{N_{Re}\sqrt{2f}}\right) \tag{4.28}$$

The friction factor between the first layer and the second layer is determined by modifying Televantos' equation as:

$$\frac{1}{\sqrt{2f_a}} = -0.86\ln\left(\frac{d_{chr}/d_{hyd}}{3.7} + \frac{2.51}{N_{Re}\sqrt{2f_a}}\right) \tag{4.29}$$

and

$$f = f_a\left(\frac{d_{chr} - d_c}{2d_c} + 1\right) \tag{4.30}$$

where the characteristic diameter is defined as:

$$d_{chr} = d_c\sqrt[3]{\frac{C_{C,II}}{C_{C,bed}}} \tag{4.31}$$

This equation also reduces to the well known Colebrook friction factor equation when the cuttings concentration approaches to zero.

For determining the viscosity of the cuttings-fluid mixture at the second layer, it is assumed that K' is a function of the cuttings concentration. Thus, the empirical equation developed by Thomas is modified and used as:

$$K'_{suspension} = K'(1 + 2.5C_{C,II} + 10.05C_{C,II}^2 + 0.00273e^{16.6C_{C,II}}) \tag{4.32}$$

Slip Velocity

Derivation of the slip velocity between the fluid and the cuttings is based on the free body diagram shown in Fig. 4.4.

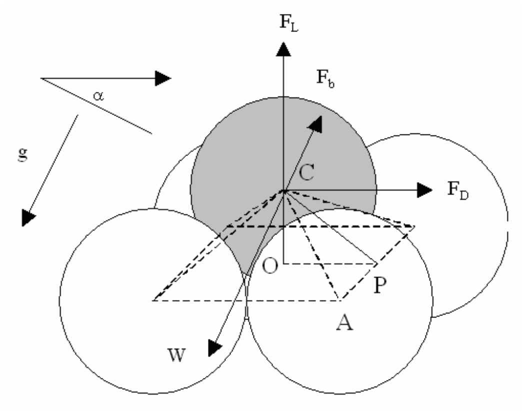

Fig. 4.4 Free body diagram for determination of slip velocity

If the sum of the moments is computed for point C with respect to point P, the equation is found as:

$$[F_D+(F_b-W)\mathrm{Sin}\alpha]d_c f(\theta(\beta)+[F_L+(F_b-W)\mathrm{Cos}\alpha]d_c f(\theta(\beta)=0 \tag{4.33}$$

where β and θ take values depending on the packing type. Slip velocity can be determined if Eq. 4.33 is solved for v_{slip}

$$v_{slip}=\sqrt{\left(\frac{4}{3}\frac{d_c\bar{g}}{(C_L\mathrm{Sin}\beta+C_D\mathrm{Sin}\theta}\right)\left(\frac{\rho_c-\rho_f}{\rho_f}(\mathrm{Cos}\alpha\cdot\mathrm{Sin}\beta+\mathrm{Sin}\alpha\cdot\mathrm{Sin}\theta)\right)} \tag{4.34}$$

In-Situ Cuttings Concentration

Determination of the in-situ concentration of the cuttings at the second layer is very important for defining the mixture density and viscosity at this layer accurately. By using the equation of continuity for a 1-dimensional system,

$$v_y\frac{\partial C}{\partial y}=N_C\frac{\partial^2 C}{\partial y^2} \tag{4.35}$$

where

$$v_y=v_{term}\mathrm{Cos}\alpha \tag{4.36}$$

Actually, from Stokes' Law

$$v_{ter}=\sqrt{\frac{4}{3}\frac{d_c\bar{g}}{C_D}\left(\frac{\rho_c-\rho_f}{\rho_f}\right)} \tag{4.37}$$

The boundary conditions for this second order differential equation are y=0, $C_C=C_{C,bottom}$ and $y=h_{II}$, $C_C=C_{C,top}$, respectively. Thus, solution of this second order differential equation gives:

$$C_C(y) = \frac{-C_{c,bottom} + C_{C,top} e^{\frac{h_{II} v_y}{N_C}} + (C_{C,bottom} - C_{C,top}) e^{\frac{v_y (h_{II} - y)}{N_C}}}{e^{\frac{h_{II} v_y}{N_C}} - 1} \tag{4.38}$$

The average cuttings concentration in layer 2 can be determined by integration of $C_C(y)$ over the thickness of layer 2 yields

$$C_{C,II} = \frac{2N_C^2 (C_{C,bottom} - C_{C,top}) + C_{C,top} h_{II}^2 v_y^2 - \frac{(C_{C,bottom} - C_{C,top}) h_{II} v_y (2N_C + h_{II} v_y)}{e^{\frac{h_{II} v_y}{N_C}} - 1}}{h_{II}^2 v_y^2} \tag{4.39}$$

Wellbore Geometry

In order to solve the equations, the area and contact surfaces are required for each layer. All possible wellbore configurations can be categorized into six major cases, as shown in Fig. 4.5. For each case, the area, contact surfaces, etc. can be determined by using basic trigonometry and geometry.

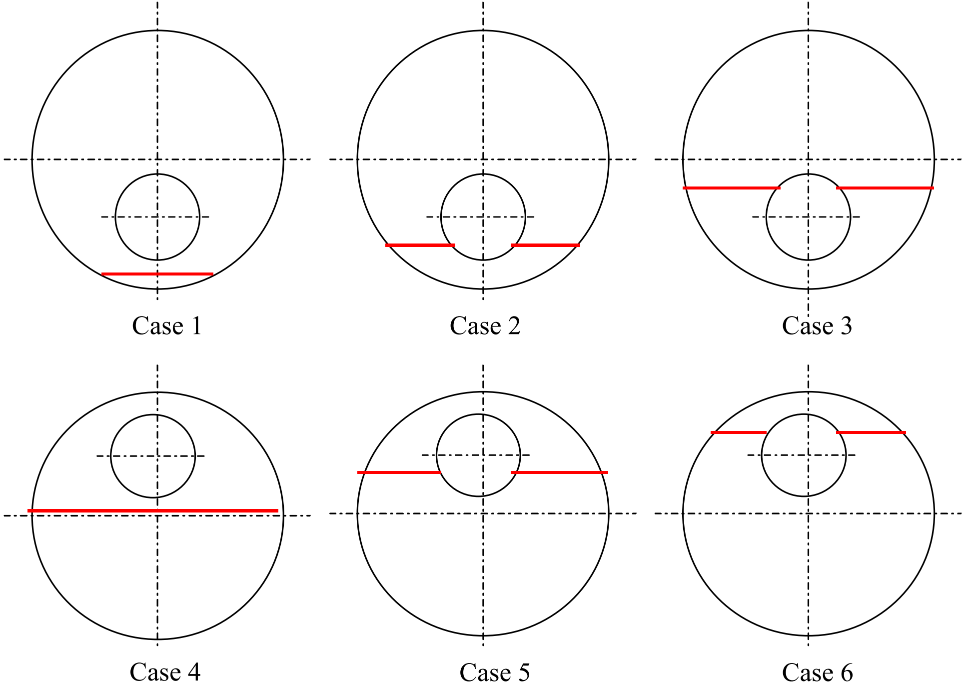

Fig. 4.5 Possible wellbore configurations

4.5 EXPERIMENTAL WORK

Cuttings transport experiments were conducted at The University of Tulsa Drilling Research Projects' low pressure-ambient temperature flow loop, which is shown in Fig. 4.6. The flow loop consists of annular and rheology test sections. The annular test section is approximately 100 ft. long and consists of an 8-inch transparent casing and a 4.5-inch drillpipe. The cuttings are introduced into the annular section from the injection tank using a rotating auger system. An industrial-size shale shaker separates the fluid from the cuttings, which are then accumulated in a collection tank. One end of the flow loop is attached to a movable platform, while the other is connected to a pulley, which enables inclination of the test section to any angle between 0° to 90° from vertical. A 75-HP (650 gpm at 50 psi) centrifugal pump is used to supply liquid phase and a compressor (working capacity 0-100 psi, maximum 800 scfm) is used to supply compressed air. Both gas and liquid phase flow rates are measured using Coriolis mass flow meters (Micro-motion™). Controlling and recording of air and liquid flow rates, drillpipe rotation, flow loop inclination, pressure and temperature are done from a control room using a data acquisition and control system (LabView ™).

Fig. 4.6 Low pressure ambient temperature flow loop (TUDRP)

Foam characterization tests were conducted in the rheology section that consists of three acrylic transparent pipes with a total length of 50 ft and diameters of 2”, 3”, and 4”. Average flow velocities varied from 3 ft/sec to 23 ft/sec for 70, 80 and 90 % foam qualities.

The pressure difference between the inlet and outlet of the rheology section is measured by a differential pressure transducer. Static pressure at the inlet of the rheology section is measured by a pressure transmitter and used for determining the foam quality.

Cuttings transport tests were performed using water and foam. Tests covered inclinations from 90° to 70° from vertical for both water and foam, in-situ annular flow velocities from 1 ft/sec to 7 ft/sec for water and 1 ft/sec to 16 ft/sec for foam, foam qualities from 70% to 90% and simulated drilling rates from 30 ft/hr to 110 ft/hr.

4.6 RESULTS & DISCUSSION

4.6.1 FOAM CHARACTERIZATION

For a fully-developed laminar pipe flow under steady conditions, the wall shear stress, τ_w, can be determined from the force balance equation. The shear rate at the tube wall can be calculated by using the Rabinowitch-Mooney equation given by:

$$\gamma_w = \frac{8v}{D}\frac{3N+1}{4N} \tag{4.40}$$

where

$$N = \frac{d\ln(\tau_w)}{d\ln\left(\frac{8v}{D}\right)} \tag{4.41}$$

For Newtonian fluids, N = 1 and the wall shear rate equation reduces to 8v/D. For non-Newtonian fluids ($N \neq 1$), and the generalized wall shear rate relationship given by Eq. 4.40 should be used to establish flow curves. Note that the slip-corrected flow rate values from Eq. 4.12 should be used to calculate the generalized wall shear rate values in Eq. 4.41. Generalized flow curve data for 70%, 80%, and 90% quality foams are plotted in Fig. 4.7.

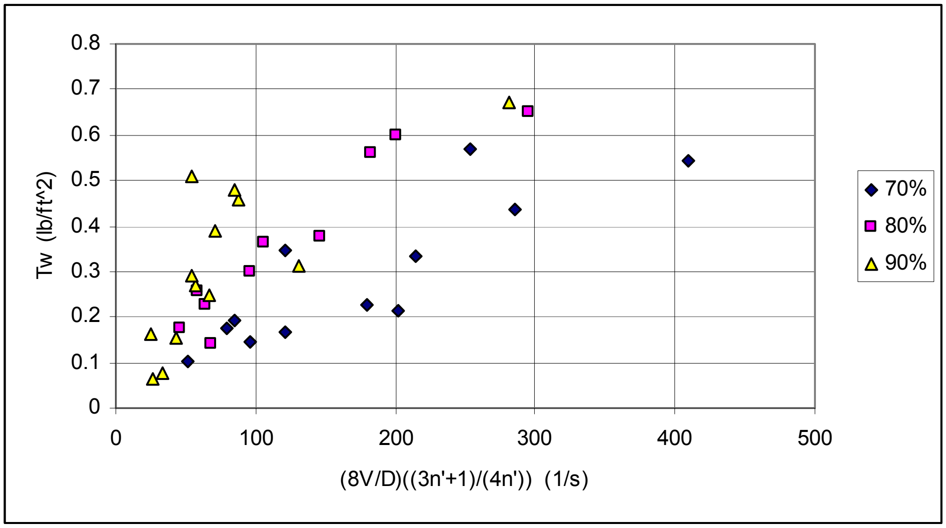

Fig. 4.7 Shear stress and shear rate plot after slip and N correction

Statistical analysis was conducted to determine the curve fitting parameters, assuming the foam flow behavior can be explained by using Power Law, Bingham Plastic and Yield-Power Law models. A summary of the estimated model parameters is given in Table 4.1.

Table 4.1 Rheological Parameters of Foam for Different Foam Qualities

Γ	$\tau = \mu(\gamma)$		$\tau = \tau_y + \mu_p(\gamma)$			$\tau = K(\gamma)^n$			$\tau = \tau_y + K(\gamma)^n$			
	μ	R^2	τ_y	μ_p	R^2	K	n	R^2	τ_y	K	n	R^2
70 %	$6.0\ 10^{-6}$	0.63	$8.14\ 10^{-4}$	$4.0\ 10^{-6}$	0.82	$1.02\ 10^{-4}$	0.53	0.94	$5.8\ 10^{-8}$	$1.0\ 10^{-4}$	0.53	0.94
80 %	$1.0\ 10^{-5}$	0.58	$1.76\ 10^{-3}$	$6.0\ 10^{-6}$	0.80	$2.92\ 10^{-4}$	0.45	0.92	$1.3\ 10^{-9}$	$2.9\ 10^{-4}$	0.45	0.92
90%	$1.2\ 10^{-5}$	0.45	$2.22\ 10^{-3}$	$7.0\ 10^{-6}$	0.81	$4.15\ 10^{-4}$	0.42	0.90	$2.0\ 10^{-7}$	$4.1\ 10^{-4}$	0.42	0.90

Figures 4.8, 4.9 and 4.10 compare experimental and calculated frictional pressure losses for 70%, 80% and 90% quality foams respectively.

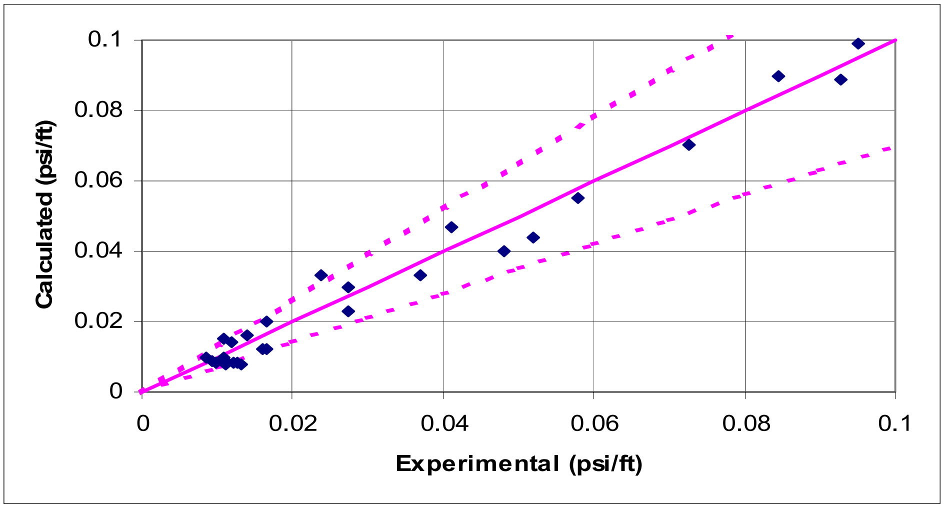

Fig. 4.8 Comparison of the pressure drop for 70% quality

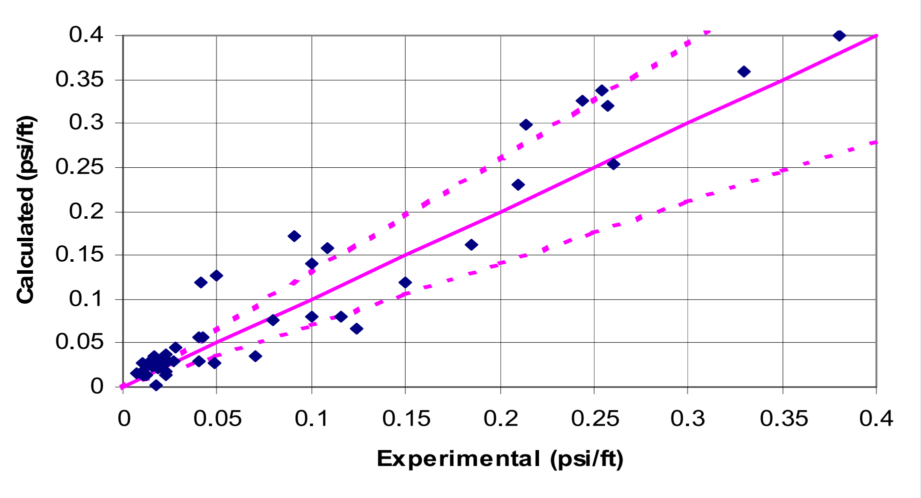

Fig. 4.9 Comparison of the pressure drop for 80% quality

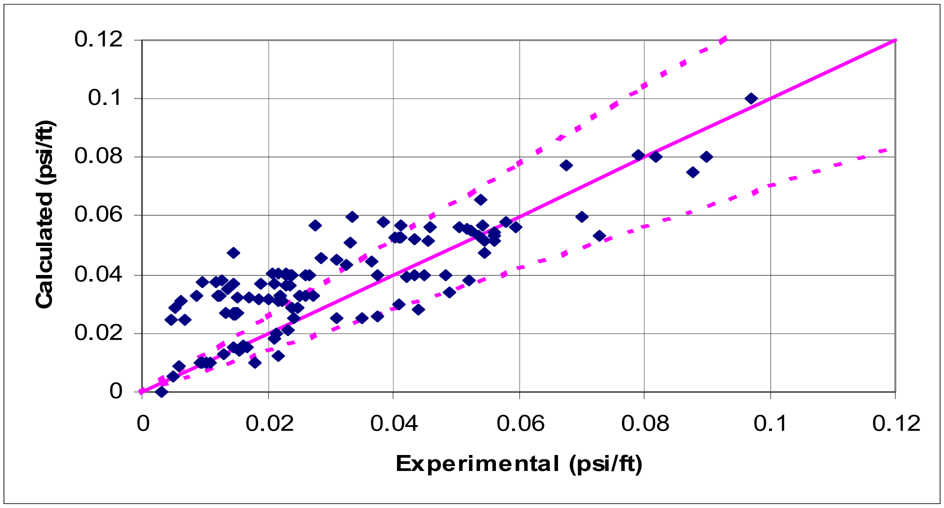

Fig. 4.10 Comparison of the pressure drop for 90% quality

For 70% and 80% quality foams, the difference between the measured and predicted pressure drop is mostly in the range of ± 25% error. However, for 90% quality foam, some of the experimental and predicted results are different with an error of 50%. Most of these data points belong to the annular section for very low flow rates. The major reason for this high error is the presence of the gas slugs in the annular section. Because of mechanical difficulties in the flow loop, it is not easy to make foam with 90% quality moving with a low flow rate without having gas slugs. The flow controllers and check valves operate automatically to keep the flow rate constant by adjusting the valves' opening and closing. Thus, the flow rates are fluctuating. Therefore, at peak points of this function, the amount of gas injected is more than the adjusted gas rate, and a gas slug occurs. This causes a decrease in the pressure drop measurement. Since the calculated pressure drops are based on average flow rates, in some cases, the calculated pressure drops are much higher than the measured pressure drops.

4.6.2 CUTTINGS TRANSPORT

Figure 4.11 shows the relation between the in-situ annular velocity and the cuttings bed development within the wellbore. As the average annular flow velocity increases, the cuttings bed within the wellbore decreases. But most interestingly, even though the average annular velocity is increased continuously, still a thick bed remains within the wellbore, as shown in Fig. 4.12. This is due to the high viscosity of the foam, which disables the turbulent effects on the cuttings bed surface. Therefore, cuttings on the bed surface cannot be picked up and bed erosion does not occur. Table 4.1 shows that as foam quality decreases, the viscosity of foam also decreases. Figure 4.11 indicates that for a constant annular velocity, the cuttings bed thickness decreases as foam quality decreases because of the reduction in the viscosity. If water is used instead of foam, the cuttings bed development is significantly lower (see Fig. 4.13). Since the viscosity of water is much lower than foam, turbulent effects can be observed on the bed surface, which enhances erosion. Thus, cuttings particles can be picked up from the bed surface and the bed thickness decreases. Also, the cuttings bed will almost disappear at an average annular velocity about 7 ft/sec. However, for foam flow, even with very high annular velocity, cuttings beds build up in the test section.

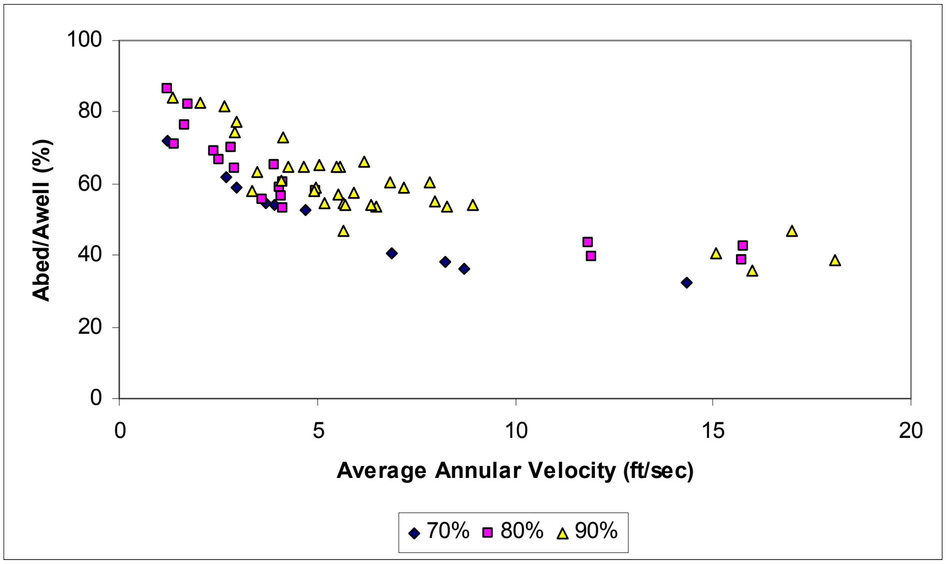

Fig. 4.11 Cuttings bed development as a function of foam flow rate

Fig. 4.12 Cuttings bed in the wellbore while 80 % foam is flowing with at 500 gpm.

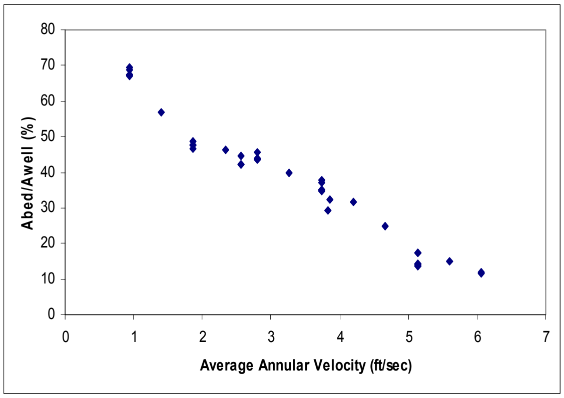

Fig. 4.13 Cuttings bed development as a function of water flow rate

Analysis of the experimental data also reveals that inclinations from 90° to 70° from vertical do not have any influence on the cuttings bed thickness, which is observed for both water and foam.

For the purpose of comparison, model predictions, experimentally determined dimensionless bed area and total pressure drop for cuttings transport tests with water are presented in Fig. 4.14 and Fig. 4.15, respectively.

The dimensionless bed area comparison plot (Fig. 4.14) shows that the model has a slight tendency to overestimate the cuttings bed. According to the total pressure gradient data (Fig. 4.15), the differences between the model predictions and the experimental data are mostly within an error range of 25%. However, the differences increase at smaller bed thicknesses. In addition, the model slightly underestimates pressure losses in the system. But the difference between the experimental data and the estimated results are mostly less than 20%, as shown in Fig. 4.15. Therefore, although the model is developed for compressible fluids, it can be applicable for incompressible fluids as well.

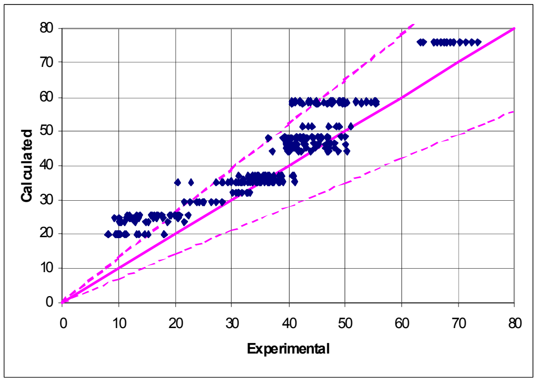

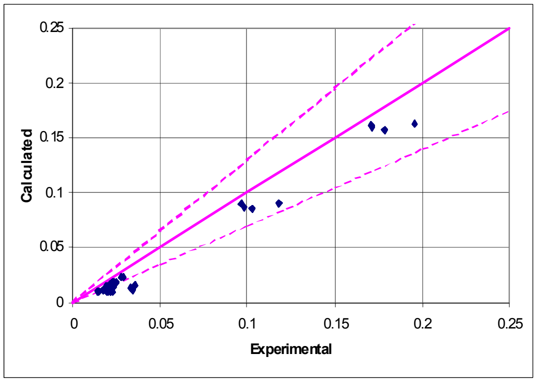

Fig. 4.14 Comparison of dimensionless bed area at different inclinations (water)

Fig. 4.15 Comparison of total pressure gradient at different inclinations (water)

Similarly, experimentally determined and model-predicted dimensionless bed areas and total pressure losses for cuttings transport tests with foam are presented in Fig. 4.16 and Fig. 4.17, respectively.

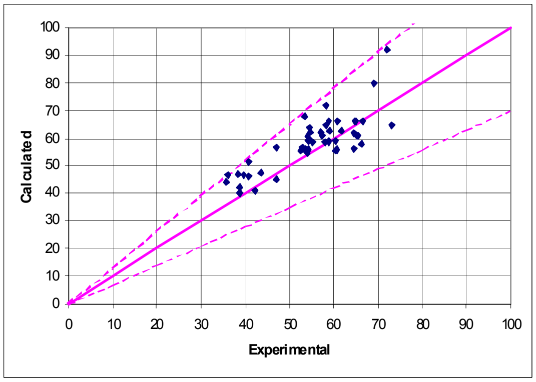

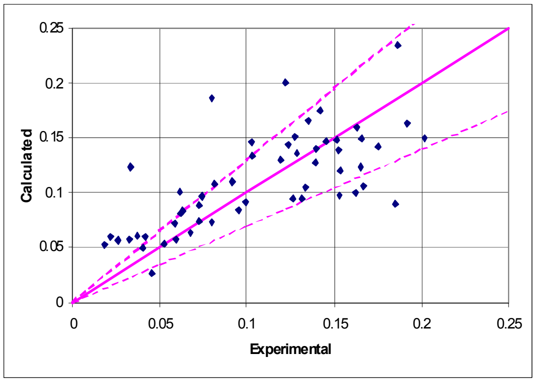

Fig. 4.16 Comparison of dimensionless bed area at different qualities and inclinations (foam)

Fig. 4.17 Comparison of pressure gradient at different qualities and inclinations (foam)

Fig. 4.16 shows that all of the bed thickness estimations are close to the experimental data, with a difference less than 20%. Nonetheless, some of pressure drop predictions are out of the ± 25% window (Fig. 4.17). Some of the pressure gradient data are considerably scattered, especially for high qualities with low flow rates. The major reason is due to the presence of uncontrolled gas slugs developing because of the low back-pressure in the system, which cause lower pressure drop measurements.

It is worthwhile to mention that the cuttings transport model has some limitations. The model cannot handle any situation other than a three-layer case with a stationary bed. At low inclination angles (near-vertical), the bed may begin to slide after a critical inclination angle; therefore, the model must be used for inclinations higher than the critical sliding angle.

4.6.3 OTHER METHODS TO DETERMINE BED THICKNESS

Although bed thickness can be determined by using the proposed model, the simulator requires an excessive amount of time; i.e., for a 2000-ft long wellbore with a grid length of 10 ft, approximately two hours of runtime on a 700 MHz processor is needed. Of course, when the simulator is used, other information (pressure losses and velocities) besides the bed thickness can be obtained. However, if only bed thickness is of interested, the processing time can be shortened by using other methods. Two other methods are presented below to determine the bed thickness in a wellbore: empirical correlations and the method of Artificial Neural Networks.

In order to develop a more general empirical correlation, which will be valid for a wide range of conditions, it is essential to describe the variables in dimensionless form. Thus, a dimensional analysis is conducted. It is generally believed that the height of a cuttings bed is essential information for controlling hole-cleaning performance and a successful drilling operation[8-14]. Major independent drilling variables, which control the development of a cuttings bed in a wellbore, considered in this study are inclination angle, feed cuttings concentration, fluid density, a term representing the apparent fluid viscosity, average velocity and dimensions of the pipe and wellbore.

A dimensional analysis is conducted by using those independent variables in order to develop dimensionless groups that can be correlated for estimating bed height. After applying the Buckingham-π Theorem, five dimensionless groups are developed and defined as:

$$\pi_1 = C_C = \text{ volume of cuttings/volume of annulus} \tag{4.42}$$

$$\pi_2 = \alpha \tag{4.43}$$

$$\pi_3 = \frac{A_{bed}}{A_w} \tag{4.44}$$

$$\pi_4 = \frac{\rho v D}{\mu} = N_{Re} \tag{4.45}$$

$$\pi_5 = \frac{gD}{v^2} = \frac{1}{N_{Fr}} \tag{4.46}$$

Empirical Correlation using Least Squares Method

The relation between the dimensionless bed area and the rest of the dimensionless groups can be written as:

$$\frac{A_{bed}}{A_w} = f(C_C, \alpha, N_{Re}, N_{Fr}) \tag{4.47}$$

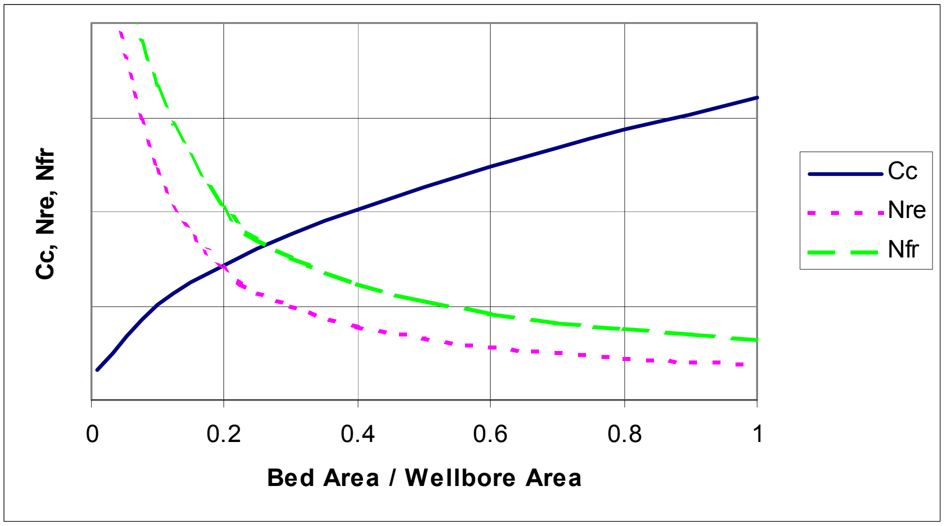

Fig. 4.18 Change of each dimensionless group with dimensionless cuttings bed area

The relation between each dimensionless group and dimensionless bed area is presented in Fig. 4.18 Flow loop experiments with a simulated drill-string have shown that inclinations up to 65° degrees do not affect the bed height. Thus, inclination angle, α, is removed from Eq. 4.47. From the analysis (Fig. 4.18), it is observed that a possible relation among these dimensionless groups is the multiplication form. Thus, a general representation of the dimensionless bed area is expressed as

$$\frac{A_{bed}}{A_w} = k_1 (C_C)^{k_2} (N_{Re})^{k_3} (N_{Fr})^{k_4} \tag{4.48}$$

In order to determine the coefficient, k_1, experimental data collected at TUDRP's LPAT flow loop is used. Information established from cuttings experiments with water, foam and polymer mud were analyzed. A set of empirical correlations was developed using multivariate regression (Statistica™). The least squares method is used during this analysis. The following equations are obtained:

For N ≥ 0.9

$$\frac{A_{bed}}{A_w} = 4.1232 (C_C)^{0.0035} (N_{Re})^{-0.2198} (N_{Fr})^{-0.2164} \tag{4.49}$$

For 0.6 < N < 0.9

$$\frac{A_{bed}}{A_w} = 0.7115 (C_C)^{0.0697} (N_{Re})^{-0.0374} (N_{Fr})^{-0.0681} \tag{4.50}$$

For N ≤ 0.6

$$\frac{A_{bed}}{A_w} = 1.0484 (C_C)^{0.0024} (N_{Re})^{-0.1502} (N_{Fr})^{-0.0646} \tag{4.51}$$

The correlation coefficients (R^2 = estimated-variation/ total-variation) for these equations are 0.8612, 0.9318 and 0.7966 respectively (perfect match: $R^2 = 1$).

Artificial Neural Networks (ANN)

Another way to estimate the cuttings bed height is using ANN. The popularity of ANN is increasing due to its wide range of possible applications, and its capability of handling the nonlinearities that cannot be described by conventional mathematical functions[23].

A neural network has a parallel-distributed architecture with a large number of nodes and connections[23]. Each connection points from one node to another and is associated with a weight. A simple view of the network structure and behavior is given in Fig. 4.19.

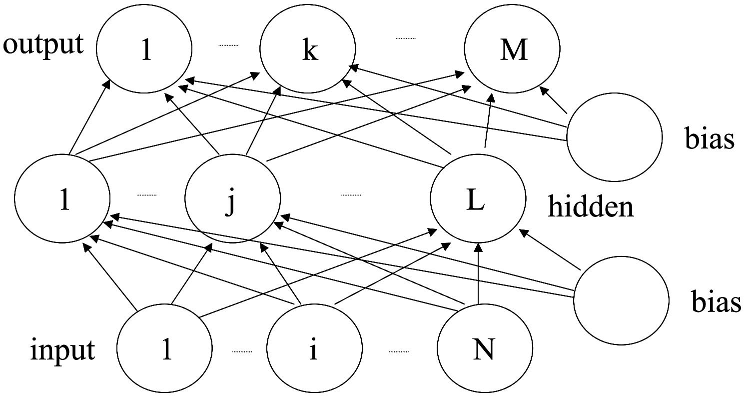

Fig. 4.19 Schematic view of a basic Neural Network System

Network Layers

The input layer: The nodes in this layer are called input units, which encode the instance presented to the network for processing. For example, each input unit may be designated by an attribute value possessed by the instance. In this study, the inputs are feed cuttings concentration, Reynolds Number and Froude Number; thus, there are three input nodes.

The hidden layer: The nodes in this layer are called hidden units, which are not directly observable and hence hidden. They provide nonlinearities for the network. In this study, a single hidden layer is used with ten hidden nodes. The number of hidden layers and nodes are determined by trial and error.

The output layer: The nodes in this layer are called output units, which encode possible concepts (or values) to be assigned to the instance under consideration. Here, the only output is the cuttings bed area; thus, there is only one output node.

Backpropagation

The backpropagation network is a technique that is probably the most well known and widely used among the current types of neural network systems available[23]. A backpropagation network is a multi-layer feed-forward network with a different transfer function in the artificial neuron and a more powerful learning rule. The learning rule is known as backpropagation, which is a kind of gradient descent technique with backward error propagation. The training instance set for the network must be presented many times in order for the interconnection weights between the neurons to settle into a state for correct classification of input patterns. While the network can recognize patterns similar to those they have learned, they do not have the ability to recognize new patterns. This is true for all supervised learning networks. In order to recognize new patterns, the network needs to be retrained with these patterns along with previously known patterns. If only new patterns are provided for retraining, then old patterns may be forgotten. In this way, learning is not incremental over time. This is a major limitation for supervised learning of networks.

Reynolds number, N_{Re}, Froude number, N_{Fr}, and feed cuttings concentration, C_C, are used as inputs for training the network. The network determines dimensionless bed area using the weight functions obtained during training.

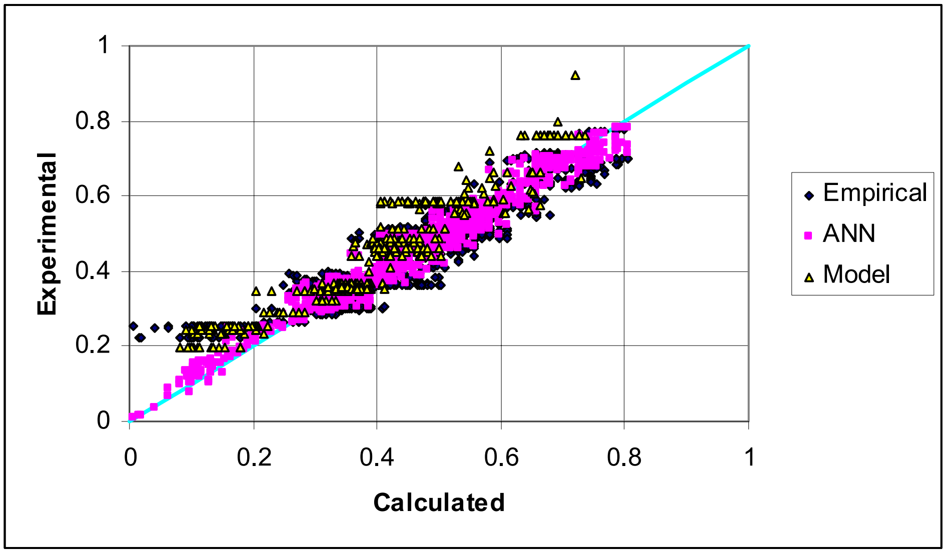

Fig. 4.20 Comparison of experimental data with the predictions of the model, empirical equations and ANN

Comparisons of the predictions of ANN with empirical equations show (Fig. 4.20) that ANN estimates the cuttings bed thickness more accurately than the empirical equations at lower bed thicknesses. For this reason, it is recommended that the ANN approach be utilized in future studies.

4.7 CONCLUSIONS

Cuttings transport and hydraulics of foam was investigated in horizontal and highly-inclined wellbores. Foam rheology and wall slip were investigated extensively. A mechanistic model was developed for describing cuttings transport with foam and a computer simulator was developed from the mechanistic model. Finally, additional methods were proposed to determine the cuttings bed thickness for practical purposes. The following conclusions are reached in this study:

Foam Rheology

- Mathematical models were developed for calculating generalized consistency index (K') and generalized flow behavior index (N) for laminar foam flow in pipes as well as in geometries associated with the existence of a cuttings bed in the annular space of a wellbore.

- Experiments were conducted to determine foam rheological properties as a function of foam quality. Analysis of the flow curves of the foam used in this study indicates that foam behaves like a pseudo-plastic fluid with a negligible yield stress. The flow behavior and consistency indices change non-linearly with foam quality. Wall slip was observed in the rheology measurement.

- A procedure is presented for calculating foam frictional pressure losses under laminar and turbulent flow regimes for pipe and annular flow using Dodge & Metzner[24] friction factor correlations. Predicted results are in good agreement with experimental measurements (difference less than ± 20%) for both pipe and annular flow geometries and foam qualities of 70% and 80%. The experimental data are considerably more scattered for 90% quality.

Cuttings Transport

- Cuttings transport experiments with water and foam consistently showed the existence of a three-layer structure in the test section; namely, a stationary bed, a moving mixture (fluid and cuttings) and clear fluid. The following observations were made during the experiment with foam:

    - The height of the stationary bed increases as foam quality increases at a given in-situ foam flow rate.
    - Very high foam flow velocities (more than 18 ft/s) are required to prevent a thick cuttings bed (less than 20% of the wellbore area) for all foam qualities.
    - The effect of inclination angle on cuttings transport is negligible at high inclination angles (i.e. 70° to 90°).

- In addition to the experimental observations, a three-layer cuttings transport model was developed using the mass and momentum conservation equations for steady, isothermal flow conditions. Theoretically, cuttings bed thickness, mixture thickness, clear fluid velocity, mixture velocity, slip velocity between the cuttings and the fluid at the mixture, in-situ cuttings concentration of the mixture and total pressure drop can be determined from the model. While a number of simplifying assumptions have been introduced to develop a workable model, the calculated results are considered to be reasonable. Cuttings bed thickness and total pressure drop for water tests were predicted with an error of less than 15% and for foam tests with an error of mostly less than 25%. Based on the simulator results, the following conclusions can be reached:

    - As the flow rate is increased, an optimum point for the frictional pressure losses is determined; this optimum frictional pressure loss can be used for design purposes.
    - Foam quality and frictional pressure gradient may vary as foam flows through a pipe or annulus.

  - The cuttings transport ratio for the moving mixture (foam and cuttings) is quite high. Therefore, one can state that the foam used in this study has good cuttings transport capacity in spite of a rather thick cuttings bed.
  - When a Newtonian fluid is investigated using the simulator, the cuttings bed area decreases with increase in flow rate, cuttings diameter and fluid density; however, the bed area increases with increase in cuttings density. Rate of penetration and eccentricity have very slight effects on cuttings bed area.

- Due to the long execution time required by the simulator, two more methods (empirical equations and Artificial Neural Networks (ANN)) are presented to estimate the cuttings bed thickness, when the cuttings bed thickness is the only concern. Both methods can estimate cuttings bed thickness with an error of less than 20% when the bed area is higher than 35% of the wellbore area. When the bed area ratio is less than 35%, empirical equations can only estimate the bed thickness with quite large errors; however, ANN can estimate the bed thickness with an error of less than 10%.

NOMENCLATURE

A	Area
a	Geometric Parameter
b	Geometric Parameter
C	Concentration, Coefficient
d	Diameter
F	Force
f	Friction Factor
g	Gravitational Acceleration
H	Distance between Two Parallel Plates
h	Height of the Fluid Element
K	Consistency Index
K’	Generalized Consistency Index
L	Length
m	Mass
n	Fluid Behavior Index
N	Generalized Fluid Behavior Index
N_{Fr}	Froude Number
N_{Re}	Reynolds Number
P	Pressure
Q	Flow Rate
R	Radius
r	Radius of the Fluid Element
ROP	Rate of Penetration
S	Perimeter
s	Space Vector
T	Temperature
TR	Transport Ratio
t	Time
v	Velocity
V	Volume
W	Weight

w	Width of the Parallel Plates

Greek Letters

α	Inclination Angle (from horizontal)
β	Angle, Slip Coefficient
ρ	Density
$\Nu$	Diffusion Coefficient
ϕ	Porosity
Γ	Quality
θ	Radial Direction, Angle
τ	Shear Stress
μ	Viscosity

Subscripts

b	Bed, Buoyancy
c	Cuttings, Capillary
chr	Characteristic
CS	Control Surface
CV	Control Volume
D	Drag
dim	Dimensionless
eq	Equivalent
f	Fluid, Foam
G	Gas
hyd	Hydraulic
I	First Layer
i	Inner
II	Second Layer
III	Third Layer
L	Lift
L	Liquid
n	Nominal
o	Outer
p	Plastic, Particle
r	Relative
s	Slip, Suspension
T	Transport
w	Wall, Wellbore
x	x-direction
y	Yield, y-direction

REFERENCES

1. Blauer, R.E., Mitchell, B.J., and Kohlhaas, C.A.,; “Determination of Laminar, Turbulent and Transitional Foam-Flow Friction Losses in Pipes” SPE 4885, paper presented at the 1974 SPE California Regional Meeting, San Francisco, April 4-5, 1974.
2. Sanghani, V.; “Rheology of Foam and Its Implications in Drilling and Cleanout Operations,” M.S. Thesis, the University of Tulsa, Tulsa, OK, U.S.A, 1982.
3. Beyer, A.H., Millhone, R.S., Foote, R.W.; “Flow Behavior of Foam as a Well Circulating Fluid,” SPE 3986, paper presented at the 1972 Annual SPE Meeting, San Antonio, October 8-11, 1972.
4. Harris P.C., and Heath S.J., “High-Quality Foam Fracturing Fluids”, SPE 35600, Gas Technology Conference, Calgary-Canada, (April 28-May 1, 1996)
5. Reidenbach,V.G.,Harris, P.C., Lee, Y.N., Lord, D.L.; “Rheology study of foam fracturing fluids using nitrogen and carbon dioxide”, SPE Production Engineering, January 1986.
6. Valko, P. and Economides, M.J.; “Volume equalized constitutive equations for foamed polymer solutions,” Journal of Rheology, August 1992 American Institute of Physics.

7. Gardiner, B.S., Dlugogorski, B.Z., and Jameson, G.J.; "Rheology of Fire Fighting Foams," accepted for publication, Fire Safety Journal, 1998.
8. Sanchez, R. A., Azar, J. J., Bassal, A. A., and Martins, A. L., "The Effect of Drillpipe Rotation on Hole Cleaning During Directional Well Drilling", SPE 37626, Presented at the 1997 Drilling Conference, Amsterdam-Holland (March 4-6, 1997)
9. Tomren, P. H., "The Transport of Drilled Cuttings in an Inclined Eccentric Annulus", M.S. Thesis, University of Tulsa, Tulsa (1979)
10. Iyoho, A. W., "Drilled-Cuttings Transport by Non-Newtonian Drilling Fluids Through Inclined Eccentric Annuli", Ph.D. Dissertation, University of Tulsa, Tulsa (April 1980)
11. Larsen, T. I., "A Study of Critical Fluid Velocity in Cuttings Transport For Inclined Wellbores", M.S. Thesis, University of Tulsa, Tulsa (1990)
12. Gavignet, A. A. and Sobey, I. J., "A Model for the Transport of Cuttings in Highly Deviated Wells", SPE 15417, Presented at the 61st Annual Technical Conference and Exhibition, New Orleans-Louisiana (October 5-8, 1996)
13. Clark, R. K., and Bickham, K. L., "A Mechanistic Model for Cuttings Transport", SPE 28306, Presented at the 69th Annual Technical Conference and Exhibition, New Orleans-Louisiana (September 25-28, 1994)
14. Nguyen, D., and Rahman, S. S., "A Three-Layer Hydraulic Program for Effective Cuttings Transport and Hole Cleaning in Highly Deviated and Horizontal Wells", IADC/SPE 36383, Presented at the 1996 Asia Pacific Drilling Technology, Kuala Lumpur-Malaysia (September 9-11, 1996)
15. Saintpere S., Marcillat Y., Bruni F., Toure A., "Hole Cleaning Capabilities of Drilling Foams Compared to Conventional Fluids", SPE 63049, Presented at the 2000 SPE Annual Technical Conference and Exhibition, Dallas-Texas (October 1-4, 2000)
16. Martins A.L., Lourenco A.M.F., de Sa C.H.M., "Foam Property Requirements for Proper Hole Cleaning While Drilling Horizontal Wells in Underbalanced Conditions", SPE Drilling and Completion (December 2001)
17. Krug, J.A., and Mitchell, B.J., "Charts Help Find Volume Pressure Needed for Foam Drilling," OGJ, pp.61-64, (February 7, 1972)
18. Okpobiri, G.A., "Experimental Determination of Solids Friction Factors and Minimum Volumetric Requirements in Foam and Mist Drilling and Well Cleanout Operations", Ph.D. Dissertation, University of Tulsa, Tulsa, (1982)
19. Gou B., Miska S., Harelard G., "A Simple Approach to Determination of Bottom Hole Pressure in Directional Foam Drilling", ASME, Jan., (1994)
20. Ozbayoglu M.E., "Cuttings Transport with Foam in Horizontal and Highly-Inclined Wellbores", Ph.D. Dissertation, University of Tulsa, Tulsa (2002)
21. Kozicki W., and Tiu C., Encyclopedia in Fluid Mechanics, Cheremisinoff, N.P., Gulf, Houston, 7-199 (1988)
22. Jastrzebski, Z.D., "Entrance Effects and Wall Effects in an Extrusion Rheometer During the Flow of Concentrated Suspensions", Ind.Eng.Chem.Fund. 6, 445-453, (1967)
23. Welstead S.T., Neural Networks and Fuzzy Logic Applications in C++, McGraw-Hill Book Company, New York, 1996
24. Dodge D.W., and Metzner A.B., "Turbulent Flow of Non-Newtonian Systems", AIChE Journal, 5, No.2, pp.189-204 (June 1959)

5. Cuttings Transport with Aerated Muds under Low Pressure Ambient Temperature Conditions (Task 7)

ABSTRACT

This study was conducted in order to gain more in-depth understanding of cuttings transport in horizontal and highly-inclined wells when using gasified fluids. Experiments were carried out in a field-scale, low-pressure flow loop which has a 90-ft annular test section (8" X 4.5"). The experiments were performed in horizontal and near-horizontal (inclination angle of 80 degrees from vertical) configurations. Gravel with 3.29 mm average diameter was used to simulate drill cuttings. Water and air were used as the liquid and gas phases, respectively. The three phases were injected into the flow loop, at different volumetric flow rate combinations. Pressure drop, cuttings accumulation, pressure and temperature in the test section were recorded in each experiment through a data acquisition system. Gas and fluid-interface distributions were observed and reported for each experiment. Likewise, the solid-liquid distributions were classified into three different patterns and reported for each experiment. The effects of gas and liquid flow rates, drilling rate, inclination angle, pressure drop and flow patterns on cuttings transport were analyzed.

During the tests, it was observed that cuttings are only transported in the liquid phase. It was also found that there are minimum air and water velocities required to avoid the formation of a stationary cuttings bed. The minimum requirements for air and water injection rates are also a function of the solids injection rate. Therefore, It is postulated that there is a minimum energy required for solids transport, and it is constant for a given solids injection rate. In addition, it was found that the inclination effect for angles close to horizontal is negligible.

5.1 INTRODUCTION

One of the primary functions of a drilling fluid is to transport efficiently drilled cuttings to the surface. During the past two decades, several studies[1-10] have been conducted to obtain a better understanding of the cuttings transport phenomena and give the drilling engineer better tools to design efficient hydraulic programs to reduce drilling time and cost. Inefficient hole cleaning can create problems such as stuck pipe and increased torque and drag, which costs the oil industry millions of dollars in losses.

Underbalanced and near-balanced drilling techniques have become excellent options to reduce drilling costs and increase well and reservoir productivities. These techniques offer several significant benefits over conventional drilling. One of the most important benefits is reduction of formation damage, which requires additional stimulation jobs. In addition to this, these drilling techniques bring cost-reduction benefits directly to a drilling operation by increasing the rate of penetration, bit life and reducing the probability of differential sticking of the drillpipe[11-13].

Applications of horizontal and deviated-well drilling have been combined in recent years with non-conventional drilling techniques, such as underbalanced drilling in which mixtures of liquid and gas are commonly used as a drilling fluid to reach the desired bottom hole pressure condition. Commonly used fluids for underbalanced drilling are aerated mud, foam and mist. The increased use of aerated fluids to drill horizontal and deviated wells has created a need for better understanding of cuttings transport with aerated fluids. Recently, Sunthankar[14] studied the hydraulics and characteristics of gasified fluid systems in annular geometries. As part of these recent efforts, this research is aimed to investigate cuttings transport in horizontal and near-horizontal wellbores when aerated drilling fluids are used.

5.2 EXPERIMENTAL INVESTIGATION

5.2.1 EXPERIMENTAL SETUP

The University of Tulsa Drilling Research Projects (TUDRP) flow loop (low pressure ambient temperature flow loop) was used for the experimental investigation. Figure 5.1 presents a schematic diagram of the flow loop, which is designed for studying cuttings transport with both conventional and compressible drilling fluids.

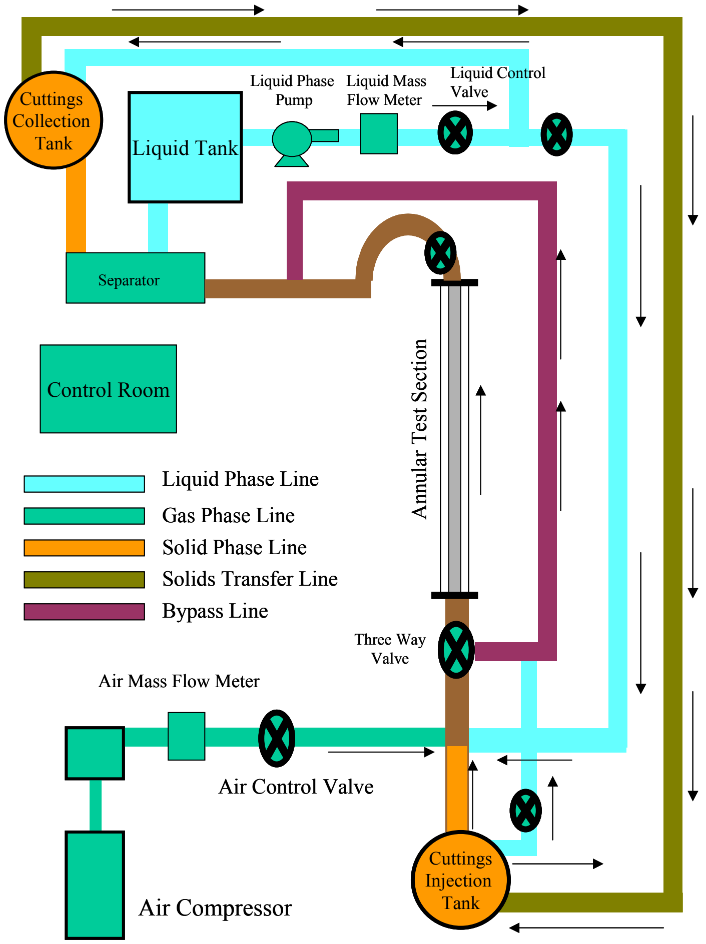

Fig. 5.1 Schematic diagram of the flow loop

The test section of the flow loop is approximately 100 ft long and has an 8-inch inside diameter. The test section is made up of a transparent acrylic pipe that simulates the wellbore and a 4 ½ inch OD inner pipe that simulates the drill pipe.

The inner pipe is attached to a variable speed motor that allows the drill pipe to rotate up to 200 RPM. The loop is supported by a steel structure that can be inclined at any angle between 10-90° from vertical. The liquid phase is stored in a 1000-gallon tank with the option to store an additional 800 gallons in a second tank. The liquid phase is delivered into the annulus by using a centrifugal pump which has flow capacity of 650 gpm. The liquid flow rate is controlled by a Fisher control valve and measured by a Coriolis mass flow meter (Micromotion).

A compressor with a working capacity of 0-125 psi and 0-1200 Scfm is used for gas injection. A small part of the compressed air is stored in an accumulator, which is used to supply air to the pneumatically operated equipment. The air flow rate to the loop is regulated by a control valve (Masoneilan valve) and measured using two air mass flow meters (capacity: 50-1600 Scfm at 0-125 psi).

During the test, cuttings are stored in a cuttings storage tank that has a capacity of 22 bbl of mud and cuttings. The tank is capable of running for 2-3 hours with an injection rate of 40-50 ft/hr. An auger that is placed at bottom of the cuttings storage tank injects the cuttings at the inlet of the test section. Part of the liquid phase from the centrifugal pump flows to the top of the storage tank to maintain a constant liquid level in the tank and steady injection of cuttings.

Three pressure taps are located on the flow loop; one at each end, at a distance of 76.06 ft from each other; and a third one located in the middle, at a distance of 36.45 ft away from the one at the upstream end. Differential pressures between the pressure taps were measured by using differential pressure transducers.

5.2.2 SCOPE OF EXPERIMENTAL WORK

Cuttings transport experiments with foam were conducted using an air-water-solid system. Commercial gravel with an average particle diameter of 3.29 mm, porosity of 38% and density of 22.28 lb/gal was used as drill cuttings. In order to reduce the test matrix, some parameters were held constant during the flow loop tests. The effects of drill pipe rotation, drill pipe eccentricity and liquid phase viscosity on cuttings transport were not covered in this investigation. Gas and liquid injection rates were set in the range of 200 to 700 GPM. 30, 50 and 70 ft/hr drilling rates (ROP) were used in the experiments. Different combinations of gas and liquid flow rates were chosen to maintain a constant total flow rate. Tables 5.1 and 5.2 present gas and liquid flow rate combinations used during the tests.

Table 5.1 Gas and Liquid injection Rates I

Total Flow (GPM)	200		300		400	
	Liquid (GPM)	**Gas (GPM)**	**Liquid (GPM)**	**Gas (GPM)**	**Liquid (GPM)**	**Gas (GPM)**
	200	0	300	0	400	0
	100	100	200	100	300	100
			100	200	200	200
					100	300

Table 5.2 Gas and Liquid injection Rates II

Total Flow (GPM)	500		600		700	
	Liquid (GPM)	**Gas (GPM)**	**Liquid (GPM)**	**Gas (GPM)**	**Liquid (GPM)**	**Gas (GPM)**
	500	0	600	0	600	100
	400	100	500	100	500	200
	300	200	400	200	400	300
	200	300	300	300	300	400
	100	400	200	400	200	500

In order to defining boundaries for the minimum gas and liquid flow rate requirements, additional tests were conducted using total flow rates higher than 700 gpm. Cuttings transport experiments were conducted using two different inclination angles, 90° and 80° from vertical. Tables 5.3 and 5.4 present test matrixes used in cuttings transport experiments at 90° and 80° inclinations, respectively.

Table 5.3 Gas and Liquid injection Rates III (90° inclination)

Horizontal Position								
30 ft/hr ROP			50 ft/hr ROP			70 ft/hr ROP		
Liquid (GPM)	**Gas (GPM)**	**Total GPM**	**Liquid (GPM)**	**Gas (GPM)**	**Total (GPM)**	**Liquid (GPM)**	**Gas (GPM)**	**Total (GPM)**
200	1300	**1500**	200	1500	**1700**	500	1000	**1500**
200	1000	**1200**	200	1000	**1200**	500	800	**1300**
200	800	**1000**	300	1400	**1700**	500	600	**1100**
200	600	**800**	300	1000	**1300**	500	400	**900**
300	1250	**1550**	300	800	**1100**	600	1000	**1600**
300	1000	**1300**	300	600	**900**	600	800	**1400**
300	800	**1100**	400	475	**875**	600	600	**1200**
300	600	**900**	500	1000	**1500**	600	400	**1000**
400	450	**850**	500	800	**1300**			
400	300	**700**	500	600	**1100**			
500	450	**950**	500	400	**900**			
500	400	**900**	600	1000	**1600**			
500	300	**800**	600	800	**1400**			
600	400	**1000**	600	600	**1200**			
600	300	**900**	600	400	**1000**			
600	200	**800**						

Table 5.4 Gas and Liquid Injection Rates IV (80° inclination)

80 Degrees from vertical					
30 ft/hr ROP			**50 ft/hr ROP**		
Liquid (GPM)	**Gas (GPM)**	**Total (GPM)**	**Liquid (GPM)**	**Gas (GPM)**	**Total (GPM)**
500	1000	1500	500	1000	1500
500	800	1300	500	800	1300
500	600	1100	500	600	1100
500	400	900	500	400	900
600	800	1400	600	600	1200
600	600	1200	600	400	1000
600	400	1000			

5.2.3 TEST PROCEDURE

Different combinations of gas and liquid flow rates were injected into the loop for a given inclination angle, cuttings injection rate (ROP) and total flow rate. The aim of this approach was to observe the effect of volumetric concentration of each phase in the transport phenomena. Gas, liquid and solid phases were mixed together before entering the annular test section. The three phases were injected into the annular test section until steady state conditions were established. It is assumed that the steady state condition occurs when the collected cuttings mass flow rate is equal to the injected cuttings mass flow rate and all other test parameters are more or less constant. The tests were maintained under steady state condition for a while to observe the flow pattern (distribution of the interfaces) and modes of cuttings transport. Once the flow patterns were observed and recorded, the three-phase mixture in the test section was trapped. Cuttings bed perimeters on the wall and liquid level were measured. The average cuttings bed height is indirectly obtained from the average cuttings bed perimeter on the wall, which is calculated from measurements obtained at ten different locations. Knowing the average perimeter of the bed on the transparent pipe wall, the average bed height (equilibrium bed height) can be easily determined using geometric parameters shown in Fig. 5.2.

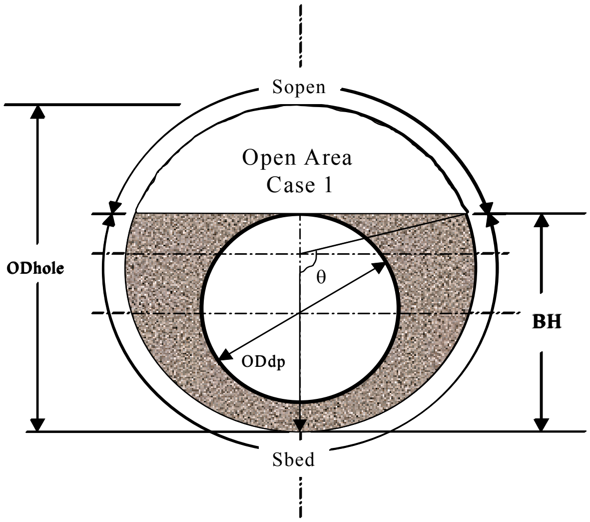

Fig. 5.2 Geometric parameters for bed height calculation

5.2.4 RESULTS

Tests were conducted using different combinations of gas-liquid flow rates for the horizontal position and the inclined position of 80 degrees from vertical. Different drilling rates (ROP) of 30, 50 and 70 ft/hr were simulated in each experiment. The amount of cuttings in the test section and the pressure drop were recorded.

Effect of Flow Pattern (Phases Interface Distribution in the Annulus)

The experiments revealed that cuttings are distributed and transported with different characteristic regimes, dependent on the gas and liquid flow rates.

Stationary bed Flow: When the total volumetric flow rate does not generate the fluid velocities required for transport of the cuttings, the cuttings particles start to accumulate at the bottom of the pipe and create a “stationary cuttings bed”, as shown in Fig. 5.3. The equilibrium bed height is reached when the fluid velocity becomes strong enough to transport the cuttings downstream, not allowing further cuttings accumulation.

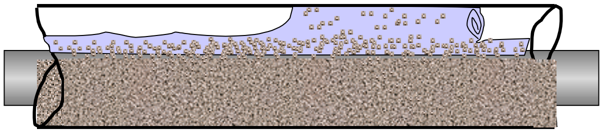

Fig. 5.3 Stationary cuttings bed

Moving Bed Flow: When increasing the volumetric flow rates, there is a point at which the cuttings bed breaks into a slowly moving cuttings bed, as shown in Fig. 5.4.

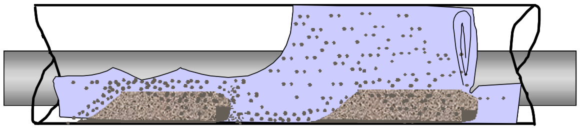

Fig. 5.4 Moving beds

Dispersed Flow: The dispersed flow normally occurs when the total volumetric flow rate is high enough to suspend all the solids particles in the liquid phase (Fig. 5.5).

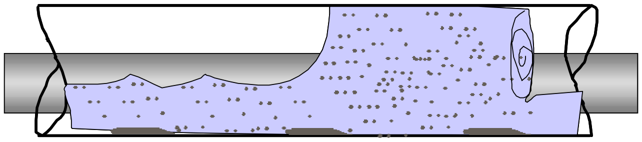

Fig. 5.5 Dispersed cuttings in the liquid phase

For horizontal configuration tests, the gas and liquid distributions were always in the intermittent region. Experimentally measured data is analyzed by calculated gas and liquid superficial velocities for each test. Superficial velocities do not represent the actual velocity of the phases but they are commonly used in multiphase flow data analysis as a reference. The superficial velocity is calculated by dividing the volumetric flow rate by the flow area.

Based on the concept of "Critical Transport Velocity", which is defined as the minimum fluid velocity needed to maintain a continuous upward movement of cuttings, it is possible to establish an approximate boundary that separates the region (see Fig. 5.6 to 5.8) in which a stationary cuttings beds are formed or not. This boundary can be created from the measured data points where the solids are in the moving bed regime, a condition that satisfies the concept of critical transport velocity. The transition boundaries for annular-intermittent and dispersed-intermittent were estimated using the computer program (FLOMAP)[34].

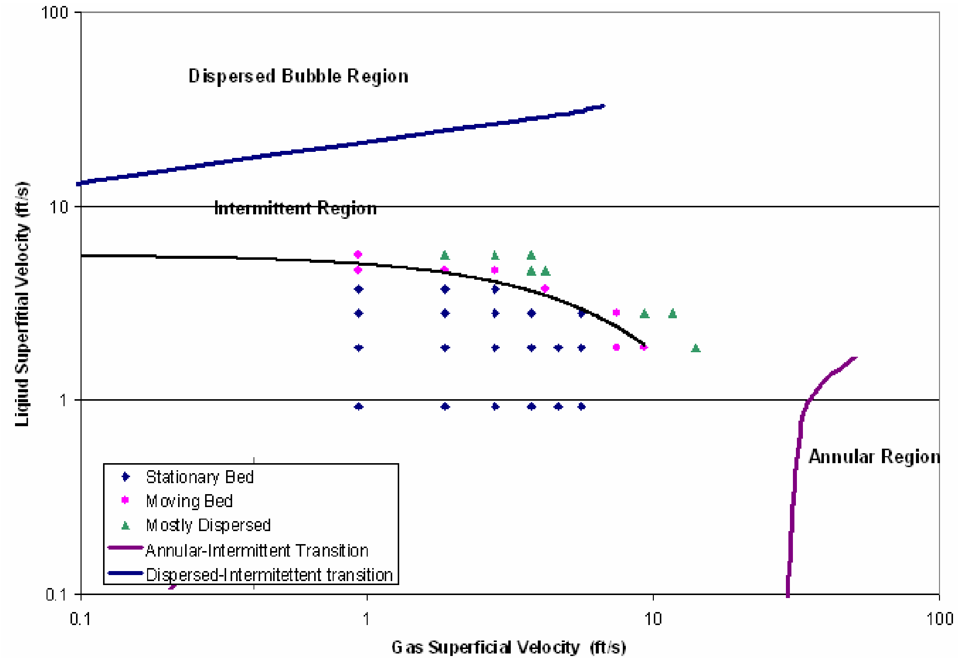

Fig. 5.6 Flow pattern map for horizontal position and 30 ft/hr ROP

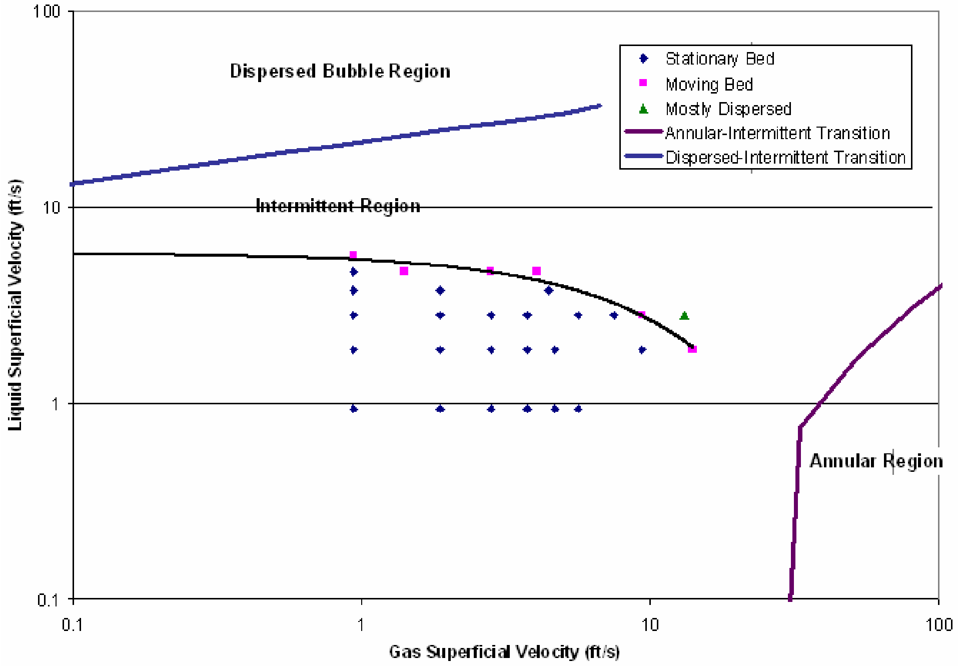

Fig. 5.7 Flow pattern map for horizontal position and 50 ft/hr ROP

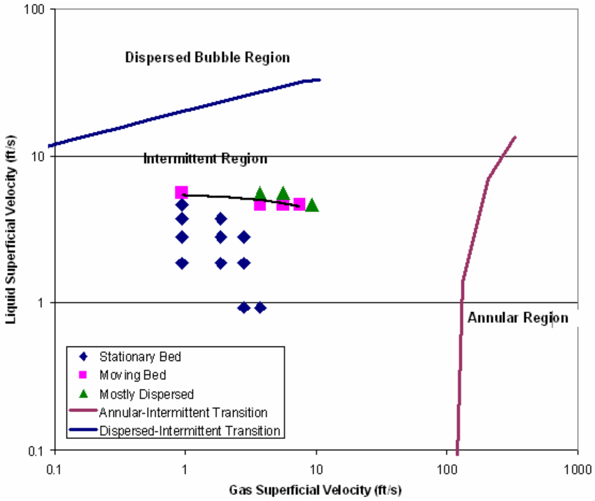

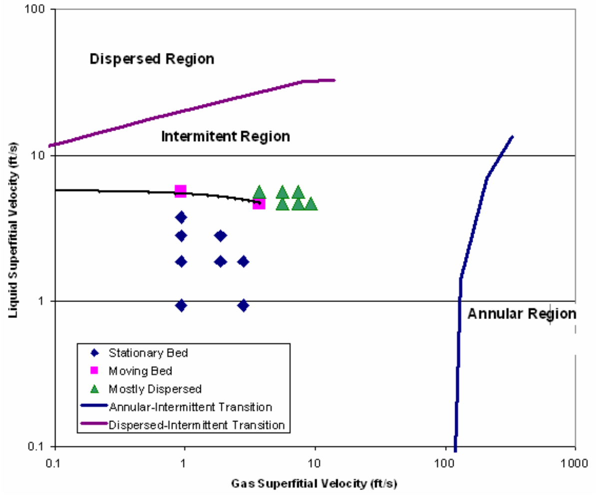

Fig. 5.8 Flow Pattern map for horizontal position and 70 ft/hr ROP

Fig. 5.9 Flow pattern map for 80-degree inclination and 30 ft/hr ROP

Similar to the horizontal configuration tests, the gas and liquid distributions for 80-degree inclination tests were always in the intermittent region in which the flow patterns varies from elongated bubbles to slug flow.

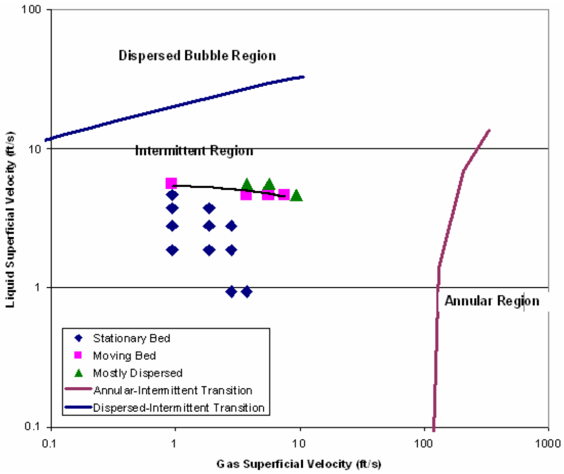

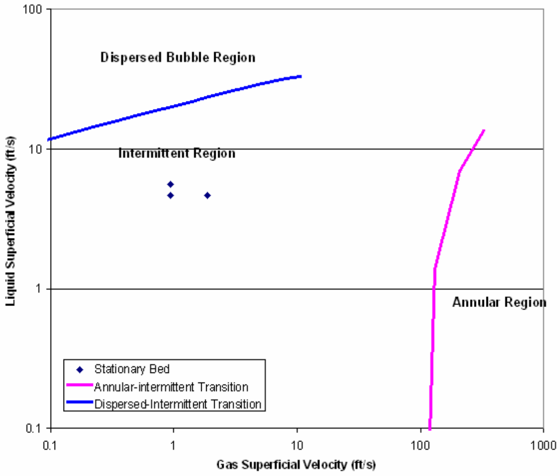

Fig. 5.10 Flow pattern map for 80-degree inclination and 50 ft/hr ROP

Fig. 5.11 Flow pattern map for 80-degree inclination and 70 ft/hr ROP

Effect of Angle of Inclination

To determine the effect of angle of inclination on the critical transport velocity, bed heights measured at different inclination angles (horizontal and 80 degrees) and presented in Figs. 5.12 and 5.13 as a function of gas-liquid ratio (GLR).It is clear that the differences in bed height for a given GLR at different angles of inclination are less than 5% on average. This leads to the conclusion that the effect of inclination is minimal at high inclination angles.

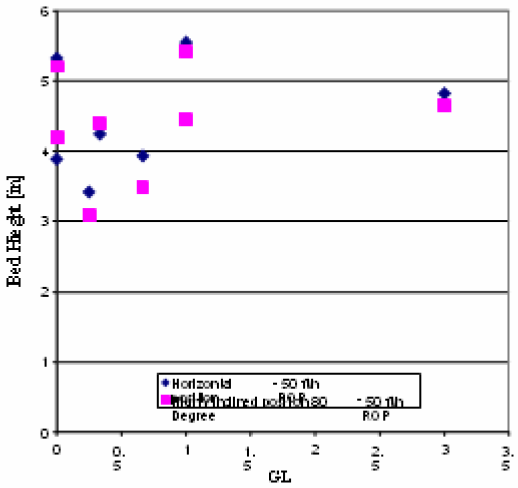

Fig. 5.12 Effect of angle of inclination on bed height for 50 ft/hr ROP

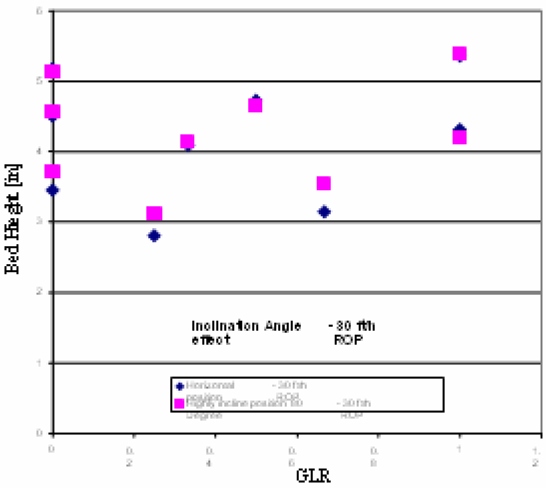

Fig. 5.13 Effect of angle of inclination on bed height for 30 ft/hr ROP

Effect of Gas and Liquid Flow Rates

The boundary between the stationary cuttings bed and moving bed regimes can be expressed as:

$$V_{sl} = Ae^{-B \cdot V_{sg}} \tag{5.1}$$

Equation 5.1 is empirically found using experimental data obtained in moving bed condition. This is a general equation for liquid superficial velocity expressed as a function of the superficial gas velocity. Empirical constants A and B depend on the drilling rate or rate of penetration. Rearranging Eq. 5.1, we have:

$$V_{sg} = \frac{1}{B} \mathrm{Ln}\left(\frac{A}{V_{sl}}\right) \tag{5.2}$$

where

$$V_{sg}\,(\mathrm{ft/s}) = 0.3208 \frac{Qg_{is}}{A_t} \tag{5.3}$$

$$V_{sl}\,(\mathrm{ft/s}) = 0.3208 \frac{Ql_{is}}{A_t} \tag{5.4}$$

Qg_{is} and Ql_{is} are the volumetric flow rate of gas and liquid in gallons per minute (GPM) at in situ conditions. A_t is the flow area (in^2):

$$A_t = \left(ID_{hole}^2 - OD_{dp}^2\right)\frac{\pi}{4} \tag{5.5}$$

ID$_{hole}$ and OD$_{dp}$ are borehole and outside drill pipe diameters (in) respectively. Substituting Eq. 5.5 into Eqs. 5.3 and 5.4 we have:

$$V_{sg}(\mathrm{ft/s}) = 0.4085\frac{Qg_{is}(\mathrm{GPM})}{\left(ID_{hole}^2 - OD_{dp}^2\right)} \tag{5.6}$$

$$V_{sl}(\mathrm{ft/s}) = 0.4085\frac{Ql_{is}(\mathrm{GPM})}{\left(ID_{hole}^2 - OD_{dp}^2\right)} \tag{5.7}$$

Using Eqs. 5.2, 5.6 and 5.7, the following expression for gas injection rate can be obtained:

$$Qg_{is} = \frac{1}{B}\cdot\frac{ID_{hole}^2 - OD_{dp}^2}{0.4085}Ln\left(\frac{A\left(ID_{hole}^2 - OD_{dp}^2\right)}{0.4085\cdot Ql_{is}}\right) \tag{5.8}$$

At this point, we have the gas volumetric flow rate, at the in-situ condition, as a function of geometric parameters, in-situ liquid volumetric flow and empirical constants (A and B). Assuming constant mass flow rate of the gas phase and applying the ideal gas law, in-situ gas volumetric flow rate can be determined by:

$$\frac{Qg_{sc}P_{sc}}{T_{sc}} = \frac{Qg_{is}P_{is}}{T_{is}} \tag{5.9}$$

where the subscript (sc) refers to standard conditions. Rearranging Eq. 5.9 and using 520° R as the temperature at standard condition and 14.7 psia as the pressure at standard condition we can estimate the gas volumetric flow rate at standard conditions:

$$Qg_{is} = \frac{1}{35.3742}Qg_{sc}\frac{T_{is}}{P_{is}} \tag{5.10}$$

By placing Eq. 5.10 into Eq. 5.8, an empirical equation for minimum gas volumetric flow rate at standard conditions required for effective cuttings transport in horizontal and near horizontal can be expressed as:

$$Q_g(\mathrm{SCFM}) \geq \frac{11.5752}{B}Ln\left(\frac{A\left(ID_{hole}^2 - OD_{dp}^2\right)}{0.4085\cdot Q_l}\right)\left(ID_{hole}^2 - OD_{dp}^2\right)\frac{P_{BH}}{T_{BH}} \tag{5.11}$$

Equation 5.11 is based on the assumption that the liquid phase is incompressible and there is no mass transfer between phases. The empirical values for the A and B coefficients (Table 5.5) were determined from experimental data obtained in the moving bed condition. The minimum gas volumetric flow rate is a function of the liquid volumetric flow rate, geometry parameters, empirical coefficients (A and B), temperature and pressure.

Table 5.5 Minimum Gas Flow Rate Coefficients for Horizontal Position

Rate of Penetration (ft/hr)	A	B
30	5.5993	0.1148
50	5.7762	0.0785
70	5.9162	0.0328

The effects of gas and liquid flow rates can be seen in Fig. 5.14, where Eq. 5.1 is plotted for the three different drilling rates. It apparent that the liquid phase has more influence on the transport phenomena than the gas phase. A small reduction in the liquid volumetric flow rate implies a considerable increase in the gas volumetric flow rate in order to maintain the same level of hole cleaning. Figure 5.14 shows that the minimum requirements for gas and liquid flow rates increase with an increase in drilling rate for the same cuttings size.

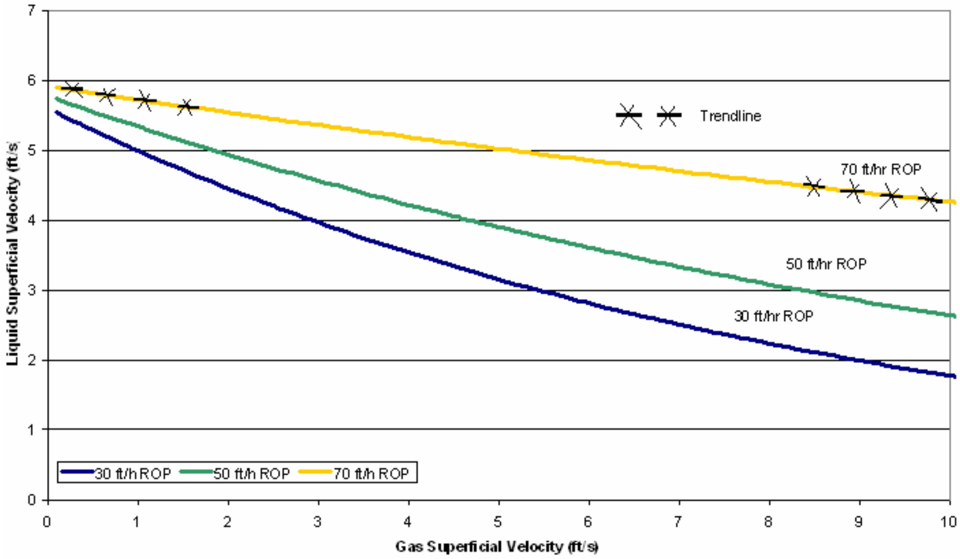

Fig. 5.14 Minimum gas and liquid superficial velocities required for effective cuttings transport in horizontal wells

Pressure Drop Effect

The experimental data indicate that pressure drop is constant for each curve for the minimum gas and liquid flow rates at a given drilling rate (Fig. 5.15). The steady-state pressure gradient is the sum of three pressure gradient components: friction, gravity and acceleration. Thus, the pressure gradient is given as:

$$\left.\frac{dP}{dZ}\right|_{\text{Total}} = \left.\frac{dP}{dZ}\right|_{\text{Friction}} + \left.\frac{dP}{dZ}\right|_{\text{Gravitation}} + \left.\frac{dP}{dZ}\right|_{\text{Acceleration}} \tag{5.12}$$

For the horizontal case, the gravitational term does not exist and the acceleration term is neglected, assuming a constant cross-section area along the pipe length. Therefore, the total pressure drop in the horizontal position will be essentially equal to the frictional component.

The existence of a minimum frictional pressure drop that assures hole cleaning in three phase flow means that there is minimum amount of kinetic energy that we need to put into the systems in order to transport the cuttings. This minimum energy is proportional to the drilling rate or solid injection rate. Increasing the drilling rate implies that more energy is required to transport the drilled cuttings.

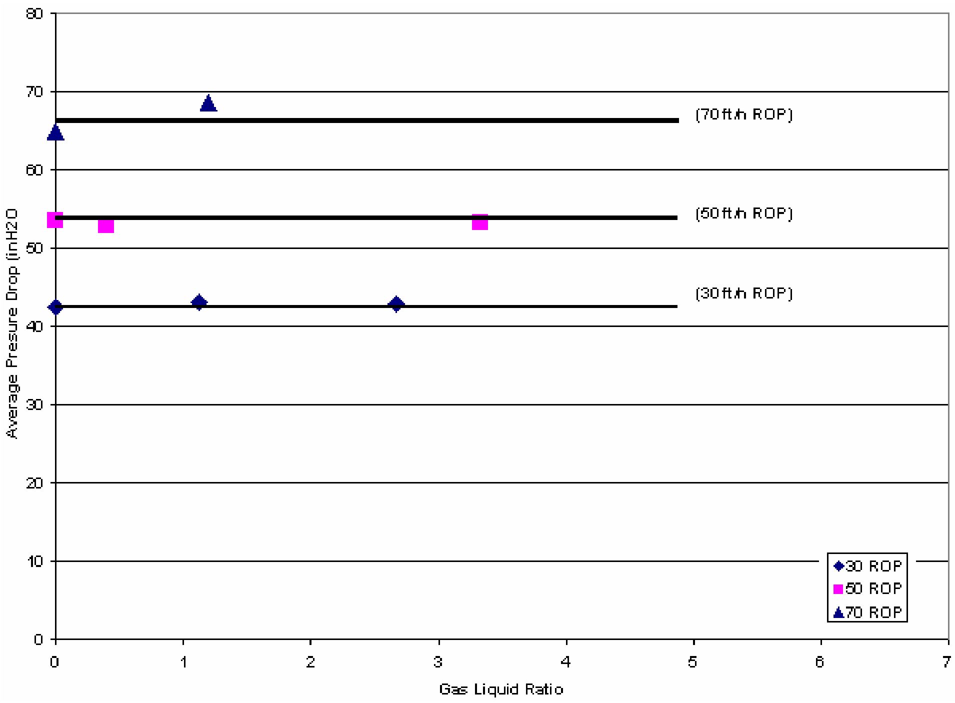

Fig. 5.15 Pressure drop data for different drilling rates without cuttings deposition in the Test Section

5.3 THEORETICAL ANALYSIS

Frictional pressure loss is an important parameter that must be estimated for three-phase flow in pipes or annular geometries. In order to accurately predict pressure loss, a valid hydraulics model must consider the distribution or flow patterns of the three different phases in the annular geometry or pipe. It is also important that the model consider the "slip" between the phases. To the best of our knowledge, there is no hydraulics model for three-phase flow that meets these requirements for annular or pipe geometries.

Sunthankar[14] modified an existing hydraulics model for two-phase flow (gas-liquid) in pipes to annular flow using the concept of hydraulic diameter. The model that Sunthankar[14] modified was Xiao's Unified Model[26] for two-phase flow in pipes. In drilling, the solids volumetric flow rate is small compared with the gas and liquid injection rates; therefore we can use the Sunthankar's modified hydraulic model, which neglects the presence of solids in the system for annular geometries to compare our experimental results with a model prediction. We compared the three-phase flow experimental data from the tests in which we observed the moving bed condition with the calculated values obtained from the model. For the hydraulic calculation the computer program, FLOCAL[27] was used. The results of the comparisons are shown in Fig. 5.16.

Figure 5.16 shows that the Xiao's modified model, which does not account for the presence of solids, underpredicts the pressure drop with more than 30% error compared with the three-phase flow data in the moving bed condition. These results show that, although the solids volumetric flow rate is small compared with liquid and gas injection rates, the solids creates an additional resistance to flow and should be included in the calculation of pressure drop.

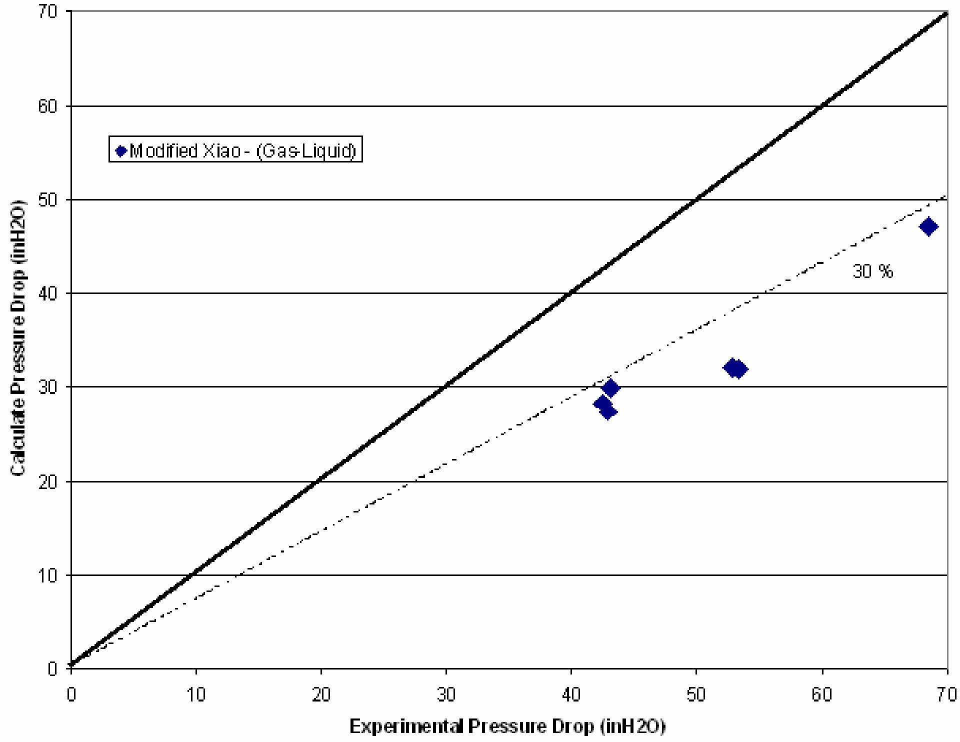

Fig. 5.16 Comparison of the three Phase flow data with modified Xiao Model

It is known that frictional pressure drop for two phase flow (gas-liquid) is mainly a function of mixture velocity, mixture density, friction factor and geometry[36].

$$\left.\frac{dP}{dZ}\right|_{Friction} = \frac{2 f \rho_m V_m{}^2}{d_h} \tag{5.13}$$

Experiments showed that solids are transported only in the liquid phase. Thus, in order to use the modified Xiao model to account for the presence of solids, it is necessary to assume that the liquid phase is a homogeneous mixture of liquid and solids (slurry). First, we need to calculate values for the equivalent slurry volumetric flow rate and slurry superficial velocity for a homogeneous mixture of solids and liquid:

$$Q_{slurry} = Q_l + Q_s \tag{5.14}$$

$$V_{slurry} = V_{sl} + V_{ss} \tag{5.15}$$

If no slip is assumed, the equivalent density of the slurry can be estimated:

$$\rho_{slurry} = \rho_l(\lambda_l) + \rho_s(1-\lambda_l) \tag{5.16}$$

Superficial velocities and densities do not change significantly, because the solids volumetric flow rates for drilling operations are very small, compared with of the solid-liquid mixture flow rates. Based on comparisons between the three-phase flow experimental data and model predictions, the effective viscosity can be considered as the dominant variable.

Several correlations for the effective viscosity of slurry flow (liquid-solid) have been developed[28-29]. All of these correlations are based on the volumetric fraction of the solids and the liquid viscosity. It has been observed that the effective viscosity from these correlations does not change significantly for small solid volume fractions[28]. Kreigel[29] suggested the following correlation for the effective viscosity:

$$\mu_e = \frac{e^{B_s \Phi}}{\left(1 - \frac{\Phi}{\Phi_{max}}\right)} \tag{5.17}$$

where the effective viscosity will be function of the coefficient B_s, which is related to the shape of the solid, the solid volume fraction and the maximum solid volume fraction. Equation 5.17 indicates that the effective viscosity increases very rapidly as the solid volume fraction approaches the maximum possible value. Based on the experimental data obtained for two-phase flow (liquid-solid), the maximum solid volume fraction ($\Phi_{max} \approx 0.58$) can be estimated. Figure 5.17 presents the Kreiger's correlation predictions and measured effective viscosities as a function of solid volume fraction.

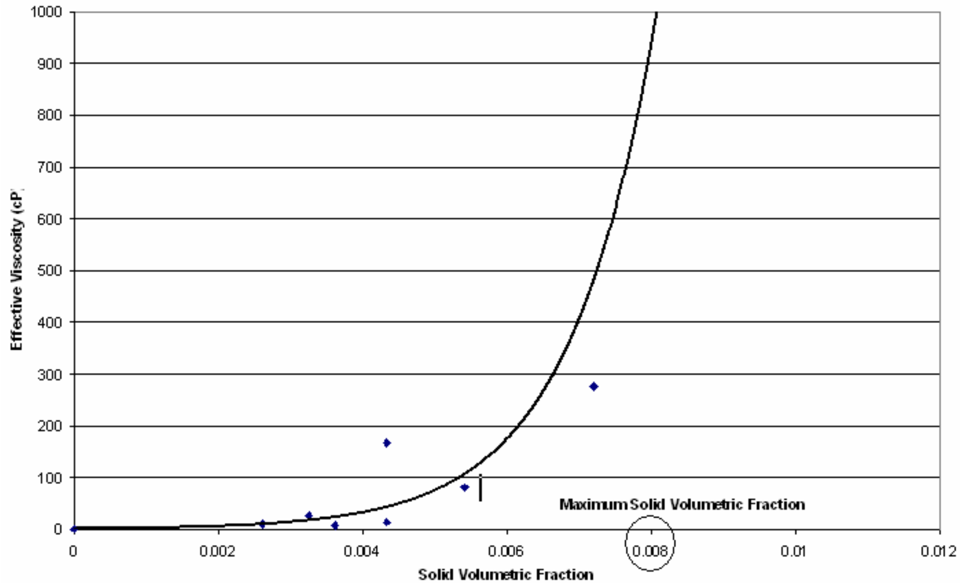

Fig. 5.17 Predicted and measured effective viscosity as a function of solid volume fraction

Previously, the three-phase flow experimental data were compared with the model predictions, but this time the model is accounting for the presence of solids as a slurry with a mixture density and an effective viscosity. The predictions of modified Xiao model are presented in Fig. 5.18. As seen from the figure, accounting for solids as a slurry improved the modified model predictions. The differences between the experimental data and model predictions are less than 30%. The model predictions are low at low solid volume fraction. However, when the solid fraction approaches the maximum solid fraction, model predictions are close to the experimental results.

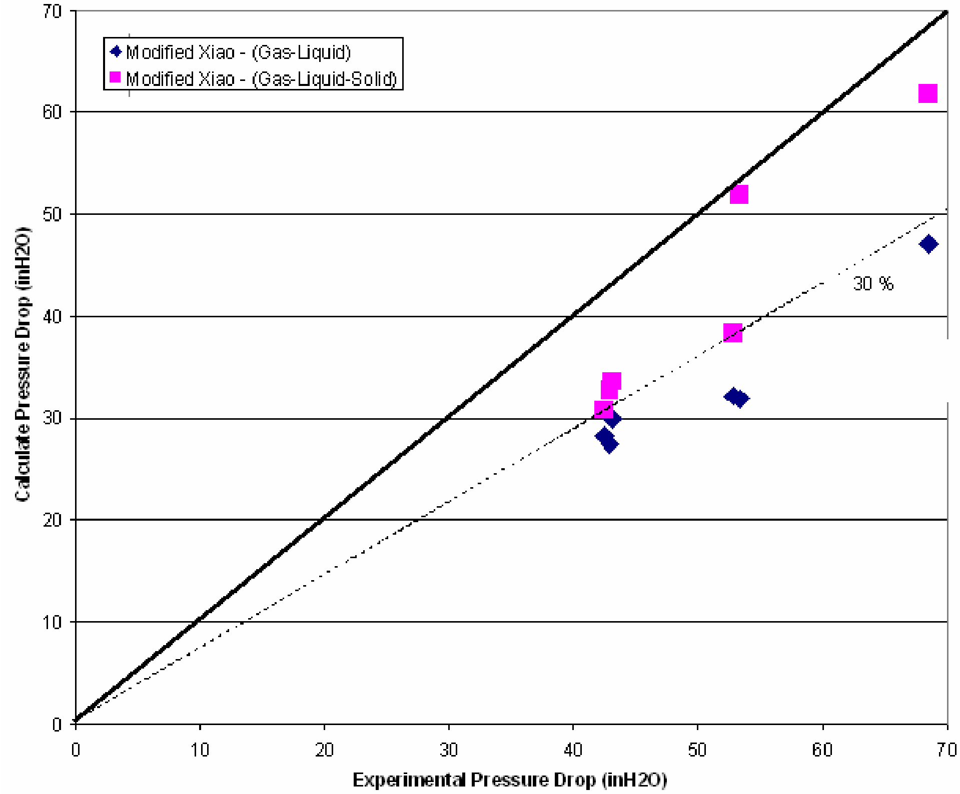

Fig. 5.18 Three-phase flow data compared with modified Xiao model

Considering the liquid phase as a slurry phase in the modified Xiao's model has improved pressure loss predictions of the model. The improvement is significant and should be taken into account, if the model is used for planning drilling operations. For the annular flow regime, the assumption of a slurry in place of the liquid phase may not be valid, since some cuttings particles could travel with the gas phase.

5.4 CONCLUSIONS

An experimental study of cuttings transport with aerated fluids in annular geometries was carried out. The effects of gas and liquid flow rates, drilling rate, flow patterns, inclination angle and pressure drop on cuttings transport with aerated fluids were analyzed. The experimental data and model predictions indicated:

- The cuttings flow patterns in the annular section are dependent on the total flow rate of each phase and may be classified as three types: "stationary cuttings bed", "moving beds" or "dispersed".
- Based on the concept of critical transport velocity, it is possible to create an approximate boundary for the minimum air and water requirements in order to avoid the formation of a stationary cuttings bed.
- The minimum requirements for gas and liquid injection for a horizontal wellbore configuration were in the intermittent region for two-phase flow (water-air).

- As the rate of penetration increases at a given total flow rate, the accumulation of cuttings in the horizontal section also increases.
- As the gas/liquid ratio increases at a given total flow rate, the cuttings accumulation in the annular test increases, while the average frictional pressure drop decreases.
- There is a minimum frictional pressure gradient or minimum energy required for continuous transporting of cuttings in an upward direction and avoiding the formation of a stationary cuttings bed.
- The minimal frictional pressure drop required to transport the cuttings in the annular section is a function of the drilling rate or cuttings injection rate.
- Ignoring the presence of solids in pressure-drop calculations for drilling operations will lead to an under prediction of the frictional pressure drop, since the presence of solids increases resistance to flow.
- The effect of the inclination angle is negligible for the near horizontal case (80 degrees from vertical).

NOMENCLATURE

AH	Hole area (in^2)
A	Minimum gas flow rate coefficient
B	Minimum gas flow rate coefficient
B_s	Solid shape coefficient
d	Distance between centers (in)
d_h	Hydraulic diameter (in)
C_c	Cuttings concentration
D_c	Equivalent solid diameter (in)
E_B	Elongated Bubbles
f	Friction factor
ID_{hole}	Hole diameter (in)
OD_{dp}	Outside drill pipe diameter (in)
Q_g	Gas volumetric flow (GPM)
Qg_{is}	Gas volumetric flow rate (GPM)
Qg_{sc}	Standard gas flow rate (GPM)
Ql	Liquid-solid mixture flow rate (GPM)
Ql_{is}	In-situ Liquid flow rate (GPM)
Ql_{is}	Standard Liquid flow rate (GPM)
Ql	Liquid volumetric flow (GPM)
Qs	Solids volumetric flow (GPM)
P	Pressure (psia)
P_{BH}	Bottom hole pressure (Psia)
P_{is}	Pressure at in-situ conditions (Psia)
P_{sc}	Pressure at standard conditions (Psia)
R_H	Hole radius (in)
R_{DP}	Drill pipe outside radius (in)
R_{OI}	Cuttings injection rate (Lb/min)
ROC	Cuttings collection rate (Lb/min)
ROP	Rate of penetration (ft/hrr)
S	Slug
S_{bed}	Hole perimeter in the bed area (in)
S_{Open}	Hole perimeter in the open flow area (in)
Q	Volumetric flow rate (gpm)

Qg_{is}	In-situ gas flow rate (gpm)
Ql_{is}	In-situ Liquid flow rate (gpm)
Q_{slurry}	Slurry volumetric flow rate (gpm)
T_{BH}	Bottom hole Temperature (R)
T_{is}	Temperature at in-situ condition (R)
T_{sc}	Temperature at standard condition (R)
$V_{cuttings}$	Cuttings volume
V_{water}	Water volume
V_T	Total mixture volume
V_t	Require cuttings transport velocity (ft/s)
V_{ts}	Terminal slip velocity (ft/s)
V_{sg}	Gas superficial velocity (ft/s)
V_{sl}	Liquid superficial Velocity (ft/s)
V_{slurry}	Slurry Superficial velocity (ft/s)
V_{ss}	Solid Superficial Velocity (ft/s)
W_{CT}	Cuttings collection tank weight (Lb)
W_{IT}	Cuttings injection tank weight (Lb)
Z	Axial distance in annular test section (ft)

Greek Letters

μ_e	Effective viscosity (cP)
λ_l	Non-slip liquid hold up (solid-liquid)
θ	Inclination angle
ρ_l	Liquid phase density (ppg)
ρ_s	Cuttings density (ppg)
ρ_{slurry}	Liquid-solid mixture density (ppg)
ρ_{mf}	Non slip mixture density (ppg)
ϕ	Solid volumetric fraction
ϕ_{max}	Maximum solid volumetric fraction
Φ_B	Cutting bed porosity

REFERENCES

1. A.M. Kamp, M. Rivero "Layer Modeling for Cutting Transport in Highly Inclined Wellbores" SPE 53942 presented at the 1999 SPE Latin and Caribbean Petroleum Engineering Conference held in Caracas, Venezuela 21-23 April 1999
2. P. Doron, D. Granica and D. Barnea "Slurry Flow in Horizontal pipes - experimental and Modeling" Int J. Multiphase Flow Vol 13, No. 4 p 535-547, 1987
3. Larsen " A Study of the Critical Fluid Velocity in Cutting Transport for Inclines Wellbores" M.S. thesis, University of Tulsa, 1990.
4. Jalukar, L. S. "A Study of Hole Size Effect on the Critical and Subcritical Drilling Fluid Velocity in Cuttings Transport for Inclined Wellbores" M.S. thesis, University of Tulsa, 1993.
5. Sanchez, R. A., Azar, J. J., Bassal, A. A., and Martins, A. L.: "The Effect of Drillpipe Rotation on Hole Cleaning During Directional Well Drilling," paper SPE 37626 presented at the 1997 Drilling Conference, Amsterdam (Mar. 4-6, 1997).
6. Azar, J.J; Sanchez, R. Alfredo. "Important Issues in Cuttings Transport for Drilling Directional Wells". paper SPE 39020 presented at the 1997 at the Fifth Latin American and Caribbean Petroleum Engineering conference, Brazil.
7. Ali A Pilehvari, J. J. Azar. "State-Of-Art Cutting Transport in Horizontal Wellbores". paper SPE 37079 presented at the 1996 at the conference on Horizontal Well Technology held in Calgary.
8. A.L. Martins, C. H. M. Sa, A. M. F. Lourenco, "Optimizing Cuttings Transport In Horizontal Well Drilling". Paper SPE 35341 presented at the Petroleum Conference & Exhibition of Mexico, 5-7 March 1996.
9. Iyoho A W; Takahashi H, "Modeling Unstable Cuttings Transport In Horizontal, Eccentric Wellbores". : SPE-27416 (Dec 1993).
10. Campos W et al., "Mechanistic Modeling Of Cuttings Transport In Directional Well" PhD Thesis, Tulsa University, Tulsa, Oklahoma, 1995.
11. Charles R et al. "New Application for Underbalanced Drilling Equipment" paper SPE/IADC 37679 presented at the 1997 Drilling Conference, Amsterdam (Mar. 4-6, 1997).
12. D.B. Bennion. "Underbalanced Drilling of Horizontal Wells: Does It Really Eliminate Formation Damage?" paper 27352 presented SPE Symposium of Formation Damage Control in Lafayette, Louisiana, 1994.
13. Teichrob, R.R. "Low-Pressure Reservoir Drilled With Air/N2 in a Closed System" Oil & Gas J. (March 21, 1994) 80-90.
14. A. A. Sunthankar et al. "New Developments in Aerated Mud Hydraulics for Horizontal Well Drilling" SPE 62897 presented at the 2000 SPE Annual Technical Conference and Exhibition held in Dallas, Texas 1-4 October 2000.
15. Matthew J. S. King, C. Paul Fairhust & Trevol J. Hill, "Solids Transport in Multiphase Flows Application to High Viscosity System". Paper submitted to the Energy Sources Technology Conference and Exhibition, New Orleans, Feb 14-17, 2000.
16. Thomas, D., 1962 "Transport Characteristics of Suspensions Part IV" AIChE Jour., 8, 373-378.
17. R.G. Gillies, M.J.McKibben, C.A. Shook, "Pipeline Flow of Gas, Liquid and Sand Mixture at Low Velocities" The Journal of Canadian Petroleum Technology, 39 (9), 36-42.
18. Tippetts, J. R. & Priestman, G. H., "Mobility of Solids in Multiphase undulating pipe flow" Paper presented at the 7 International Conference of Multiphase Production, Cannes, France 18-20 June 1997.

19. S. Holte et al (1987), "Sand Bed Formation in Horizontal and Near Horizontal Gas-Liquid-Sand Flow" European Two-Phase Group Meeting, Trondheim, June 1987.
20. D. Barnea, D. Granica, P. Doron and Y. Taitel " Hydraulic Transport Of Course Particles With Gas Injection" 10th International Conference on the Hydraulic Transport of Solid in Pipes, Innsbruck, Austria: 29-31 October 1986.
21. Q. T. Doan , M. Oguztoreli, Y. Masuda, T. Yonozawa, A. Kobayashi, A. Kamp. "Modeling of Transient Cuttings Transport in Underbalanced Drilling" presented at the 2000 IADC/SPE Asia Pacific Drilling Technology held in Kuata Lumpur, Malaysia, 11-13 September 2000.
22. J. Li and S. Walker "Sensitive Analysis of Hole Cleaning Parameters in Directional Wells" SPE paper number 54498.
23. Buyon Guo, Geir Hareland, Jerzy Rajtar. " Computer Simulator Predicts Unfavorable Mud Rate and Optimum Air Injection Rate for Aerated Mud Drilling". Paper SPE 26892 presented at the Eastern Regional Conference & Exhibition held in Pitsburgh, PA. U.S.A., 2-4 November 1993.
24. Campos W., "Mechanistic Modeling Of Cuttings Transport In Directional Well" PhD Thesis, Tulsa University, Tulsa, Oklahoma, 1995.
25. Shoham O. " Two Phase Flow Modeling" Tulsa University - Two Phase Flow Modeling Course Notes, Aug. 1997.
26. Xiao, J. J., et al.: "A Comprehensive Mechanistic Model for Two-Phase Flow in Pipelines," paper SPE 20631, presented at SPE Annual Fall Meeting, New Orleans, Louisiana, (September 23-26, 1990).
27. A. A. Sunthankar et al. "Prediction of Bottom Hole Pressure - Modified Unified Pipe Flow Model (FLOCAL)" Tulsa University Drilling Research Projects.
28. Barnea, J. Mizrahi "A generalized Approach to the Fluid Dynamics of Particle Systems" Chemical Engineering Journal, 5 (1973) 171-189.
29. C.A. Shook, M.C. Roco "Slurry Flow, Principles and Practice" 1991 by Butterworth-Heinemann, a division of Reed Publishing (USA).
30. Okranji, S.S.:"Mud Cuttings Transport in Directional Well Drilling" TUDRP Post-Doctoral Report, University of Tulsa, Tulsa 1981.
31. Okranji, S.S. and Azar, J.J.:"Mud Cuttings Transport in Directional Well Drilling" SPE Paper 14178, presented at the annual meeting in Las Vegas, Nevada, Sep. 22-25, 1985.
32. Barnea, D., Shoham, O. and Taitel, Y. "Flow Pattern Transition for Vertical Downward Inclined Two Phase Flow; Horizontal to Vertical" Chem. Eng. Sci. 37, No. 5, 735-740 (1982a).
33. Guoqiu Fang. " An Experimental Study of Free Settling of Cuttings in Newtonian and No Newtonian Drilling Fluids: Drag Coefficient and Settling Velocity" Paper SPE 26125, 1992.
34. A. A. Sunthankar et al. "Estimation of Flow Pattern Maps for Two-Phase Flow in Horizontal and Nearly Horizontal Annuli (FLOMAP)" Tulsa University Drilling Research Projects.
35. A. Bourgoyne, K. Milheim, M. Chenevert, F. S. Young. "Applied Drilling Engineering" SPE text book series, Vol. 2.
36. J. P. Brill, H. Mukherjee. "Multiphase Flow in Wells" Monograph; Society of Petroleum Engineer; Vol. 17

6. Study of Synthetic Drilling Fluids under Elevated Pressure and Temperature Conditions (Task 8)

ABSTRACT

Rheological and volumetric properties of synthetic based drilling fluids are sensitive to downhole conditions. As a result, there is a discrepancy between calculated and measured frictional pressure losses. For that reason, the effects of pressure and temperature on rheological and volumetric properties of paraffin-based drilling fluids have been investigated.

Rheological parameters were determined for Bingham Plastic, Power Law and Yield Power Law fluids. An elevated pressure and elevated temperature flow loop that has pipe and annular sections was used to measure frictional pressure losses. Experimental data was collected at various pressure and temperature conditions.

Pressure loss predictions were made using different hydraulic models. In laminar pipe flows, predictions of the hydraulic models are significantly different from each other, particularly for high yield stress and high viscosity fluids. Bingham Plastic model estimations are the highest among the three models. In turbulent flow, predictions of the models are comparable.

In laminar annular flows, model predictions are higher than the measured data. Discrepancy between model predictions and the measured data decreases as temperature increases. In almost all cases, model predictions are higher than the measured data. Therefore, a more accurate hydraulic model should be developed to determine pressure losses of non-Newtonian fluids in annuli.

6.1 INTRODUCTION

Due to environmental regulations and restrictions, drilling fluid contaminated cuttings discharge is one of the most important challenges in offshore operations. For this reason, drilling fluids used in offshore operations must not only fulfill the operational advantages of conventional drilling fluids but they also should address environmental issues. As a result of this, new drilling fluid types have been introduced to the drilling industry. These types of fluids are called "Synthetic Based Drilling Fluids (SBDFs)". Being invert emulsions like oil-based drilling fluids, SBDFs exhibit the same operational advantages as oil-based drilling fluids, and they are more environmentally friendly.

Prediction of pressure losses can be important for a successful drilling operation. In most cases, non-Newtonian fluid models and parameters determined at surface conditions are used to calculate frictional pressure losses through out the well bore. Most of the time, calculated pressure losses do not match those measured in the field.

The aim of this study is to investigate the flow behavior of paraffin-based drilling fluids under down-hole conditions and to determine a suitable hydraulic model that estimates the frictional pressure losses in pipes and annuli under laminar, transitional and turbulent flow conditions. Rotational viscometer data were used to calculate the pressure losses using three different rheology models. The objective was to determine whether rheological parameters determined from rotational viscometer data can be used to estimate frictional pressure losses of invert emulsions flowing through pipes and annuli.

A paraffin-based drilling fluid, obtained from Petrobras, was used in this study. Various properties of the fluid were measured. The shear-stress/shear-rate relations of the fluid were determined at different temperature and pressure conditions. A high-pressure and high-temperature (HPHT) rotational viscometer (Fann 70) was used to determine the rheological properties of the fluid. PVT measurements were carried out to determine the density of the fluid at different temperature and pressure using a Mercury-free PVT instrument. An empirical correlation that relates density of the fluid to pressure and temperature was developed. Effects of temperature and pressure on the density of water, paraffin-based oil, water-based drilling fluids, low-toxicity oil-based drilling fluids and paraffin-based drilling fluids were compared. The results indicated that the densities of some of fluids can be affected significantly by changes in down-hole conditions.

The Advanced Cuttings Transport Study (ACTS) flow loop was used for pipe and annular flow experiments. An experimental procedure was developed to test these kinds of fluids at elevated pressures. Measured pressure losses from the ACTS flow loop were compared with model predictions based on different rheological and hydraulic models. Rotational viscometer data were used in the hydraulic models.

6.2 EXPERIMENTAL INVESTIGATION

In some instances, high pressure high temperature (HPHT) flow loop experiments are required to simulate flow of drilling fluids in downhole conditions. Obviously hydraulic models predictions are highly dependent on fluid density and rheological properties that are affected by temperature and pressure. Therefore, in the experimental part of this investigation, we have included rheology and PVT measurements under HPHT conditions in addition to the main flow loop experiments.

6.2.1 PVT ANALYSIS

The densities of synthetic drilling fluids are sensitive to changes in down-hole conditions. To get accurate pressure losses predictions, not only the rheological behavior but also the densities of these kinds of drilling fluids should be corrected for down-hole conditions. A mercury-free PVT system, which is shown Fig. 6.1, was used to determine the effect of pressure and temperature on density and compressibility of paraffin-based drilling fluid and on an n-paraffin-based oil. The n-paraffin-based oil contains C14-C15 hydrocarbons, while the paraffin-based drilling fluid is an invert emulsion made of water and synthetic oil components (paraffins, emulsifiers, etc.). Volumes of these fluids in a PVT cell at different temperatures and pressures were measured. Both the density and the compressibility variations of the fluids as a function of pressure and temperature were determined. The initial temperature and pressure conditions for each experiment were 80°F and 30 psig, respectively.

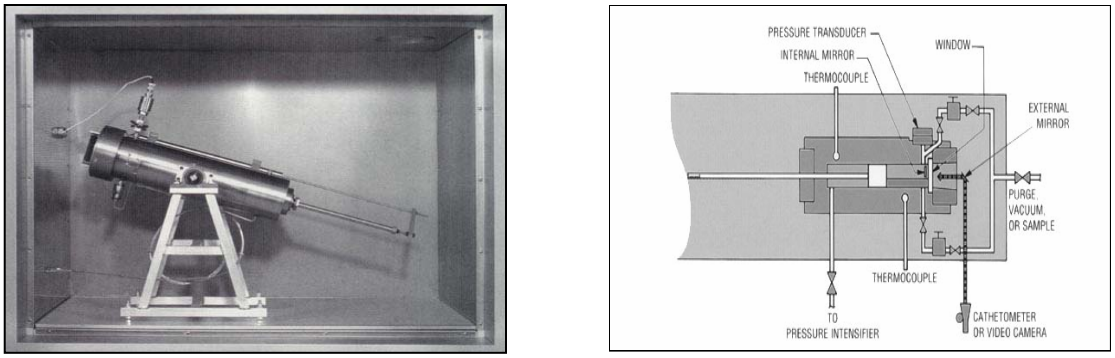

(a) **(b)**

Fig. 6.1 PVT Equipment: (a) Outside view; and (b) Interior view from top

The result indicated that for a given test temperature, increasing the pressure increases the density of the n-paraffin-based oil. This is expected since mass of the oil in the PVT cell is kept constant; therefore, the increase in pressure will decrease the volume of the oil. The relation between density and pressure under isothermal conditions for slightly compressible fluids can be shown as;

$$\rho = \rho_i \exp(X * P) \tag{6.1}$$

It has been found that Eq. 6.1 can be used to approximate the behavior of the n-paraffin-based oil at different temperatures with high accuracy. The combined effect of pressure and temperature on density the oil is shown in Fig. 6.2. The PVT data shows that as the temperature increases from 80 to 280°F (which is typically observed in deep and ultra deep drilling) the density of the oil decreases, depending on the pressure. As mentioned previously, density of the oil increases as pressure increases under isothermal conditions. However, isothermal compressibility of the oil is not constant for all temperatures, where the isothermal compressibility is defined as:

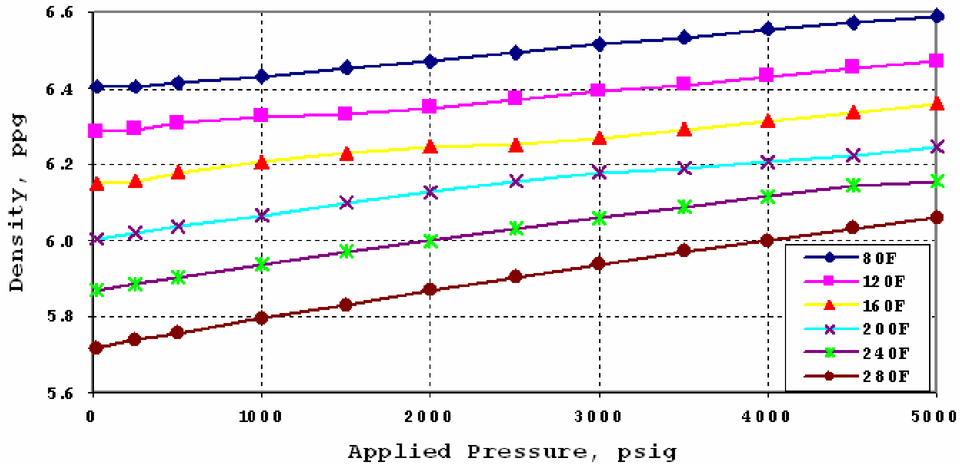

Fig. 6.2 Effects of pressure and temperature on density of n-paraffin-based oil

$$\left(C_o\right)_T = \left(\frac{1}{\rho}\right)\left(\frac{\partial\rho}{\partial P}\right)_T \tag{6.2}$$

The change in compressibility of the n-paraffin-based oil with temperature and pressure is shown in Fig. 6.3. Isothermal compressibility of the oil is approximately constant for pressure ranging from 30 psig to 5000 psig. This is another indication of the fact that this oil can be classified as a slightly compressible fluid. However, at higher temperatures (greater than 160°F) as the temperature increases, the compressibility of the oil increases significantly. When the temperature increases from 80 to 120°F, the compressibility of the oil decreases slightly. It should be noted that, although the n-paraffin-based oil can be classified as only a slightly compressible fluid, the compressibility values are 2 to 3.5 times higher than distilled water in similar conditions.

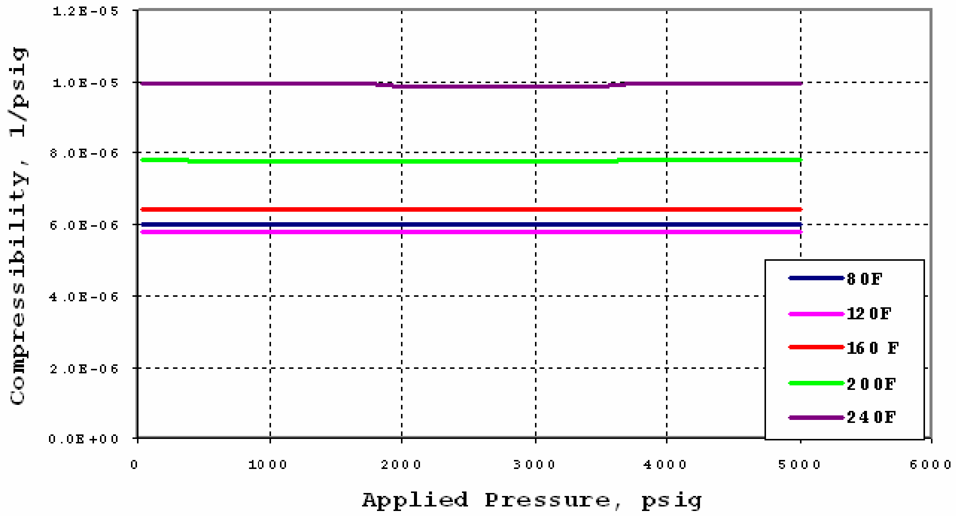

Fig. 6.3 Change in compressibility of n-paraffin-based oil with pressure and temperature

In addition to the n-paraffin-based oil, PVT experiments were carried out for the n-paraffin-based drilling fluid. Similarly, the initial condition for each experiment was taken as 80°F and 30 psig conditions as a reference point. The results indicate that the effects of pressure and temperature on volumetric behavior of n-paraffin-based drilling fluids are more significant compared to that of water based drilling fluids. The change in the density of the n-paraffin-based drilling fluid was analyzed intensively. Figure 6.4 shows the combined effects of pressure and temperature on the density of the n-paraffin-based drilling fluid.

Increasing the pressure at constant temperature conditions resulted in reduction of the volume of the fluid. Hence, the density of the fluid increased since the mass is kept constant. Although compressibility of a fluid at a specific pressure condition depends on temperature at which the pressure is applied, pressure always tends to decrease the volume of a fluid. On the other hand, the fluid expands as temperature is increased, and consequently, the density decreases under isobaric conditions. In other words, temperature and pressure act oppositely on volumetric behavior of the paraffin-based drilling fluids and diminish each other's effect on density. However, the effects of temperature are more dominant compared to the effects of pressure, and especially under low pressures, an increase in temperature may decrease the density of the drilling fluid significantly.

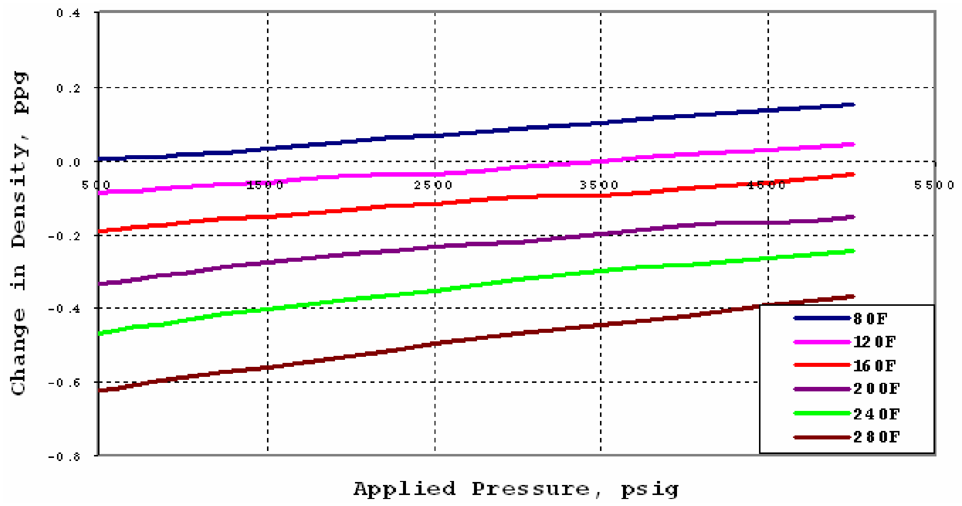

Fig. 6.4 Effects of pressure and temperature on the density of n-paraffin-based drilling fluid

The experimental data show that when the temperature is increased from 80°F to 280°F, the density of the synthetic based drilling fluid decreases depending on the pressure. Roughly 7% maximum decrease in density was observed. These data clearly show the magnitude of considering the effects of pressure and temperature in pressure loss calculations. Not introducing the effects of pressure and temperature may result in less accurate estimation of bottomhole pressure, and as a result, well control problems might occur.

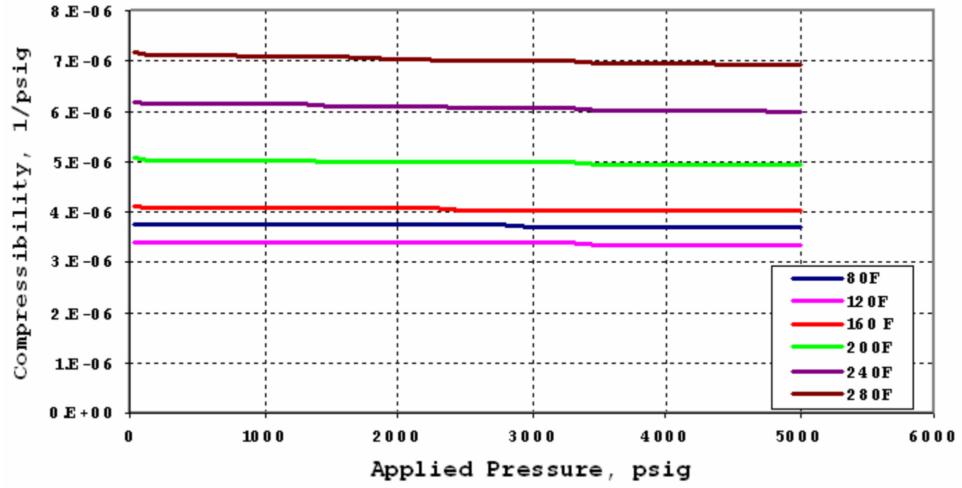

Fig. 6.5 Effects of pressure and temperature on compressibility of n-paraffin-based drilling fluid

Isothermal compressibility of n-paraffin-based drilling fluid, shown in Fig. 6.5, is almost constant as the pressure varies from 30 psig to 5000 psig. Although, compressibility of the fluid decreases slightly with increasing pressure under isothermal conditions, this fluid still can be classified as a slightly compressible fluid like water and the n-paraffin-based oil.

Comparisons of compressibilities of the n-paraffin-based oil and n-paraffin-based drilling fluid show that the oil is more compressible than the drilling fluid under all pressure and temperature conditions. This might be due the fact that, the presence of water in the drilling fluid decreases its compressibility. Therefore it could be concluded that the compressibility of the n-paraffin-based drilling fluid can be adjusted by changing the water to synthetic oil ratio. However it should be noted that this also changes the density and rheology of the fluid.

6.2.2 DEVELOPMENT OF PVT MODELS

This part of the study focuses on developing an empirical correlation that relates fluid density to pressure and temperature. Linear and non-linear regression techniques are used for this purpose. As mentioned above, the relation between density and pressure under isothermal conditions was analyzed; and it was concluded that the n-paraffin-based drilling fluid can be classified as "slightly compressible fluid".

Once the relationship between density and pressure in isothermal conditions is found in the form of Eq. 6.1, the effect of temperature on the coefficient, ρ_I, can be modeled as:

$$\rho_i(T) = W * T^2 + B * T + C \tag{6.3}$$

where, W, B and C are experimentally determined constants. For the n-paraffin-based drilling fluid these constants are found to be: W = -5.357E-06 ppg/°F^2; B = -1.267E-03 ppg/°F; and C = 8.717 ppg. Estimation of coefficient "ρ_i" using Eq. 6.3 is accurate and the error between calculated and measured data is less than 0.08%.

Similar analysis was done for exponent, X, as well. Using regression analysis, the relation between X and temperature can be modeled as:

$$X(T) = D * T^2 + E * T + F \tag{6.4}$$

where D, E and F are constants. For the n-paraffin-based drilling fluid these constants are found to be: D = 9.452e-11°F^2/psig; E = -1.530e-8°F/psig; and F = 4.192e-6 psig^{-1}. Analysis show that the accuracy of Eq. 6.4 in estimating the coefficient, X, is good and the error between calculated and measured values is always less than 5%.

By substituting Eq. 6.3 and Eq. 6.4 in to Eq. 6.1, an empirical correlation that relates density of the n-paraffin-based drilling fluid to the downhole pressure and temperature can be written as:

$$\rho(P,T) = \left(A * T^2 + B * T + C\right)\exp\left[\left(D * T^2 + E * T + F\right) * P\right] \tag{6.5}$$

Equation 6.5 is accurate in estimating experimental results. The average error between calculated and measured densities is always less than 0.25 % for all pressures and temperatures that the fluid was tested (Fig. 6.6). By using this correlation in the Fanning friction factor equation, frictional pressure loss can be estimated at high temperature and pressure conditions.

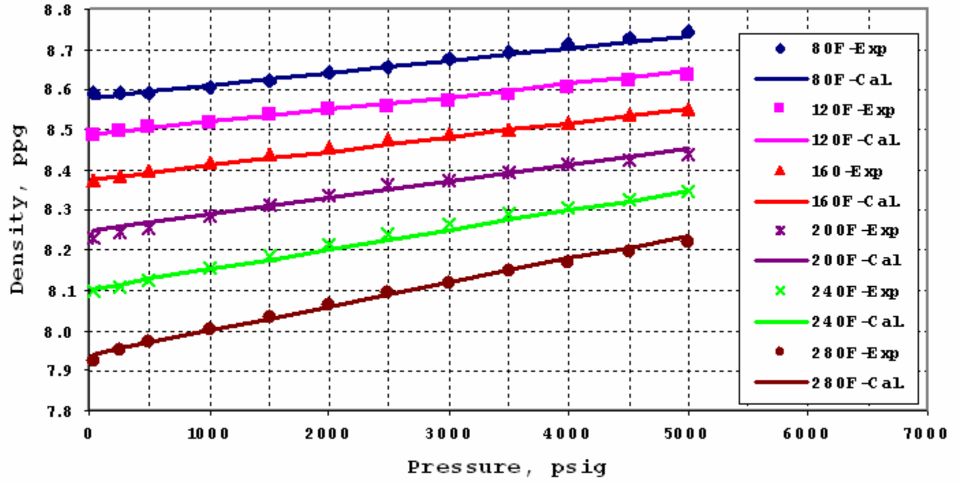

Fig. 6.6 Comparison of calculated and experimental densities n-paraffin-based drilling fluid

6.2.3 RHEOLOGICAL MEASUREMENTS

Rheological measurements were made before the n-paraffin-based drilling fluid was introduced to the ACTS flow loop. These experiments were run in order to estimate the effect of pressure and temperature on rheological properties of the fluid. The test matrix for rheology experiments covered a wider range of temperatures and pressures than the ACTS flow loop test. This gives a better understanding of the rheological behavior of the fluid, which is appropriate for deep and ultra-deep drilling conditions. For this reason the rheology experiments are called “Wide Range Rheology Experiments”.

After completion of the ACTS flow loop experiments, another set of rheology tests was carried out at pressures and temperatures comparable to the flow loop tests. The objective was to use rheological parameters obtained from those experiments in the frictional pressure loss estimation models to determine the applicability of rotational viscometer based parameters on calculating frictional pressure losses in pipes and annuli. Since these tests were conducted at lower temperatures and pressures with respect to the first set of rheology experiments, these experiments are called “ACTS Flow Loop Matrix Rheology Experiments”.

Both rheology tests were performed using a HPHT rotational viscometer (Fann 70). The relationships between shear stress and shear rate at different pressures and temperatures were determined to verify whether or not the rheology of the fluid can be defined with a single model for a wide range of different downhole conditions. In addition to this, rheological behavior of the fluid under surface conditions was determined using a Chan 35 rotational viscometer.

Software (RHEO) was used to determine a rheological model that best fits rheology of the fluid. The software result suggested that the Yield Power-Law model predicts the rheology of the fluid at surface conditions with an error of 1.03%, while the Power-Law and Bingham Plastic models predict the rheology with errors of 22.8% and 10.8%, respectively. It was also observed that in other test temperatures and pressures, the Yield Power-Law model predicts the rheology with higher accuracy than the Power-Law and Bingham Plastic models.

6.2.4 FLOW LOOP EXPERIMENTS

Test Set-up

The flow loop has the ability to increase the test pressure and temperature up to 1500 psig and 200°F. The schematic view of the ACTS flow loop is presented in Fig. 6.7. The loop has three pipe viscometers (rheology measuring sections) with nominal diameters of 2”, 3” and 4”. In addition, a drilling section is available to study flow of drilling fluids through annular geometry. The drilling section consists of a 6” annulus and 3.5” drill pipe. The actual inner diameter of each pipe and the length interval from which the pressure drop measurements are taken are shown in Table 6.1.

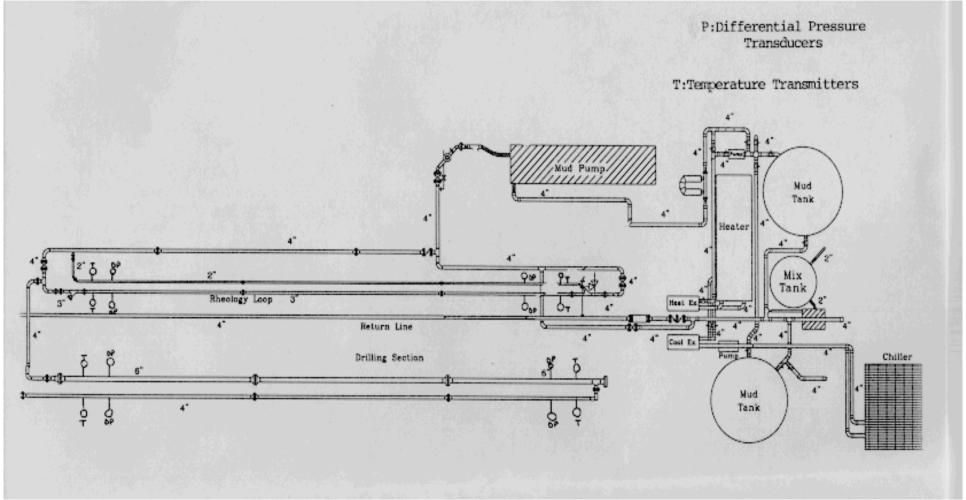

Fig. 6.7 Plan view of ACTS flow loop

Table 6.1 Dimensions in the ACTS Flow Loop

Section	Internal Diameter	ΔP Measurement Length
2” Pipe	1.918”	52’ 9”
3” Pipe	2.900”	52’ 9”
4” Pipe	3.826”	66’ 6”
6” × 4” Annulus	5.761” × 3.500”	57’ 4”
4” pipe	3.826”	66’ 6”

A mud pump (Halliburton Model HT 400 triplex fracturing pump) circulates the fluid through the flow loop. As shown in Fig. 6.7, the test sections are connected in series so that the same flow rate passes through all the test sections (2”, 3”, 4” and annular section). This helps to determine the effect of diameter on the flow regime and to maintain the same flow rate in all testing sections.

A Coriolis mass flow meter (Micromotion) is used to determine the flow rate at which the fluid circulates through the system. Differential pressure transmitters (Rosemount Model 3051CD) are installed to measure the differential pressure across the test sections. They measure from 0.5” to 250” water column pressure differentials with an accuracy of 0.075%. Since the pressure losses in the 2” pipe section are higher than a 250” water column, a higher range differential pressure transmitter was installed which can measure 5” to 2500” water column with an accuracy of 0.75%. Beside this, ten temperature transmitters (Rosemount Model 3144) are installed to measure the temperature of the fluid in the system.

Two plate heat exchangers regulate the temperature of the circulating fluid. The exchangers are installed to work in parallel. One exchanger is used for heating the fluid while the other one is used for cooling the fluid when it is required. During flow loop tests, the fluid can be heated or cooled by the heat exchangers while circulating through the flow loop. In addition, the heating system allows the piping and the rest of system to be heated. By insulating the system, heat loss from the system to the surrounding is minimized. When the desired temperature is reached, experiments at elevated pressures and temperatures are conducted at different flow rates.

A cooling tower is installed to supply cold water for the cooling plate heat exchanger. It reduces the cooling water temperature as low as the “wet bulb” temperature. A boiler (Glycol Heater) supplies a heating media (glycol + water) to the heating plate heat exchanger to raise the temperature of the fluid that is under investigation. The temperature of the fluid can be increased up to 185 °F using the boiler.

Two 2-inch ceramic-lined Fisher Valves are installed in parallel on the return line to regulate the backpressure of the system. In addition to ceramic valves, a 4-inch Fisher Valve is installed upstream of the ceramic-lined valves to regulate the backpressure. These valves are remotely regulated by the data acquisition and control system.

The flow loop has one storage tank with 100-bbl capacity and a mixing tank that has 5 bbl capacity. Since paraffin-based drilling fluid segregates in a short time, mixers are installed in both tanks to mix the fluid and maintain a homogeneous mixture.

Differential pressure transducers, absolute pressure transmitters, temperature sensors, control valves and mass flow meter are all connected to the computerized data acquisition and control system. As a result, online measuring, regulating and recording of the test parameters are achieved. The data acquisition system utilizes LabView® software. Data can be sorted and averaging intervals can be controlled in the system.

The flow loop consists of many devices and equipment that have to be controlled for successful experimental analysis. In order to determine the accuracy of these devices and reliability of the data acquisition system, preliminary experiments were conducted with water. The results obtained from the ACTS flow loop were compared with the theoretical pressure loss calculations available in the literature for Newtonian fluids. In all tests the flow regime of water was fully turbulent even at the lowest flow rate of 50 gpm. Therefore, the Colebrook equation for the friction factor, together with the Fanning frictional pressure drop equation, is used to determine frictional pressure losses in pipes and the annulus.

Test Procedure and Results

The ACTS flow loop was used to simulate flow of the paraffin-based drilling fluid in drill pipes and boreholes under laminar, transitional and turbulent flow conditions. The fluid was tested under various temperature and pressure conditions. In order to simulate laminar, transitional and turbulent flow regimes, the flow rate was varied from 50 to 240 gpm. After experimental procedures were established and the flow loop was modified, flow experiments with the fluid under elevated pressure and elevated temperature conditions were carried out. During the high temperature test run, vapors came out of the tank where drilling fluid was stored. The composition of this vapor was determined since it might affect the rheology of the mud, which in turn affects the pressure losses obtained from the system. In order to determine the composition of this vapor, a condenser was installed at the top of the tank and vapor was condensed and collected in an Erlenmeyer flask. A chemical analysis of the condensate fluid was done. The vapor was found to have the same composition as the test fluid. Chan 35 viscometer readings of the fluid samples taken after the test were higher than the original values (i.e. readings before the test).

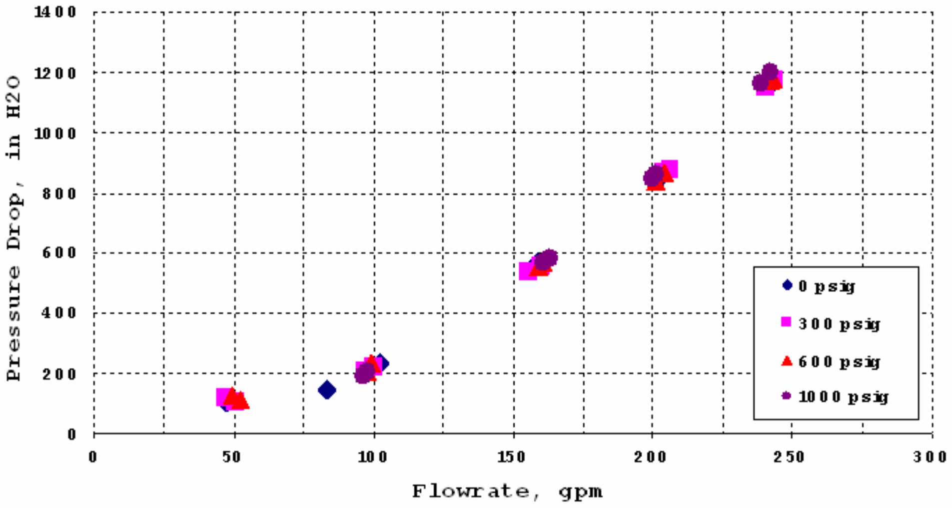

Fig. 6.8 Frictional pressure loss vs. flow rate at different pressures (2-inch pipe, T= 75°F)

The 2-inch pipe frictional pressure loss data is presented in Fig. 6.8. In this pressure range (i.e. 0 to 1000 psig), the effect of pressure on the frictional pressure loss is negligible. After analyzing the effect of pressure on pressure losses at other temperatures, it is concluded that the effect of pressure on frictional pressure losses is not as much as the effect of temperature. In other words, the effect of pressure on fluid rheology is minimal; hence, there is only little increase in pressure losses measured at different pressures. This agrees with the information obtained from Wide Range Rheology Experiments, in which the effect of pressure on viscosity becomes significant after 4000 psig.

Figure 6.9 shows the effect of test pressure on frictional pressure loss in the 3-inch pipe at 75°F. The experimental data is relatively scattered at 100 gpm, where the flow is in the transitional regime. Since the experimental procedure prevents the thixotropic effects to a certain degree, the reason for scatter in the data might be because of temperature hysteresis of the fluid. Keeping the temperature at a constant value was difficult during the test. Extensive analysis of the data showed higher pressure losses recorded under isobaric conditions, which were taken during the cooling process. Similar temperature hysteresis of synthetic based drilling fluids were reported by Davison et al. [1] who stated that synthetic based drilling fluids display more viscous behavior while they are being cooled than when heated. As the flow rate or temperature increases, the flow regime becomes turbulent and the scattering of the data diminishes. Under these conditions, again slight change in frictional pressure losses was observed.

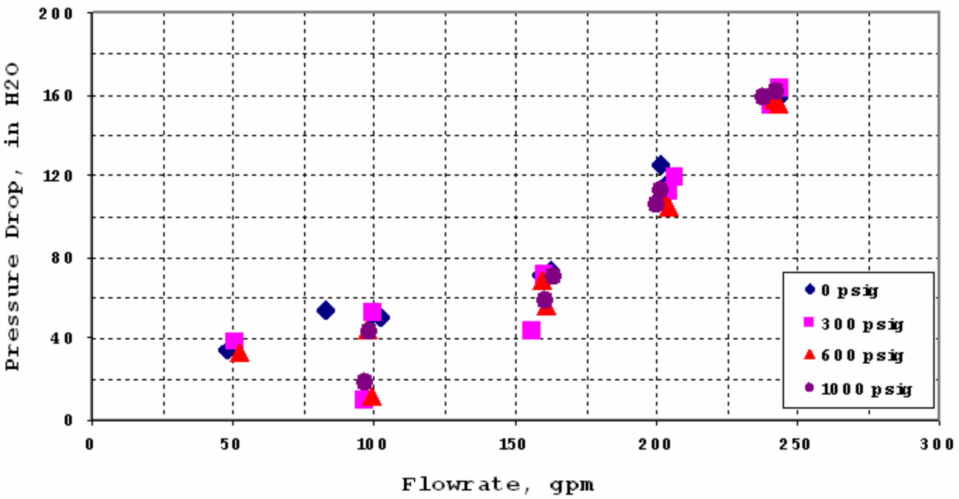

Fig. 6.9 Frictional pressure loss vs. flow rate at different pressures (3-inch pipe, T= 75°F)

The 4-inch pipe frictional pressure loss measurements (Fig. 6.10) showed considerable scattering. The flow regime was mostly laminar in the 4-inch pipe and scattering of the data was much higher than the 3-inch pipe. Another possible explanation of this observation could be the flow regime. The frictional pressure loss measurements in transitional flow can be highly scattered. When temperature is increased to 100°F, the fluid becomes thin enough to maintain turbulent flow conditions in the 4-inch pipe; as a result, slight influence of pressure is seen on pressure loss measurements. Detailed analysis of the data shows that the fluid experienced similar temperature cycles in 4-inch pipe during the experiment. Results obtained from 4-inch pipe demonstrate the importance of temperature hysteresis of the fluid under laminar flow conditions.

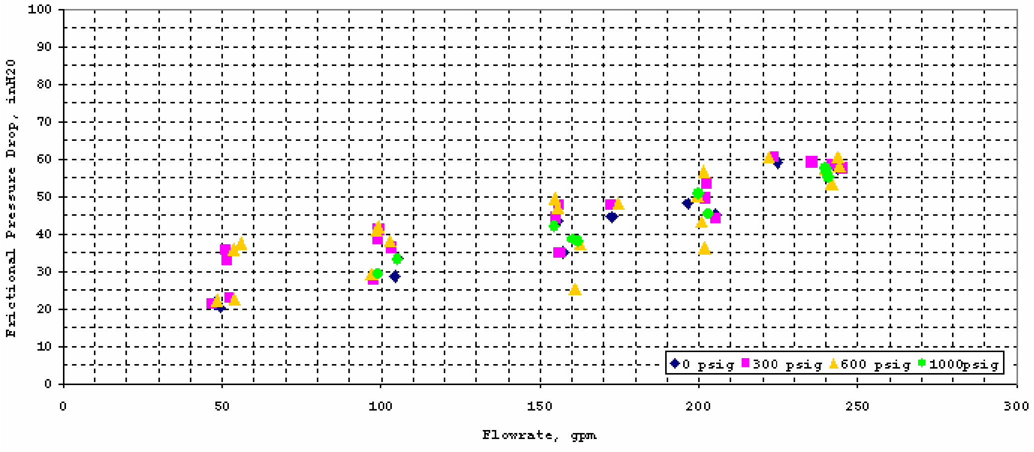

Fig. 6.10 Frictional pressure loss vs. flow rate at different pressures (4-inch pipe, T= 100 °F)

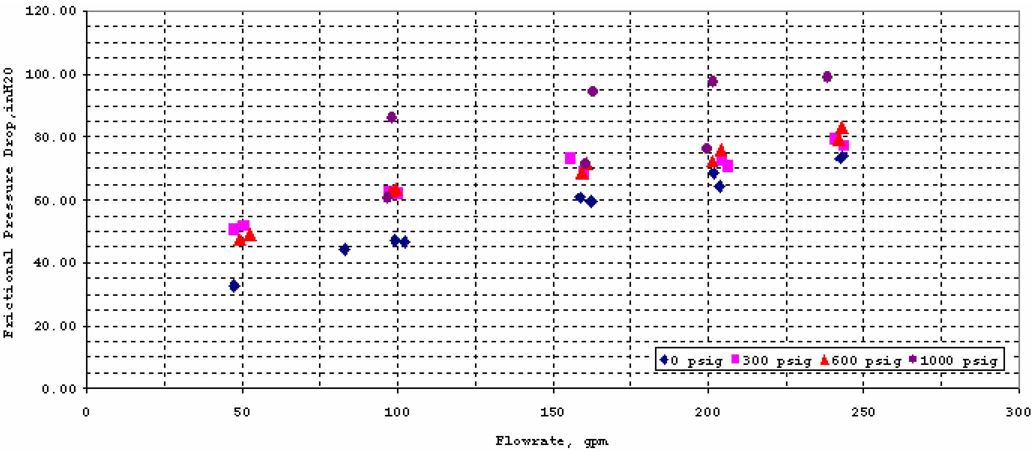

Fig. 6.11 Frictional pressure loss vs. flow rate at different pressures (Annulus, T= 75°F)

Annular pressure loss data at different operating pressure conditions are presented in Fig. 6.11. In the case of annular flow, temperature hysteresis again affects the data and highly scattered data was obtained at all the test temperatures since flow was fully laminar in the annulus. Again, detailed analysis of the experimental data in the annulus shows that the fluid exhibits higher frictional pressure losses during the cooling processes, as in the case of pipe flow situations.

6.3 PRESSURE LOSS CALCULATION MODELS

This part of the report presents an overview of the hydraulic models that are used to determine the rheological parameters and frictional pressure losses in the pipes and the annulus for different flow regimes.

6.3.1 BINGHAM FLUID PRESSURE LOSS CALCULATIONS

Laminar Flow

In order to determine frictional pressure losses of Bingham Plastic fluids, plastic viscosity and yield point should be determined first. Frictional pressure losses of Bingham Plastic fluid flowing in pipes and annuli under laminar flow conditions is determined by the methods of Hanks and Pratt [2]. The narrow slot approximation is used in derivation of laminar frictional pressure losses for Bingham Plastic fluids flowing through annuli. Higher pressure losses are encountered in the case of Bingham Plastic fluid flow due to the yield point.

Turbulent Flow

In turbulent flow, due to similarity between Newtonian flow and Bingham Plastic flow, equations developed for Newtonian fluids can be used to determine pressure losses of Bingham Plastic fluids. The Newtonian viscosity is replaced by a plastic viscosity in the

Reynolds number to determine flow regime. However, prediction of the onset of turbulence is the major issue in Bingham Plastic drilling fluids and yield point of the fluid plays an important role in determining the critical flow rate where turbulence starts.

Hanks' turbulence criterion was used to determine the flow regime of the fluid. Hank included plastic viscosity and yield point in his dimensional analysis and found two independent dimensionless groups (Reynolds number and Hedstrom number). When Reynolds number is greater than the critical Reynolds number, a turbulent friction factor should be determined. In this case the Colebrook equation is used to calculate the turbulent friction factor for Bingham Plastic fluids.

Using the method of successive iterations, the friction factor (f) can be found from the Colebrook equation. After friction factor is determined, pressure losses in pipes and annuli can be determined by using the Newtonian turbulent flow equations.

6.3.2 POWER LAW FLUID PRESSURE LOSS CALCULATIONS

Power Law pressure loss calculations are based on the procedure given in API 13-D Recommended Practice on the Rheology and Hydraulics of Oil-Well Drilling Fluids [4]. In order to determine pressure losses of Power Law drilling fluids, flow behavior index (n) and consistency index (K) should be determined.

Laminar Flow

In the case of Power Law fluid flowing in pipes, effective viscosity can be found by equalizing the laminar frictional pressure loss equations of Newtonian fluids and Power Law fluids in pipes and annuli. The effective viscosity allows the use of Newtonian relations to determine frictional pressure losses of Power Law fluids flowing through pipes and annuli under laminar and turbulent flow conditions. The Reynolds number, which is based on effective viscosity, is used to determine the flow regime. If the Reynolds number is less than 2100, the flow is assumed laminar and the friction factor can be estimated using the Newtonian friction factor equation.

Turbulent Flow

When Reynolds number is higher than 2100, Schuh's correlation is used to determine friction factor in the turbulent regime. Once the friction factor is determined, frictional pressure drop of Power Law fluids flowing through pipes and annuli can be determined using the Fanning equation.

6.3.3 YIELD POWER LAW FLUID PRESSURE LOSS CALCULATIONS

Merlo et al. [5] pressure loss calculation procedure is used. This procedure estimates the frictional pressure losses of Yield Power Law drilling fluids flowing through pipes and annuli under laminar and turbulent regimes. The procedure is based on Yield Power Law rheological properties n, K and τ_0. These parameters are determined using the subprogram

RHEO in the YPL/TUDRP Annular Flow program by putting the HPHT rotational viscometer (Fann 70) data into the pressure loss equations.

6.4 COMPARISON OF EXPERIMENTAL DATA WITH MODEL PREDICTIONS

Three different hydraulic models were used to calculate frictional pressure losses. Frictional pressure losses are determined for Bingham Plastic, Power-Law and Yield Power-Law models since these rheological models are widely used in the petroleum industry to define the shear rate-shear stress relationship of drilling fluids.

6.4.1 COMPARISON OF 2-INCH PIPE DATA

Measured data and model predictions for 2-inch pipe at 75°F and different pressures are shown in Figs. 6.12 and 6.13. The flow in the 2-inch pipe was dominantly in turbulent conditions. The critical Reynolds number indicates that the expected transition between laminar and turbulent flow should be in the range of 30-90 gpm (critical flow rate), depending on pressure and temperature conditions that the fluid is experiencing during the flow. Theoretical models show that critical flow rate between laminar and turbulent flow regime decreases as temperature increases under isobaric conditions. This is because the rheological properties of the fluid such as viscosity and yield point decrease with increasing temperature. This behavior of the fluid is defined as “temperature thinning”. On the contrary, as the pressure increases the laminar-turbulent transition critical flow rate increases slightly.

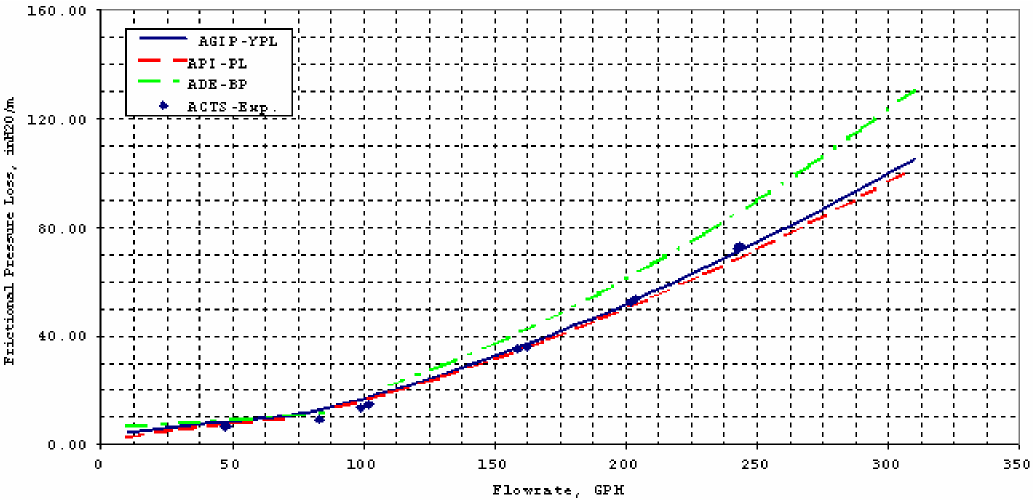

Fig. 6.12 Model predicted and measured pressure losses in 2-inch pipe at ambient condition (P=14.7 psi & T = 75°F)

At ambient conditions, the experimental results are in good agreement with the pressure loss predictions of AGIP and API-13D hydraulic models. Experimental results are slightly higher than the pressure drops determined by each of these models, especially at higher flow rates. The reason for such behavior might be due to using smooth pipe equations in the models. As the flow rate increases, the effect of pipe roughness increases and the difference between calculated and measured data increases. Bingham plastic model predicts pressure losses higher than the experimental pressure losses in both laminar and turbulent flow. Another interesting observation was that when the fluid has lower yield point and consistency index values, AGIP Yield Power Law and API-13D Power Law pressure loss predictions are the same.

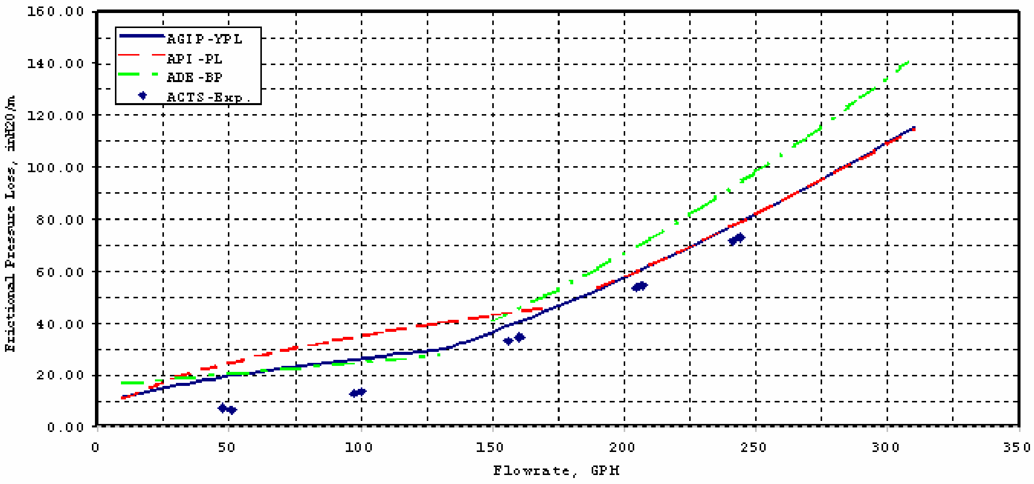

Fig. 6.13 Model predicted and measured pressure losses of in 2-inch pipe (P = 300 psig & T = 75°F)

At 300 psig, the frictional pressure loss predictions of the models do not agree with the measured data. Model predictions are considerably higher than the measured values in laminar and transition flow regimes (less than 150 gpm). Under turbulent flow conditions, AGIP and API models' predictions are closer to the experimental pressure losses. This might be due to negligible effects of viscous forces under turbulent flow conditions.

Comparisons of the predicted and measured pressure losses in the 2-inch pipe at other pressures and temperatures showed similar results. The Bingham Plastic model predicts higher pressure losses in both laminar and turbulent conditions. The API-13D Power Law model's predictions agree more with measured values at high flow rates and high temperature-high pressure conditions when flow is fully turbulent. In the case of laminar flow, API-13D agrees with the AGIP Yield Power Law model for this highly non-Newtonian fluid whose n varies between 0.784-0.301. Generally, in laminar flow regime, pressure loss predictions of the models are higher than experimental pressure losses at elevated pressures.

6.4.2 COMPARISON OF 3-INCH PIPE DATA

The 3-inch pipe was used to compare measured and predicted pressure losses in laminar flow conditions. Comparisons between calculated and measured pressure losses at 100°F are shown in Figs. 6.14 and 6.15. The critical flow rate between laminar and turbulent regimes varies in the range of 100 gpm to 150 gpm. API-13D Power Law model predictions are very close to experimental results in both laminar and turbulent flow conditions at all temperatures except 150°F. At this temperature, API-13D Power Law model pressure loss predictions for laminar flow are higher than experimental values. AGIP model predictions are also in agreement with the flow loop data. However, it should be noted that AGIP pressure loss predictions are higher than API-13D model predictions in laminar flow and vise versa in turbulent flow. Although pressure loss predictions of Bingham Plastic model for the 3-inch pipe are closer to the experimental values, the model still predicts higher values than the measured data in both flow regimes.

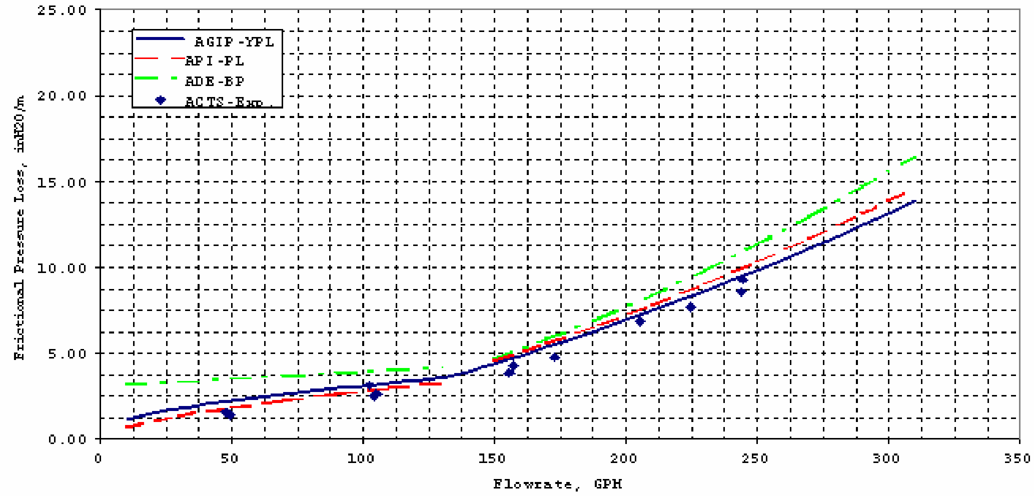

Fig. 6.14 Model predicted and measured pressure losses in 3-inch pipe for ambient condition (P = 14.7 psi & T = 100°F)

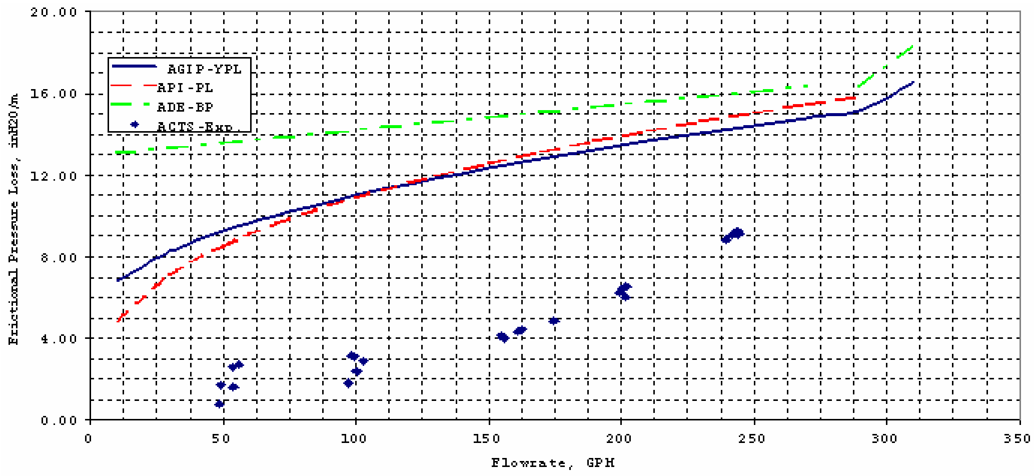

Fig. 6.15 Model predicted and measured pressure losses in 3-inch pipe (P = 600 psig & T = 100°F)

Significant discrepancies between the model predictions and experimental data are observed at high pressure (i.e. 600 psig). The API-13D Power Law model pressure loss predictions have the highest discrepancy. This could be due to poor estimation of rheological parameters using linear interpolation between 50°F and 100°F. Another reason for this discrepancy might be due to high increase in viscosity of the drilling fluid, which was observed during high pressure viscometric experiments. Using high consistency index, high plastic viscosity and high yield point values might be the reason for higher pressure loss predictions at elevated pressures and higher discrepancy between model predictions and measured data. The discrepancies observed under these conditions are higher than those observed in the 2-inch pipe under the same conditions. This is mainly due to the flow regime, because flow in the 3-inch pipe was fully laminar and viscous forces became dominant. This observation shows the importance of rheological parameter modeling at

lower temperatures and the importance of obtaining reliable rotational viscometer data, especially under laminar flow conditions. Although the flow is laminar, as temperature increases, the rate of change of viscosity with change in temperature and the discrepancy between model predictions and measured data both decrease.
At ambient pressure condition, AGIP model approximates the measured data accurately. However, after the unusual jump in the viscous properties of the fluid, predictions with the AGIP model are higher than measured values. Another important remark on pressure loss predictions of AGIP Yield Power Law models is that as flow becomes more non-Newtonian with increasing pressure (Flow Behavior Index n < 0.5), the AGIP model's pressure loss predictions under laminar flow conditions agree with those of API-13D Power Law model. This is seen at pressures of 600 psig and 1000 psig in all temperature ranges.

It should be also noted that at 300 psig, pressure loss estimations of the API-13D model are higher than those of the AGIP model and the Bingham Plastic model. However, as pressure increases, Bingham model predictions become higher.

6.4.3 COMPARISON OF 4-INCH PIPE DATA

The 4-inch pipe is the largest pipe size in the rheology section. Other than at the high flow rates at ambient pressure, the flow regime was laminar in the 4-inch pipe. The comparisons of theoretical pressure loss predictions to the measured data at 125°F and different pressures are presented in Figs. 6.16 and 6.17.

Analysis of measured and model-predicted pressure losses in the 4" pipe shows how the hydraulic models differently predict the pressure losses in laminar flow conditions. For ambient pressure turbulent flows, all model predictions are the same and agree with the measured data. In laminar flow regime, Bingham Plastic model predicts higher pressure losses than the measured ones. API-13D Power Law pressure loss predictions agree with the experimental data in both turbulent and laminar flow conditions, except for 125°F data, which is higher than the model predictions. AGIP Yield Power Law model predictions agree with the experimental data in both flow regimes.

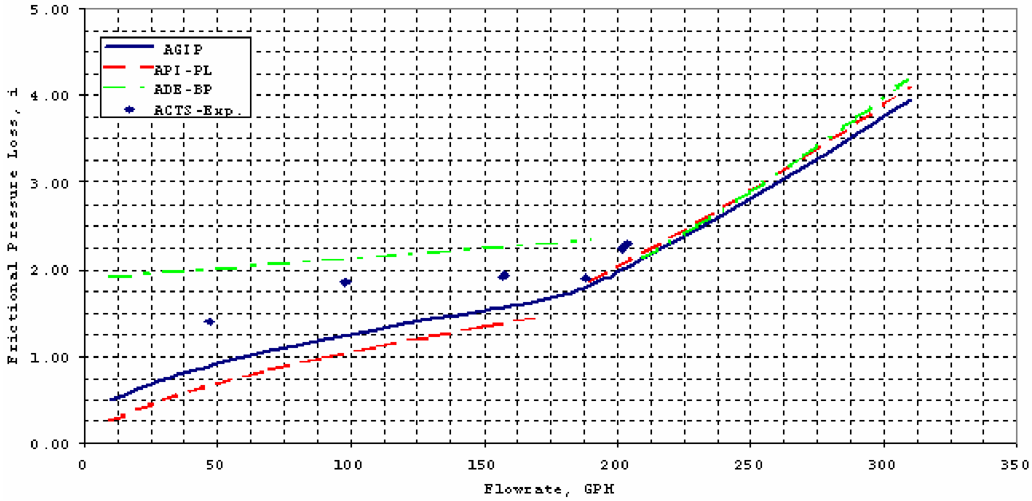

Fig. 6.16 Model predicted and measured pressure losses of in 4-inch pipe (P = 0 psig & T = 125°F)

Similar to the 3-inch pipe, model predictions are higher than the measured data at high pressure and ambient conditions (300 psig and 75°F). This can be a result of using rheological parameters that are obtained at elevated pressure conditions.

It should be noted that the discrepancies between model predictions and experimental data for the 4-inch pipe are greater than those for the 2-inch and 3-inch pipes. This is due to the fact that flow in the 4-inch pipe is predominantly laminar due to bigger pipe diameter. Obviously, for laminar flow the effect of rheological parameters on pressure losses is significant.

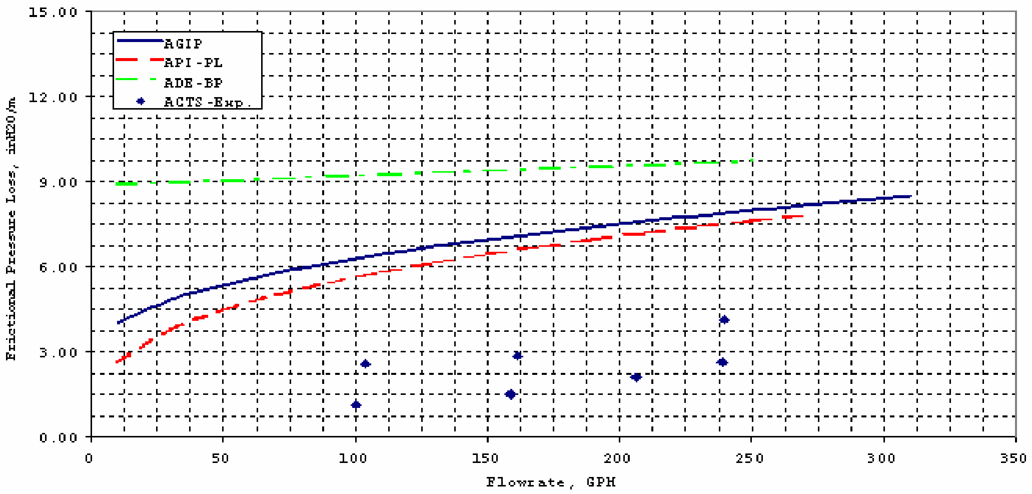

Fig. 6.17 Model predicted and measured pressure losses in 4-inch pipe (P = 1000 psig & T = 125°F)

Another interesting observation is that at high pressures, the pressure drop curve created using the Bingham Plastic model is essentially flat. This might be because of high yield stresses and high plastic viscosities encountered at high pressure conditions. The effect of flow rate on pressure losses is small and high yield point can be the major factor that dominates frictional pressure losses. The Bingham Plastic model predicts higher values than the measured data for elevated pressure and temperature conditions.

The flow behavior index of the fluid is low, resulting in similar pressure predictions in both the API-13D Power Law and AGIP Yield Power Law calculations. Since the fluid is highly shear thinning, frictional pressure drops do not increase much with increasing flow rate. At high pressure and temperature conditions, the high consistency index resulted in high predictions of pressure losses compared to the experimental values. Although the AGIP model pressure loss predictions were based on the Yield Power Law rheology model, for highly non-Newtonian systems it matches with the API-13D Power-Law model pressure loss predictions.

6.4.4 COMPARISON OF 6” × 3.5” ANNULUS DATA

After comparison of the experimental data with the predictions of hydraulic models in pipes, a similar comparison was carried out for the annular pressure loss data. Model-predicted and measured pressure losses in the annulus at 75°F and 150°F are presented in Figs. 6.18 and 6.19, respectively. At both temperatures, the graphs of measured pressure loss versus flow rate do not show strong influence of flow rate on the pressure loss. This could be because of the shear thinning behavior of the fluid.

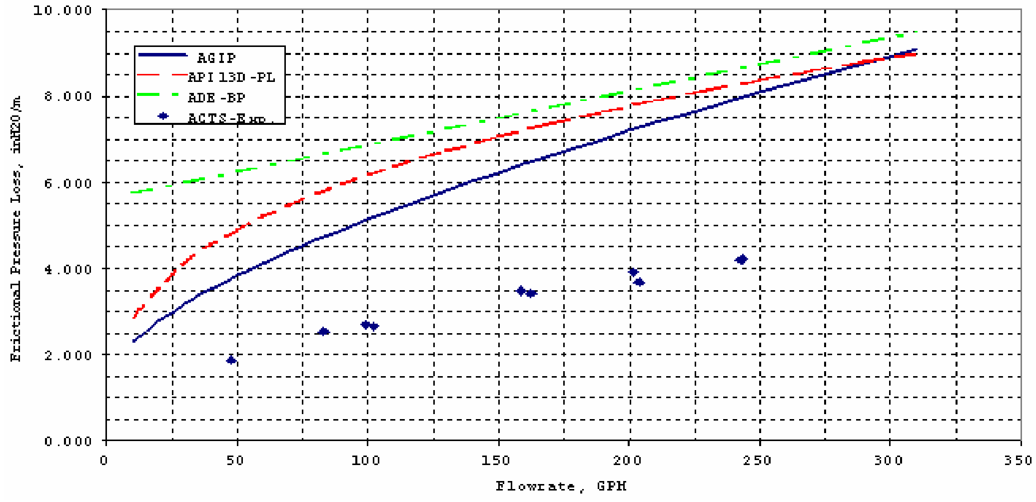

Fig. 6.18 Model predicted and measured pressure losses in the annulus (P = 0 psig & T = 75°F)

For both cases (75°F and 150°F), model predictions are higher than the measured data. For flow rates less than 310, the hydraulic models predict laminar flow conditions in the annulus. Better agreement between experimental and predicted pressure losses is achieved as the temperature increases. The AGIP Yield Power Law model gives relatively better predictions.

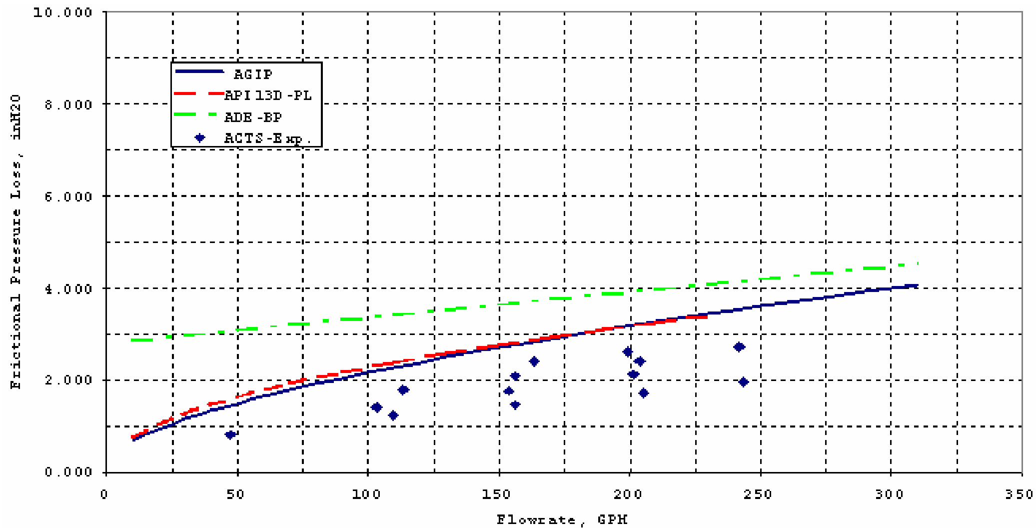

Fig. 6.19 Model predicted and measured pressure losses in the annulus (P = 0 psig & T = 150°F)

6.5 CONCLUSIONS

1. The effects of pressure on density of n-paraffin-based oil and paraffin-based drilling fluid under isothermal conditions can be shown using slightly compressible fluid relations. It should be stated that n-paraffin-base oil is slightly more compressible than paraffin-based drilling fluid at all temperatures and pressures.

2. The effects of temperature on density of the paraffin-based drilling fluid are more dominant than the effects of pressure. The largest change in density from the standard value was observed at low pressure-high temperature conditions and high pressure-low temperature conditions.

3. The rate of change of density of the paraffin-based drilling fluid with change in pressure, under isothermal conditions, is independent of water to synthetic oil ratio, solid content or emulsifiers present in the drilling fluid system. It is only dependent on the type of base oil used in the invert emulsion.

4. Flow loop experiments indicate that effect of pressure on frictional pressure losses in the pressure range of 0 psig to 1000 psig is smaller than the effect of temperature.

5. Laminar pipe flow predictions of the hydraulic models are significantly different from each other, particularly for high yield stress and high viscosity fluids with highly non-Newtonian properties. The Bingham Plastic model estimations are the highest among the three models. Predictions of pressure losses in turbulent flow are the same for all the models since viscous effects of the fluid diminish in turbulent flow.

6. Although the AGIP Yield Power Law Hydraulic model and the API 13-D Power Law Hydraulic model pipe flow predictions are in agreement with the experimental data at 0 psig, there are discrepancies between model predictions and experimental data at elevated pressures. For pipe flow, AGIP Yield Power Law hydraulic model predictions are in agreement with the experimental data in both flow regimes.

7. Laminar annular flow predictions of the models are higher than the measured data. Discrepancy between model predictions and the measured data decreases as temperature increases. Model predictions are predominately higher than the measured data. Therefore, a more accurate hydraulic model should be developed to determine pressure losses of non-Newtonian fluids in annuli.

8. Comparison of the annular data at 75°F shows that rheological behavior of the fluid at lower temperatures should be modeled carefully in order to estimate pressure losses accurately, especially in the case of laminar flow. This is due to the rapid increase in fluid viscosity as temperature decreases.

9. Experimental data and model predictions for highly non-Newtonian systems ($n < 0.3$), show the effects of flow rate on pressure losses is very small and pressure losses increase only slightly with increasing flow rate when the flow is laminar.

7. Study of Foam Flow under Elevated Pressure and Temperature Conditions (Task 9)

ABSTRACT

An extensive experimental study on the flow behavior of foam in pipe and annular geometries was conducted using a full-scale flow loop. The tests were conducted at pressures up to 700 psig and temperatures up to 185°F. The main objective of this research is development of an improved mathematical model for hydraulics of foam drilling. At the same time, flow properties of foam, its stability and compressibility were also investigated. A conventional drilling fluids hydraulic model, based on the Herschel-Bulkley rheological model, is adopted for foams using the principle of "Volume Equalization". A detailed discussion on the effects of foam generation, foam quality, pressure, temperature and geometry on foam flow behavior is presented. Results have shown that foam texture and quality significantly affect foam rheology. Pressure and temperature appear to have secondary effects. The importance of accounting for wall slippage in foam flow is highlighted and a new concept to evaluate the slip velocity in annuli is proposed. Results have shown that foam rheology can be characterized by a Power-Law model. A computer code was written based on the modified hydraulic model. Satisfactory agreement with experimental data in frictional pressure loss predictions was obtained for the flow of foams through pipes and annuli.

7.1 FOAM FLOW EXPERIMENTS

The University Tulsa Advanced Cuttings Transport Facility was used to conduct this experimental investigation. Foam rheology tests were performed to cover pressures from 100 psi to 650 psi, temperatures from 80°F to 180°F and foam quality ranging from 60% to 90%.

7.1.1 EXPERIMENTAL FACILITY

The experimental facility (flow loop) was designed to simulate foam flow under borehole conditions. The flow loop consists of pipe and annular test sections. The pipe section (rheology section) has three different size pipes (Table 7.1). Using the rheology section it is possible to determine the wall slip and rheology of foam under borehole conditions.

Table 7.1 Dimensions of Test Sections

Nominal Diameter (In)	Pipe ID (in)	Length (ft)
2	1.918	52'9"
3	2.9	52'9"
4	3.826	66'6"
Annular (6 x 3.5)	5.761x 3.5	57'4"

Table 7.2 lists major equipment used during the experiments. The flow loop is fully instrumented and all information is managed by a data acquisition and control system based on a LabView 5.0 environment. Table 7.3 shows a list of major important data acquisition and control instruments installed in the flow loop. In addition, automatic control of the most important variables is available. Figure 7.1 shows a simplified schematic of the flow loop.

Table 7.2 Lists of Major Equipment Used During the Experiments

Equipment	**Characteristics**
Injection tank	100 bbl
Return Tank	100 bbl
Liquid Injection Pump	100 GPM at 200 psig and 200°F
Multiphase Pump	Multiphase pump, 500 GPM total flow rate, 500 psi maximum differential pressure
Surfactant Pump	Maximum 0.84 GPM, 2000 psig, adjustable volumetric rates
Defoamer Pump	Maximum 0.15 GPM, 2300 psi, adjustable injection frequency and volume
Separation Tower	20 ft high, auto-controlled venting system, liquid level control and demister pads
Air Compressor	400 SCFM at 200 psig discharge
Boiler	10000 Btu / h ft^2
Heat Exchangers	Alfa-Laval Plate Model
Chiller	Water Cooling Tower

Table 7.3 List of Data Acquisition and Control Instruments

Variable	**Instrument**
Temperature	Thermo-resistance sensor with smart transmitter, 0 to 212°F
Pressure	Diaphragm sensor with smart transmitter, 0 to 4000 psi.
Differential Pressure	Diaphragm sensor with smart transmitter, 0 to 250 in H_2O and 0 to 1500 in H_2O
Air Flow rate	Micromotion flow meter, 1000 lb/min maximum mass flow rate

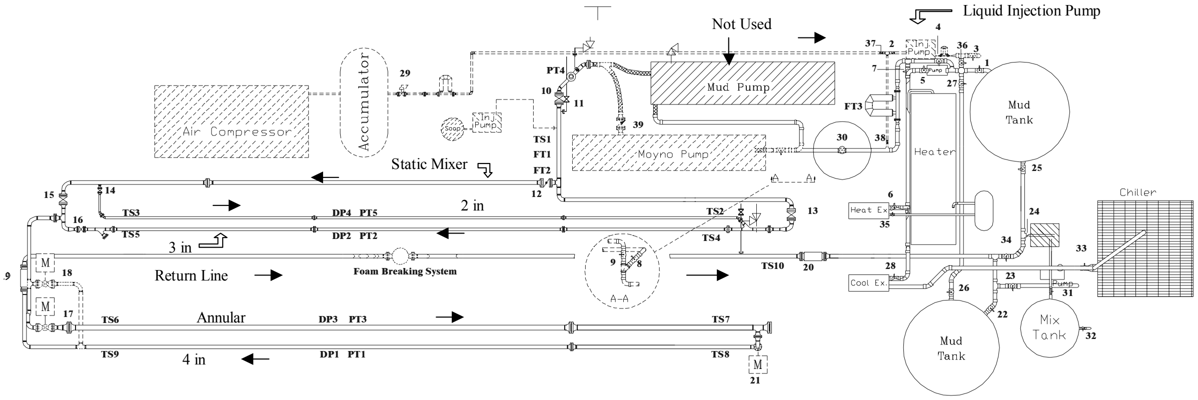

Fig. 7.1 Schematic View of the ACTS Experimental Facility

7.1.2 EXPERIMENTAL PROCEDURE

Each experiment consists of pressure loss measurements across the pipe sections and the annular section for a given test condition (air and liquid injection rates, pressure and temperature). Test variable parameters were pressure, temperature, foam quality and in situ foam volumetric flow rate. Water was the liquid phase and air was the gaseous phase for all experiments. During these experiments, the surfactant (Alkyl Ether Sulfate, anionic) concentration was 1% v/v. The experiments were carried out in a single pass throughout the test sections configured in series. Foam was generated in a static mixer, and then passed through 2-inch and 3-inch pipe sections, the annular section and finally through the 4-inch section. Foam breaker solution (10 % v/v silicon-based) was injected in a return line upstream of a vertical two-phase separator where air is vented and liquid is directed to a disposal tank.

The following steps summarize the most important actions to set and run during a particular test:

1. Heat the flow loop up to desired temperature with water;
2. Attain the desired test pressure, foam quality and in situ foam velocity and establish steady state flow conditions;
3. Start surfactant and defoamer (10% to 15% v/v of the surfactant) injections;
4. Record data: temperature, static pressure, differential pressure, liquid and air flow rates.

In order to investigate the effect of texture on foam rheology, two different sets of experiments were carried out, where the only difference was the foam generation procedure. The procedures were:

1. Foam generation using the static mixer (baseline foam tests);
2. Foam generation using the static mixer and a ball valve (stiffer foam tests).

The ball valve is located downstream of the multiphase pump (Moyno pump) and upstream of the static mixer. When foam was generated using the static mixer and ball valve, the differential pressure across the ball valve was kept at 100 psi. In fact, foam texture could not be strictly controlled or evaluated during the tests, but these procedures were useful to study the effect of texture on foam rheology by varying foam generation methods. Using measurements of pressure drop across the pipe sections and foam volumetric flow, the shear stress at the pipe wall and Newtonian shear rate were calculated for all tests.

7.2 MATHEMATICAL MODELING

7.2.1 FOAM RHEOLOGY

When rheological measurements of a non-Newtonian fluid are available, it is possible, at least in principle, to predict the laminar flow properties of such a fluid in conduits of simple cross section. In this way, the flow curve for a fluid can be rigorously and easily derived from pressure drop and flow rate data obtained with a capillary-tube or pipe viscometer of diameter D and length L. Metzner and Reed[1] observed experimentally that for most fluids the following relation for the shear stress at the wall is expected:

$$\tau_w = \frac{D\Delta P}{4L} = K'\left(\frac{8v}{D}\right)^{n'} \tag{7.1}$$

From the slope of a logarithmic plot of viscometric data in the form DΔP/4L versus 8v/D, the derivative, n', can be evaluated. For Power-law fluids, K' and n' are constant over a wide range of shear rates and shear stresses. This graphical evaluation of the parameter n' enables the construction of a flow curve for a Power-law fluid from laminar pipe-flow data. It can be shown that $(-dv_r/dr)_w$ and (8v/D) are identical except for the constant multiplying factor (3n'+1)/4n'. In view of these facts, an analytic expression for the shear stress-shear rate behavior of the fluid can be written in the form of a Power-law relationship with:

$$\tau_w = K\left(\frac{8v}{D}\left(\frac{3n'+1}{4n'}\right)\right)^{n'} \tag{7.2}$$

where v is the average fluid velocity and,

$$K = K'\left(\frac{4n'}{3n'+1}\right)^{n'} \tag{7.3}$$

7.2.2 DEVELOPMENT OF MASTER FLOW CURVES FOR FOAMS

Valko and Economides[2] introduced the concept of the Volume Equalized Principle. Accordingly, a master flow curve for foams may be obtained for different qualities and pressures if the constitutive equation is given as:

$$\frac{\tau_w}{\varepsilon_s} = K_{VE}\left(\frac{\gamma_w}{\varepsilon_s}\right)^{n} \tag{7.4}$$

where ε_s is specific volume expansion ratio given by:

$$\varepsilon_s = \frac{\rho_L}{\rho_f} \tag{7.5}$$

where ρ_L is the density of the liquid phase, ρ_f is the density of foam and K_{VE} is the volume equalized consistency index.

7.2.3 WALL SLIP

Several authors[3,4,5] have reported the existence of wall slip when foam flows through conduits and pipes. Drainage (syneresis) of liquid from foam produces a thin liquid film at solid boundaries, which enables wall slip. This phenomenon leads to incorrect computations of shear rates and a wrong evaluation of rheological parameters. Foams may move as nearly pure plug flow due to slippage at the wall. Hence, it is very important to have more than one pipe diameter for experimental measurements whenever capillary-type rheometers are used. Thus, the wall slip can be identified and corrections for the wall slip are made based upon the measurements from different pipe sections. In principle, the rheological behavior of a particular time independent fluid should not change with geometry of the conduit. However, this is what appears to happen when slippage occurs.

Many variables such as shear stress, pipe diameter, quality, bubble shape and bubble size distribution, liquid phase viscosity, gas phase viscosity and wall roughness are believed to affect the behavior of a liquid film. There is currently no theoretical method that is capable of accounting for all of these variables. Among the available methods, the Oldroyd-Jastrzebski[6] model shows superior performance over the others. In this approach, the slip velocity is modeled as:

$$v_{slip} = \frac{\beta_c \tau_w}{D} \tag{7.6}$$

where β_c is the slip coefficient. The actual flow rate ("observed" flow rate) incorporates the "shear flow" or true flow rate associated with shearing of the foam plus the "slip flow", the flow rate associated with the slip. The flow rate associated with shearing of the foam, "shear flow", is given by,

$$Q_{shear} = 2\pi \int_0^R (v - v_{slip}) r dr \tag{7.7}$$

where R is pipe radius. This flow rate is used to compute the "true" Newtonian shear rate of the foam at the wall. From Eq. 7.4 and Eq. 7.5, the following expressions can be written in terms of pipe diameter for the observed Newtonian shear rate:

$$\gamma_{obs\text{-}Newt.} = \gamma_{true-Newt.} + \frac{8\beta_c \tau_w}{D^2} \tag{7.6}$$

$$\gamma_{obs\text{-}Newt.} = \frac{8v}{D} \tag{7.7}$$

where v is the average velocity of foam inside the pipe, which also includes the slip velocity at the wall. The slope of a plot of "observed" shear rate versus $1/D^2$ at a given shear stress gives the slip coefficient. Hence, it is possible to obtain the relation between slip coefficient and shear stress.

Another method for computing the slip coefficient is to develop an empirical model based on experimental data. Developing a model for slip coefficient that accounts for all the parameters is extremely difficult. In an attempt to eliminate the effects of quality and pressure, the specific volume expansion ratio was introduced into the slip coefficient model. Thus, an empirical model for volume equalized slip coefficient is expressed as:

$$\beta_{VE} = \frac{a\tau_w^b}{\varepsilon_s^c} \tag{7.8}$$

Slip velocity prediction methods are not available for annular flows. A similar slip velocity model is proposed for annular flows. In this case, the wall shear stress and pipe diameter in Eq. 1 are replaced by the average wall shear stress in concentric annuli and the hydraulic diameter. The slip coefficient for the annulus was calculated assuming the same functionality with shear stress observed in the pipe sections, but using the average wall shear stress in place of the pipe wall shear stress.

7.2.4 FRICTIONAL PRESSURE LOSS PREDICTIONS

This section presents models used for the calculation of frictional pressure loss in horizontal pipes and annuli.

Pipe Flow

Reed[7] developed a general model for the flow of non-Newtonian drilling fluids in pipes and annuli. The model was developed based upon the introduction of an “effective diameter” that is not only a function of geometry, but also fluid properties. The “effective diameter” enables a connection between Newtonian pipe flow and non-Newtonian annular flow. The model is valid for all flow regimes and accounts for wall roughness. The generalized Reynolds number, Re, for non-Newtonian fluids can be defined in terms of effective diameter as:

$$\mathrm{Re}_G = \frac{\rho_f v D_e}{\mu_{eff}} \tag{7.9}$$

where the effective diameter and viscosity, D_e and μ_e are expressed as:

$$D_e = D\left(\frac{4n'}{3n'+1}\right) \tag{7.10}$$

and

$$\mu_e = \frac{\tau_w D_e}{8v} \tag{7.11}$$

where ρ_f is the density of the foam at actual flow pressure and temperature, given by:

$$\rho_f = (1-\Gamma)\rho_L + \Gamma\rho_{air} \tag{7.12}$$

Since the wall shear rate depends on n’ and is unknown, a relation is needed for the evaluation of n’. For a Herschel-Bulkley fluid, Reed[7] presented a relation for n’ which is expressed as:

$$\frac{1}{n'} = -3 + \tau_w\left(\frac{(1+m)}{\left(m(\tau_w-\tau_y)\right)} + \frac{2\left((\tau_w-\tau_y)\right)}{\left(A(3m+1)\right)} + \frac{2\tau_y}{\left(\left(A(2m+1)\right)\right)}\right) \tag{7.13}$$

where m is the non-Newtonian behavioral index of a Herschel-Bulkley fluid

$$A = \frac{(\tau_w - \tau_y)^2}{(3m+1)} + \frac{2\tau_y(\tau_w - \tau_y)}{(2m+1)} + \frac{\tau_y{}^2}{(m+1)} \quad (7.14)$$

The friction factor for laminar flow condition can be computed as:

$$f = \frac{16}{Re_G} = \frac{\tau_w}{0.5\rho_f v^2} \quad (7.15)$$

Similarly for turbulent flows, the friction factor is calculated by adopting the Colebrook equation for non-Newtonian fluids as:

$$\frac{1}{\sqrt{f}} = -4\log\left[0.27\frac{\varepsilon}{D} + \frac{1.26}{Re_G\sqrt{f}}\right] \quad (7.16)$$

Concentric Annular Flow

Pressure loss predictions in the annulus are also based upon the introduction of an “effective” diameter that is a function of the equivalent diameter. The average wall shear rate and shear stress concepts are also used in place of the corresponding parameters at the pipe wall. Zamora and Lord[8] developed correlations based on the analytical solution first developed by Fredrickson and Bird[9]. Accordingly, the friction pressure loss for laminar flows in annuli is given by:

$$\frac{dP}{dL} = (4K/D_h)\left[\frac{8vG}{D_h}\right]^n \quad (7.17)$$

where:

$$G = \frac{\left(\frac{D_o - D_i}{D_L}\right)^2 \left[(3-Z)n+1\right]}{\left[(4-Z)n\right]} \quad . \quad (7.18)$$

$$Z = 1 - \left[1 - (D_o - D_i)^Y\right]^{\frac{1}{Y}} \quad (7.19)$$

$$Y = 0.37n^{-0.14} \quad (7.20)$$

$$D_L = \left[(D_o + D_i)^2 - \frac{(D_o - D_i)^2}{\left[Ln\left(\frac{D_o}{D_i}\right)\right]}\right]^{1/2} \quad (7.21)$$

For transitional and turbulent flows the concept of imaginary velocity is applied. The imaginary velocity is defined as the velocity of a laminar flow that would create the same pressure drop as the actual turbulent non-Newtonian flow. It is evaluated by:

$$v_i = \frac{\left(\frac{\left(\left(\frac{dP}{dL}\frac{D}{4}\right) - \tau_y\right)}{K}\right)^{\frac{1}{n}} \text{Deff}}{8} \quad . \tag{7.22}$$

where dp/dL is annular frictional pressure loss given by:

$$\frac{dp}{dL} = \frac{2f\rho_f v^2}{D_h} \tag{7.23}$$

The form of the generalized Reynolds number remains the same, but the imaginary velocity is used to calculate the wall shear rate and the corresponding effective viscosity. With these modifications, the same procedure of pressure drop calculations is applied to the turbulent flow of non-Newtonian fluids in concentric annuli.

7.3 STABILITY AND VOLUMETRIC PROPERTIES OF FOAMS

Stability and volumetric properties of foams were investigated before the comprehensive experimental study on its flow behavior. As far as stability is concerned, static drainage experiments were conducted in a glass cylinder. The method represented a simple way to verify minimum requirements for the flow-loop experiments and general trends of stability properties in foam systems.

Two typical contaminants (Salt and hydrocarbons) of foams in underbalanced drilling operations were tested. Mineral salt (99% complex chlorides) concentrations were from 5 to 30 grams per milliliter of surfactant solution during the test. The influence of 5% v/v and 10% v/v of mineral oil was also tested. The main component of the anionic surfactant is the Sodium Alkyl-Ether-Sulfonate. Parameters such as half-life (the time for half of the foam solution to drain) and drainage rates were used to evaluate foam stability. Results revealed that the average half-life of the samples was approximately 7 min. A good ability to generate foam and tolerance to the contaminants at concentrations of 1% v/v surfactant was observed.

The PVT behavior of foams was also investigated and an attempt to develop an equation of state for foams based on an experimental approach was made. Foams have high surface areas and their bubble structure (change in size and shape) depend on quality and generation conditions. Therefore, it is logical to think that those variables may influence the way foam behaves with changes in pressure and temperature, especially at high pressures and temperatures. On the other hand, the inclusion of surface and structural effects in an equation of state is far from trivial. Even when it is included, the resultant equation of state may become complicated for engineering purposes.

7.4 RESULTS

7.4.1 EFFECT OF FOAM GENERATION ON RHEOLOGY

Figure 7.2 shows the effect of foam generation method on rheology. The figure presents the profile of the measured pressure drop in the 4-inch pipe section as a function of differential pressure drop across the ball valve located upstream of the static mixer. The 4-inch pipe pressure drop almost tripled, in the 90% quality test, with the increase in differential pressure and associated shear during foam generation. This effect was also observed in the 70% quality test, but to a lesser extent. Results indicate the existence of a range of shear rate and/or hydraulic power where good foam texture is achieved, but completely different rheological responses can occur. After a certain level of shear rate, there is no significant change in pressure drop.

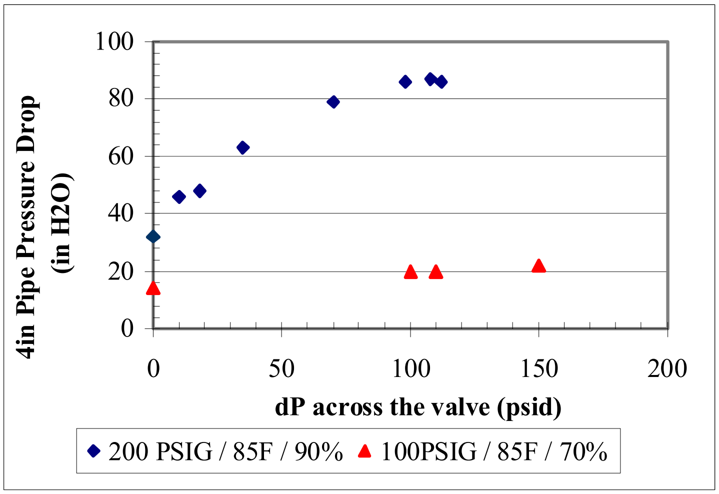

Fig. 7.2 Effect of foam generation on foam rheology (Stiffer Foam)

Fig. 7.3 Removable view port and bottom sample port

A removable view port (Fig. 7.3) installed in the 4-inch pipe allows visual inspections using a microscope of foam samples at actual pressure and temperature conditions. These observations did not provide a good way to properly quantify the bubble size and shape distribution, but did enable qualitative observations. The results indicate a reduction in bubble size and a narrower distribution of bubble size for foam, under the same operational conditions, when generated with higher shear rates. Harris[10] also observed a decrease in bubble size and narrower bubble size distribution with increases in shear rate. Prud'homme and Khan[11] observed an increase in viscosity of emulsions with a decrease in drop size of the dispersed phase. The trend makes sense since the number of bubbles per unit volume of fluid increases with a decrease in bubble size. Consequently, the interaction forces among them increase. Another fact is that for a particular unit volume, the surface area increases with a decrease in bubble size. Therefore, the resistance to flow in a structured fluid like foam should increase as bubble size decreases. Harris[10] observed that the viscosity of low quality foams was not as susceptible to bubble size effects at high shear rates.

Figure 7.2 confirms these observations. One possible explanation for this phenomenon is related to foam structure. Foams with less than 70% quality normally form spherical bubbles with thicker liquid films between the bubbles. High quality foams exist as polyhedral-type bubbles with thinner liquid films. The structure of polyhedral bubbles is more rigid and more resistant to shearing than the spherical type.

For a certain volume of fluid, an equivalent reduction in bubble size causes a more severe increase in the surface area and number of links in a polyhedral bubble than in a spherical one. Thus the viscosity of low quality foams is probably less sensitive to bubble size changes. The test results demonstrate the importance of bubble size characterization for proper rheological evaluation of foams. Variables of bubble shape and size distribution must be included in the rheological evaluation in order for a hydraulic model to be totally independent of the method of foam generation. Figure 7.4 confirms the increase of viscosity after the new foam generation procedure. A more detailed investigation is needed to fully elucidate these phenomena.

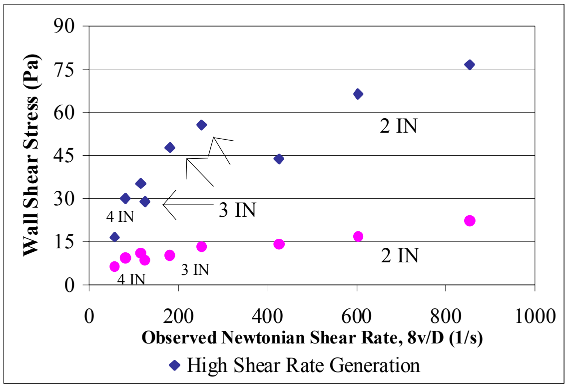

Fig. 7.4 Effect of foam generation on rheology of 90% quality foam at 100 psig and 85°F

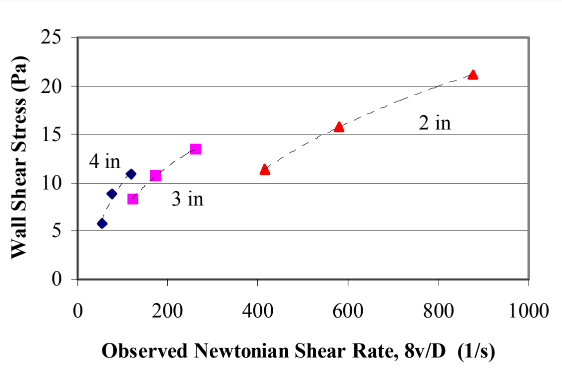

Fig. 7.5 Effect of wall slip on rheology of 90% quality foam at 100 psig & 150°F (baseline tests)

7.4.2 EFFECT OF WALL SLIP

During foam rheology experiments, the slippage effect was also observed. Figure 7.5 shows the effect of slip on rheology of foam for a particular experiment condition. It appears as if the foam has different rheology in different pipe sizes. Without wall slip, the rheological behavior of a particular time-independent fluid should not change with the pipe size.

Oldroyd-Jastrzebski[6] method is employed to determine the slip coefficient. Figure 7.6 shows a procedure of this particular method. Hence, it is possible to obtain the relation between slip coefficient and shear stress. Figure 7.7 shows this relation for a particular test. When this relation is known, the "true" Newtonian shear rate, $\gamma_{\text{true-Newt}}$, can be calculated using Eq. 7.6. The trend of slip coefficient presented in Fig. 7.7 is characteristic of the majority of tests. However, in some experiments, an increase in the slip coefficient with increasing the shear stress is noticed.

Figure 7.8 presents wall shear stress versus corrected wall shear rate for 80% quality foam at 300 psig and 100°F. After correction, data from the different pipe diameters tend to lie on a single curve. The Oldroyd-Jastrzebski[6] method is not able to explicitly describe each effect influencing the slip at wall. In spite of this, it assumes that they are implicitly accounted for by the wall shear stress.

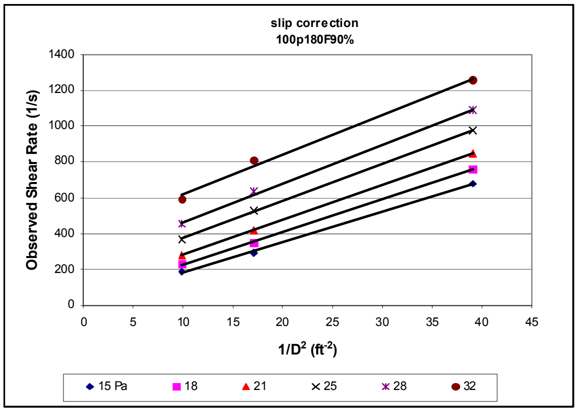

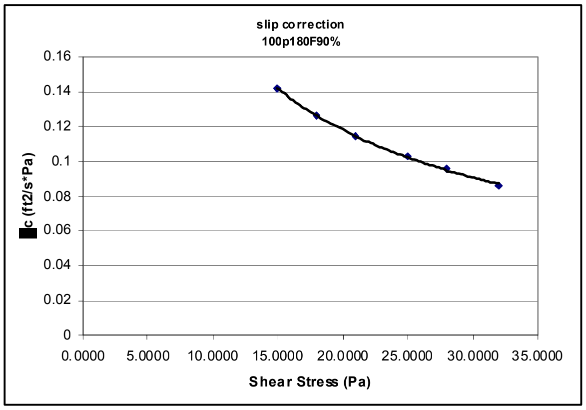

Fig. 7.6 Graphical method for slip Correction

Fig. 7.7 Slip Coefficient vs. wall shear Stress

The effect of wall roughness is not clearly understood either. It is known that a rough surface tends to eliminate or reduce wall slip. Princen[12] suggested that the effect of wall roughness is a function of the ratio of the absolute roughness (ε) to the average bubble size. In general, the slippage was more severe in the 2-inch pipe. This makes sense since it is the smoothest pipe, and has the smallest diameter and is the highest shear stresses for a particular foam flow rate. Another interesting observation is the decrease of slippage at the wall between the 3-inch and 4-inch pipes (points with lower shear rates) for the foam generated at high shear rates and having smaller bubbles. One possible explanation is that these smaller bubbles may be sufficiently small to lock into the small bumps of the rough surface, diminishing the slip effect. Calibration tests performed with water in fully turbulent flow conditions indicated that wall roughness is greatest in the 4-inch pipe and least in the 2-inch pipe. This also could have caused progressively less wall slip with increasing pipe diameter.

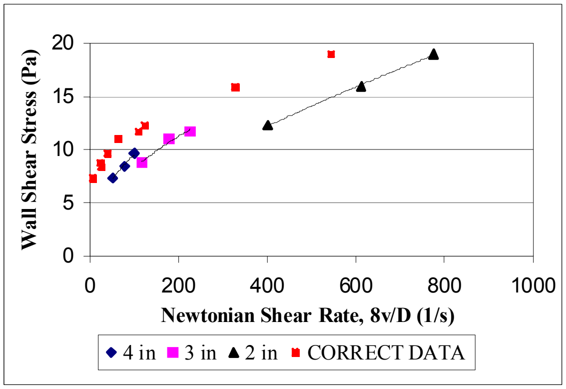

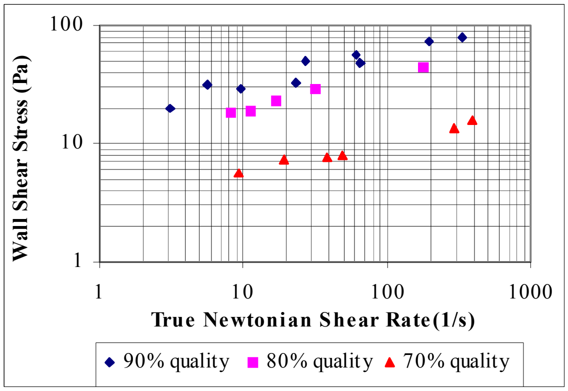

Fig. 7.8 Shear stress vs. shear rate for 80% quality foam at 300 psig & 100°F (baseline tests)

Fig. 7.9 Effect of quality on rheology of stiffer foam at 300 psig and 80°F

In Fig. 7.8, the slip-corrected data suggest the presence of an apparent yield point. In some experiments an apparent yield point appears after the slip correction for low shear rate data, especially in high quality foams. It is called apparent yield point because the foam is flowing nearly as a plug in the conduits with a velocity almost equal to the slip velocity. The difference between the slip velocity and the actual average velocity (based on pump rate and pipe diameter) causes shearing of the foam inside the perimeter of the slip layer. The corresponding velocity profile is determined by the rheology of the foam. As the slip velocity approaches the actual velocity, there is progressively less shearing of the foam, and the velocity profile tends to become flat and independent of rheology.

7.4.3 EFFECT OF QUALITY

Quality is one of the most important variables affecting foam rheology. The non-Newtonian behavior of foams comes from the presence of bubbles in the fluid. This behavior is usually enhanced with an increase in the percentage of gas in the foam. Usually a shear thinning behavior is observed in the flow of foams. Figure 7.9 shows the effects of quality over a range of experimental conditions. For a particular true Newtonian shear rate the high quality foams present higher shear stresses, meaning a higher effective viscosity. Newtonian shear rate is used here because the intention at this point is only to highlight the effect of quality and not to evaluate the true rheological parameters.

7.4.4 EFFECTS OF PRESSURE

Figure 7.10 shows flow curves of 90% quality foams measured at different test pressures. The results did not reveal a significant effect of pressure on foam rheology at a constant quality. This was observed for both the baseline tests and experiments with the stiffer foams. Some authors[10,13] have reported a more pronounced effect of pressure on foam rheology, but over a wider range of pressure. In spite of this, the same authors found different trends for the effect of pressure on foam rheology. Harris[10] found an increase of shear stress at the same shear rate with a decrease in pressure, whereas, Cawiezel, et al.[13] found the opposite. It is expected that a greater mechanical and chemical interaction occurs between the bubbles as pressure increases. If true, this should result in an increase of the viscosity of a foam. Apparently, this effect is not significant enough to modify the rheological measurements found in this study.

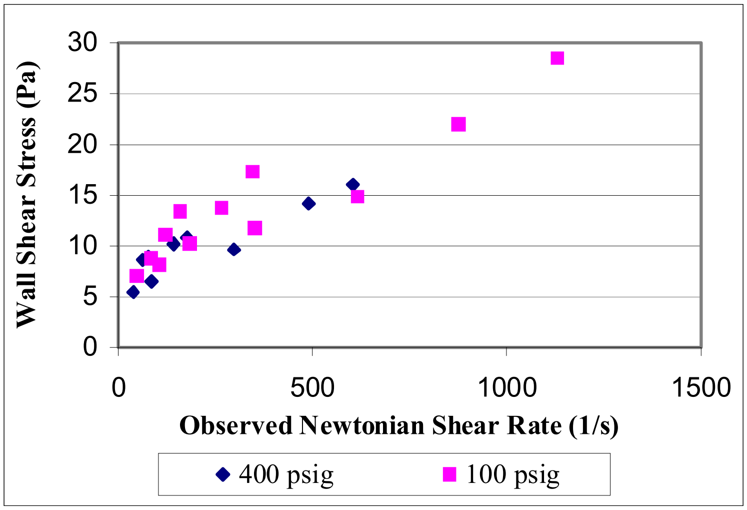

Fig. 7.10 Effect of pressure on 90% quality foam rheology at 100°F (baseline test)

7.4.5 EFFECTS OF TEMPERATURE

Figure 7.11 shows the effect of temperature on the rheological behavior of foams based on the experimental data. The figure does not indicate a significant influence of temperature on the rheological properties of foams. A thinning of foam was expected at higher temperatures as a result of a decrease in viscosity of the liquid phase, but this could not be clearly observed in the data from these tests. Similar results for stiffer foams are presented in Fig. 7.12. Results indicate that the rheological behavior can be characterized by a Power-Law Model. Table 7.4 shows the volume equalized rheological parameters after regression analyses. Note that these are wall slip parameters despite the fact that Fig 7.11 and Fig. 7.12 show the true Newtonian shear rate.

Table 7.4 Volume-equalized Rheological Parameters

Parameter	Baseline Tests	Stiffer Foam		
		High Quality	Low Quality (80 °F)	Low Quality (150 °F)
K_{VE} (Pa s^n)	0.879	3.193	0.808	0.409
n	0.303	0.294	0.373	0.494
(R)	0.91	0.93	0.94	0.94

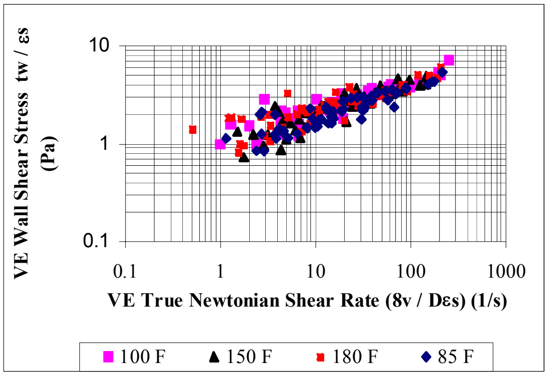

Fig. 7.11 Volume-equalized master flow curves for baseline foams at different temperatures and pressures

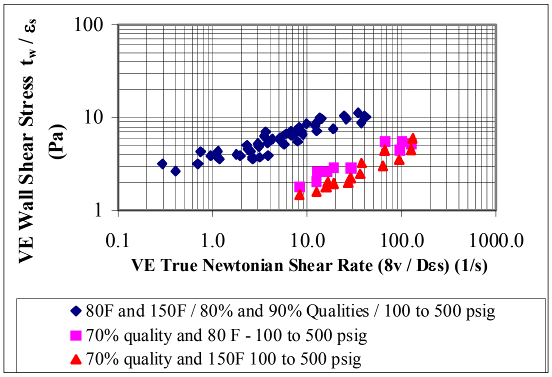

Fig. 7.12 Volume-equalized master flow curves for stiffer foams at different temperatures and pressures

7.5 COMPARISONS OF RESULTS AND MODEL PREDICTIONS

Figures 7.13 to 7.17 show the results of theoretical predictions of Reed's modified model against experimental data in the pipe and annular sections. A band representing 15% absolute error in the prediction is also shown.

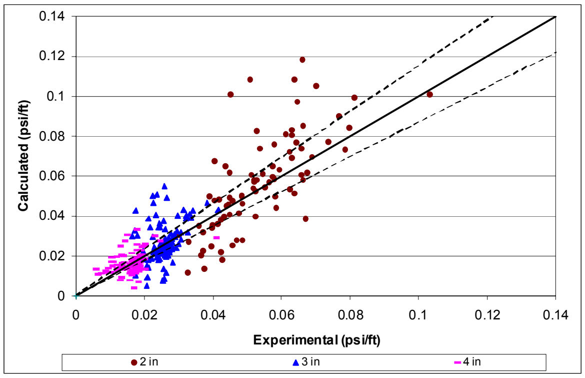

Fig. 7.13 Comparison of measured data with model predictions in 3-inch pipe (baseline tests)

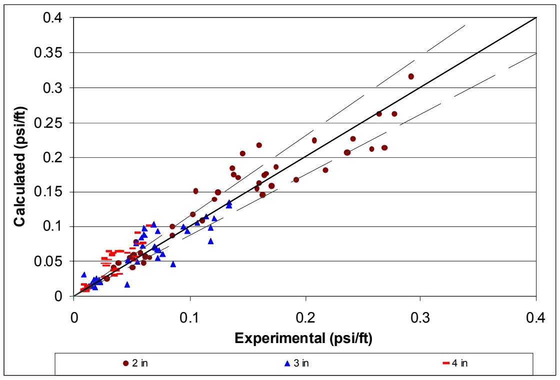

Fig. 7.14 Comparison of measured data with model predictions in 3-inch pipe (stiffer foam)

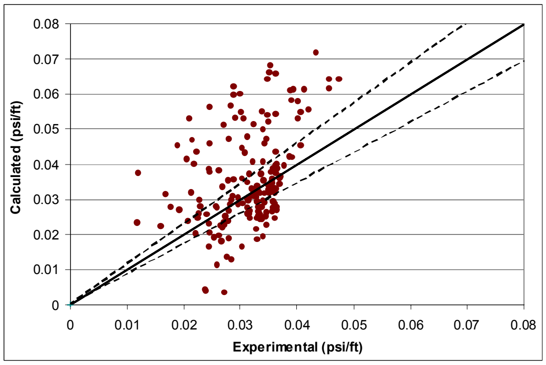

Fig. 7.15 Comparison of measured data with model predictions in the annulus (baseline tests)

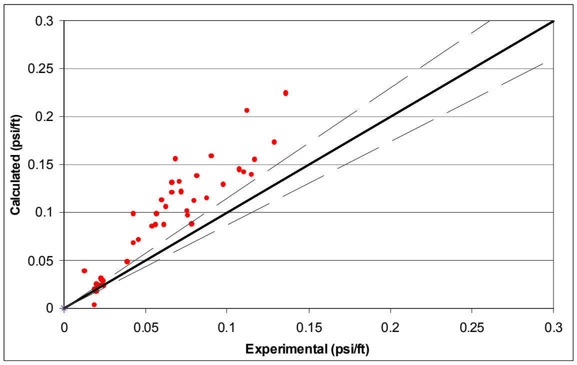

Fig. 7.16 Comparison of measured data with model predictions in the annulus (stiffer foam)

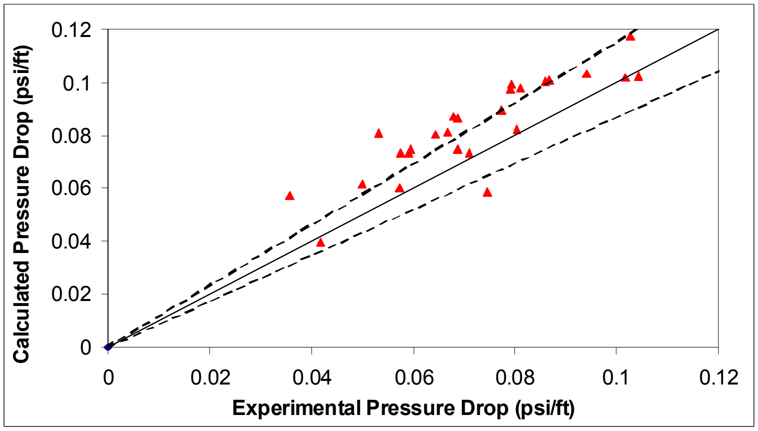

Fig. 7.17 Comparison of measured data with model predictions in 2-inch pipe (transitional & turbulent flow conditions)

7.6 CONCLUSIONS

1. In addition to foam quality, the experimental results indicate a strong influence of texture on foam rheology. The effects of temperature and pressure on foam rheology are secondary;
2. Foams generated at high shear rate conditions have smaller bubbles and higher effective viscosities;
3. Slippage at the wall is one of the most important phenomena to be considered in foam flow. Empirical correlations for slippage coefficient, independent of quality, were developed. In addition, the average wall shear stress and hydraulic diameter is used for calculating slip velocity in annuli. This assumption seems to under predict slippage effects for stiff foams;
4. The Volume-equalized principle demonstrated good results in generating flow curves for foams. However, two flow curves are obtained for the stiffer foam, one for high quality and another for low quality foams. These results suggest the need for incorporating texture effects into the model;
5. The effect of shear rate during foam generation on foam rheology is more significant for high quality foams. Consequently, the lower the quality of foam downhole, the less is the effect of flow through bit nozzles. Hydraulic models for foam drilling should have texture linked with a rheological model in order to properly estimate flow properties inside the drillstring and annular sections;
6. The predictions for friction pressure losses are satisfactory considering the many variables involved in the flow of foams. Structure properties and a reliable model for the prediction of slip velocity must be incorporated into the model in order to generate a truly general model. In spite of this, the work represents one the first attempts to develop a general hydraulic model for foam flow in pipes and annuli in all flow regimes.

NOMENCLATURE

a = parameter
b,c = dimensionless parameters
ECD = Equivalent Circulating Density
D = Internal Pipe Diameter, L, m
K = Consistency Index,
L = Pipe Length, L, m
Q = Volumetric Flow Rate
R = Pipe Radius
v = average velocity
p = absolute pressure
n’ = Behavior Index

Greek Letters

τ = Shear Stress
γ = Shear Rate
εs = specific expansion ratio
βc = Slip Coefficient
Δ = variation

Subscripts

w = wall
avg = average
h = Hydraulic
VE = Volume Equalized
r = radius

REFERENCES

1. Metzner A. B., Reed J. C., (1955), “Flow of Non-Newtonian Fluids – Correlation of the Laminar, Transition, and Turbulent-flow Regions”, A.I.Ch.E. J.
2. Valko, P., Economides, M. J., (1992) “Volume Equalized Constitutive Equations for Foamed Polymer Solutions”, Journal of Rheology.
3. Kraynik, A. M., (1988), “Foam Flows”, Ann. Rev. Fluid Mech., vol 20, pp 325-57.
4. Enzendorfer,C., Harris, R.A , Valko, P., Economides, M. J., Fokker P.A., Davies, D.D., (1995), “Pipe viscometry of foams”, Journal of Rheology, 39 (2), 345 - 358.
5. Gardiner, B. S., Dlugogorski, B. Z., Jameson, G. J., (1998), “Rheology of Fire-Fighting Foams”, Fire Safety Journal.
6. Jastrzebski, Z. D., (1967), “Entrance Effects and Wall Effects in an Extrusion Rheometer During the Flow of Concentrated Suspensions”, Ind. Eng. Chem. Res., p. 445 to 454, vol 6.
7. Reed, T. D., Pilehvari, A. A., “A New Model for Laminar, Transitional, and Turbulent Flow of Drilling Muds”, SPE 25456, 1993.
8. 17. Zamora, M., Lord, D. L., “Practical Analysis of Drilling Mud Flow in Pipes and Annuli”, SPE 4976, 1974.
9. Frederickson, A.G., and Bird, R.B., “ Non-Newtonian Flow in Annuli”, Ind. Engr. Chem., 50, 347-52, 1958.
10. Harris, P. C., (1989), “Effect of Texture on Rheology of Foam Fracturing Fluids”, SPE 14257.
11. Pred’homme, R., Khan, S., (1996), “Experimental Results in Foam Rheology”, Chap. 4 in FOAMS: Theory, Measurements and Applications, R. Pred’homme and S. Khan eds, Marcel Dekker, New York.
12. Princen, H. M., (1985), “Rheology of Foams and Highly Concentrated Emulsions – II. Experimental Study of the Yield Stress and Wall Effects for Concentrated Oil-in-Water Emulsions”, J. of Colloid Interface Sci., 105, 150.
13. Cawiezel, K. E., Niles, T. D., (1987), “Rheological Properties of Foam Fracturing Fluids Under Downhole Conditions”, SPE 16191.

8. Experimental Investigation of Foam Rheology and Development of Foam Generator/Viscometer (Task 9b)

ABSTRACT

One of the important findings from research Task 9 is that foam texture (i.e., bubble size, shape & size distribution) has a considerable effect on the apparent viscosity of foam. This identified the need to have an instrument that can generate foam with a controlled bubble size and is able to measure simultaneously its rheological properties. This has led to the development of a new concept for achieving these objectives. This became a new instrumentation task, and it was designated Task 9b. A foam generator/viscometer was developed as a part of this research task. The instrument can generate foam with desired properties and measure its rheological properties. It is capable of controlling the following six variables independently: i) foam quality (ratio of gas to liquid), ii) pressure, iii) temperature, iv) surfactants and other additives, v) bubble size, and vi) surface roughness inside the viscometer.

An experimental study of foam rheology has been proposed. This research task is more focused on the phenomenon of "wall slip". In order to quantify the wall slip, a variety of roughnesses were applied to the surfaces that the foam is in contact with while rheology measurements are being made. Foam rheology tests were performed using a Couette-type rotational viscometer with different cup-rotor assemblies of different surface roughnesses. Foams with varying foam qualities were generated using the foam generator/viscometer system and the dynamic testing facility (see Section 11) and tested under ambient temperature and low pressure conditions. Experimental results indicated that foams behave as non-Newtonian fluids with shear thinning properties. Rheological measurements obtained using different cup-rotor assemblies showed significant differences that indicate the phenomena of wall slip.

8.1 INTRODUCTION

The overall objective of this project is to characterize foams using a Couette-type rotational viscometer (Thermo Haake RS 300) and provide new data that will help drilling engineers achieve better results. To achieve this objective, the phenomenon of wall slip and how it affects foam rheology was investigated. A photo of the viscometer is in Fig. 8.1a. This viscometer was chosen because of its essential features. It is designed to: i) allow in-line rheology measurements through a cup-rotor assembly shown in Fig. 8.1b; and ii) operate at pressures up to 100 bars (1500 psi) and temperatures up to 150°C (302°F). It is a Couette-type viscometer with a stationary cup (Fig. 8.4c). The gap between the rotor (Fig. 8.4d) and cup is 2 mm for all the cup-rotor assemblies.

Typically, foams form a liquid film at solid surfaces. This layer inhibits the shearing of the foam, which causes the viscosity reading to be lower than the true viscosity of the foam. This project is the initial attempt to investigate the addition of wall roughness over all surfaces that contact the foam. Theoretically, this would allow the liquid layer to reside inside the roughness elements, while the protrusions of the roughness contact the foam causing it to be sheared directly. This should allow the viscometer to give a more accurate reading of shear stress and shear rate, which in turn provides a true apparent viscosity (rheological parameters).

Fig. 8.1a Viscometer (RS300)

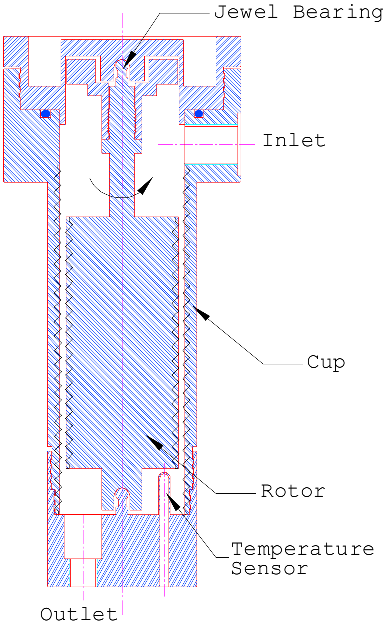

Fig. 8.1b Cup-rotor assembly of RS300

Fig. 8.1c Roughened cups

Fig. 8.1d Roughened rotors

8.2 OBJECTIVE

The purpose of this project is to study the rheology of dynamic foam using a rotational viscometer (Thermo Haake RS300). In the viscometer, an inner cylinder rotates inside a cup. Typically, foams form a liquid film at solid surfaces. This layer inhibits shearing, which causes the torque reading to be lower than the true torque of the foam. The theory this project begins to investigate is that with the addition of wall roughness over all surfaces that contact the foam the liquid layer will sit inside the roughness elements, while the protrusions from the roughness contact the foam causing it to be sheared. This should allow the viscometer to give a more accurate reading for shear stress and shear rate.

8.3 QUANTIFICATION OF ROUGH SURFACE

The next step was to quantify these roughnesses in a standardized manner. This required a roughness measuring instrument, which is commonly used by the surface coatings industry. Many possibilities were explored before purchasing the roughness measuring instrument (Surftest 401). This instrument will provide an accurate surface roughness measurement, not only for rotors and cups, but also for the inside of the ACTS Flow Loop, in which hydraulic tests with foams are planned. The instrument has a diamond stylus that passes over the top of the roughened surfaces. This instrument is capable of evaluating surface textures including waviness with a variety of parameters according to various national and international standards. The measured results are displayed digitally and graphically on a touch panel, and output to a built-in printer. Some of the output includes: i) average roughness, Ra, which is the arithmetic mean of the absolute values of the profile deviations (Y_i) from the mean line; and ii) standard deviation of the surface roughness, Rq. The formulas for Ra and Rq are mathematically written as:

$$\mathrm{Ra} = \frac{1}{N}\sum_{i=1}^{N} | Y_i | \tag{8.1}$$

$$\mathrm{Rq} = \left[\frac{1}{N}\sum_{i=1}^{N} Y_i^2\right]^{0.5} \tag{8.2}$$

Two stainless steel cups with 0.025-inch and 0.010-inch surface roughnesses were manufactured. Rotors were also manufactured and milled to create diamond shaped projections from the surface to contain the slip layer and shear the foam. Surface roughness measurements were made twice. Initial measurements indicated that the 0.025-inch and 0.010-inch cups have average roughnesses of 10.31 μm and 14.85 μm, respectively. The 0.025-inch and 0.010-inch describe the distance from one peak to the next peak of the protrusions. Recently, average roughness measurements were made by taking different profile samples from the cups and rotors. The results of these measurements are presented in Table 8.1.

Table 8.1 Results of Roughness Measurements

	Surface Type	**Mean Roughness [μm]**	**Standard Deviation [μm]**
Cups	Smooth	3.1	3.7
	Roughness # 1	13.0	15.6
	Roughness # 2	21.0	25.6
Rotors	Smooth	2.0	2.4
	Roughness # 1	38.0	45.5
	Roughness # 2	44.0	50.0

8.4 FOAM GENERATOR/VISCOMETER

Findings from Research Task #9 suggested that foam texture influences the rheology of foam. To measure foam rheology, one commonly-used method is by using a pipe viscometer, and normally three pipes are required if there is “wall slip”. A pipe viscometer such as large-scale flow loop can be expensive to operate. Will it be possible to measure foam rheology the same way as a conventional drilling fluid? Two hurdles need to be overcome to use a rotational viscometer to measure foam rheology. First, be able to generate foams with controllable properties (such as bubble size etc.); and second, to develop a process that will enable measurements of the viscous properties of foams that are free of the influences of drainage and bubble coalescence, and can quantify the effects of surface roughness on wall slip. This led to the development of a new foam Generator/Viscometer. The instrument is capable of controlling the following six variables independently: i) foam quality (ratio of gas to liquid), ii) pressure, iii) temperature, iv) surfactants and other additives, v) bubble size, and vi) surface roughness inside a viscometer. A US Patent was filed on October 28, 2002 for the design of an instrument that can generate a variety of foams under elevated pressures and temperatures and then transfer the test foam to a viscometer for measurements of rheology.

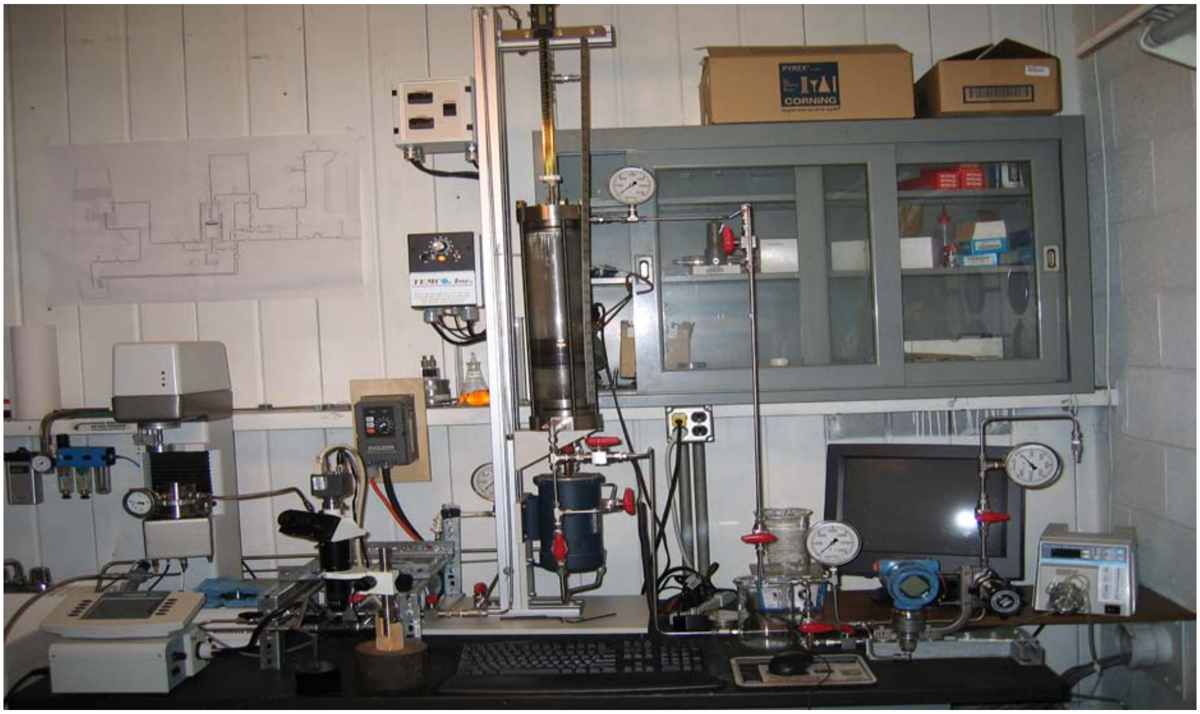

Fig. 8.2 Foam Generator/Viscometer system

The Foam Generator/Viscometer shown in Fig. 8.2 is capable of conducting experiments up to 1500 psig and 150°C. The construction and assembly of this instrument was completed. A simplified flow diagram for the foam Generator/Viscometer system is presented in Fig. 8.3. Calibration of the foam generator was completed. Preliminary rheology tests were conducted at ambient pressures and temperatures and only one type of surfactant was used. During initial trials, it was determined that the mixing propeller could not supply sufficient thrust to fully involve the foam. Several propellers and propeller combinations were tried to achieve even mixing. A 3-inch propeller that was modified for additional thrust performed well. We were able to generate up to 95% quality foam. After calibrating the system, preliminary foam rheology and bubbles size measurement tests were performed.

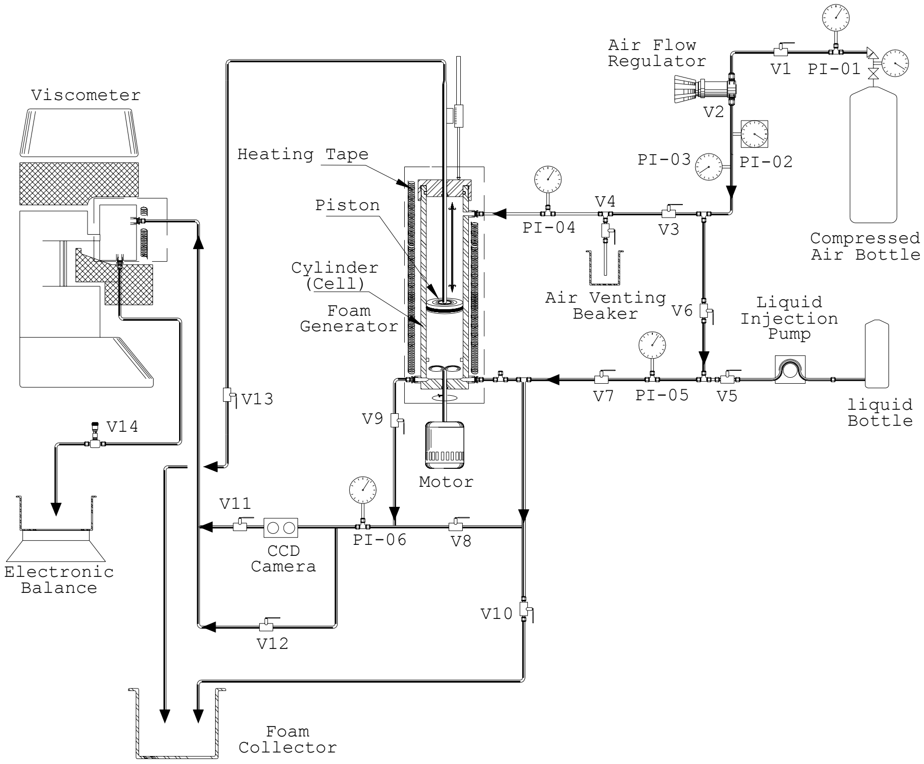

Fig. 8.3 Schematic of foam Generator/Viscometer system

Fig. 8.4a Foam Generator

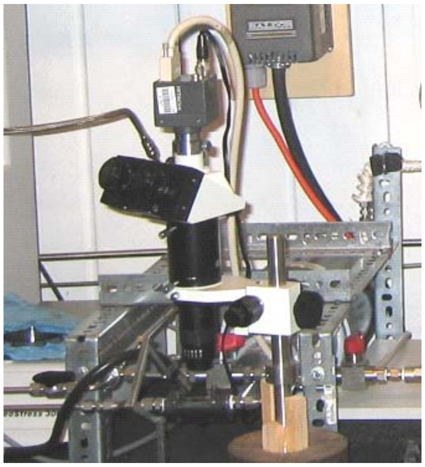

Fig. 8.4b CCD Camera together with a microscope

The foam Generator/Viscometer system consists of: i) rotational viscometer; ii) foam generator (Fig. 8.4a); iii) CCD camera together with a microscope (Fig. 8.4b); iv) liquid injection pump (Fig. 8.5); v) compressed air and liquid bottles; and vi) electronic balance. The foam generator is made of a cylinder (cell) with piston and mixer (Fig. 8.6). Two types of cylinders were manufactured: i) a stainless steel cylinder for elevated pressure and elevated temperature applications; and ii) a transparent PVC cylinder for ambient conditions. The foam Generator/Viscometer system provides a means by which the rheology of foams or other shear-sensitive media can be measured. Liquid components (such as surfactant and water) are selectively combined with a gas (such as nitrogen, air or other gases) in various ratios and allowed to flow under controlled conditions (pressure, temperature, and flow rate) through a modified (variable surface roughness) Couette-type rotational viscometer at such a rate that the viscosity of the foam is determined while its properties (bubble size, quality, pressure, temperature, and viscosity) are maintained constant.

Fig. 8.5 Liquid injection pump

Fig. 8.6 Mixer with variable speed drive

The generator allows the desired ratio of gas and liquid to be precisely placed into a mixing cell that is designated as the Foam Generator. Foam is formed by means of a propeller driven over a wide-range of rotary speeds by a variable speed motor. Design of the generator permit proper loading and mixing of components. The shape of the propeller is designed to circulate the mixture up through the center of the generator and then downward along the chamber walls to promote uniform mixing. The Generator is equipped with a floating piston that maintains the pressure. The floating piston separates the cell into two sections: i) mixing cell (bottom part); and ii) top of the piston. An appropriate heat source enables the foam to be heated. The foam bubble size can be visually assessed via a view port to ascertain when the foam has stabilized and reached steady state at the desired conditions. Foam enters the top of the viscometer and leaves through the bottom. This assures that any liquid drainage from the foam is quickly removed and does not affect the measurement. If the foam characteristics change within the viscometer, the flow rate can be adjusted to reduce or increase the average fluid residence time within the viscometer. Furthermore, the interior surfaces of the viscometer are modified with different surface roughnesses to assess the effects of this variable on wall slip and measurements of foam rheology.

The test process begins by combining water and surfactant in desired ratios and quantities in the liquid bottle. From there, measured quantities of the liquid phase are pumped using the liquid injection pump into the mixing cell. The cell is then isolated from the pump by means of a valve (V5) and compressed air is supplied from a compressed air bottle. The temperature of the foam generator is then adjusted to the desired value by means of electrical resistance heating tapes, if necessary. Temperature inside the mixing cell is measured by a thermostat connected to a thermocouple.

Once injection of the gas and liquid phases is completed, valves (V3 and V6) are manipulated to apply gas to the top of the piston. This piston maintains constant pressure on the foam. Next, a propeller inside the foam generator is rotated at a desired speed and for a selected length of time to generate the foam. Propeller design, rotation speed and length of mixing time determine the amount of shear energy applied and the resulting bubble size. A needle valve downstream of the modified Couette-type rotary viscometer regulates flow from the generator to the viscometer. This is an essential feature of the Generator/Viscometer system. The system is designed to carefully maintain integrity of the foam. Pressure and temperature are constantly monitored.

A CCD camera placed between the viscometer and foam generator measures the bubble size and bubble size distribution while the foam continuously flows through the viscometer. Both the CCD camera and the viscometer outputs are displayed and recorded by a computer. Digital pictures obtained from the camera are used to determine the average bubble size and bubble size distribution.

Due to the axial flow through the viscometer, the rheological measurements can easily be affected by the foam flow rate. High flow rates can alter the actual shear rate measurements; and very low flow rates are not recommended because of foam drainage. In order to keep the flow rate in the optimum range, flow rate measurement through the viscometer is required. Foam flow rate can be approximately determined by measuring the mass of the liquid phase collected at outlet of the viscometer. Therefore, the foam leaving the viscometer is collected constantly in a beaker placed on an electric balance to measure the mass of the liquid phase collected as a function of time.

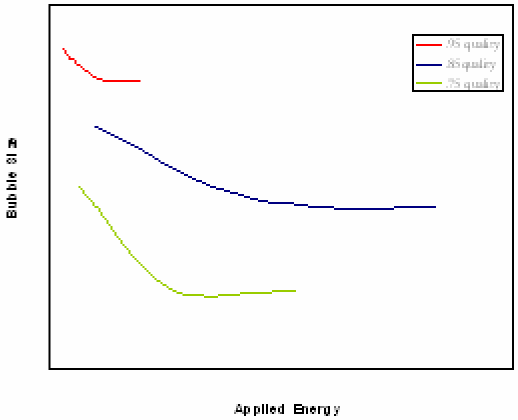

Fig. 8.7 Bubble size as a function of applied energy

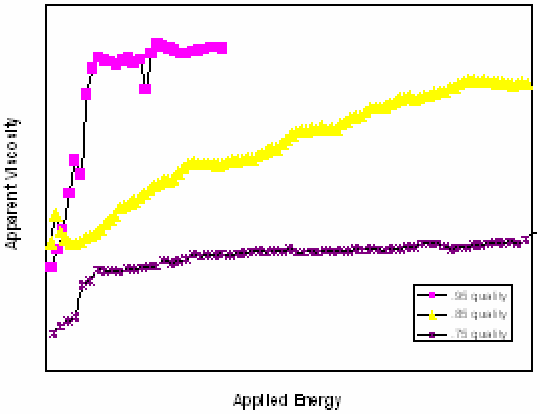

Fig. 8.8 Apparent viscosities as a function of applied energy

Preliminary experimental results presented in Figs. 8.7 and 8.8 demonstrated a potential relationship between applied shear energy, the statistical description of foam, and its rheological performance: i) that bubble size decreases with added shear energy (Fig. 8.7) and becomes asymptotic at some size that is a function of foam quality, and ii) foam apparent viscosity at a given shear rate increases with added shear energy (Fig. 8.8) and becomes asymptotic at some value that is a function of bubble size. These two graphs are intentionally shown here without units because the torque meter for the foam generator was not operative at the time. These experimental values are only approximate readings, although they should properly indicate the trend of the data.

8.5 RHEOLOGICAL MEASUREMENTS WITH A SMOOTH CUP AND ROTOR

Rheologies of foams with surfactant concentrations of 0.5%, 1%, and 2% were tested with the viscometer using a smooth cup and rotor. Test foam was generated by using the Dynamic Testing Facility (DTF). DTF is an apparatus primarily designed for the purpose of creating foam and studying it under dynamic conditions. A detail of this facility is presented in Section 11. DTF design parameters are:

Flow Rate:	1.8 – 23 gpm
Main Loop Volume:	6 gallons
Loop Construction:	1-1/2” steel pipe
Maximum Operating Pressure:	150 psi
Operating Temperature:	Ambient

8.5.1 TEST MATRIX

A test matrix, presented in Table 8.2, was devised to identify the experiments to be performed. According to this test matrix, three types of foam formulations were used. The basic surfactant (FF4000) was provided by Bachman Drilling and Production Specialties, Inc. The FF4000 is an ethoxy alcohol ether sulfate $[C_nO(CH_2CH_2O)_xSO_3\text{-}NH_4^+]$, which is widely utilized in underbalanced drilling. In this experiment, concentrations of 0.5%, 1.0% and 2.0% per volume of water were used to provide a variety of foams. The qualities of these foams were 70%, 75%, 80%, and 85%. The average bubble size was approximately 53 microns. The cup and rotor were smooth except for 0.025 inch of roughnesses added around magnet and at the bottom of the cup. It is important to allow enough foam to flow through the viscometer to eliminate the effect of drainage, but not flow so fast that a considerable helical flow pattern is formed inside the viscometer.

Table 8.2 Test matrix for Rheological Measurements

	Test #1	Test #2	Test #3
Foam Formulation	0.5% F4000 by volume	1% F4000 by volume	2% F4000 by volume
Quality	70, 75, 80, 85	70, 75, 80, 85	70, 75, 80, 85
Bubble Size	53 microns	53 microns	53 microns
Wall Roughness	Smooth except around magnet and bottom of cup	Smooth except around magnet and bottom of cup	Smooth except around magnet and bottom of cup

8.5.2 DETERMINING THE OPTIMUM FLOW RATE OF FOAM

Figure 8.9 is a simplified of schematic the DTF together with the viscometer. The needle valve, V1, controls the flow of foam through the viscometer. From this experiment, it was determined that the needle valve should be set at 15 turns closed. In order to determine the optimum flow rate, 80% quality foam was generated in the DTF and torque measurements in the viscometer were recorded while opening and closing the valve. The shear rate was set at a desired rate for 30 minutes. The test began at 0 minutes with needle valve V1 completely open.

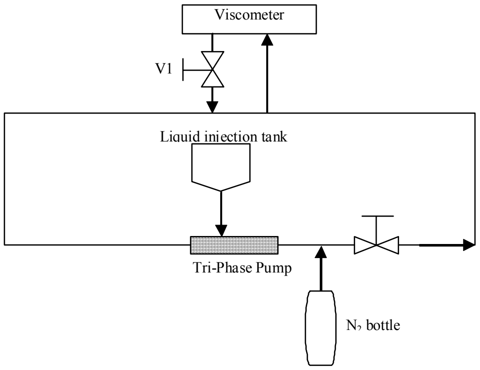

Fig. 8.9 Schematic of RS300 connected to DTF

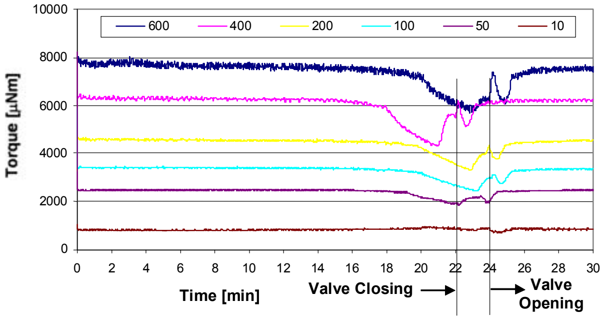

Fig. 8.10 Torque reading versus time (number of turn)

It requires 22 turns to completely close this needle valve. While watching a clock, every minute the needle valve was closed one turn until it was closed completely. At this point, the needle valve was left completely closed for another minute to watch the effect on the foam. Then the needle valve was opened one turn every minute, until the 30-minute run was complete. This experiment was run for shear rates of 600, 400, 200, 100, 50, and 10 sec-1. The experiment was repeated for shear rates of 600, 400, 300, 200, 50 and 10 sec-1. Figure 8.10 presents the results of the test with shear rates of 600, 400, 200, 100, 50, and 10 sec-1. When needle valve, V1, reached the completely closed point, the foam could be seen collapsing (Fig. 8.10), resulting in a large drop in the torque readings. As the needle valve was reopened, fresh foam began to displace the collapsed foam.

8.5.3 BUBBLE SIZE ANALYSIS

In order to measure bubble size, photographs of foams were captured through a viewport in the DTF using a CCD camera together with a microscope. The procedure includes:

- Aligning the microscope (Nikon SMZ800) with the glass view port cell on the DTF;
- Capturing a microscopic image with a CCD camera attached to the microscope;
- Transferring this image to a computer with a frame grabber;
- Determining bubble sizes measured from images on an 8 ½ x 11 piece of paper;
- Evaluating the average bubble size from at least 100 bubbles.

From the picture of the bubbles, a ruler was used to measure the comparative sizes of the bubbles. Measurements were recorded and put into a spreadsheet to determine the average bubble size, taking into consideration the magnification. A summary of bubble size analysis during the test is presented in Table 8.3. Bubble size distribution of the foam samples is shown in Fig. 8.11.

Table 8.3 Summary of Bubble Size Analysis

Quality [%]	68.1	74.7	74.8	79.0	78.4
Valve position [turns open]	1.5	1.5	1.5	1.5	1.5
Flow Rate Pump [gpm]	6.8	6.8	6.8	6.8	6.8
Mean bubble size [µm]	65	52	47	53	49
Std. Dev. [µm]	24	20	19	23	19

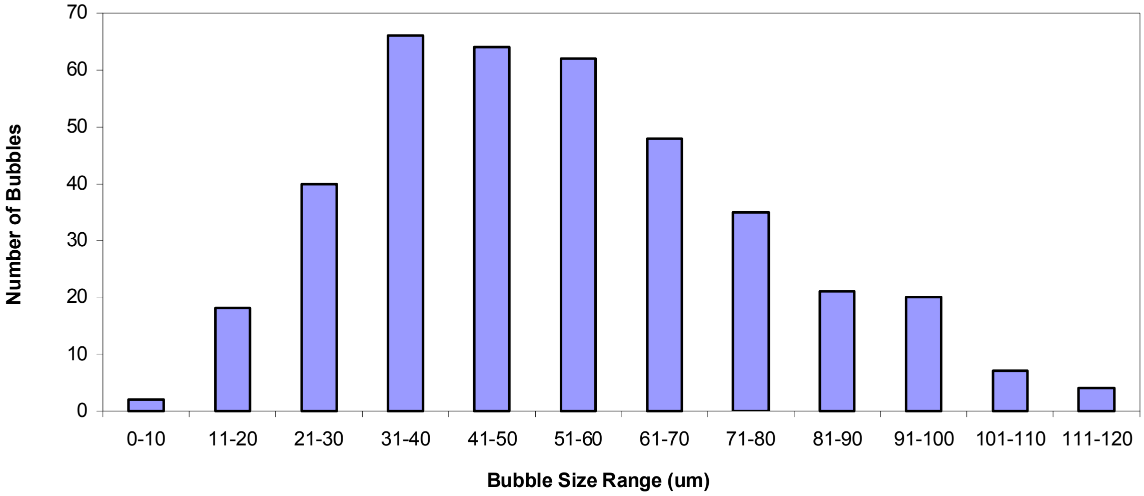

Fig. 8.11 Test foam bubble size distribution

8.5.4 FOAM QUALITY MEASUREMENT

The DTF Foam Quality Measurement Cell is used to determine the gas to liquid ratio of the foam being generated in the DTF. The procedure for using this device is:

1. Fill the Foam Quality cell (FQ cell) completely with water;
2. Attach the FQ cell to the DTF. Be sure that the FQ cell is vertical and that the attachment to the DTF is at the top of the cell;
3. Open the valve to the DTF;
4. Open the ball valve on the top of the FQ cell;
5. Slowly open the needle valve on the bottom of the FQ cell until a slow stream of water is attained;
6. Once foam begins to slowly exit from cell, continue until foam is a continuous stream (≈ 5 sec after foam first appears). Do not let foam “jet” from cell;
7. Close all valves and detach the FQ cell from the DTF;
8. Remove foam from the inlet and outlet ports of FQ cell;
9. Weigh the FQ cell filled with foam and calculate the foam quality

8.5.5 RHEOLOGY TEST RESULTS

Rheologies of foams with surfactant concentrations of 0.5%, 1%, and 2% were tested with the viscometer using a smooth cup and rotor. The tests were repeated three times in order to determine a procedure to obtain reliable results. Measured data from the first and the second sets were skewed due to inexperience and inadequate procedures. Finally, necessary procedural modifications were made to get consistent viscosity trends. The procedural modifications include:

- Changing the needle valve, V1, from 18-turn closed to 15-turn closed position to avoid the breakdown of foam.
- The corrosion inhibitor was more completely drained from the DTF by draining the Tri-phase pump and the low pressure side of the pump.
- Before beginning on the viscosity tests, (after the foam quality is correct for the test and the pressure drop is established) shear stress is measured at a constant shear rate to confirm that the foam is stable and gives a constant viscosity.

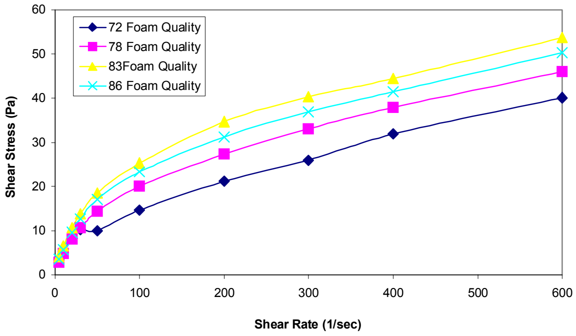

Fig. 8.12 Shear stress vs. shear rate for aqueous foams at different qualities (0.5% Surfactant)

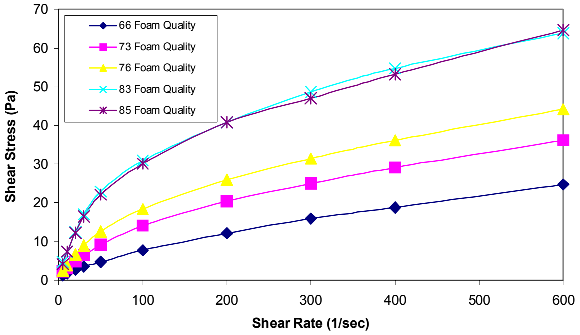

Fig. 8.13 Shear stress vs. shear rate for aqueous foams at different qualities (1% Surfactant)

After the necessary procedural modifications, testing with foams was performed using the viscometer. The rheologies of aqueous foams with different surfactant concentration (0.5%, 1.0%, and 2.0%) were measured with the “smooth” (the cup and rotor with roughness only around the magnet and on the bottom of the cup) set of the cup and rotor. Figures 8.12, 8.13, and 8.14 illustrate the rheology data collected after the modifications. For 0.5% surfactant concentration foams, Fig. 8.12 shows that the shear stress curves steadily increase as the quality increases. However, for 1% and 2% surfactant concentration foams the graphs (Fig. 8.13 and 8.14) show that the shear stress curves steadily increase as the quality increases until the quality reaches a certain value (≈ 83%). Figure 8.15 presents measured rotational torque as a function of foam quality for different surfactant concentrations at a given rotational speed (shear rate). The tests showed an interesting parabolic shape at high foam qualities (≈ 83%).

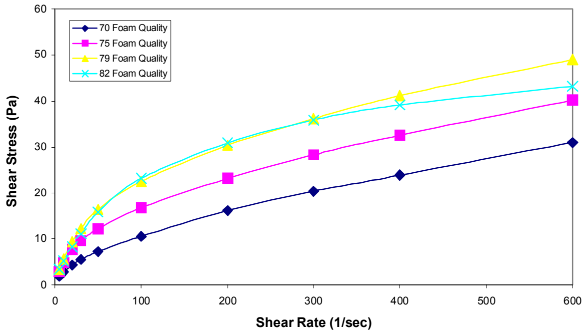

Fig. 8.14 Shear stress vs. shear rate for aqueous foams at different qualities (2% Surfactant)

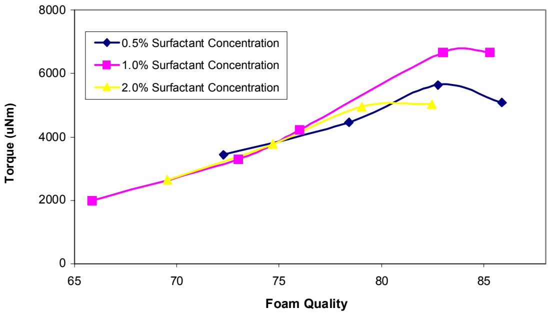

Fig. 8.15 Torque versus foam quality at a shear rate of 200 sec^{-1}

8.5.6 DISCUSSION

The cups and rotors were machined to produce a uniform, reproducible roughness to the outside of the rotor and the inside of the cup. The original gap inside the viscometer remained unchanged. Samples of surface roughness were made in order to decide the best roughnesses to begin with compared to the bubble sizes in the foam that will be used. A surface roughness measuring instrument was purchased. Also, the viscometer was set up and calibrated.

The preliminary foam rheology tests were performed in order to help determine a final procedure, while four new cups and rotor sleeves were being machined with rough surfaces. A surface roughness of 0.025 inch was applied to the rotor magnet and the bottom of the cup. Drainage grooves were also machined to the bottom of the cup to promote drainage of liquid that occurs as a result of foam decay. The first two rotor sleeves and cups have surface roughnesses of 0.025 inch and 0.010 inch, respectively. The remaining two rotor sleeves and cups will remain smooth for the time being until experimentation indicates whether smoother or rougher surfaces are necessary. This task will be part of a future project.

Testing with foams was performed on the DTF. The 0.5%, 1.0%, and 2.0% concentrations of foam were tested on the “smooth” set of the cup and rotor. It is believed that slip or breakage of the foam could cause the parabolic graph that occurs when foam quality is plotted versus torque (Refer to Fig. 8.15). The torque values increase as foam quality increases until a certain point where the torque values begin to decline. This will be verified when testing with the rough surfaces is completed in a future project. If slip is important, adding roughness to the surfaces of the cup and rotor should increase the torque, especially at higher shear rates because the slip layer will be removed and the foam will be in direct contact with the surface of the cup and rotor. If adding roughness makes no difference, then other factors must be considered, such as whether the particular surfactant we used is too unstable and breaks down at high foam quality. Testing foams made from a variety of surfactants could test this hypothesis.

The 1% surfactant concentration appears to be optimal in this experiment due to the highest viscosity readings. The 0.5% and 2% surfactant concentration viscosity results for foam qualities of 70-85% were considerably lower. One possible explanation for this can be described in two parts: i) the surface tension of the liquid phase; and ii) the foaming ability of the surfactant concentration added. In the 0.5% surfactant concentration, the surface tension of the liquid phase is high due to the small amount of surfactant added, but the foaming ability is low. The opposite is true for the 2% surfactant concentration; the surface tension of the liquid phase is low due to the large amount of surfactant added, but the foaming ability is high. The 1% surfactant concentration shows the highest viscosity readings because the surface tension of the liquid phase is not significantly weakened due to an over abundance of surfactant, yet it still has an adequate amount of foaming ability to create a stable foam. Further experimentation is needed to better understand these results.

The data collected after the procedural modifications were made was analyzed based on a Power Law fluid model. There is not agreement among rheologists on whether foam is a Power Law fluid or a Yield Power Law fluid. However, in this experiment, at a shear rate of 5 sec-1 a shear stress greater than 5 Pa was not recorded. Therefore, if this foam has yield stress, it is very small. Due to this fact, any yield stress was neglected.

The issue of end effects was then considered. Due to the large gap difference between the bottom of the cup and the bottom of the rotor in comparison with the 2 mm gap between the side of the rotor and the side of the cup, the bottom end effects were neglected. The same was done for the end effects due to the gap between the lid and the top of the rotor. Power Law fluids are based on the equation, $\tau = k\,\gamma^n$. In order to find n and k, log τ was plotted versus log $\dot{\gamma}$ as shown in Figs. 8.16, 8.17, and 8.18. Due to the approximately straight lines in these plots, the data appears to fit the Power Law model relatively well. The slope of this line is equal to n and the y-intercept is equal to log k. Therefore, $k = 10^b$, where b is the y-intercept. Figure 8.19 shows that the sheer thinning ability of the fluid increases with increasing foam quality for the 1% surfactant concentration, yet the trend is not well defined for the 2% and 0.5% surfactant concentrations.

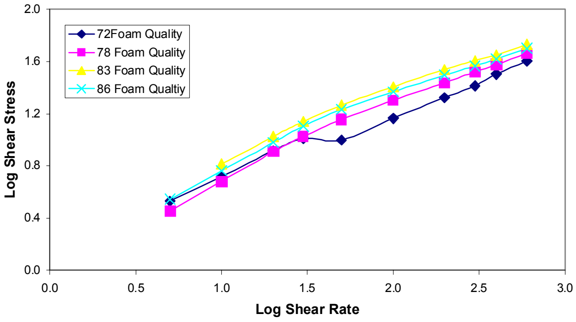

Fig. 8.16 Shear stress vs. shear rate plots for 0.5% surfactant foams at different qualities

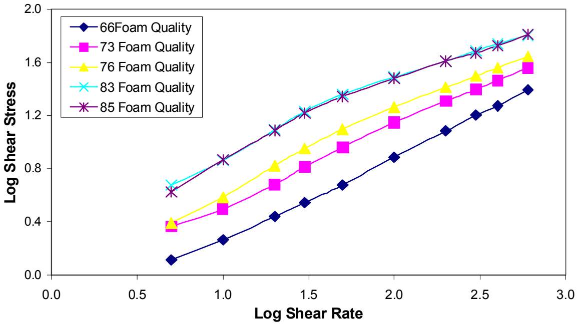

Fig. 8.17 Shear stress vs. shear rate plots for 1% surfactant foams at different qualities

As previously mentioned, the best results were obtained using the 1% surfactant concentration. Further testing is needed to better interpret these results. Figure 8.20 illustrates that the consistency index of the foams increases as the foam quality increases from 70-85%.

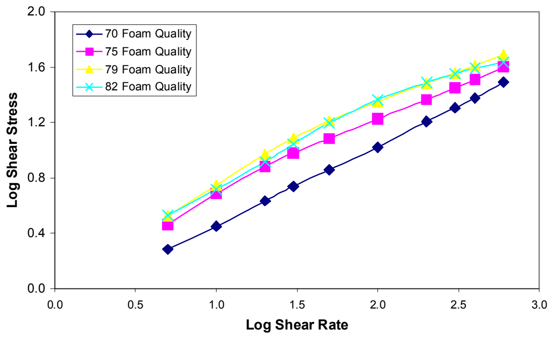

Fig. 8.18 Shear stress vs. shear rate plots for 2% surfactant foams at different qualities

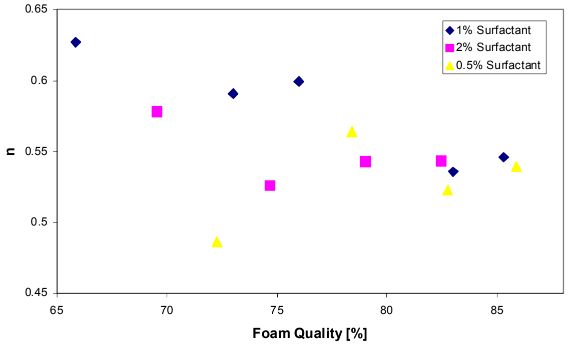

Fig. 8.19 Power law exponent versus quality for different surfactant concentrations

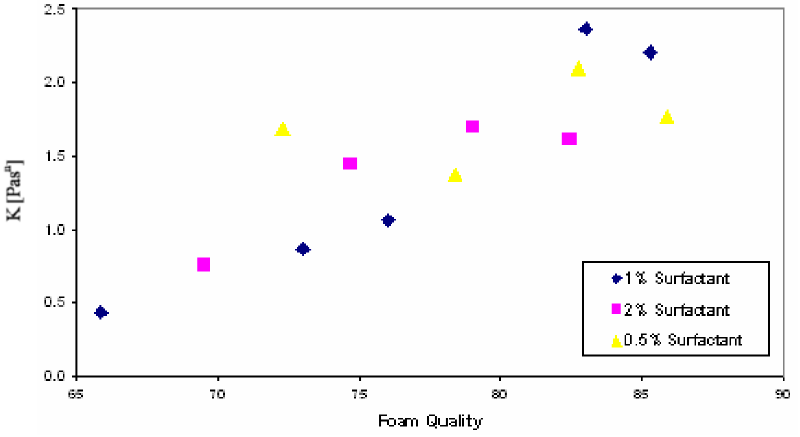

Fig. 8.20 Consistency index, k, versus foam quality at different surfactant concentrations

8.5.7 SUMMARY

- Calibration of the viscometer was performed using standard calibration oils;
- Procedures for using the RS300 and the Dynamic Testing Facility with flowing foam were developed;
- Two new cups were machined with 0.025 inches and 0.010 inches surface roughnesses;
- One smooth lid, two smooth cups, and four smooth rotor covers were machined;
- Preliminary foam tests with the Dynamic Test Facility flow loop were completed;
- Non-linear torque vs. shear rate was observed for various foam qualities;
- Foam testing with the DTF and the “smooth” cup and rotor under ambient conditions were completed;
- Rheology measurements for dynamic foam using a rotational viscometer were obtained. No measurements of this kind have been previously reported in the literature;
- Power Law fluid model was used to describe foam rheology measurements.

8.6 RHEOLOGY MEASUREMENT USING ROUGHENED CUP-ROTOR ASSEMBLIES

In this study, the newly-developed foam generator/viscometer, which is presented in Section 8.4, was used to generate different quality foams. Surfactant (Weatherford KLEAN-FOAM™) concentration in the liquid phase for all the tests was 1 percent by volume. Rheologies of foams were measured using three different cup-rotor assemblies that have different surface roughness. The relationship between surface roughness and foam rheology was investigated.

8.6.1 TEST PROCEDURE

The rheology tests consisted of foam generation, rheology and bubble size measurements. The tests were performed at different foam qualities and cup-rotor assemblies. The test procedure includes:

1. Filling the foam generator with the required amount of liquid phase using the liquid injection pump (Fig. 8.4b);
2. Injecting the required amount gas phase into the foam generator;
3. Starting the viscometer and its accessories;
4. Generating foam using the propeller-type mixer;
5. Adjusting the needle valve, V14 (Fig. 8.3) and using an electronic balance to maintain optimum foam flow rate (approximately 15 ml/min) through the viscometer;
6. Measuring the shear stress at different shear rates;
7. Closing V12 and opening V11 to take foam pictures, when the rheology test is completed;
8. Closing V14 and switching off the mixer and taking foam pictures using the CCD Camera.

8.6.2 TEST MATRIX

The test matrix for foam rheology measurements is shown in Table 8.4. According to this test matrix, test pressure and temperature were constant. The wall roughness of the cup and rotor were varied to investigate the effect of roughness on the slip velocity. Measurements were made at different foam qualities to determine the effect of quality on foam rheology and wall slip. Five foam qualities (70%, 75%, 80%, 85%, 90%) were considered during the test. All foams were generated using the foam generator with the almost identical mixing time, so that for each given foam quality, equilibrated foam is generated before the rheology measurement.

Another important issue during the test was how to maintain optimum foam flow rate through the viscometer. On one hand, it is important to allow enough foam to flow through the viscometer to eliminate the effect of foam drainage on the measurements; on the other hand, flow rate can not be too fast to allow the axial shearing of the foam inside the viscometer. The optimum foam volume flow rate (approximately 15 ml/min) is obtained and controlled for each foam quality, based on the criteria of nominal axial shear rate less than 1

s^{-1} at the wall and an average foam residence time of 4 min in the viscometer. Our previous aqueous foam drainage experiments indicate that the half life times of the test foams under static conditions are in the range of 10 to 12 minutes. Therefore an electronic balance shown in Fig. 8.3 is used to determine mass flow rate of foam passing through the viscometer. By controlling the needle valve, V14, the foam flow rate is maintained at the desired level.

Table 8.4 Test Matrix for Foam Generator/Viscometer Rheology Measurements

Wall Roughness	**Smooth**	**Roughness #1***	**Roughness #2***
Quality	70%, 75%, 80%, 85%, 90%	70%, 75%, 80%, 85%, 90%	70%, 75%, 80%, 85%, 90%
T (°C)	25	25	25
P (psig)	25	25	25

* Details of roughness measurements are presented in Table 8.1.

8.6.3 CALIBRATION TEST

The purpose of calibrating this viscometer using viscosity standards is to correct for end effects and bearing drags. The end effects have a tendency to increase measured torque due to the shearing of the fluid between the space above and below the rotor inside the cup (Fig. 8.1b). The viscometer readings are based on the measured torque acting on the rotor. In addition to the size and geometry of the rotor, properties of the test fluid, the end effects, and bearing drag all affect the torque measurements. The basic purpose of a calibration test is to quantify the magnitude of the end effects and bearing drag so that they can be subtracted from the reading in order to obtain the actual torque required to shear the fluid in the gap. In addition, the calibration test helps to verify that the instrument is functioning properly.

Four viscosity standards (calibration oils from Canon Instrument) with nominal viscosity 50 cP, 100 cP, 200 cP and 500 cP were used to calibrate the smooth cup-rotor assembly. This range of viscosity (i.e. 50 to 500 cP) covers most of the viscosity range of aqueous foams. Using the calibration oils, thirteen different viscosity data points (Table 8.5) were measured to calibrate the viscometer. Measured and calculated torques were compared. A calibration curve for each shear rate was prepared.

The viscometer was calibrated at shear rate of 1000, 600, 400, 300, 200, 100, 50, 30, 20 and 10 s^{-1}. As expected, the measured torque is higher than the calculated torque for all the shear rates. The calibration curve used for correcting the measured data at shear rate of 400 s^{-1} is presented in Fig. 8.21. Similar curves are prepared to correct the measured torque at each given shear rate.

After the calibration, corrected torques can be obtained from these curves. In a foam test, each measured torque corresponds to a corrected torque and once the corrected torque is obtained, corrected shear stress can be obtained. A computer code was developed to interpolate between calibrated data points from the curve.

A limited number of calibration tests was performed using the roughened cup-rotor assemblies to determine the effect of roughness and rotor weight on the calibration curve. Calibration oil with 200 cP nominal viscosity was used for testing roughened cup-rotor assemblies at 20 and 40°C. Theoretically, without wall slip the measurement should be the same for all the cup-rotor assemblies. Fig. 8.22 shows the measured torque using different cup-rotor assemblies as a function of shear rate for different viscosity standards. Approximately identical torque readings were recorded, which indicates that the cup-rotor assemblies are geometrically more or less identical and have the same friction drags. Therefore, any torque measurement difference resulting from different cup-rotor assemblies is most probably due to other factors.

Table 8.5 Viscosity Standards Used for Calibrating the Viscometer

Nominal Viscosity (cP)	True Viscosity (cP)	Temperature (°C)
50	52.98	20.0
	43.31	30.0
	29.98	50.0
	21.58	70.0
100	105.4	20.0
	71.14	40.0
200	206.7	20.0
	170.32	29.6
	139.3	40.0
	116.7	50.0
	78.01	75.0
500	520.0	20.0
	349.5	40.0

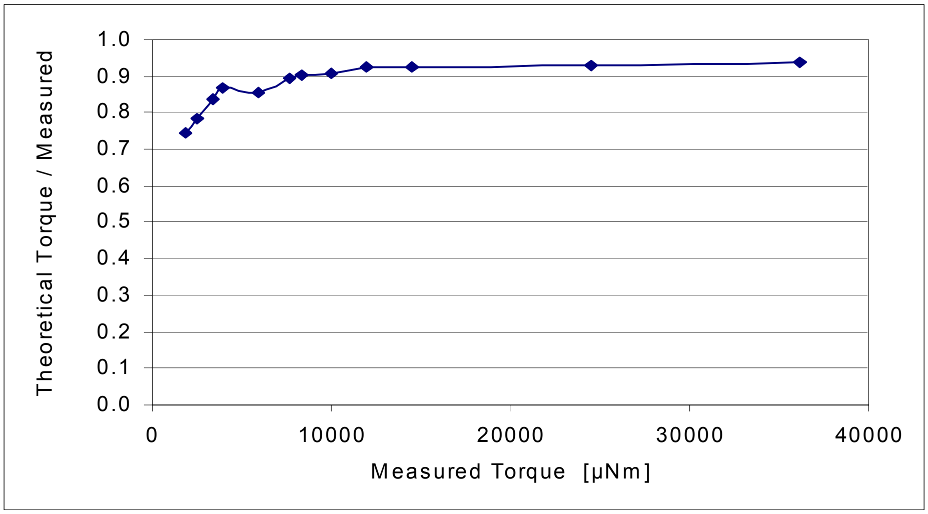

Fig. 8.21 Calibration curve obtained at 400 s^{-1} shear rate

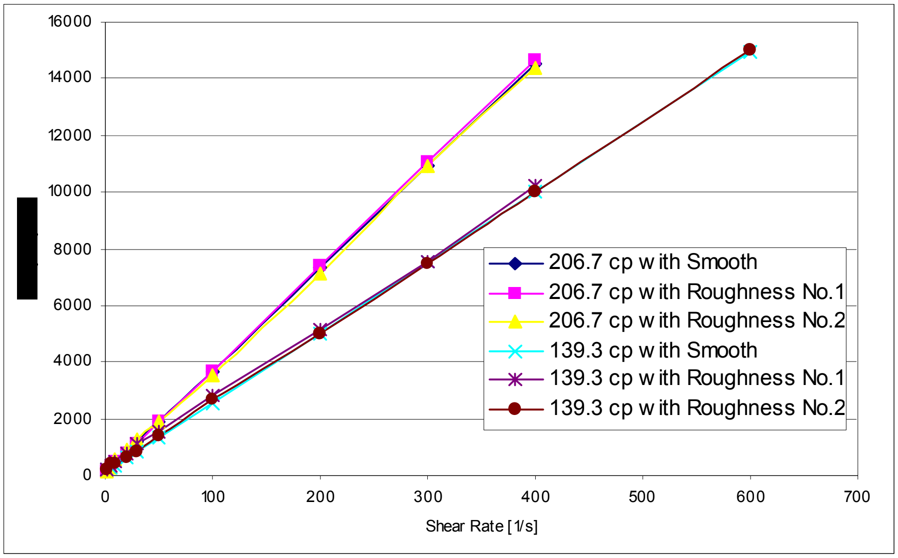

Fig. 8.22 Measured torques vs. shear rate for different cup-rotor assemblies

8.6.4 RESULTS AND DISCUSSION

The viscosity of dynamic foam was tested using smooth and roughened cup-rotor assemblies. Measured shear stress readings were corrected using the calibration curves presented previously. Fig. 8.23 shows foam rheology measurements obtained using smooth cup-rotor assembly. Generally foam behaves like a shear thinning fluid and apparent foam viscosity increases with foam quality. Similarly rheology measurements are presented in Fig. 8.24 that were obtained using roughened cup-rotor assembly (Roughness No. 1). It is apparent from the figures that at a given shear rate the shear stress measured with the roughened cup-rotor assembly is considerably higher that the smooth assembly. This shows the presence of wall slip since the only difference between these two cup-rotor assemblies is their roughness.

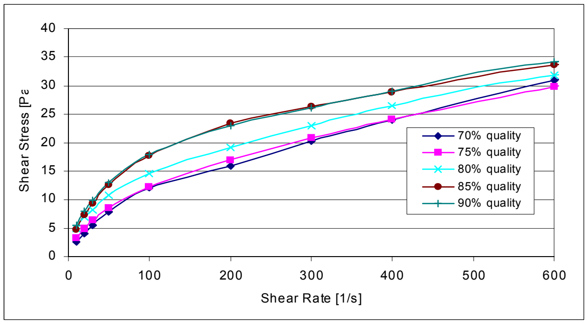

Fig. 8.23 Foam rheology measured using smooth cup-rotor assembly

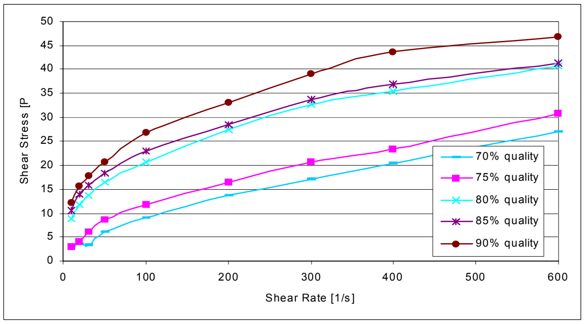

Fig. 8.24 Foam Rheology measured using roughened cup-rotor assembly (Roughness No. 1)

It appears that measuring foam rheology with a smooth rotational viscometer underestimates the apparent foam viscosity; therefore measurements obtained using smooth and roughened cup-rotor assemblies are necessary to determine the wall slip effect and the correct rheology. Here the question is what level of roughness is sufficient to determine the wall slip. In order to get the effect of roughness on foam rheology, measurements were performed using a more roughened cup-rotor assembly (Roughness No. 2). Figure 8.25 shows flow curves of foams measured using the more roughened cup-rotor assembly. The result shows that most of these measurements are less than the measurements obtained using the other roughened cup-rotor assembly (Roughness No. 1).

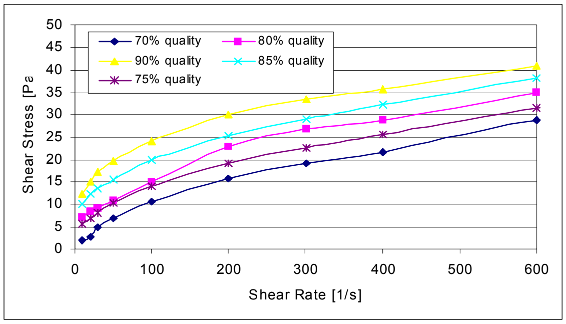

Fig. 8.25 Foam rheology measured using very rough cup-rotor assembly (Roughness No. 2)

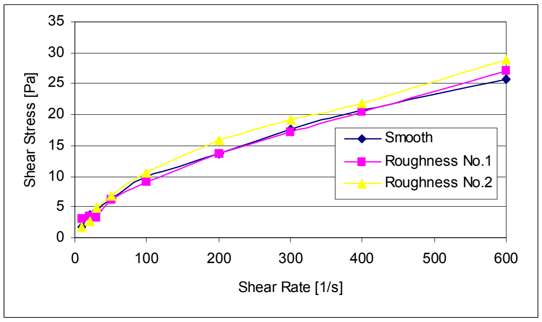

Fig. 8.26 Flow curves of 70% quality foam measured using different cup-rotor assemblies

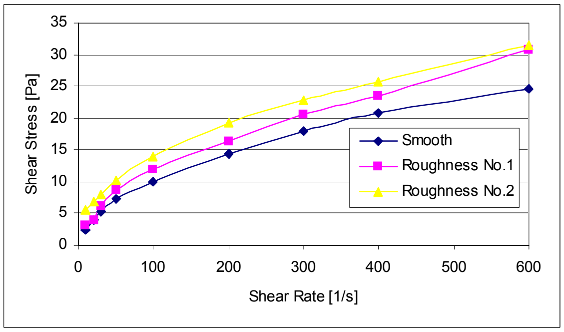

Fig. 8.27 Flow curves of 75% quality foam measured using different cup-rotor assemblies

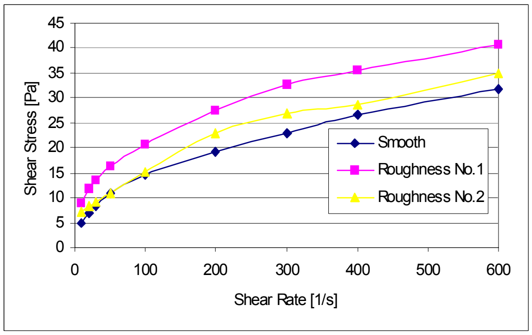

Fig. 8.28 Flow curves of 80% quality foam measured using different cup-rotor assemblies

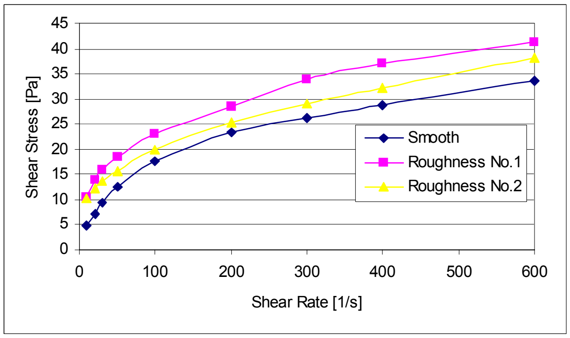

Fig. 8.29 Flow curves of 85% quality foam measured using different cup-rotor assemblies

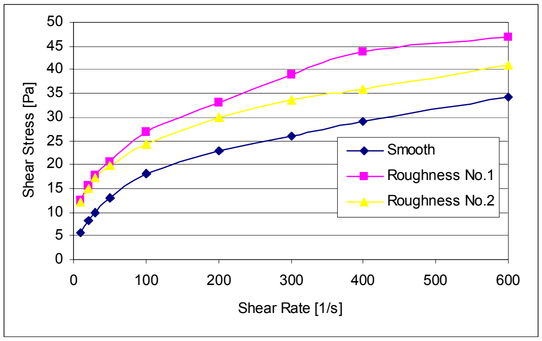

Fig. 8.30 Flow curves of 90% quality foam measured using different cup-rotor

Figures 8.26 through 8.30 show the measured shear stress versus shear rate for a given quality foam. In each plot, there are three flow curves, representing rheology measurements obtained using the three different cup-rotor assemblies that have different surface roughnesses. At a given shear stress, a distinct difference in shear rate is observed. These variations could be due to the wall slip. For foam quality greater than 75%, measurements obtained using the most roughened cup-rotor assembly (Roughness No. 2) is less than measurements with Roughness No. 1. This is an unexpected result. In depth investigation of this phenomenon is necessary to present a more scientific reasoning for this observation.

REFERENCES

1. Gucuyener, I. Haaki, Mustafa Versan Kok and Taner Batmaz. “End Effect Evaluation in Rheological Measurement of Drilling Fluids Using Coutte Coaxial Cylinder Viscometer.” Energy Sources, 24, 2002, 441-449.
2. Herzhaft, Benjamin. “Correlation between Transient Shear Experiments and Structure Evolution of Aqueous Foams”, Journal of Colloid and Iinterface Science, 247, 2002, 412-423.
3. Hu, Hua, R. G. Larson and J.J. Magda. ”Measurement of wall-slip-layer rheology in shear-thickening wormy micelle solutions.” Journal of Rheology, 46, 2002, 1001-1021.
4. Kakadjian, Sarkis and Benjamin Herzhaft. ”Hp/Ht rheology of Aqueous Compressible Fluids for Underbalanced Drilling Using A Reirculating Rheometer.” Society of Petroleum Engineering, SPE 80207, 2003.
5. Khan, Saad A. and R.C. Armstrong. “Rheology of foams: I. Theory for dry foams.” Journal of Non-Newtonian Fluid Mechanics, 22, 1986, 1-22.
6. Lummus, James L. and J.J. Azar. Drilling Fluids Optimization: A Practical Field Approach. PennWell, Tulsa. 1986.
7. Schramm, Laurier L. and Fred Wassmuth. Foams: Fundamentals and Applications in the Petroleum Industry American Chemical Society, 1994.
8. Steffe, James F. Rheological Methods in Food Processing Engineering. Freeman Press, East Lansing, 1996.
9. Sani, Abu M. and Subhash N. Shah. “Experimental Investigation of Xanthan Foam Rheology.” SPE 67263. 2001.
10. Martins, A. L., A. M. F. Lourenco, C. H. M. Sa, and V. Silva Jr. “Foam Rheology Characterization as a Tool for Predicting Pressures While Drilling Offshore Wells in UBD Conditions.” SPE/IADC 67691. 2001.
11. Hutchins, Richard D., and Matthew J. Miller. “A Circulating Foam Loop for Evaluating Foam at Conditions of Use.” SPC 80242. 2003.
12. Khade, Sudhakar D., and Subhash N. Shah. “New Rheological Correlations for Guar Foam Fluids.” SPE 80895. 2003.
13. Fredd, Christopher N., Matthew J. Miller, and Baudel W. Quintero. “Impact of Water-Based Polymer Fluid Characteristics on CO2 Foam Rheology.” SPE 86493. 2004.
14. Harris, Phillip C. and Stanley J. Heath. “High Quality Foam Fracturing Fluid.” SPE 35600. 1996.
15. Harris, P.C. “Effects of Texture on Rheology of Foam Fracturing Fluids.” SPE 14257. 1985.
16. Louenco, A.M.F., (2002). “Study of Foam Flow Under Simulated Downhole Conditions”, MSc Thesis, Univ. of Tulsa.
17. Skelland, A.H.P. Non-Newtonian Flow and Heat Transfer. John Wiley & Sons, Inc. New York. 1967.
18. David, Amiel. “The Rheology of Foam.” A Dissertation Submitted to the Department of Petroleu Engineering and the Committee on the Graduate Division of Stanford University in Partial Fulfillment of the Requirements for the Degree of Doctor of Philosophy. November 1968.

9. Study of Cuttings Transport with Aerated Mud under Elevated Pressure and Temperature Conditions (Task 10)

ABSTRACT

Aerated mud experiments were conducted at elevated pressures and elevated temperatures (EPET) in ACTF flow loop. During test runs, water and air flow rates were in the range of 50-250 gal/min (0.19-0.95 m^3/min) and 50-150 scf/min (1.42-4.25 m^3/min); and measurements of frictional pressure drop and mixture density over the entire annular section were carried out. Stratified and slug flow were the two flow patterns observed over the range of the chosen test matrix. The experimental results indicate that temperature influences the two-phase flow patterns and frictional pressure losses.

Cuttings transport experiments were carried out at elevated pressures and temperatures ranging from 185 to 500 psi (1.27-3.45 MPa) and 80 to 175°F (27-80°C). The following test parameters were measured: i) cuttings weight in the annulus (the volumetric cuttings concentration); ii) mixture density; and iii) frictional pressure losses. The results clearly show that temperature, in addition to the liquid and gas flow rates, considerably affects the cuttings transport efficiency of aerated muds. The volume of cuttings which accumulated in the annulus was very sensitive to the liquid flow rate. Predominately, elevated temperature was found to cause a significant increase in the cuttings volumetric concentration at given flow conditions. The injection of air has both negative and positive effects on cuttings transport, depending on other flow parameters. The effect of pressure on cuttings concentration and frictional pressure loss is insignificant.

The mechanistic model for cuttings transport with aerated mud is developed by combining two-phase hydraulic equations, turbulent boundary layer theory and particle transport mechanism, which can be useful for predicting the cuttings volumetric concentration in the annulus and critical pressure drop for preventing cuttings from deposition. Predictions of the mechanistic model are in agreement with measured data.

9.1 INTRODUCTION

The need for technologies to reduce cost and improve recovery from existing hydrocarbon reserves is well known. One of the most effective methods of cost reduction relies on improvements in drilling technologies. Particularly, development of UBD technology is beneficial for drilling partially depleted reservoirs and re-entry wells. During conventional (overbalanced) drilling, mud filtrate penetrates the near-wellbore formation because of high equivalent circulation density (ECD). This alters near wellbore pore-flow properties. As a result, well productivity decreases significantly. As a result, UBD is often used to minimize problems associated with formation damage, lost circulation and differential sticking. It has great potential to reduce drilling time and cost. High rates of penetration and longer bit life can be obtained using UBD. This technology is also important in offshore, deep water drilling to avoid fracturing of unconsolidated formations.

In field applications, many different techniques are available for achieving underbalanced conditions. These mostly involve circulating low density fluids such as aerated mud. Nonetheless, multiphase flow behavior of aerated muds is complex and it is difficult to predict cuttings transport efficiency of aerated muds. As a result, cuttings accumulate in the borehole when this technique is applied. In-situ concentration of cuttings in the wellbore is not equal to the concentration near the drill bit. Similarly, in-situ gas mass fraction is not the same as the injection gas mass fraction. This will significantly affect flow behavior of the fluid. Using low density fluids alone does not always guarantee underbalanced conditions. Excessive frictional pressure loss due to poor hole cleaning may result in overbalanced conditions even with low density fluids. Therefore, transport mechanisms of cuttings with aerated fluids should be well understood to control ECD and optimize hole cleaning and hydraulics.

Several solids transport models have been proposed in the literature to predict solids transport in pipe flow. However, very few of them are related to aerated muds. Compared to pipe flow, little work has been done for flow through annuli. To our knowledge, no studies are in the literature concerning cuttings transport using aerated fluids at elevated pressures and elevated temperatures. Major objectives of this study are:

1. Development of two-phase flow model for aerated fluids under elevated pressure and temperature conditions inside an annulus in a horizontal position without pipe rotation;
2. Investigation of the cuttings transport ability of aerated fluids under elevated pressure and temperature conditions;
3. Determination of the gas/liquid flow rates for effective cuttings transport;
4. Development of a computational tool to predict frictional pressure losses in aerated mud flows under elevated pressure and temperature conditions.

9.2 MATHEMATICAL MODELING

9.2.1 MODELING HYDRAULICS OF AERATED MUD FLOWS

Flow Pattern Transition Criteria

For a given flow of aerated mud in a pipe or annular space, four different flow configurations (patterns) are often considered: stratified flow (smooth or wavy), slug flow, dispersed bubbly flow and annular flow. Assessment of the flow regime occurring under borehole conditions is necessary for an accurate prediction of the wellbore hydraulics. An important aspect of assessing a flow regime involves consideration of the boundaries between regimes and how one flow regime transitions or changes into one or more different regimes.

Stratified to Non-Stratified Flow. The criterion for the transition from stratified flow to non-stratified flow is based on Kelvin-Helmholtz stability analysis. It predicts whether a small disturbance on the surface will lead to the interface being stable, wavy, or unstable with wave growth that destroys the stratification. According to this analysis, the governing mechanisms are the gravity and surface tension forces that tend to stabilize the flow; however, the relative motion of the two layers creates a suction force that tends to destroy the stratified structure. Based on this approach the following mathematical criterion can be stated:

$$\begin{cases} Stratified, Vg < \left(1-\dfrac{h_L}{D}\right)\sqrt{\dfrac{(\rho_L-\rho_G)g\cos\theta A_G}{\rho_G S_i}} \\ Non-stratified, Vg > \left(1-\dfrac{h_L}{D}\right)\sqrt{\dfrac{(\rho_L-\rho_G)g\cos\theta A_G}{\rho_G S_i}} \end{cases} \qquad (9.1)$$

Slug to Annular Flow. When the gas or the liquid flow rate increases, the stratified flow structure becomes unstable and transition from stratified to non-stratified occurs. It is suggested that the transition from slug to annular flow depends exclusively on the liquid level in the pipe. Intuitively, a value of $h_L/D = 0.5$ was proposed for this transition. Recent studies modified this value to 0.35 to account for the fact that the slug body does not consist of liquid only, resulting in the following criterion:

$$\begin{cases} Annuular, \left(\dfrac{h_L}{D}\right) < 0.35 \\ Slug, \left(\dfrac{h_L}{D}\right) \geq 0.35 \end{cases} \qquad (9.2)$$

Slug to Dispersed Bubbly Flow. This transition occurs at high liquid flow rates. The mechanism involves turbulent fluctuations in liquid phase that are strong enough to overcome the net buoyant forces which tend to retain the gas as a pocket at the top of the pipe. Thus, the criterion is expressed as follow:

$$\begin{cases} Slug, V_L \leq \sqrt{\dfrac{4A_G g\cos\theta}{S_i f_L}\left(1-\dfrac{\rho_G}{\rho_L}\right)} \\ Dispersed.Bubble, V_L > \sqrt{\dfrac{4A_G g\cos\theta}{S_i f_L}\left(1-\dfrac{\rho_G}{\rho_L}\right)} \end{cases} \qquad (9.3)$$

According to the proposed models, flow pattern transition boundaries for horizontal flows can be determined by the following steps:

1. Estimating equilibrium liquid level (h_L);
2. Checking stratified to non-stratified transition boundary (Eq. 9.1);
3. If flow is not stratified, checking the transition to annular flow (Eq. 9.2);
4. If the flow is not annular, checking the slug to dispersed bubble transition boundary (Eq. 9.3).

Liquid Holdup and Pressure Drop Predictions

For stratified aerated mud flow in inclined channels, the momentum equations for the two phases can be expressed as:

$$-A_L\left(\frac{dp}{dx}\right)+\tau_i S_i-\tau_L S_{LD}-\tau_L S_{Ld}-A_L\rho_L\sin\theta=0 \tag{9.4}$$

$$-A_G\left(\frac{dp}{dx}\right)-\tau_i S_i-\tau_G S_{GD}-\tau_G S_{Gd}-A_G\rho_G\sin\theta=0 \tag{9.5}$$

By eliminating the pressure gradient from Eq. 9.4 and Eq. 9.5, the combined momentum equation for aerated mud flows can be expressed as:

$$\tau_G\frac{S_{GD}}{A_G}-\tau_L\frac{S_{LD}}{A_L}+\tau_i S_i\left(\frac{1}{A_L}+\frac{1}{A_G}\right)-\tau_L\frac{S_{Ld}}{A_L}+\tau_G\frac{S_{GD}}{A_G}-(\rho_L-\rho_G)g\sin\theta=0 \tag{9.6}$$

The combined momentum equation for stratified flow is an implicit equation for the liquid level in the pipe (h_L). It combines all the forces that act on the liquid and gas phase, which in turn determines the location of the liquid level in the pipe. By checking the transition boundaries for stratified flow, the liquid level in the pipe (h_L), liquid holdup and pressure drop can be determined. Determining the liquid level, h_L from Eq. 9.6, requires reasonable estimations of wall and interfacial shear stresses that involve calculations of various borehole geometric parameters. Hence, pressure drop can be predicted by solving Eq. 9.4 or Eq. 9.5. If the flow is slug flow, liquid holdup is calculated by dividing the flow into two zones: slug body zone and film zone. In slug body zone, the liquid holdup is estimated by an empirical correlation as:

$$H_{LLS}=\frac{1}{1+\left(\frac{V_M}{8.66}\right)^{1.39}} \tag{9.7}$$

The pressure drop in slug body is given by:

$$\Delta P_{LLS}=\frac{\tau_{LLS}L_{LLS}}{D-d} \tag{9.8}$$

In the film zone, the flow can be treated as stratified and the liquid film height can be calculated by using Eq. 9.6. The pressure drop can be estimated using Eq. 9.4 or Eq. 9.5. Thus, the pressure drop across a slug unit is determined as:

$$\Delta P_U=\Delta P_{LLS}+\Delta P_F \tag{9.9}$$

where ΔP_F is pressure drop across the film.

9.2.2 MODELING CUTTINGS TRANSPORT WITH AERATED MUD

A mechanistic model for cuttings transport with aerated mud has been developed. The hydraulics of one-dimensional, two-phase (air-water) flow is coupled with mechanisms of cuttings transport in the formulation of the model. The model predicts in-situ cuttings volumetric concentration and mixture density in a horizontal concentric annulus. The following assumptions are used to develop the model:

- Steady-state condition, cuttings injection rate is equal to collection rate;
- Cuttings are transported in the liquid phase;
- The liquid phase and cuttings particles are incompressible;
- Cutting particles are assumed uniform and spherical;
- The flow is assumed isothermal Newtonian and turbulent;
- The effects of inner pipe rotation are not considered;
- Air and water are considered as the gas and liquid phases;
- No mass transfer takes place between the gas and liquid phases;
- Physical properties of air, water and cuttings are constant with each slug unit;
- Equilibrium cuttings bed surface is uniform along the test section;
- Horizontal concentric annular flow.

Cuttings transport mechanism in aerated flows is analyzed and critical condition for particle movement is determined by considering forces and moments acting on a single protruding particle in a cuttings bed. Figure 9.1 presents the major forces acting on the particle. Accordingly, the moments acting on the bed particle due to the lift force, drag force and buoyancy force tend to roll the particle downstream of the flow while the moment created by gravity tends to prevent the particle from rolling. By considering turbulent flow conditions, the local velocity profile near the bed surface, u(y), can be estimated using the law of the wall. The minimum wall shear stress and pressure gradient for cuttings transport are determined from the velocity profile. Finally, the hydraulic model is coupled with a cuttings transport model by considering that the pressure gradient generated by the aerated mud flow should be equal to the minimum pressure gradient which is required for rolling the cuttings at the surface of bed.

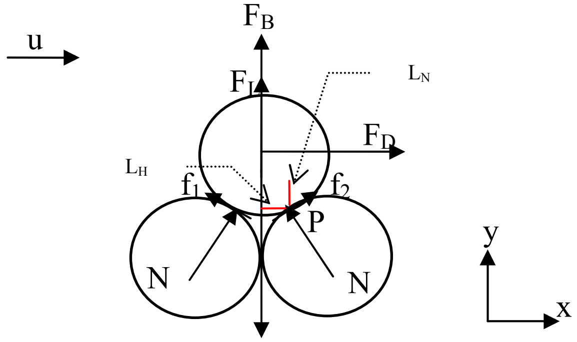

Fig. 9.1 Forces Acting on a Single Bed Particle

F_L and F_D are the lift force and drag force around the particle. F_G and F_B are the gravity and buoyancy forces. N_1 and N_2 are normal forces which are acting on the contact points between the particles. The friction forces at the contact point are f_1 and f_2. In order to initiate rolling of the bed particle, the moments of forces ($F_B + F_L + F_D$) at the contact point P tending to cause downstream rotation must exceed the moment of the gravitational force that tends to prevent downstream rotation. At the same time, the bed particle can also be lifted up if the sum of the forces in the upward direction is greater than the downward direction. Therefore, the condition for initiation of particle rolling at the bed surface is given by:

$$\begin{aligned} &F_B L_H + F_L L_H + F_D L_N > F_G L_H \\ &\Rightarrow \\ &F_B + F_L > F_G - F_D \frac{L_N}{L_H} \end{aligned} \tag{9.10}$$

Here the moments of the normal and friction forces are taken to be zero; because when particle rolling is about to begin, the normal force, N_1 and the friction force, f_1 become zero. Similarly, normal and friction forces at contact points are taken to be zero when particle lifting is about to occur. Therefore, the condition for initiation of particle lifting at the bed surface is given by:

$$F_B + F_L > F_G \tag{9.11}$$

L_H and L_N are the perpendicular distance to the line of action. The values of L_H and L_N are approximately determined by considering three equal bed particles with 60° angle of repose:

$$L_N = \frac{d_p \cos(\pi/6)}{2} \tag{9.12}$$

$$L_H = \frac{d_p \sin(\pi/6)}{2} \tag{9.13}$$

By comparing Eq. 9.10 with Eq. 9.11, the sum of buoyancy and lift forces required for rolling the particle is less than the sum of forces required for lifting the particle, since F_D is considered to be always greater than zero. This means that particle rolling occurs at lower flow velocities than lifting. Therefore, Eq. 9.10 is considered the main criterion for particle movement initiation. The equations used for calculating the forces in Eq. 9.10 are presented in Table 9.1. By substituting the equations into Eq. 9.10 and rearranging, the local critical velocity for particle motion becomes:

$$u_c^2 = \frac{\frac{4}{3} d_p g \left(\frac{\rho_S - \rho_L}{\rho_L} \right)}{C_L + \sqrt{3} C_D} \tag{9.14}$$

To apply the above equation, a proper expression for u_c, C_L and C_D must be found that relates each to the overall characteristics of the flow. Often, turbulent flow velocity profiles consist of a viscous sublayer, logarithmic layer and an intermediate layer (overlapped layer) that exists between the other two layers, as shown in Fig. 9.2. This velocity profile is widely used for mathematical modeling and analysis of turbulent flow near a rough surface.

Table 9.1 List of Equations for Calculating Forces Acting On the Particle

Force	Equation
Gravity, F_G	$F_G = \frac{1}{6}\rho_S g \pi d_P^3$
Buoyancy, F_B	$F_B = \frac{1}{6}\rho_L g \pi d_P^3$
Lift, F_L	$F_L = \frac{1}{2} C_L \rho_L u^2 A_P$
Drag, F_D	$F_D = \frac{1}{2} C_D \rho_L u^2 A_P$

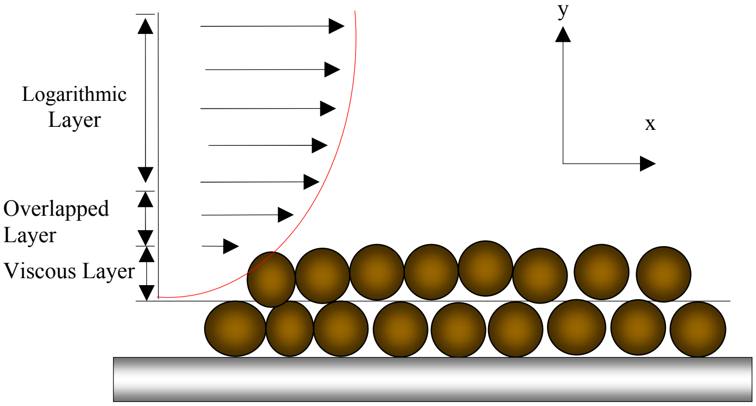

Fig. 9.2 Near-bed velocity profile of turbulent flow

When the bed particle diameter is smaller than the viscous sublayer (i.e. d+ < 5, where $d^+ = \rho_L d_p u^*/\mu_L$), the following expression for local velocity near the particle can be used:

$$u = \frac{d_p \tau_w}{\mu_L} \tag{9.15}$$

At steady state condition, the average wall shear stress can be expressed as:

$$\tau_w = \frac{\Delta p}{\Delta x}\frac{D_{hy}}{4} \tag{9.16}$$

By inserting Eq. 9.15 into Eq. 9.16, the relationship between the local velocity and frictional pressure gradient is expressed as:

$$u = \frac{d_p D_{hy}}{4\mu_L}\left(\frac{\Delta P}{\Delta x}\right) \tag{9.17}$$

The critical frictional pressure gradient to cause particle motion in the viscous sublayer is obtained by substituting Eq. 9.14 into Eq. 9.17. After simplification, the critical pressure gradient is expressed as:

$$\left(\frac{\Delta P}{\Delta x}\right)_{\text{Critical}} = \left(\frac{4\mu_L}{d_p D_{hy}}\right)\sqrt{\frac{\frac{4}{3}d_p g\left(\frac{\rho_S - \rho_L}{\rho_L}\right)}{C_L + \sqrt{3}C_D}} \tag{9.18}$$

Equation 9.15 is applicable when particles are inside the viscous sublayer. For particles that are larger than the thickness of the viscous sublayer (i.e., when particles are in the overlapped layer or protrude into the logarithmic layer), the logarithmic velocity profile can be used to develop an expression for the critical pressure gradient. In this situation (i.e. $d^+ > 5$), the logarithmic velocity profile can be used for local velocity near the particle. Therefore, the local velocity can be expressed as:

$$u = u^* 2.5 \mathrm{Ln}\left(\frac{y u^* \rho_L}{\mu_L}\right) + 5.5 u^* \tag{9.19}$$

where u* is the friction velocity, $u^* = (\tau_w/\rho_L)^{0.5}$. Using Eqs. 9.14 and 9.19, the following expression for the friction velocity is obtained:

$$2.5 u_C^* \mathrm{Ln}\left(\frac{d_p u_C^* \rho_L}{\mu_L}\right) + 5.5 u_C^* = \sqrt{\frac{\frac{4}{3}d_p g\left(\frac{\rho_S - \rho_L}{\rho_L}\right)}{C_L + \sqrt{3}C_D}} \tag{9.20}$$

where u^*_C is the critical friction velocity that corresponds to the critical flow condition for rolling. Hence, the pressure gradient at the critical rolling condition is given by:

$$\left(\frac{\Delta p}{\Delta x}\right)_{\text{critical}} = \frac{4\rho_L u_C^{*\,2}}{D_{hy}} \tag{9.21}$$

When the dimensionless bed particle size, d^+, is greater than 70, the velocity profile becomes highly dependent on the roughness of the bed; therefore, Eq. 11 may not be applicable. In this case, the velocity profile can be estimated by:

$$u = 2.5 u^* \ln\left(\frac{y}{d_p}\right) + 8.5 u^* \quad . \tag{9.22}$$

9.2.3 NUMERICAL SCHEME

Equations 9.18 and 9.20 are implicit equations that require a numerical procedure to obtain their solutions. Estimation of lift and drag coefficients involves determination of flow pattern, equilibrium bed height, in-situ gas-liquid ratio and cuttings concentration in the liquid phase. In drilling operations, a cuttings bed normally forms when the fluid flow rate in the annulus can not prevent the cuttings particles from depositing. As the bed grows, the fluid velocity and frictional pressure loss increase until an equilibrium condition is reached. At the equilibrium condition, the rates of cuttings deposition and resuspension become equal. At steady state condition, the cuttings concentration in the liquid phase is approximately equal to the input cuttings concentration, if the slip between the cuttings particles and the liquid phases is negligible. The equilibrium bed height, flow pattern and in-situ gas-liquid ratio are determined using the hydraulic model presented in Section 9.2.1. The hydraulic model considers two different layers (upper layer and stationary bed) and employs mass and momentum conservation equations. Figure 9.3 presents a schematic drawing that describes cuttings transport in aerated muds based on experimental observations. As presented in the figure, the system consists of: an upper layer and stationary cuttings bed at the bottom. The upper layer contains gas phase and liquid phase together with suspended cuttings. At the surface of the bed, particles roll due to hydrodynamic forces.

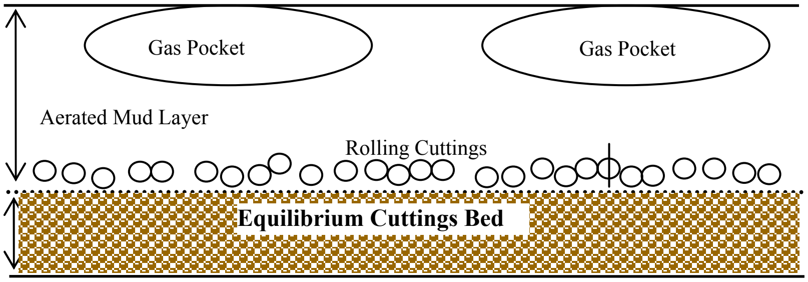

Fig. 9.3 Schematic drawing of cuttings transport with aerated mud in horizontal annulus

Non-linear systems of equations are formed when Eq. 9.18 or Eq. 9.20 is coupled with the hydraulic equations. A special numerical procedure was employed to maintain the stability of a solution. A computer program is developed based on the mathematical model. The program assumes zero equilibrium bed height to begin an iterative procedure and calculates the area of the upper layer using geometry relationships. Using the bed area, the program predicts the gas-liquid flow pattern and determines the frictional pressure loss (ΔP_f). The boundary layer thickness, y^+, near the bed surface is obtained using the frictional pressure loss. The boundary layer thickness is used to determine whether the protruding particles are within the viscous sublayer or not. Subsequently, the program uses Eq. 9.18 or Eq. 9.21 to calculate the critical pressure loss (ΔP_c) and compares its value with ΔP_f. If $|\Delta P_f-\Delta P_c|/\Delta P_f<\varepsilon$ (convergence criteria), then the program ends. If $|\Delta P_f-\Delta P_c|/\Delta P_f > \varepsilon$, then the program adjusts the bed height and repeats the calculation until $|\Delta P_f-\Delta P_c|/ \Delta P_f < \varepsilon$.

9.3 EXPERIMENTAL STUDY

The Advanced Cuttings Transport Flow Loop (ACTF) at the University of Tulsa was used for this experimental study. This investigation involved two types of tests: i) aerated mud flow test; and ii) cuttings transport test with aerated mud. Cuttings transport tests with aerated mud primarily involved measuring liquid and air flow rates, cuttings weight in the test section, mixture densities and frictional pressure losses. The aerated flow mud tests consisted of liquid holdup and frictional pressure loss measurements in the test section.

9.3.1 TEST FACILITY

The test facility consists of: i) pumping or recirculation facilities; ii) air compression and injection system; iii) heating and cooling facilities; iv) pipelines and test section; v) multiphase measurement system; vi) cuttings injection and collection system, vii) data acquisition and control system; and viii) water storage tanks. The test section consists of a 73-ft (22-m) long annulus with 6-inch (152-mm) casing and 3.5-inch (89-mm) concentric drillpipe. Figure 9.4 presents a schematic drawing of the flow loop. An experiment begins by filling a 100-bbl storage tank with a requisite amount of water. A centrifugal pump delivers the water from this tank through a heat exchanger. After the heat exchanger the water flows through two parallel paths: one path is through a metering pump, which accurately feeds a desired amount of the water to a multiphase pump. The other path is to a fracturing (mud) pump. The multiphase pump is used for both pumping the liquid phase (in this case, water) and further compression of the gas phase (in this case, air). Compressed air at 200 psi (1.38 MPa) is fed to the multiphase pump by an air compressor. The compressed air is mixed with the water coming from the metering pump at the inlet of the multiphase pump. The multiphase pump can produce an additional pressure increase of up to 500 psi (3.45 MPa). The air-water mixture discharged from the multiphase pump is mixed with the water coming from the mud pump and flows through a 4-inch (102-mm) pipe, where the cuttings are injected to the system. A total of three Coriolis mass flow meters measure the amounts of water and air injected to the flow loop. The aerated water mixes with the cuttings and this mixture flows to the annular test section. Two gamma-ray densitometers measure the mixture density. Before a "steady state" is reached, some of the cuttings deposit in the test section. The fluid carries undeposited cuttings to a separation tower via a 4-inch (102 mm) pipe section. The separation tower has a screen with 0.06-inch (1.5 mm) hole size to

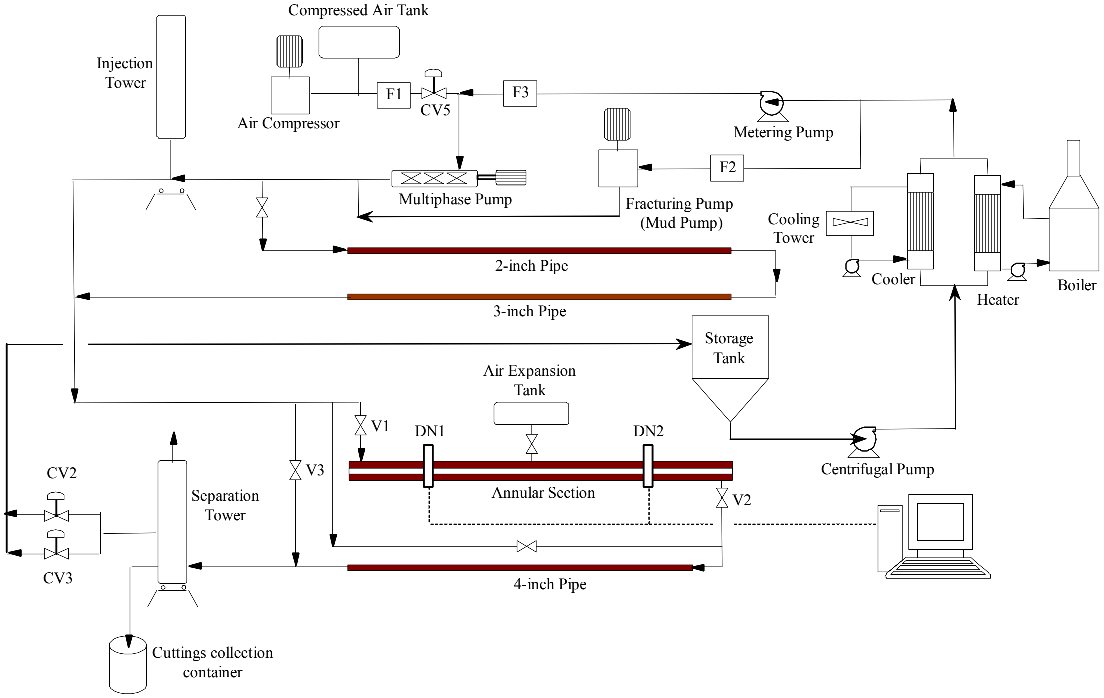

Fig. 9.4 Schematic drawing of ACTF flow loop

remove cuttings from the fluid. Most of the gas phase is vented to the atmosphere from the separation tower. Two backpressure valves (CV2 and CV3) down stream of the separation tower control the test section pressure. After the separation tower, fluid returns to the storage tanks.

The heating and cooling system includes: a boiler (glycol heater), glycol circulation tank, heat exchangers and cooling tower. The liquid phase can be heated up to 200°F. Flow lines are fully insulated to keep the loop temperature at the desired level.

The injection tower is used for storing and injecting cuttings. In order to evaluate weight changes of injection and separation towers, three load cells are installed underneath each tower. The load cells are placed 120° apart. A data acquisition system displays and continuously records the load cell measurements. This information is used to determine the cuttings injection and collection rates.

The multiphase flow measuring system consists of five components: i) two quick-closing valves (V1 and V2); ii) one bypass valve (V3); iii) two nuclear densitometers (DN1 and DN2); iv) pressure and temperature transmitters, and v) air expansion tank. Differential pressure is measured by excluding the entrance and exit parts of the test section. The entrance and exit parts have 10-ft-long and 6-ft-long sections respectively, to minimize end effects on frictional pressure loss measurements. When steady-state flow conditions are established and maintained for the desired test duration, the quick-closing valves (V1 and V2) are closed simultaneously while opening the bypass valve (V3) to allow the mixture to flow directly to the return line. This enables a certain amount of air, water and cuttings to be trapped in the annular test section. After trapping the fluid in the test section, the air expansion tank is used to estimate the volume of the trapped air using PVT and conservation equations.

Two nuclear densitometers (DN1 and DN2) are installed on the annular section to measure local mixture density at a given time. One of the densitometers is placed in the middle of the test section while the other one is placed 7 ft from the outlet. Ten radiation sources (Cesium-137) are aligned at the top of the pipe and the radiation detector is mounted at the bottom. The radiation is able to cover the whole cross-sectional area. Calibrations of the nuclear densitometers were conducted to get reliable density measurements.

9.3.2 EXPERIMENTAL INVESTIGATION OF AERATED MUD FLOWS

Test Procedure

The aerated mud flow tests consisted of liquid holdup and pressure drop measurements in the test section. The tests were performed at different pressures, temperatures, and gas and liquid flow rates. For all experiments, water and air were used as the liquid and gas phases, respectively. The procedures for the tests were:

1) Heating the flow loop to the desired temperature by circulating the liquid phase;
2) Starting the metering pump to deliver water from the centrifugal pump to the multiphase pump as lubrication;

3) Starting the multiphase pump and injecting air into the flow loop;
4) Adjusting the multiphase pump speed to get the desired air flow rate;
5) Choking down the backpressure control valves (CV2 and CV3) to get the desired annular pressure;
6) Adjusting the mud pump rotation speed to obtain the desired water flow rate;
7) Keeping a steady flow rate for at least 5 minutes;
8) Closing the holdup valves (V1 and V2);
9) Measuring the air content in the test section using the expansion tank.

Test Matrix

Two different sets of experiments (Test Set #1 and Test Set #2) were carried out at different temperatures. Details of these test sets are presented in Tables 9.2 and 9.3. Another set of tests (Test Set #3) was conducted, which covered a wide range of pressures, temperatures, gas flow rates and liquid flow rates. Details of Test set #3 are given in Table 9.4. This set of tests covered pressures from 100 psi to 400 psi and temperatures from 80°F to 175°F. During the experiment, flow patterns were observed and recorded by a camcorder through a view port on the annulus.

Table 9.2 Injection Rates for Test Set #1 (T=80ºF & 200 Psi)

	Liquid Injection Rates (gal/min)				
	Q_L=50	**Q_L=100**	**Q_L=150**	**Q_L=200**	**Q_L=250**
Gas Injection Rates (Scf/min)	50	50	50	50	50
	75	75	75	75	75
	100	100	100	100	100
	125	125	125	125	125

Table 9.3 Injection Rates for Test Set #2 (T=140ºF & 200 Psi)

	Liquid Injection Rates (gal/min)				
	Q_L=50	**Q_L=100**	**Q_L=150**	**Q_L=200**	**Q_L=250**
Gas Injection Rates (Scf/min)	50	50	50	50	50
	75	75	75	75	75
	100	100	100	100	100
	125	125	125	125	125

Table 9.4 Injection Rates for Test Set #3

P (psi)	**T=80°F**		**T=120°F**		**T=150°F**		**T=175°F**	
	Q_g (scf/min)	**Q_L (gal/min)**	**Q_g (scf/min)**	**Q_L (gal/min)**	**Q_g (scf/min)**	**Q_L (gal/min)**	**Q_g (scf/min)**	**Q_L (gal/min)**
100	60	100	80	100	100	100	120	100
200	60	150	80	150	100	150	120	150
300	60	200	80	200	100	200	120	200
400	60	250	80	250	100	250	120	250

Test Results

The experiments with aerated fluids were mainly focused on flow pattern observation, mixture density and frictional pressure loss measurements in the test section. For all experiments, water and air were used as the liquid and gas phase, respectively. The parameters measured during an individual test include: air flow rate, water flow rate, pressure, temperature, differential pressure and mixture density in the annulus.

Flow patterns observed in aerated mud Test Set #1 (80°F and 200 psi) and model-predicted flow pattern boundaries are presented in Figure 9.5. Stratified smooth flow was observed at low air and water superficial velocities (i.e. 50 scf/min and 50 gal/min) and stratified wavy flow was also observed at 75 scf/min and 50 gal/min. The gas-liquid interface was not smooth in the wavy flow. Increasing the water flow rate turns the stratified smooth flow into the wavy flow. Further increasing air flow rate increases the suction force resulting in slug flow. Transition predictions of the model show satisfactory agreement with our observations, except for two data points at low water injection rates and high air flow rates. The reason may be because at the transition boundary of slug flow and stratified wavy flow, it is difficult to determine the flow pattern by observation. Both the model predictions and the test observations indicate that for a practical range of drilling applications, the aerated mud flows are predominately slug flows.

Figure 9.6 shows the flow patterns that were observed in Test Set #2 (140°F and 200 psi) together with model-predicted flow pattern boundaries. The stratified smooth flow was not observed at this time; however, stratified wavy flow occurs at low air and water flow rates. Increasing the air or water flow rate results in slug flow. Test Set #3 was conducted at higher water flow rates ($Q_L \geq 100$ gal/min); all flow patterns were found to be slug flows.

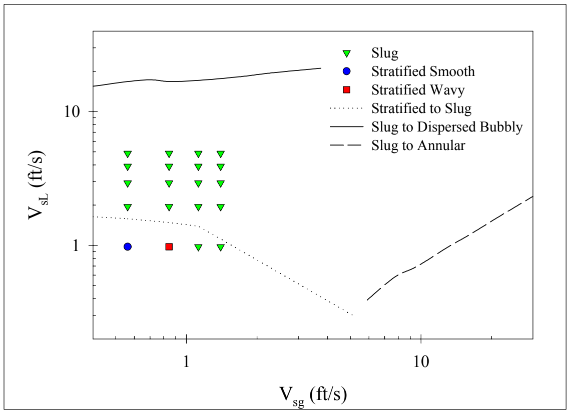

Fig. 9.5 Observed flow pattern and model-predicted flow pattern boundaries for Test Set #1

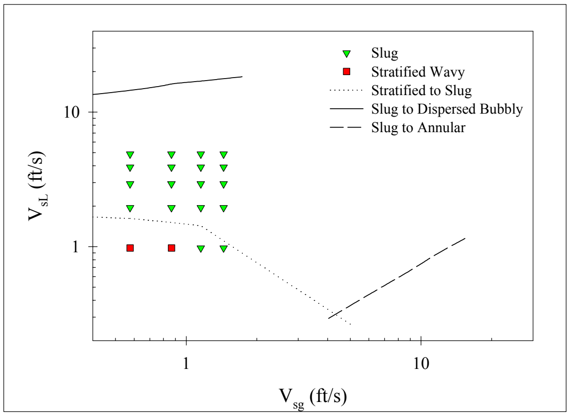

Fig. 9.6 Observed flow pattern and model-predicted flow pattern boundaries for Test Set #2

The mixture density was measured by using the gamma-ray densitometers. Figure 9.7 shows the measured mixture density results obtained from Test Set #1. The data show clearly that the mixture density decreases as the air flow rate increases. The mixture densities were continuously recorded during the test run; however, those data which were collected at steady state were used to calculate the average density of the fluid in the test section. The maximum readings of the densitometers were approximately 1.0, which indicates the annulus space was almost full of liquid. The minimum readings were as low as

0.38, which means gas pockets with a liquid film were passing through the densitometers. This verifies the slug flow pattern, which is characterized by a slug body pushed by a gas pocket.

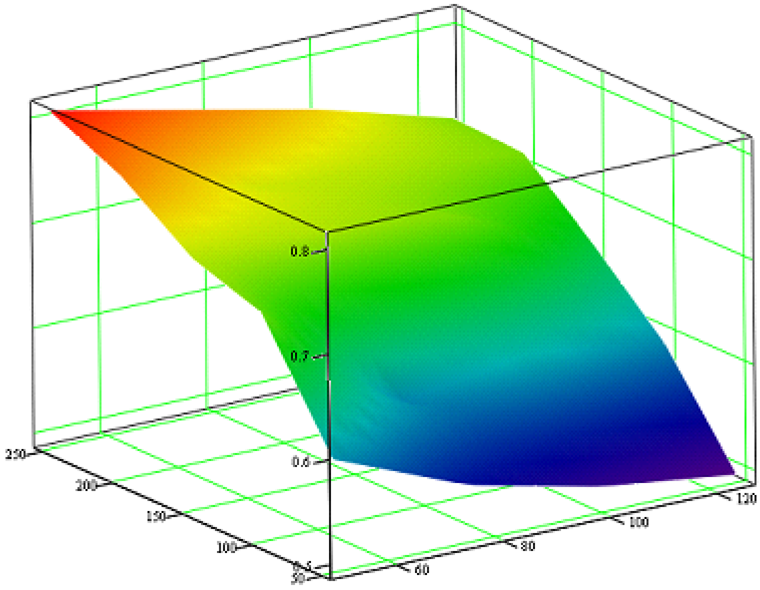

Fig. 9.7 Measured liquid hold-up as a function of liquid and gas injection rates for test set #1

Frictional pressure losses across the annular section were measured for all the test sets. Figures 9.8 and 9.9 show the differential pressure changes with respect to liquid flow rate for Test set #1 and Test set #2, respectively. The curve indicates the frictional pressure losses are not sensitive to the air injection rate. There is a slight increase in frictional pressure loss when air flow rate reach the maximum value (i.e. 125 scf/min).

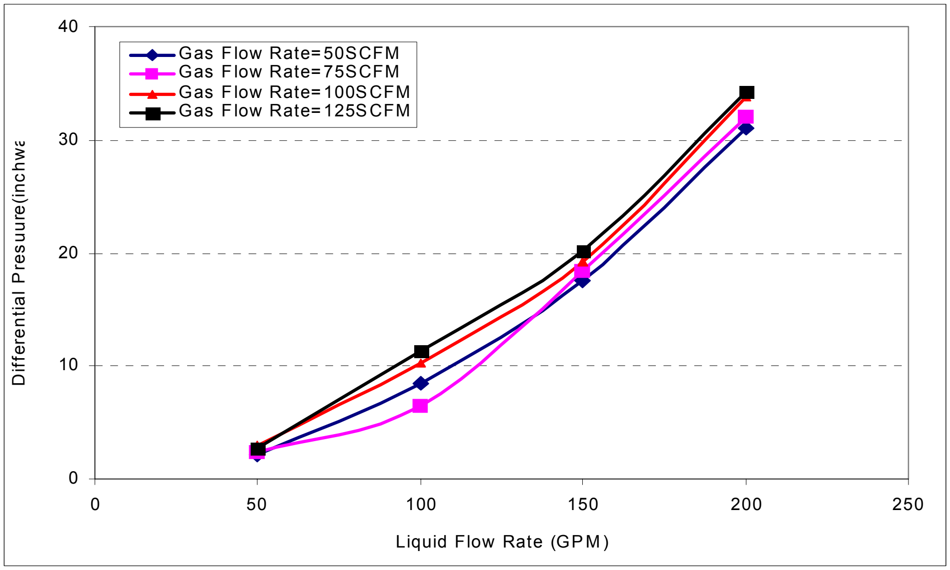

Fig. 9.8 Measured differential pressure vs. liquid flow rate for Test Set #1 (T= 80 F, P=200 psi)

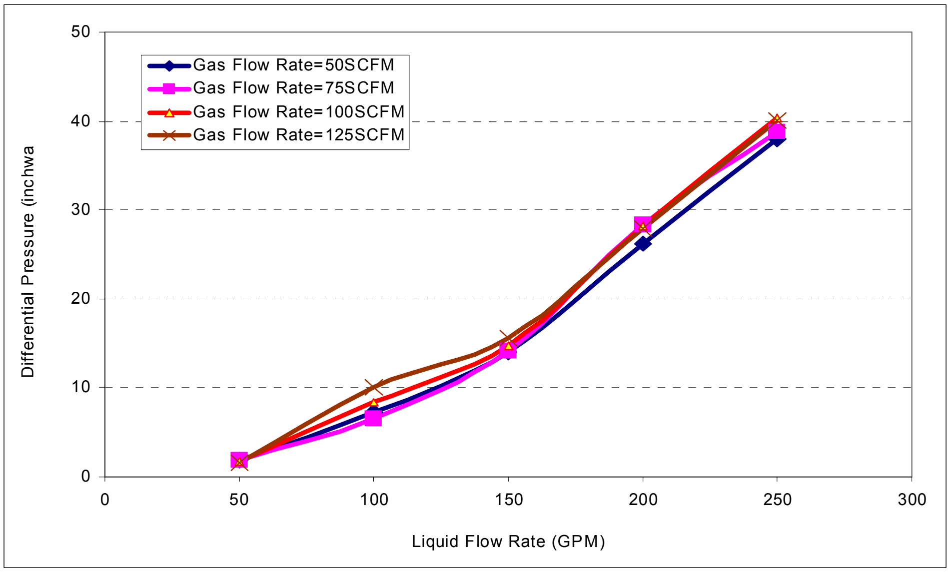

Fig. 9.9 Measured differential pressure vs. liquid flow rate for Test Set #2 (T= 140 F, P=200 psi)

Figure 9.10 shows the effect of temperature on frictional pressure loss for air injection rate of 100 scf/min at 200 psi. The curves indicate that the pressure losses in the annulus decrease as the temperature increases. Similar results were obtained for other test sets and are presented in Table 9.5.

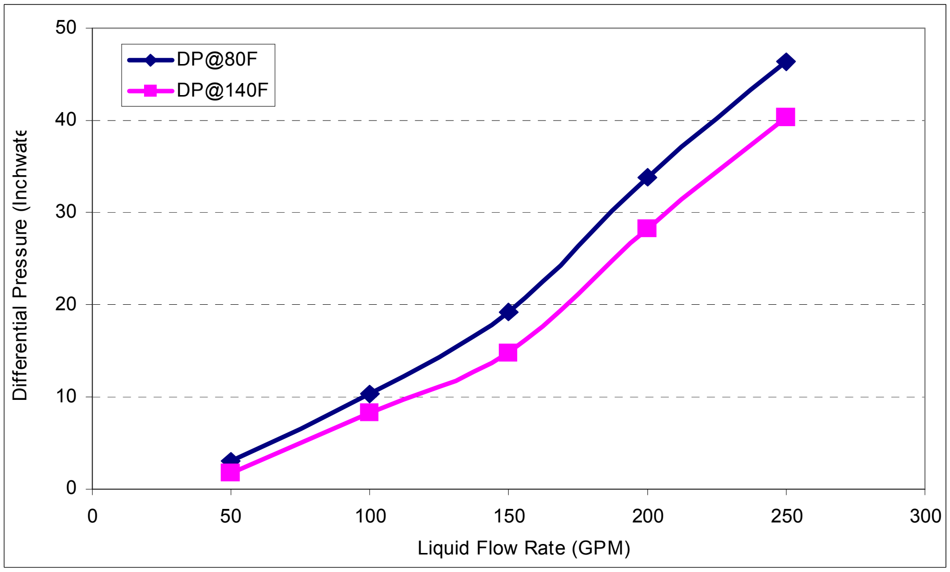

Fig. 9.10 Comparison of measured pressure losses at different test temperatures

Table 9.5 Measured Differential Pressures for Test Sets #1 and 2

T=80F, P=200 Psi			
Q_g=50 (scf/min)	Q_g=75 (scf/min)	Q_g=100 (scf/min)	Q_g=125 (scf/min)
2.15	2.37	2.97	2.75
8.53	6.42	10.28	11.34
17.56	18.33	19.17	20.22
31.06	32.05	33.82	34.27
43.14	44.69	46.4	44.87
T=140 F, P=200 Psi			
Q_g=50 (scf/min)	Q_g=75 (scf/min)	Q_g=100 (scf/min)	Q_g=125 (scf/min)
1.82	1.82	1.75	1.54
7.20	6.49	8.29	10.03
13.95	14.11	14.78	15.59
26.17	28.31	28.22	27.89
37.92	38.87	40.38	40.10

9.3.3 EXPERIMENTAL INVESTIGATION OF CUTTINGS TRANSPORT

Test Procedure

Cuttings transport flow loop experiments were conducted at different pressures, temperatures, and air and water flow rates. For all the experiments, cuttings were injected at a rate of approximately 15 Lbm/min (6.8 kg/min). The cuttings have an average diameter of 0.118 inch (3 mm), density of 163 Lbm/ft^3 (2610 kg/m^3) and porosity of 38%. During a test, water and air are used as the liquid and gas phases respectively. The test procedures include:

1. Heating the flow loop up to desired temperature by recirculating the liquid phase using the centrifugal pump;
2. Controlling the liquid phase flow rate through the multiphase pump by using the metering pump;
3. Regulating the compressed air flow rate using the multiphase pump;
4. Maintaining the desired annular pressure using backpressure control valves (CV2 and CV3);
5. Adjusting the mud pump rotation speed to obtain the desired liquid injection rate into the flow loop;
6. Keeping steady air and liquid phase flow rates for 5 minutes;
7. Injecting cuttings until steady state conditions are reestablished;
8. Trapping the three-phase mixture in the test section by quickly closing the holdup valves (V1 and V2);
9. Performing expansion measurements;
10. Flushing cuttings from the annular test section to the collection container.

The cuttings transport experiments primarily consisted of measurements of cuttings weight in the annulus (the volumetric cuttings concentration), mixture densities and frictional pressure losses. The tests were conducted at a constant cuttings injection rate, 15 Lbm/min. River gravel was used to simulate the drill cuttings. The average cuttings diameter is 0.118 inch and the density is 163 Lbm/ft^3. The porosity of the cuttings is 38%. Figure 9.11 presents a sample of experimental data from Test Group #1.

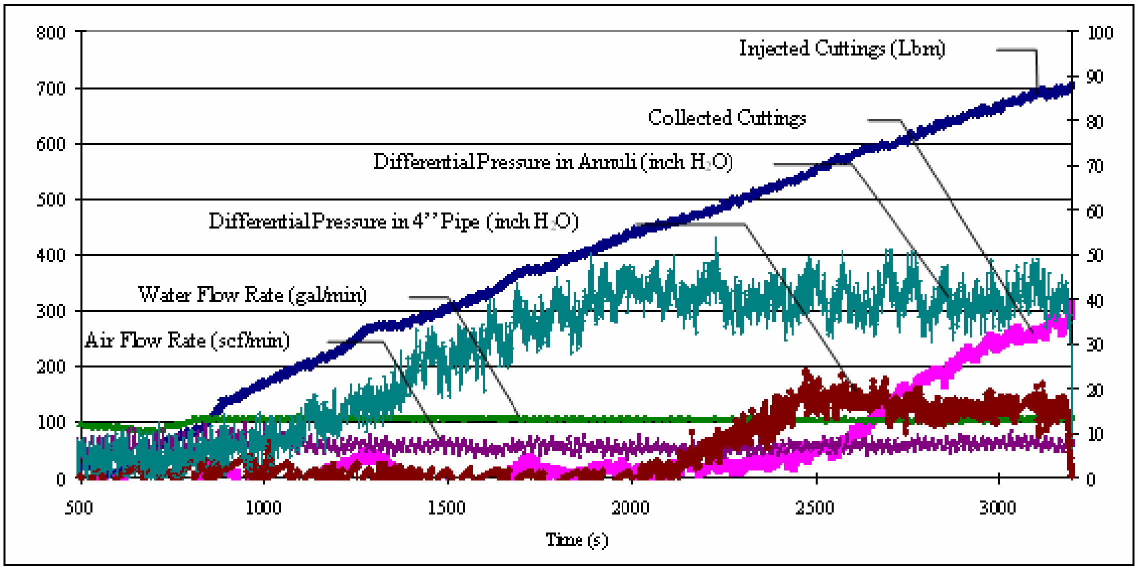

Fig. 9.11 Sample of Experimental Data for Cuttings Transport with Aerated Mud

On the plots, the x-axis is test run time in seconds; the y-axis on the left side can be water flow rate (gal/min), air flow rate (scf/min), weight of cuttings injected (Lbm) and cuttings collected (Lbm); the secondary y-axis on the right side is differential pressure (inches of H_2O) in the annulus and in the 4-inch pipe. Results include the cuttings weight, cuttings volumetric concentration, and frictional pressure loss across the test section.

Test Matrix

Cuttings transport mechanisms with aerated water at various conditions (different air and water flow rates, different pressures and temperatures) were investigated. It was observed that the annulus can be cleaned sufficiently (i.e. cuttings concentration is less than approximately 10%), when the liquid phase flow rate reaches 150 gal/min. As a result, the maximum liquid flow rate was set at 150 gal/min. Similarly, the minimum liquid flow rate was set at 80 gal/min. At this liquid flow rate the cuttings concentration was in the range of 40 to 50 percent. This was mainly done to optimize the number of tests because the complexity of three-phase flow and high temperature and pressure conditions made the test procedure very difficult. Four groups of tests were conducted during the investigation. Table 9.5 shows the test pressures and temperatures for each test group. A total of 39 tests were performed. The base case (Test Group #1) includes 16 tests. Test parameter details of the base case are presented in Table 9.6. Other test groups include: 8 low temperature tests, 8 high temperature tests and 7 high temperature and high pressure tests. Pressure and temperature were varied to maintain a constant gas-liquid ratio (GLR). Due to compressibility of the gas phase, the GLR varies with temperature and pressure. For each group, tests were performed at four different GLRs (0.0, 0.12, 0.24, and 0.38). At high GLRs (i.e. greater than 0.38), the flow loop becomes mechanically unstable. Therefore, GLRs greater than 0.38 were avoided for safety reasons.

Table 9.6 Test Parameters of Cuttings Transport Experiments

	Group Identification	Number of Tests	P (psi)	T (°F)
Group #1	Base case	16	200	120
Group #2	Low Temperature	8	185	80
Group #3	High Temperature	8	220	170
Group #4	High Temperature & Pressure	7	500	175

Table 9.7 Air and Water Flow Rates for Base case (T=120°F and P=200 psi)

GLR*	Q_L (gal/min)			
0	80	100	120	150
0.12	80	100	120	150
0.24	80	100	120	150
0.38	80	100	120	150

* GLR is injection gas volume fraction calculated at test temperature and pressure (i.e. GLR=$Q_g/(Qg+Q_L)$).

Test Results

Figure 9.12 presents measured cuttings concentration for the base case (Test Group #1) as a function of liquid flow rate for different GLRs. Cuttings concentration in the annulus decreases as the water flow rate increases for a given GLR. The curves clearly indicate that the cuttings concentration is more sensitive to water flow rate than GLR. Therefore, a small

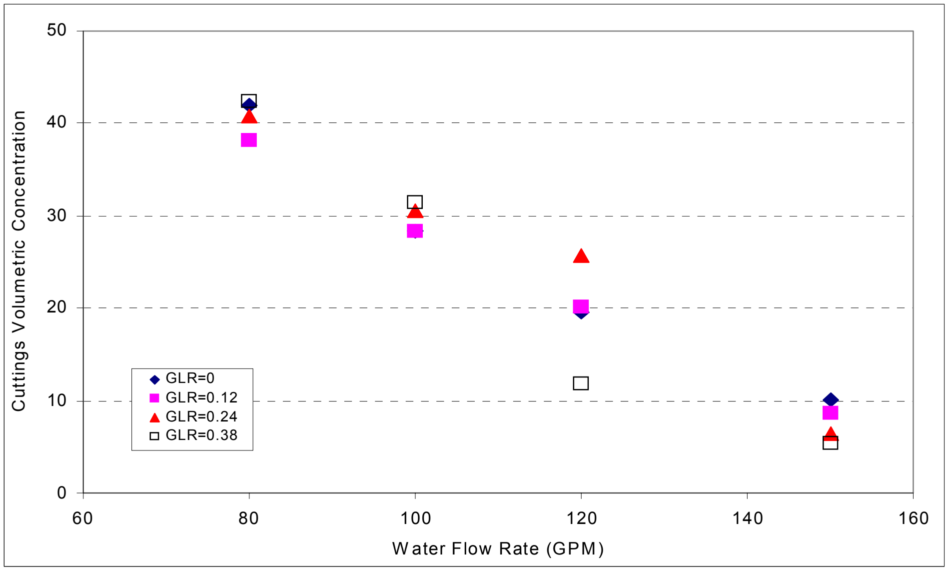

Fig. 9.12 Measured cuttings concentration vs. water flow rate for the base case (T =120°F & P=200 psi)

variation in liquid flow rate can cause significant change in cuttings transport capacity of an aerated mud.

Measured cuttings concentration for the base case is again presented in Fig. 9.13 as a function of GLR at different liquid flow rates. The effect of GLR on cuttings transport appears sensitive to other flow parameters; and it is highly influenced by the liquid flow rate. For instance, at 150 gal/min water flow rate, cuttings concentration in the annulus slightly decreases as GLR increases. This means that the injection of air has a positive effect on cuttings transport at high water flow rates. GLR has a negative effect on cuttings transport at 120 gal/min and GLR less than 0.24, but the effect becomes positive for GLR greater than 0.24. At low water flow rates (80 and 100 gal/min) the effect of air injection is negligible.

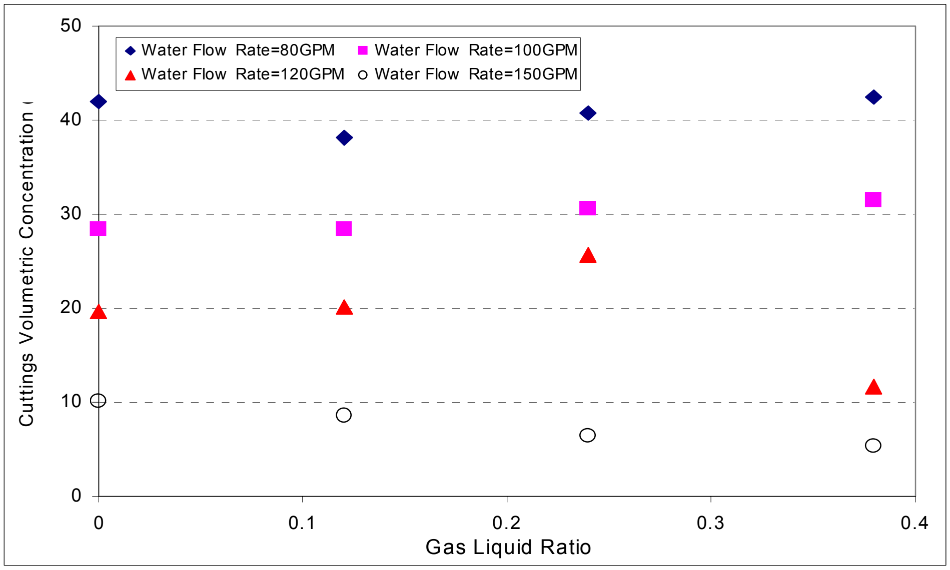

Fig. 9.13 Measured cuttings concentration vs. GLR for the base case (T =120°F & P=200 psi)

Figure 9.14 presents cuttings concentration as a function of GLR for low temperature tests (Test Group #2). At 120 gal/min water flow rate, cuttings concentration in the annulus decreases as GLR increases. This means that for this particular test case the injection of air has a positive effect on cuttings transport at 120 gal/min. However, at 100 gal/min the effect of air injection on the cuttings transport is negative for GLR less than 0.24 and positive for GLR greater than 0.24.

Measured cuttings concentrations for high temperature tests (Test Group #3) are presented in Fig. 9.15 as a function of GLR at different liquid flow rates. Unlike the base case and low temperature tests, at high water flow rate (i.e. 120 gal/min), cuttings concentration increases as GLR increases. However, at low water flow rate (100 gal/min), cuttings concentration decreases as GLR increases. This means that the injection of air may have a positive effect on the cuttings transport at low water flow rates and negative effect at high water flow rates in high temperature tests.

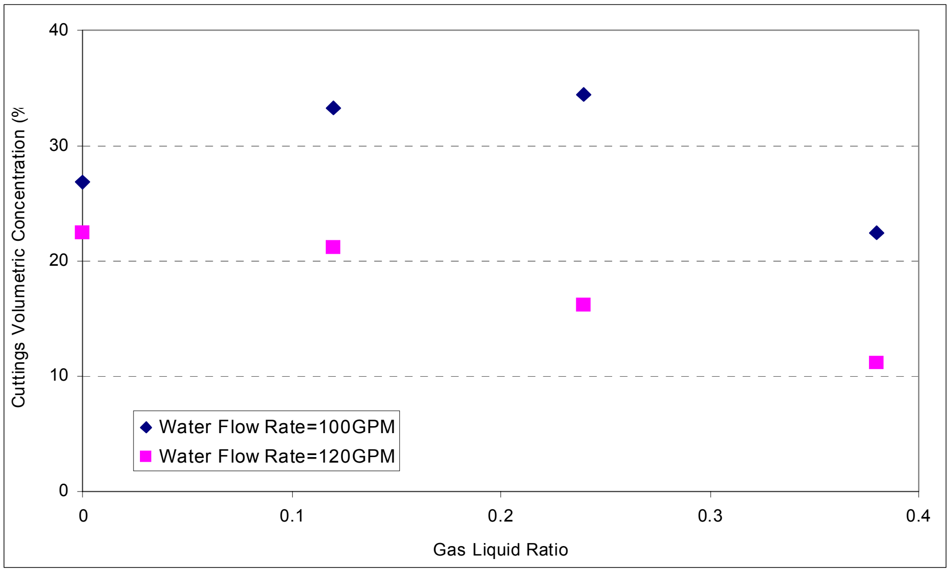

Fig. 9.14 Measured cuttings concentration vs. GLR at different water flow rates for low temperature tests (T =80°F & P=185 psi)

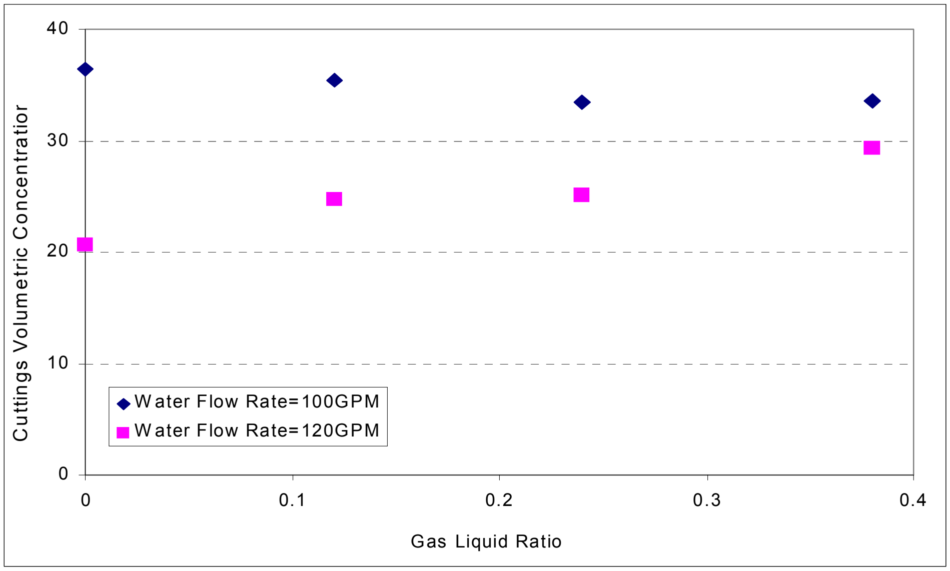

Fig. 9.15 Measured cuttings concentration vs. GLR at different water flow rates for high temperature tests (T =170°F & P=222 psi)

In the same way, high pressure and high temperature test (Test Group #4) results are presented in Fig. 9.16. In this case, a slight change in cuttings concentration is observed when the GLR increases at a given flow rate.

Figures 9.17 and 9.18 show the measured cuttings concentration versus test temperature at different GLR values for liquid flow rate of 100 and 120 gal/min, respectively. The results clearly show that in addition to liquid flow rate and GLR, temperature significantly affects the cuttings transport efficiency of aerated muds. Obviously, the temperature greatly affects the viscosities of the two phases and the interfacial tension. At 100 gal/min liquid flow rate, when temperature is increased from 80 to 170°F, except for two data points, the measured cuttings concentration shows an increasing trend. Changing the temperature from 80 to 170°F results in a cuttings concentration increase of up to 56%. A similar concentration trend is also observed at 120 gal/min. The measured cuttings concentration predominately increases as the temperature increases. As with the 100 gal/min case, two data points measured at low temperature don't follow this pattern.

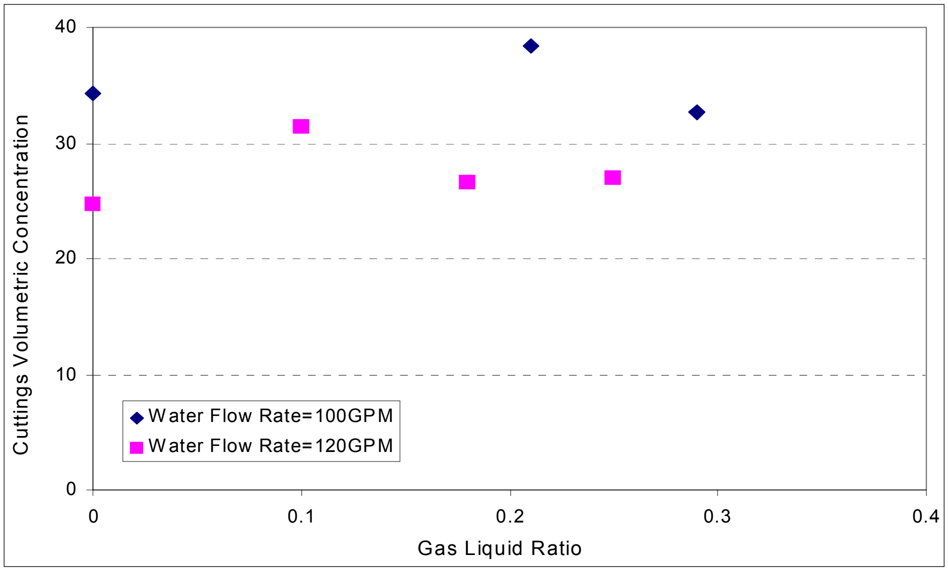

Fig. 9.16 Measured cuttings concentration vs. water flow rate for high temperature and pressure tests (T =175°F & P=500 psi)

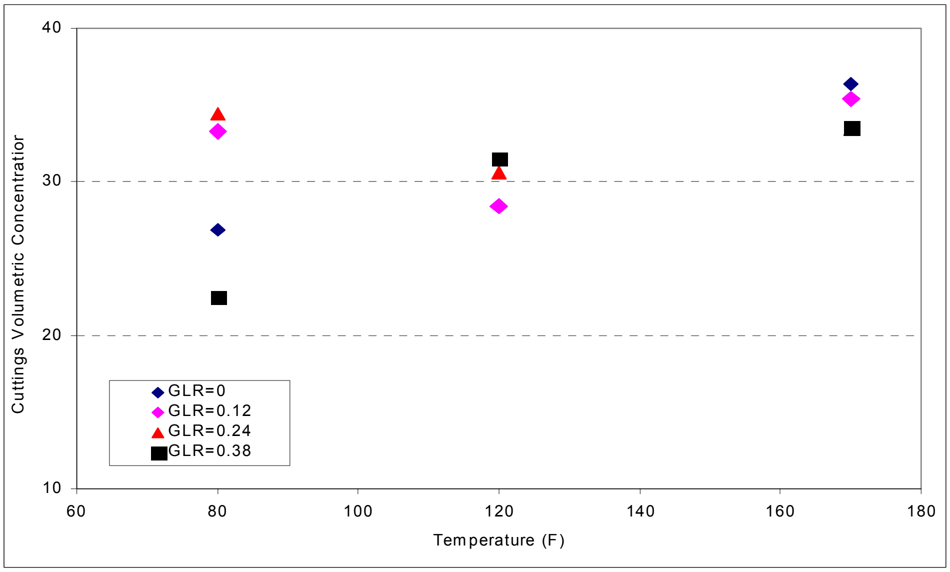

Fig. 9.17 Cuttings volumetric concentration vs. temperature (Q_L= 100 gal/min)

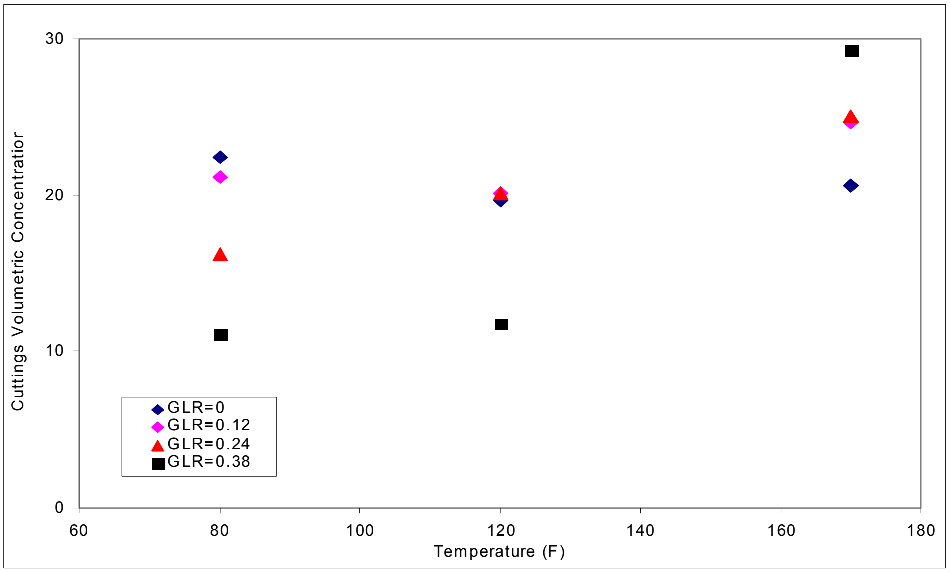

Fig. 9.18 Cuttings volumetric concentration vs. temperature (Q_L= 120 gal/min)

9.4 COMPARISONS OF MODEL PREDICTIONS WITH THE MEASURED DATA

9.4.1 COMPARISONS OF CUTTINGS TRANSPORT PREDICTIONS

Measured cuttings concentrations for the base case (Test Group #1) are presented along with the model predictions in Table 9.8. The absolute average differences between measured and predicted cuttings concentrations at liquid flow rates of 80, 100, 120 and 150 gal/min are 13.45%, 12.54%, 12.67% and 22.06%, respectively. For 150 gal/min water flow rate, the absolute average difference is the highest (i.e. 22%) because at high liquid flow rates the cuttings concentration is low. Hence, test measurement relative error is higher than at low liquid flow rate tests. The overall absolute average difference for the base case is 15.2%. In addition to the liquid flow rate, GLR affects the accuracy of the model predictions. It appears that the model accuracy decreases with increasing GLR.

Figures 9.19 and 9.20 compare cuttings concentration predictions of the model together with experimentally measured data for low temperature tests (Test Group #2). For this set of tests the model predictions are very close to the measured data. For instance the model predictions at 100 gal/min liquid flow rate show only 10% absolute average difference. At 120 gal/min liquid flow rate, the absolute average difference becomes 22%. The overall absolute average difference for the group is 16%.

For high temperature tests (Test Group #3), the model predictions have an absolute average difference of 30% at liquid flow rate of 100 gal/min. At 120 gal/min liquid flow rate, the absolute average difference is 35%. The overall absolute average difference for high temperature tests is 32%. The increase in discrepancy between the measured and predicted values may be attributed to the use of empirical equations that are obtained from ambient temperature two-phase flow experiments. Figures 9.21 and 9.22 present cuttings concentration predictions of the model together with experimentally measured data for high temperature and pressure tests (Test Group #4). As shown in the figures, the model predictions follow the trends of the experimental data, but underestimate the cuttings concentration. For this test group, the model gives an absolute average difference of 28% at liquid flow rate of 100gal/min. At higher liquid flow rate (120 gal/min), the absolute average difference is 34%. The overall absolute average difference for this test group is 30%.

Table 9.8 Model Predictions and Measured Data for the Base Case ((P=200 psi, T =120°F)

	GLR	Measured Cuttings Concentration (%)	Predicted Cuttings Concentration (%)	Absolute Difference (%)
Q_L =80 gal/min	0.00	42.02	37.60	10.52
	0.12	38.20	39.00	2.09
	0.24	40.80	34.00	16.67
	0.38	42.40	32.00	24.53
Average Absolute Difference (%)				13.45
Q_L=100 gal/min	0.00	28.42	26.00	8.52
	0.12	28.42	29.40	3.45
	0.24	30.56	27.50	10.01
	0.38	31.48	22.60	28.21
Average Absolute Difference (%)				12.54
Q_L =120 gal/min	19.63	19.10	2.70	19.63
	20.17	22.50	11.55	20.17
	25.67	18.00	29.88	25.67
	11.77	11.00	6.54	11.77
Average Absolute Difference (%)				12.67
Q_L =150 gal/min	0.00	10.16	9.60	5.51
	0.12	8.63	10.00	15.87
	0.24	6.49	5.00	22.96
	0.38	5.35	3.00	43.93
Average Absolute Difference (%)				22.06

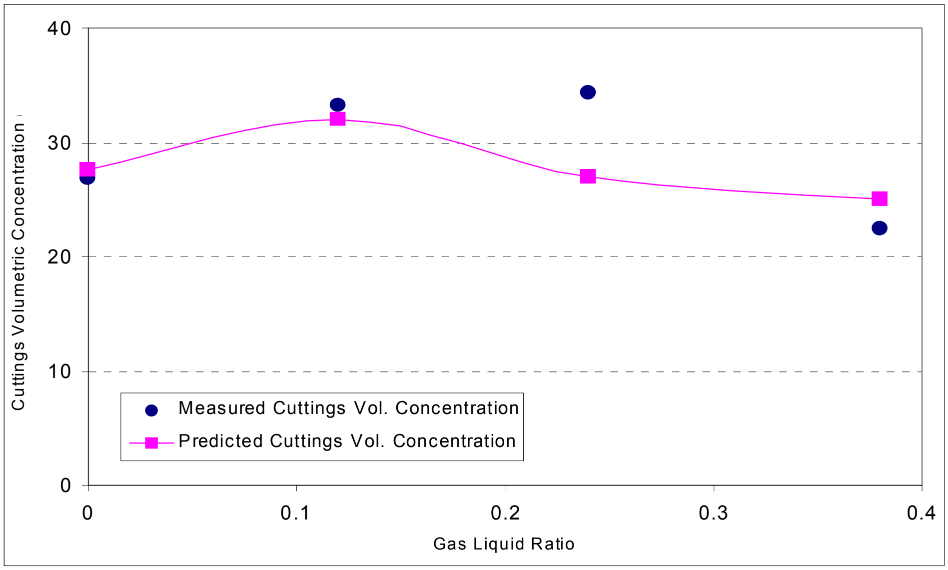

Fig. 9.19 Measured and predicted cuttings concentrations vs. GLR (Q_L=100 gal/min, T =80 ^oF, P=185 psi)

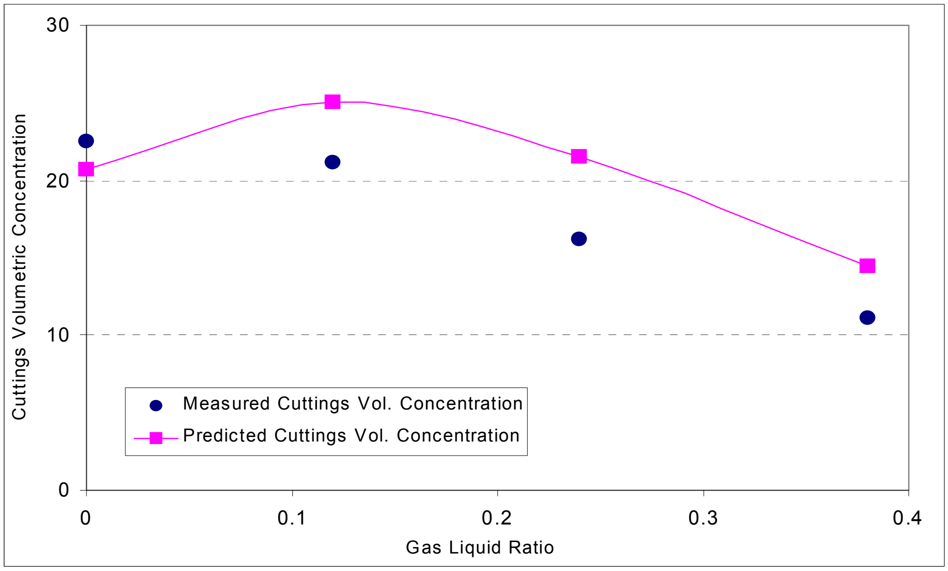

Fig. 9.20 Measured and predicted cuttings volumetric concentration vs. GLR (Q_L=120 gal/min, T =80 °F, P=185 psi)

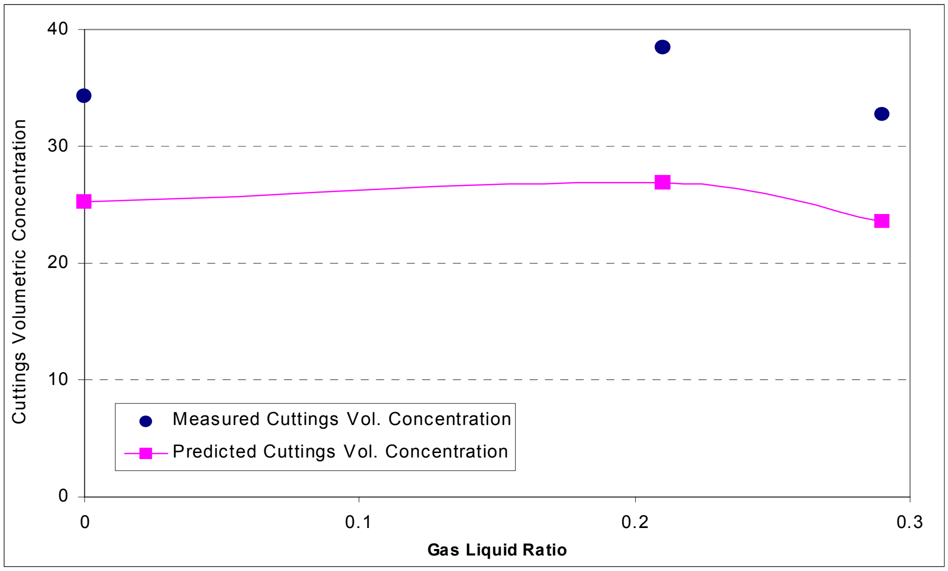

Fig. 9.21 Measured and predicted cuttings volumetric concentration vs. GLR (Q_L=100 gal/min, T =175 °F, P= 500 psi)

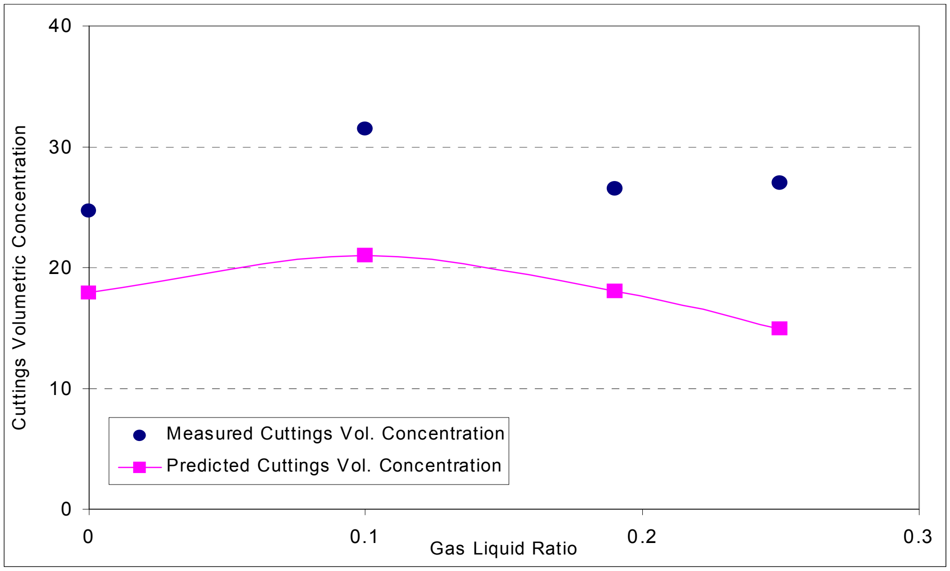

Fig. 9.22 Measured and predicted cuttings volumetric concentration vs. GLR (Q_L=120 gal/min, T =175 °F, P= 500 psi)

In order to examine the effect of pressure on cuttings concentration, experiments were performed at two different test pressures (200 psi and 500 psi) while keeping the liquid flow rate and GLR constant. Standard gas volume flow rates were different. However, the actual volume flow rates were the same. This was done to observe separately the effect of pressure without changing the GLR. The effect of gas density is neglected because cuttings are mainly transported in the liquid phase. The measured and predicted cuttings concentrations are presented as a function GLR for different test pressures in Fig. 9.23. Both the experimental data and model predictions indicate that the effect of pressure on cuttings concentration is insignificant. Therefore, if the effect of pressure on GLR is taken into account using a PVT equation, the effect of pressure on cuttings transport is minimal.

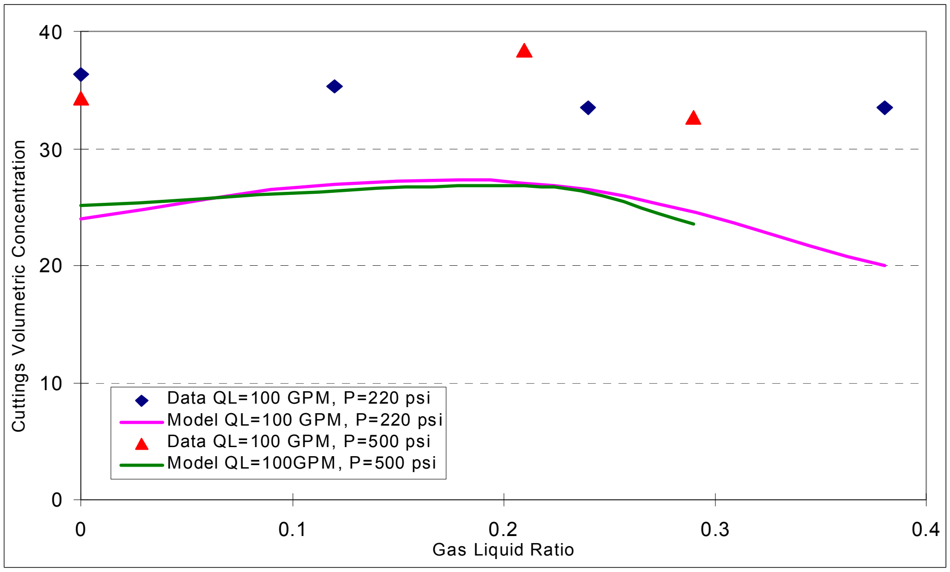

Fig. 9.23 Measured and Predicted Cuttings Volumetric Concentration vs. GLR (Q_L=100 gal/min, T=170 °F)

9.4.2 COMPARISONS OF PRESSURE LOSS PREDICTIONS

Table 9.9 compares the measured frictional pressure losses during cuttings transport tests with model predictions for the base case (Test Group #1). The absolute average differences between measured and predicted differential pressure at Q_L = 80, 100, 120 and 150 gal/min are 27.3%, 4.99%, 7.99% and 13.89%, respectively. The overall average absolute difference for the base case is 13.5%.

Table 9.9 Comparisons of Model Predictions with Measured Data for the base case

	GLR	Measured Pressure Loss (inch H_2O)	Predicted Pressure loss (inch H_2O)	Absolute Difference (%)
Q_L =80 gal/min	0.00	36.30	45	23.97
	0.12	33.30	50	50.15
	0.24	38.48	47	22.14
	0.38	39.84	45	12.95
Average Absolute Difference (%)				27.3
Q_L=100 gal/min	0.00	40.38	40.00	0.94
	0.12	39.72	42.00	5.74
	0.24	40.36	41.50	2.82
	0.38	35.42	39.00	10.11
Average Absolute Difference (%)				4.90
Q_L =120 gal/min	0.00	37.80	37.80	0.00
	0.12	40.69	39.20	3.66
	0.24	42.48	37.00	12.90
	0.38	40.18	34.00	15.38
Average Absolute Difference (%)				7.99
Q_L =150 gal/min	0.00	33.50	34.00	1.49
	0.12	30.06	34.20	13.77
	0.24	28.95	33.00	13.99
	0.38	25.33	32.00	26.33
Average Absolute Difference (%)				13.89

The experimental frictional pressure loss data for the high pressure tests and model predictions are presented in Figs. 9.24 and 9.25. The average absolute difference is 24.8% at Q_L=100 gal/min and 14.67% at Q_L=120 gal/min. As can be seen from the figures, the model follows the trend of the data curve but over predicts. The overall absolute average difference for the high pressure tests is 19.7%.

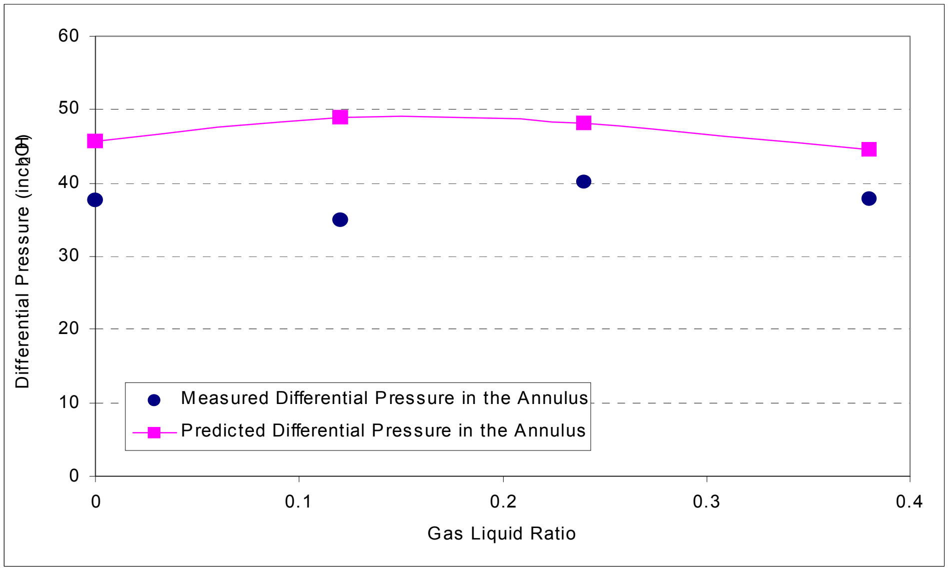

Fig. 9.24 Measured and predicted differential pressure vs. GLR (Q_L=100 gal/min, T=80°F, P= 185 psi)

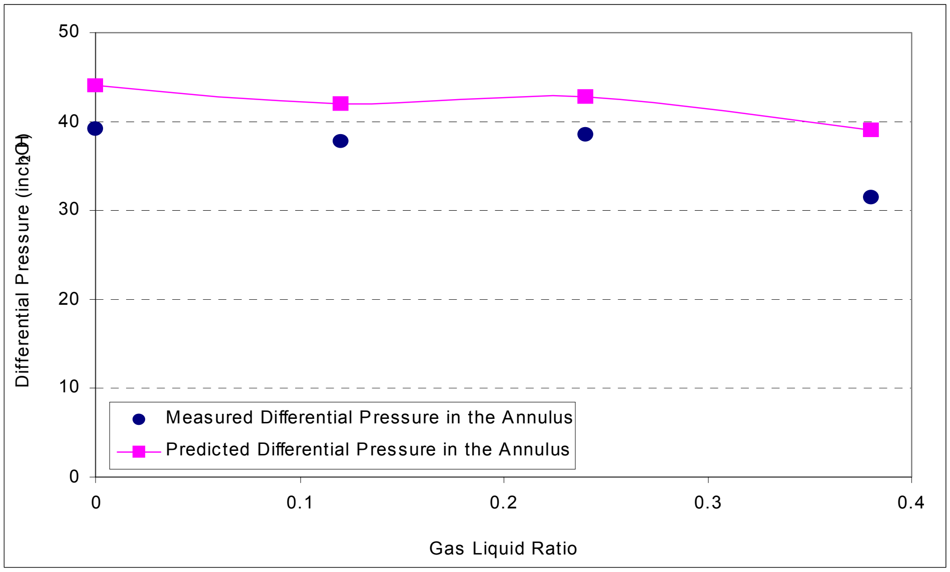

Fig. 9.25 Measured and predicted differential pressure vs. GLR (Q_L=120 gal/min, T=80°F, P= 185 psi)

9.5 DEVELOPMENT OF COMPUTER SIMULATOR

A computer program was developed based on the mathematical model. The program was written in Visual Basic version 6.0 and runs in a Windows environment. It consists of several subroutines for simulating and predicting aerated mud flow and cuttings transport. The simulator structure is shown in Fig. 9.26.

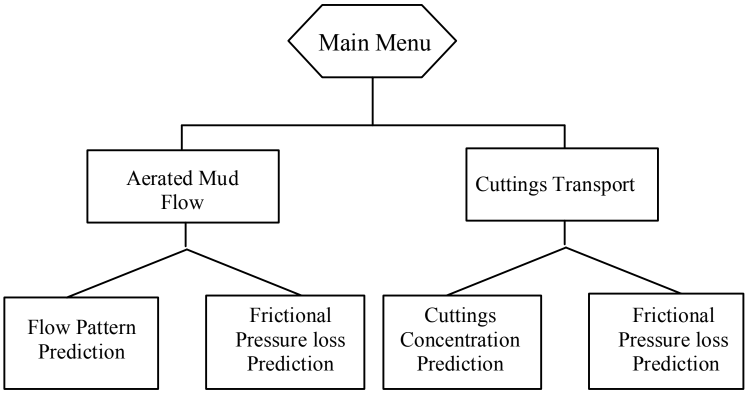

Fig. 9.26 Computer simulator structure

Figure 9.27 shows the interface of the simulator. Inputs for the computer simulator include: i) Pressure and temperature at the inlet of the section under investigation; ii) Water and air flow rates; iii) Annular geometric parameters; iv) Average cuttings diameter, specific gravity and porosity; v) Average cuttings injection rate; vi) Liquid phase density and viscosity (water is used as the default liquid phase). Outputs of the computer simulator are:

- Flow pattern
- Mixture density
- Frictional pressure loss
- Cuttings volumetric concentration
- Equilibrium bed area

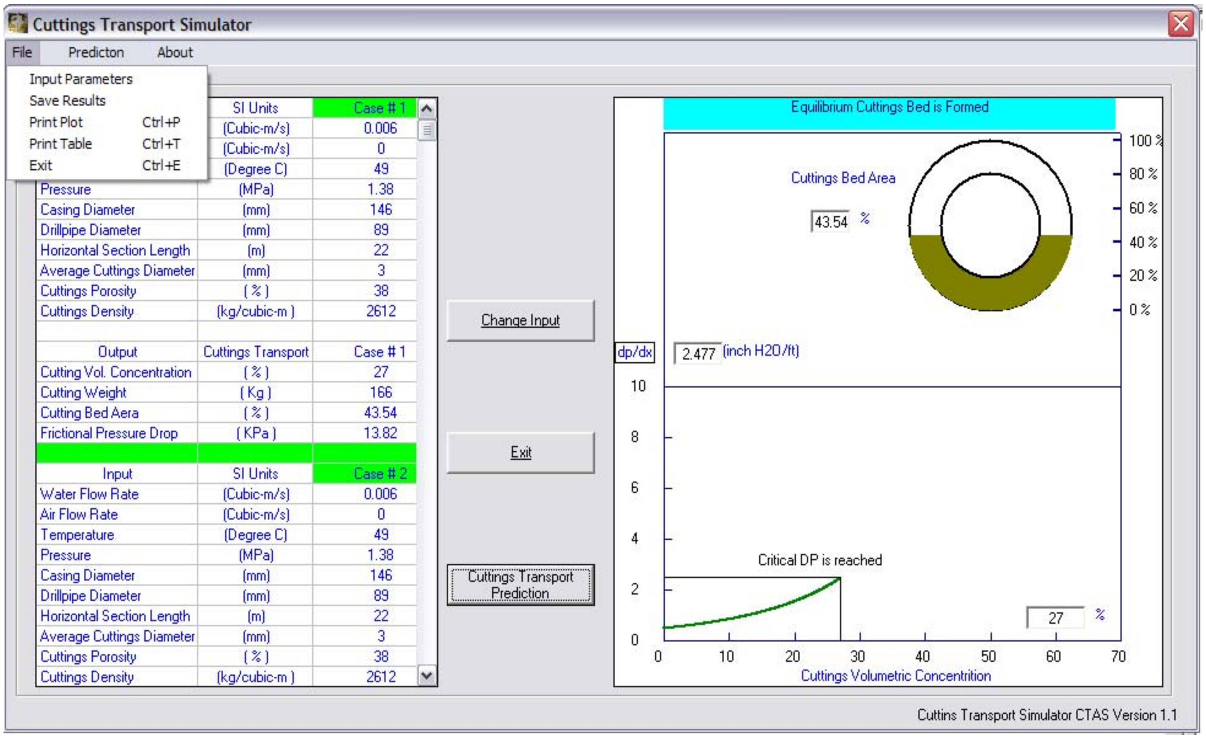

	SI Units	Case # 1
	(Cubic-m/s)	0.006
	(Cubic-m/s)	0
	(Degree C)	49
Pressure	(MPa)	1.38
Casing Diameter	(mm)	146
Drillpipe Diameter	(mm)	89
Horizontal Section Length	(m)	22
Average Cuttings Diameter	(mm)	3
Cuttings Porosity	(%)	38
Cuttings Density	(kg/cubic-m)	2612
Output	Cuttings Transport	Case # 1
Cutting Vol. Concentration	(%)	27
Cutting Weight	(Kg)	166
Cutting Bed Aera	(%)	43.54
Frictional Pressure Drop	(KPa)	13.82
Input	SI Units	Case # 2
Water Flow Rate	(Cubic-m/s)	0.006
Air Flow Rate	(Cubic-m/s)	0
Temperature	(Degree C)	49
Pressure	(MPa)	1.38
Casing Diameter	(mm)	146
Drillpipe Diameter	(mm)	89
Horizontal Section Length	(m)	22
Average Cuttings Diameter	(mm)	3
Cuttings Porosity	(%)	38
Cuttings Density	(kg/cubic-m)	2612

Equilibrium Cuttings Bed is Formed

Cuttings Bed Area 43.54 %

dp/dx 2.477 (inch H2O/ft)

Critical DP is reached

27 %

Cuttins Transport Simulator CTAS Version 1.1

Fig. 9.27 Computer simulator interface

9.6 CONCLUSIONS

9.6.1 HYDRAULICS

The experimental results of aerated mud flows indicate that the two-phase flow patterns can be affected by temperature. The flow pattern changed from stratified smooth to stratified wavy flow when the temperature increases from 80°F to 140°F for the flow with air and liquid injection rates of 50 scf/min and 50 gal/min respectively. The effect of temperature on aerated mud flows can be mainly through viscosity and surface tension of the liquid phase.

As anticipated, the measured data show a decrease of frictional pressure loss in the annulus as temperature increases. A mechanistic model has been presented for steady two-phase flows. In its present form, the model can be applied for simulated downhole conditions. The model formulations include: flow pattern prediction models, and hydraulic models for stratified and slug flows. The proposed model was evaluated and compared to the three sets of experimental data. The overall performance of the model shows a satisfactory agreement with the measured data. Comparisons between hydraulic predictions and measurements show an average error of 3.8% and an absolute average error of 12.2%.

9.6.2 CUTTINGS TRANSPORT

Cuttings transport experiments were carried out in a concentric annular test section at elevated pressures and elevated temperatures. The gas-liquid ratio was varied from 0.0 to 0.38. A cuttings transport database is presented. A mechanistic model for cuttings transport with air-water flow has been developed to predict cuttings concentration in horizontal wells. The experimental results and model predictions clearly show that:

- The volume of cuttings accumulated in the annulus is very sensitive to the liquid flow rate;
- Temperature significantly affects the cuttings transport efficiency of aerated muds;
- Predominately, elevated temperature causes a significant increase in the cuttings concentration at given flow conditions;
- Gas-liquid ratio has both negative and positive effects on cuttings transport, depending on other flow parameters;
- The effect of pressure (up to 500 psi) on cuttings concentration is minimal;
- The mechanistic model cuttings concentration predictions show satisfactory agreement with the measured data.

NOMENCLATURE

A_p = project area, m^2
C_L = lift coefficient
C_D = drag coefficient
d_p = particle diameter, m
d^+ = dimensionless particle size
D_{hy} = hydraulic diameter, m
f_1, f_2 = frictional forces, N
F_D = drag force, N
F_L = lift force, N
F_B = buoyancy force, N
F_G = gravitational force, N
g = acceleration due to gravity, m/s^2
N_1, N_2 = supporting forces, N
L_H, L_N = perpendicular distance to the line of action, m
u = local velocity, m/s
u^* = friction velocity, m/s
u_C^* = critical friction velocity, m/s
u^+ = dimensionless velocity
y^+ = dimensionless distance from the wall
y = distance from the wall, m
$\Delta P/\Delta X$ = pressure gradient, pa / m

Greek Letters

μ = dynamic viscosity, pa.s
ρ_s = solid density, kg/m^3
ρ_L = liquid density, kg/m^3
τ_w = wall shear stress, Pa

10. Development of Cuttings Monitoring System (Task 11)

10.1 OBJECTIVE

The ultimate objective of this task is to develop a non-invasive technique for quantitatively determining the location of cuttings in the drill pipe. There are four different techniques that could be examined:

1. Ultrasound;
2. X-Ray/γ-Ray;
3. Optical;
4. Electrical Impedance.

Due to the fact that the pipes are metallic the contrast in conductivity and dielectric constants are of very limited use. Therefore, only three have good potential for success. These are:

1. Ultrasound;
2. X-Ray/γ-Ray;
3. Optical.

The optical approach has potential in transparent fluids. Therefore, we kept this as a possible option if the other two approaches did not prove to be either economically or technically feasible.

X-ray/γ-ray approach has good potential for success. However, there may be health risks associated with these so we would utilize them in a limited capacity unless ultrasound approach proves to be uneconomical or not feasible. Additionally, the cost of the X-ray/γ-ray sensors appears to be higher.

We have concentrated our efforts on the ultrasound technique. If this technique did not prove to be successful then we planned to switch to the other techniques or use a hybrid system that would utilize a combination of these techniques.

10.2 TEAM COMPOSITION

The instrumentation team charged with completing Tasks 11 consisted of Dr. Gerald R. Kane and Dr. Kaveh Ashenayi both registered professional engineers and professors of Electrical Engineering Department at the University of Tulsa. MS level graduate students assisted them. These students have BS degrees in EE and CS. This particular combination works well because successful completion of this project requires skills needed in both disciplines. To achieve objectives of this task we developed a very complicated electronic hardware/sensor and a software package that correctly interprets the data received. In addition, Dr. Len Volk is a member of this team working on Task 12.

10.3 SELECTION OF SENSORS AND DESIGN OF DATA ACQUISITION BOARDS

After doing the literature survey and research we decided to employ an Ultrasonic method for this task. For implementing ultrasonic technique we reviewed various ultrasonic transducers available and selected E-152/75 from Massa Corporation. Figure 10.1 shows this ultrasonic transducer.

Fig. 10.1 Ultrasonic Transducer (E 152/75)

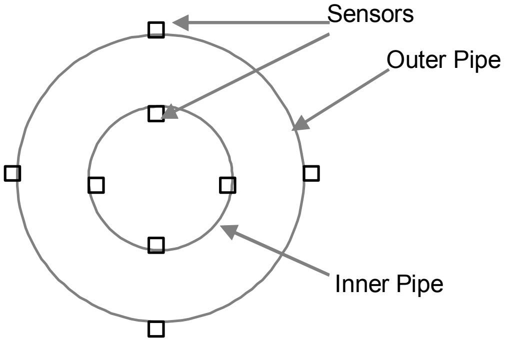

Fig. 10.2 Basic envisioned setup

By using these ultrasonic transducers an initial idea of mounting these sensors in two rings on the inner and outer concentric pipes and having many such rings along the length of the annular pipes was envisioned. Figure 10.2 shows the envisioned arrangement. Since placing the inner rings of sensors adds significant complexity to the project implementation, we decided to revise our approach. So we decided to initially use just the outer rings of sensors. Later on if needed we could perform the experiments with inner rings as well. The arrangement with just the outer rings of sensors is shown in Fig. 10.3.

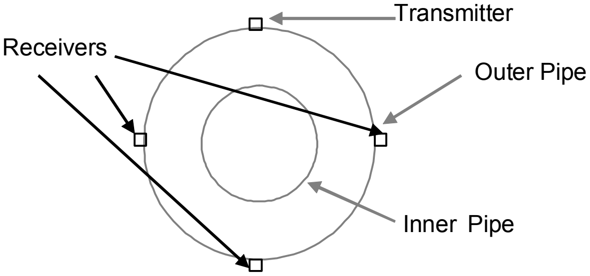

Fig. 10.3 Basic setup with only outer rings of sensors

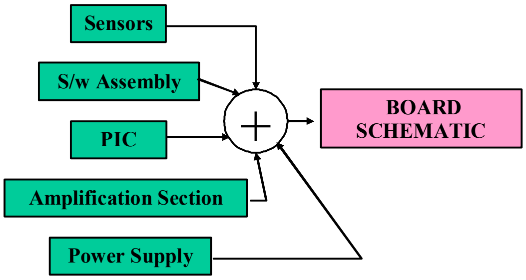

Fig. 10.4 Building blocks of data acquisition scheme

The basic objective is to use a technique similar to MRI technology. At each instant of time only one sensor in each ring acts as the transmitter and remaining three sensors act as receivers. The sensor acting as transmitter in each ring will be changed every time a measurement is being made. Hence, at every instance we can capture a different view of the cuttings as they move along the length of the pipe with the flow. Then the data collected creates an image of what is happening in the pipe. Data collected is time stamped so they can all be correlated. In order to control the operation of sensors as transmitters and receivers and to acquire the received data from the receivers a data acquisition board is required for each ring. The data acquisition system can be imagined being made up of different modules or blocks as shown in the Fig. 10.4.

10.3.1 SENSORS AND TUNING CIRCUITS

The ultrasonic transceivers can be configured as transmitter or receiver. Figures 10.5 and 10.6 show the designs of the respective tuning circuits for each configuration of the transceivers.

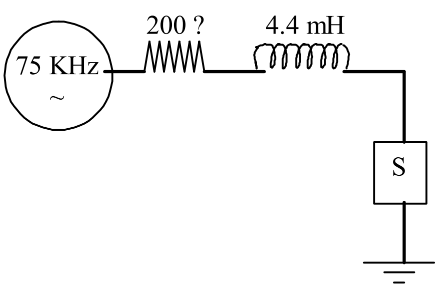

Fig. 10.5 Transmitter tuning circuit

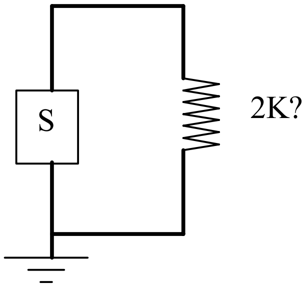

Fig. 10.6 Receiver tuning circuit

10.3.2 SWITCHING ASSEMBLY

Since a transceiver acts either as a transmitter or as a receiver at any given time a relay switch and sensor are used to achieve the switching between the transmitter and receiver circuits. Figures 10.7 and 10.8 show the schematic of the relay and control scheme of the sensor.

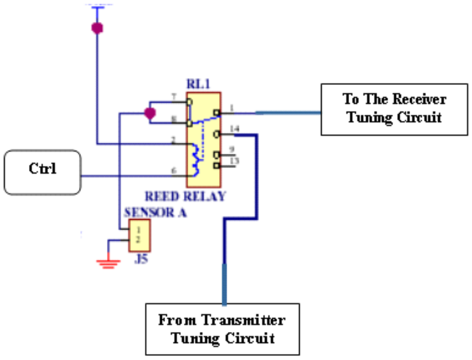

Fig. 10.7 Schematic of reed relay

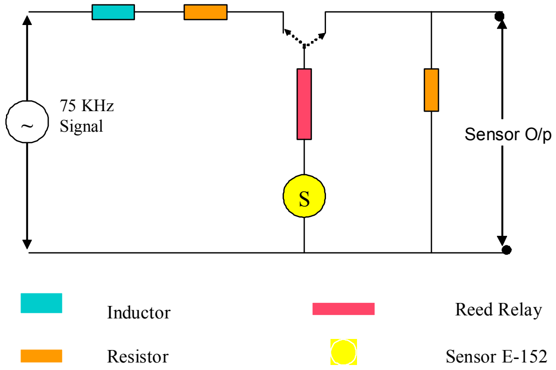

Fig. 10.8 Control scheme of a sensor

10.3.3 PROGRAMMABLE INTERRUPT CONTROLLER

A microcontroller (PIC 16F876) is used to operate the relay and the sensor used to switch between the transmitter and receiver configurations. Figure 10.9 shows the schematic of the PIC 16F876. The microcontroller also converts the analog data received from the sensors to digital data by using its 10-bit analog to digital converter (atod) and then transports it to the PC using it's built-in Universal Asynchronous Receiver Transmitter (UART) to the serial communication port on the PC. The sampling rate at which the data is acquired is much faster than the flow rate of the system and hence the received data is averaged. The firmware necessary to carry out these operations is developed which incorporates following commands.

1. Reset: Used to reset the system;
2. Set Transmitter: Used to configure a particular sensor as transmitter;
3. Sampling rate: Used to set desired sampling rate in multiples of 2X;
4. Acquire data: Convert the received analog data to digital data and send it to PC.

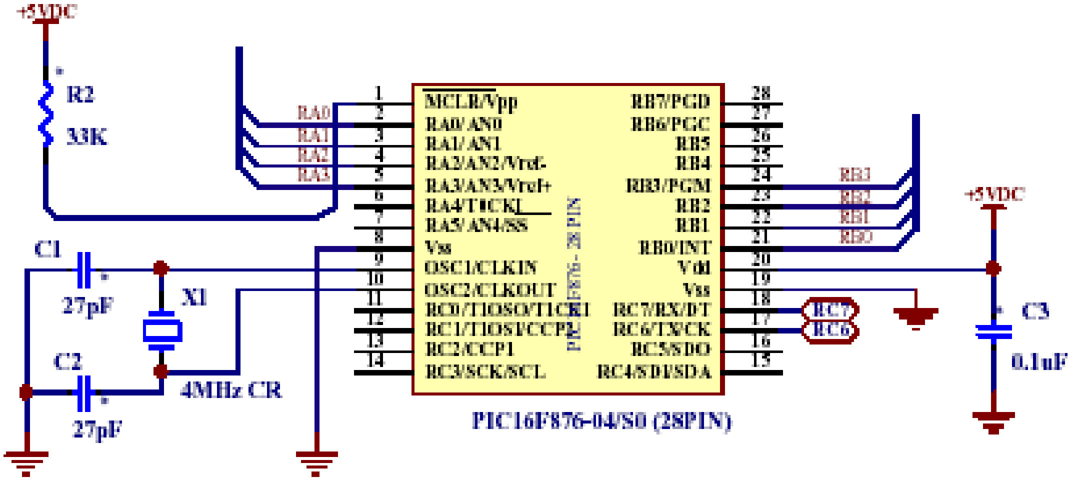

Fig. 10.9 Schematic of microcontroller (PIC 16F876)

10.3.4 AMPLIFICATION SECTION

The voltage sensed by the sensors is very low and hence it is necessary to amplify the received signal. Also a pre-amplification of the 75 KHz input signal to the transmitter is necessary for the satisfactory operation of the system. Figures 10.10 and 10.11 show the pre and post amplification sections respectively.

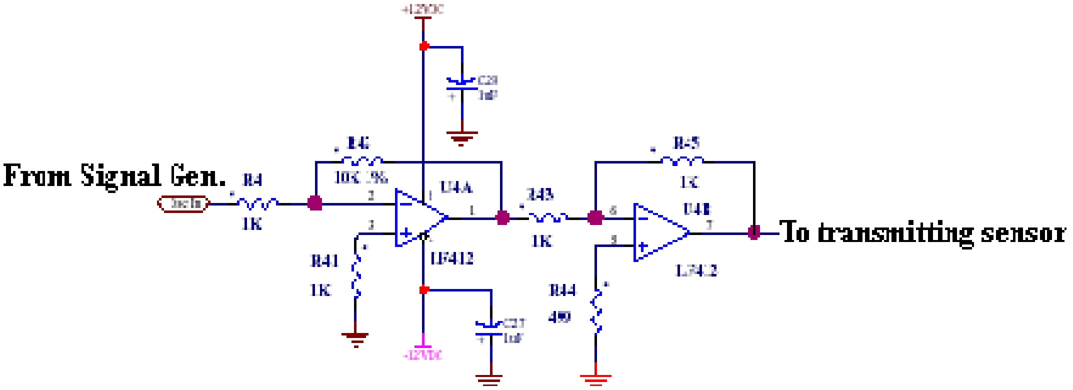

Fig. 10.10 Preamplifier section for transmitter

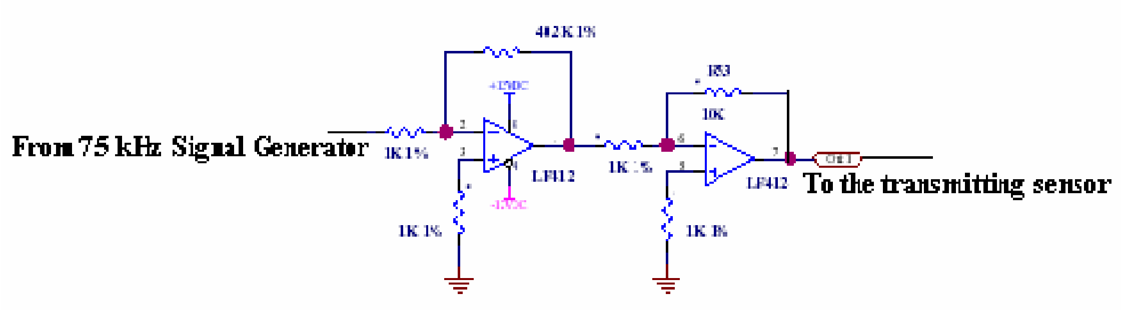

Fig. 10.11 Post amplification section for the receiver

All the data acquisition and control boards of each ring are daisy chained and they communicate with the PC through serial communication. Figure 10.12 shows a photograph of the first version of data acquisition board.

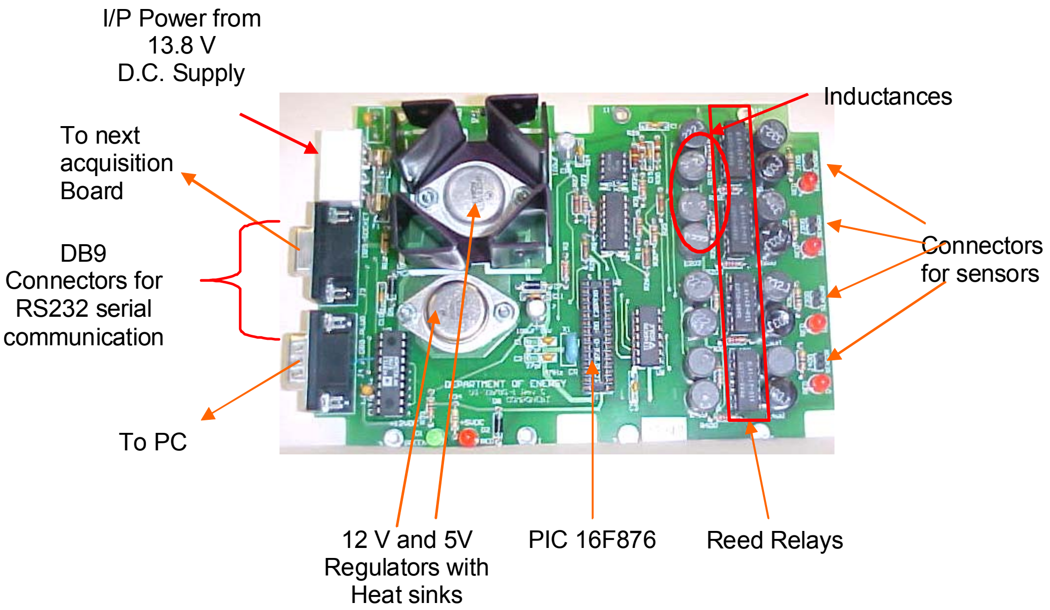

Fig. 10.12 Initial version of data acquisition and control board

After testing the initial board we found out that the acquisition and control board had a severe noise problem. Two different sources of noise were identified as high frequency ground noise and noise from radiating components at 75 KHz. To eliminate the radiated 75 KHz noise we decided to reduce the number of inductors used. We did so by using a common set of inductors for the transmitter tuning circuit because at any given time only one sensor is configured as the transmitter. Also, we replaced the leaky reed relays by the solid-state relays and physically isolated the common inductances of the transmitter tuning circuit from the receiver tuning circuit. We also implemented optical isolators to isolate the microcontroller from noise signal radiated by the inductances in the transmitter tuning circuit. After incorporating these changes the modified acquisition and control board appeared as shown in Fig. 10.13. A graph presented in Fig. 10.14 indicates reduction in noise level achieved by the new design of the board. After reducing the noise we were able to perform static tests for verifying the performance of the acquisition system. For performing these static tests we devised two simple static test cells.

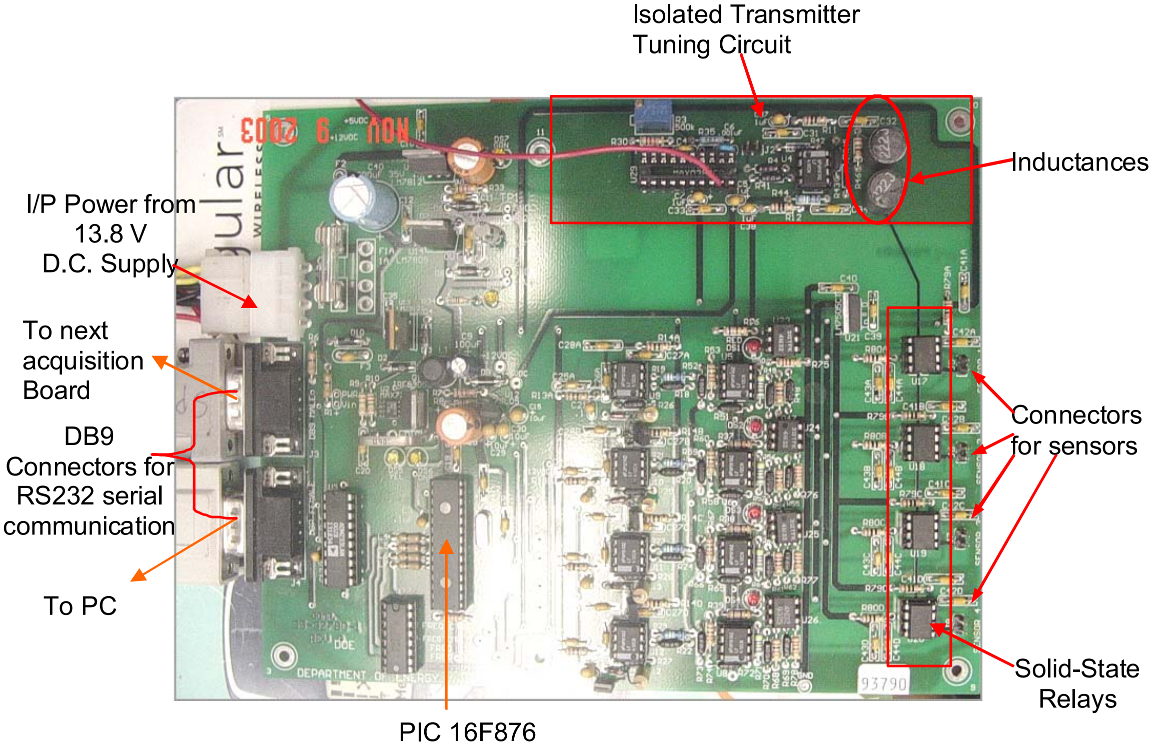

Fig. 10.13 Modified data acquisition and control board

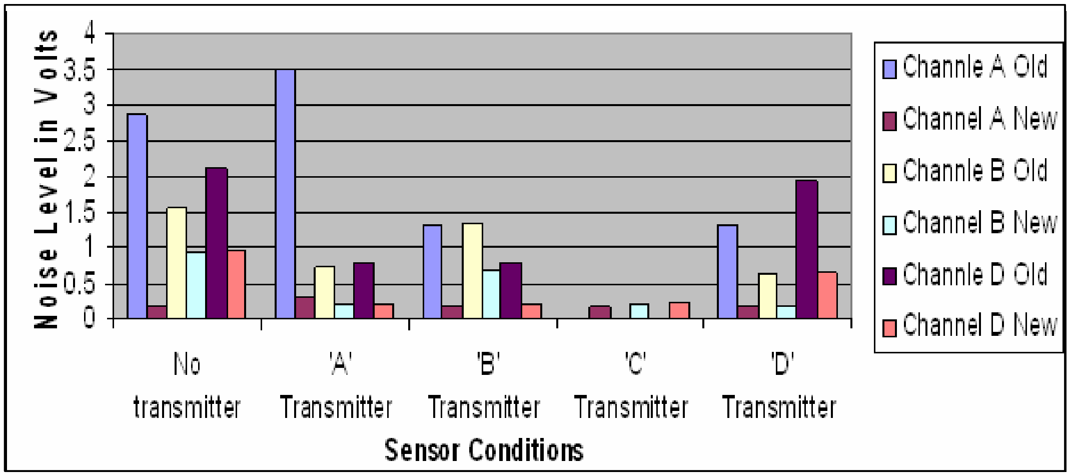

Fig. 10.14 Noise reduction due to new board design

10.4 STATIC AND HEAT TESTS

Figure 10.15 show these static test cells and the results obtained with these test cells are listed in Tables 10.1 and 10.2.

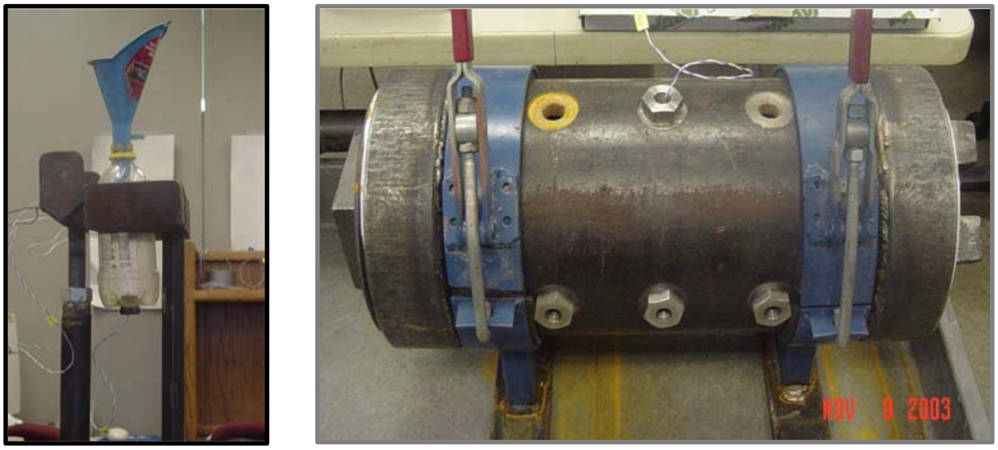

(a) (b)

Fig. 10.15 Static Test Cells: a) Transparent plastic bottle; and b) Opaque Steel test cell

Table 10.1 Static Test Cells

Conditions	Average Voltage Received
Empty bottle	1.348 V
Bottle entirely filled with water	5.000 V
With 1” Sand in bottle filled with water	3.367 V
With 2” Sand in bottle filled with water	2.980 V
With 3” Sand in bottle filled with water	2.130 V

Table 10.2 Static Test Results Obtained by Using Transparent Plastic Bottle

Conditions	Average Voltage Received
Steel test cell entirely filled with water	5.00 V
With 1” sand in steel test cell filled with water	3.10 V
With 2” sand in steel test cell filled with water	2.60 V
With 3” sand in steel test cell filled with water	1.69 V
With 4” sand in steel test cell filled with water	1.05 V

The cuttings bed height in the opaque steel test cell is geometrically determined. Figure 10.16 shows the geometric representation of the test cell, which is used to calculate the height of cuttings bed; where D_o and D_i are the outer and inner diameters of the test cell; L is the length of the test cell; H_s is the height of the cuttings bed added at a time in the test cell.

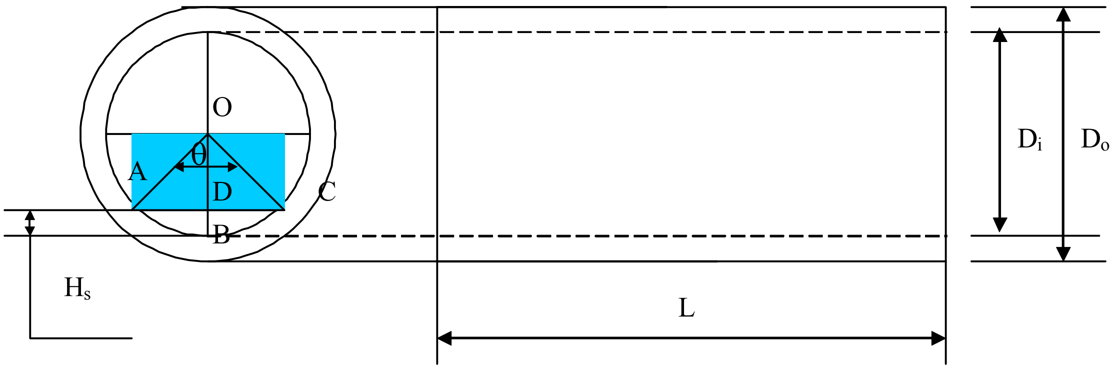

Fig. 10.16 Geometric representation of the static steel cell

To verify our findings of the static test on the steel cell we also conducted a static test by using the new test cell with clear see-through plastic on one end. The system did classify different sand levels differently and we observed that as sand was added the system response changed. But there was inconsistency in the readings due to varying sensor positions in the caps and different cuttings bed distributions due to different ways of pouring the sand and human error. To overcome this inconsistency it is necessary to secure the sensors in the caps in a particular way every time. Slight variation in position causes inconsistency in performance. To achieve this consistency we tried many methods such as stuffing papers and using earplugs. After many such trials we devised a secure and repeatable way of positioning the sensors in the cap 'exactly the same way every time' by devising 'inserts with threads' and rubber washers for cushioning. Figure 10.17 shows a photograph of the way the sensors are positioned in the cap.

Fig. 10.17 Sensor positioning scheme

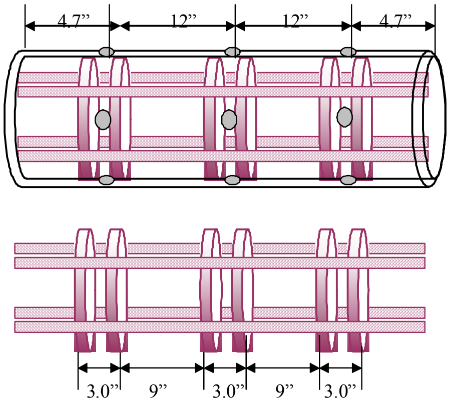

Fig. 10.18 Arrangement of screens and wire framework

We need consistent data to be able to train Artificial Neural Network (ANN) for analysis of the result. Unknown/unaccounted variations in cuttings bed height while collecting data also cause inconsistency in the performance of the ANN analysis tool. To prevent this, and to prevent sand from getting into the rest of the low-pressure test system, we are using a test cell with screens and wire frame to section off the portion underneath the sensor ring. The sand poured in these restricted sections will attain a consistent bed height. Due to this consistency in bed height, determining the cuttings bed height geometrically is justifiable. Figure 10.18 shows the schematic for the arrangement of the screens and wire framework.

We also performed a heat test to verify the durability of sensors and effect of heat on the sensors. Figure 10.19 presents the average received voltage as a function of temperature. It is observed from the heat test results that variation in sensor response with increase in temperature is linear and hence can be compensated in analyzing the data obtained at various temperatures.

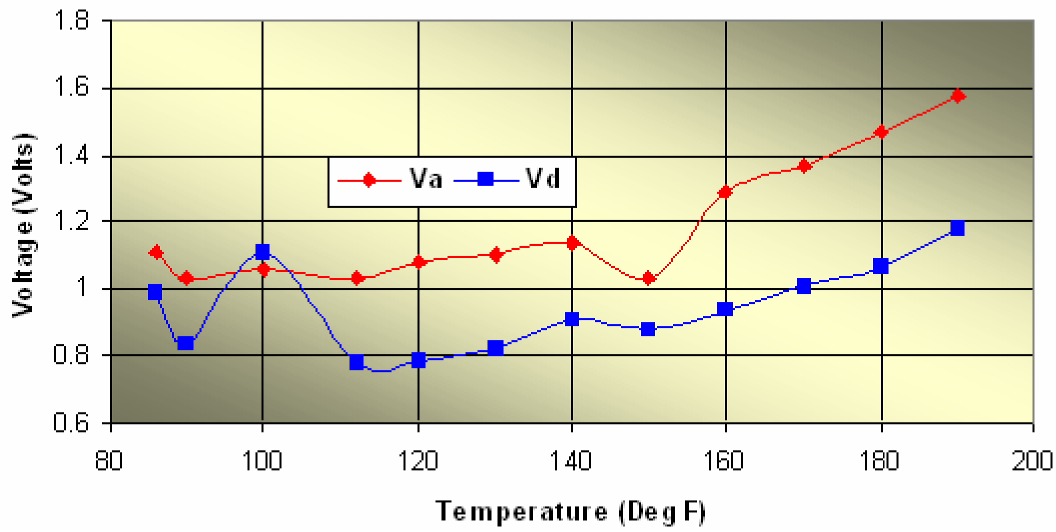

Fig. 10.19 Response of the sensors versus temperature

We have developed the data collection software. The software starts by allowing the user to setup the communication characteristics of the system. Then it proceeds to identify the number of boards connected. The data received from the sensor board is in the form of ASCII characters. We developed and tested the conversion algorithm that allows us to calculate the numerical voltage value corresponding to the character combinations that are received. We revised the software and the firmware for higher precision and accuracy.

Using the screens and wire framework for achieving consistent cuttings bed height and the devised sensor-positioning scheme we performed static and dynamic tests under low-pressure conditions. The test data is gathered and processed by the software, and is stored and managed using MS Access. This data is exported as a text file to be used as input for the neural network development package we purchased. We have trained some neural networks using Thinks Pro Neural Networks Version 1.05 for these static and dynamic tests.

For training the neural network we used different architectures and configurations of the network along with different preprocessing techniques for the input data. We also used different transfer functions for the hidden layer and output layer of the network. For input data we considered differences in the readings as cuttings bed height is increased in 1” increments with respect to readings for the no-sand condition. Using consecutive cuttings bed height differences we generated a different data set. In this case we used differences between the successive 1” increase in cuttings bed height. We used both normalized and non-normalized input data for training. For testing the trained neural networks we used different data sets acquired during the static and dynamic tests performed. Table 10.3 shows a summary of the results obtained from trained neural networks for different test data. The nomenclature used for identifying different networks is shown in Fig. 10.20.

A preliminary test was conducted on the main flow loop at 100 gpm flow rate and 20 lb/min cuttings injection rate. The measured bed thickness using ultrasonic method showed a satisfactory agreement with nuclear densitometer readings. The test involved installing two rings of sensors. We then proceeded and calibrated the sensors. This process was repeated several times due to different mechanical failures. The following outlines some of the reasons. We had a cap that was leaking and that put the unit into saturation. Long untwisted wire acts as an antenna and picks up stray RF signals. We had another cap that was sheared so it was not sitting flat. We had to replace wires due to the length effect on the value read. After we calibrated the sensors, we started to collect data. We collected a total of thirty different data points. These were collected after the test section was put in liquid hold mode. Readings indicated 2.5 to 2.7 inches of sand. The corresponding nuclear densitometers readings were between 2.5 and 3.1 inches.

Table 10.3 Neural Network Results for Different Test Data

Training Set	Testing Set	Transfer Function	Nodes in hidden layer	Classification
1961OPD0	2561OPD0	Sigmoid Bipolar	8	68.00%
2561OPD0	1961OPD0	Sigmoid Bipolar	8	70.00%
1961OPD0	2561OPD0	Sigmoid Bipolar	6	71.00%
2561OPD0	1961OPD0	Sigmoid Bipolar	6	68.00%
1961OPD0	2561OPD0	Sigmoid Bipolar	4	76.00%
2561OPD0	1961OPD0	Sigmoid Bipolar	4	66.00%
1961OPDC	2561OPD0	Sine Bipolar	8	89.00%
2561OPDC	1961OPD0	Sine Bipolar	8	89.00%
1961OPDC	2561OPDC	Sine Bipolar	6	80.00%
2561OPDC	1961OPDC	Sine Bipolar	6	80.00%
1961OPDC	2561OPDC	Sine Bipolar	4	92.20%
2561OPDC	1961OPDC	Sine Bipolar	4	88.00%
1961OPD0	2561OPD0	Sigmoid Bipolar	8	68.00%
2561OPD0	1961OPD0	Sigmoid Bipolar	8	70.00%
1961OPDC	2961OPDC	Sine Bipolar	4	19.44%
1961OPD0	2961OPD0	Sigmoid Bipolar	4	50.00%
1963OPDC	2563OPDC	Bipolar	4	70%
2563OPDC	1963OPDC	Bipolar	4	59%
F2961OPDC	F2161OPDC	Sine Bipolar	4	44%
F2961OPDC	F2161OPDC	Sine Bipolar	8	45%
N1963OPD0	N2563OPD0	Sine	4	50%

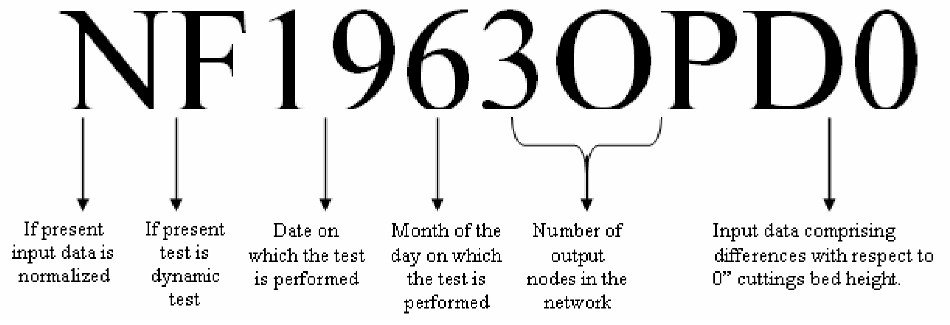

Fig. 10.20 Neural network nomenclature

In all of these cases there were 16 input nodes representing the 16 values read by each sensor ring when each of the four sensors acted as transmitter. The output nodes varied between one (1) to three (3) nodes. The single output node seems to perform the best.

We used the standard error backpropagation (BP) technique to train the neural networks studied. We did use different non-linearity functions as is evident from Table 10.3. The objective of this experimentation was to see if multi-threshold functions perform better or not.

We also needed to preprocess the training data. Also, the actual data collected needs to be preprocessed in similar fashion. In what follows we will describe the process.

Preprocessing the Collected Data

1. Arrange the training data in ascending order. By this operation the data is batched with respect to increase in height of the cuttings bed. Table 10.4 shows the arrangement of training data.
2. Segregate the collected data according to the transmitters as shown in Table 10.5. For a ring of four sensors there would be 4 sets of columns and for every transmitter in the ring there would be 4 sub-columns. Hence there would be 16 columns all together. Note that multiple values are collected for each case. We used 5 data points for each case.
3. Perform Difference by zero operation on the voltages read.

Table 10.4 Arrangement of Training Data

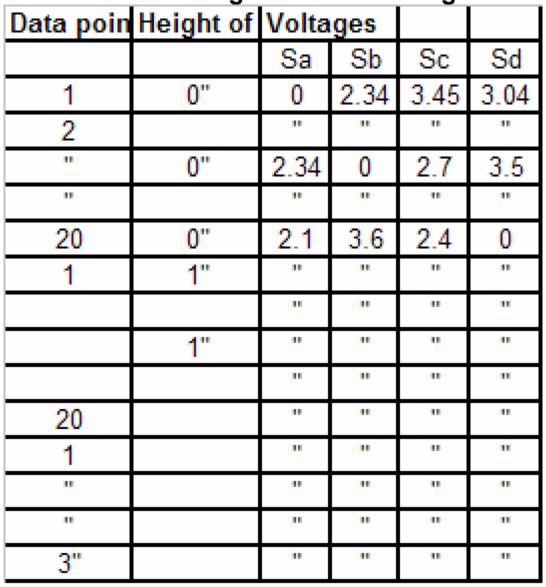

Data poin	Height of	Voltages			
		Sa	Sb	Sc	Sd
1	0"	0	2.34	3.45	3.04
2		"	"	"	"
"	0"	2.34	0	2.7	3.5
"		"	"	"	"
20	0"	2.1	3.6	2.4	0
1	1"	"	"	"	"
		"	"	"	"
	1"	"	"	"	"
		"	"	"	"
20		"	"	"	"
1		"	"	"	"
"		"	"	"	"
"		"	"	"	"
3"		"	"	"	"

Difference by zero operation is defined as calculating the ratio of difference of voltages recorded at different height of cuttings with the reference voltage (data recorded at zero cuttings height) to the maximum voltage read by a sensor.

Note: The maximum voltage, which can be recorded by the sensor in database, is 5 Volts. For example, for increase in height of cuttings from 0” to 1” for transmitter A and receiver B value is given by (RbTa at 0” – RbTa at 1”)/ 5, where RbTa = voltage read by sensor B when B is the receiver and A is the transmitter. Similarly the difference by zero is calculated for all the data points collected.

Table 10.5 Sample Data Collected From the Transmitters

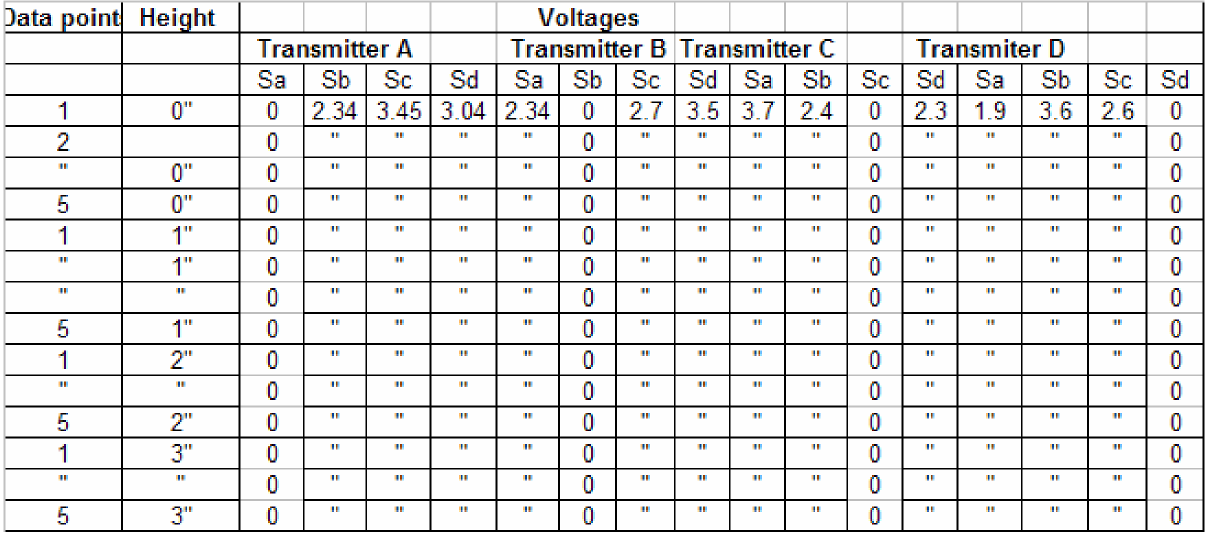

Data point	Height	Voltages															
		Transmitter A				Transmitter B			Transmitter C				Transmiter D				
		Sa	Sb	Sc	Sd	Sa	Sb	Sc	Sd	Sa	Sb	Sc	Sd	Sa	Sb	Sc	Sd
1	0"	0	2.34	3.45	3.04	2.34	0	2.7	3.5	3.7	2.4	0	2.3	1.9	3.6	2.6	0
2		0	"	"	"	"	0	"	"	"	"	0	"	"	"	"	0
"	0"	0	"	"	"	"	0	"	"	"	"	0	"	"	"	"	0
5	0"	0	"	"	"	"	0	"	"	"	"	0	"	"	"	"	0
1	1"	0	"	"	"	"	0	"	"	"	"	0	"	"	"	"	0
"	1"	0	"	"	"	"	0	"	"	"	"	0	"	"	"	"	0
"	"	0	"	"	"	"	0	"	"	"	"	0	"	"	"	"	0
5	1"	0	"	"	"	"	0	"	"	"	"	0	"	"	"	"	0
1	2"	0	"	"	"	"	0	"	"	"	"	0	"	"	"	"	0
"	"	0	"	"	"	"	0	"	"	"	"	0	"	"	"	"	0
5	2"	0	"	"	"	"	0	"	"	"	"	0	"	"	"	"	0
1	3"	0	"	"	"	"	0	"	"	"	"	0	"	"	"	"	0
"	"	0	"	"	"	"	0	"	"	"	"	0	"	"	"	"	0
5	3"	0	"	"	"	"	0	"	"	"	"	0	"	"	"	"	0

Running a neural network

Having completed the preprocessing we then need to run the data through the ANN for classification. The following outlines steps involved:

1. Open one of the saved trained networks in the ThinksPro application software;
2. Click on the test set and copy the preprocessed data to it;
3. Disable the training feature of the network and then run the test.

Note: This data does not have a desired output; Output of this data is calculated by the help of the trained network).

Classification of the Data

1. Locate the maximum and minimum values of the outputs in the training set.
2. Find the testing criteria by following the procedure explained below.

   Testing criteria is acquired by dividing the range of values in the training set in to three equal parts. These parts will denote the volume of cuttings added to get 1”, 2” and 3” of height of the cutting bed.

   <u>Example</u>

   Assume the minimum value of the output is 0.33853

   The maximum value of the output is 0.894302

   Set point= (0.894302- 0.33853)/ 3 = 0.185257

Therefore, for 1” bed, the range would be = 0.33853 to 0.33853+0.185257
= 0.33853 to 0.523787
Similarly for 3”, the range would be = 0.894302 - 0.185257 to 0.894302
= 0.709045 to 0.894302.
And for 2”, the range would be = 0.523787 to .0.523787.

Note: The values 0.523787 and 0.70945 are the testing criteria for this network. That is values less than 0.523787 denotes 1” of cuttings bed and the values above 0.70945 denotes 2” of cuttings bed.

3. These criteria are applied to the test output. An approximated height of bed is calculated.
4. These values are then analyzed to give the efficiency of classification of the test network.

For example

Number of values denoting 1” of cutting bed =7
Number of values denoting 2” of cutting bed=24
Number of values denoting 3” of cutting bed= 9

The values clearly indicate that the height of cuttings bed is equal or greater than 2” and not equal to 3” or 1”.

Note: The network performance in terms of accurate classification will greatly depend on the training set used. Hence, the ANN should be periodically retrained when new data is collected.

Calculating the volume of cuttings bed in the pipe section

1. Find the maximum and minimum values of the test output;
2. With help of the testing criteria discard the bad data points (in this case discard all the values denoting 1” of cutting bed height);
3. From the example it is clear that the height of cuttings bed is in the 2” – 3” range. Apply the boundary condition (maximum and minimum values) and the testing criteria (from the network with highest efficiency) to further divide the range to give the actual volume multiple of each data point;
4. Calculate the average of all volume multiples;
5. The volume to the cuttings inside the pipe section is given by the product of the volume multiple to the volume of cuttings required to attain 1” cuttings bed height in the pipe section;
6. Calculate the standard deviation and the confidence interval of the volume obtained;

7. Look up these values in the look up table provided to give the height of cuttings bed in the Flow loop.

Calculating the height of cuttings bed in the pipe section

1. Look up the corresponding height of cuttings bed for the volume calculated.

   Note: the look up table created was for volume of cuttings required for every 0.005 increase in bed height.

2. Find the corresponding confidence interval for the height of cuttings bed.

   Note: All of the above calculations were made for a pipe section without drill pipe inside it. For the pipe section with the drill pipe we need to add a correction factor to get actual height of cuttings bed. Correction factor is calculated using geometrical methods. Since all the dimensions are known we can estimate the displaced volume and calculate the corresponding rise in the sand height.

Schematics of the Final Version of the Sensor Control Board

The final version of data acquisition and sensor control board is a four-layer board with a ground plane between different signal planes to reduce radiated noise and cross talk. In what follows we will present the schematics and routing diagrams.

Figures 10.21 through 10.25 in the following pages provide the schematic for different parts of the final version of the data acquisition and control board. Figure 10.21 shows the over all schematics of the board. Figure 10.22 shows the circuitry used for the onboard oscillator circuit that produces the 75 kHz signal used to drive the ultrasound devices. The signal produced by this sub circuit is fed into the sensors via the connection marked as “OSC IN” on the sensor control (Green boxes) in the schematic.

Details of the sensor control circuit represented as green boxes in Fig. 10.21 are shown in Fig. 10.23. This block controls the operation of the transceivers. Using this circuit we can switch the units between transmitter and receiver mode via the onboard micro-controller.

Figure 10.24 represents the actual routing of the signal traces in the board. Special attention has been given to separate signals and isolate different sub systems to make sure that noise and cross talk are minimized.

Figure 10.25 shows the ground plane that was used to eliminate the radiated noise. The required inductors were mounted below the ground plane.

In Table 10.6 the bill of material (BOM) used for assembling the control board is presented. The BOM lists all components used. It describes each component and provides the quantity needed. It also, provides a designator that will identify where on the board this part will be used. In addition, the footprint used for each component is specified.

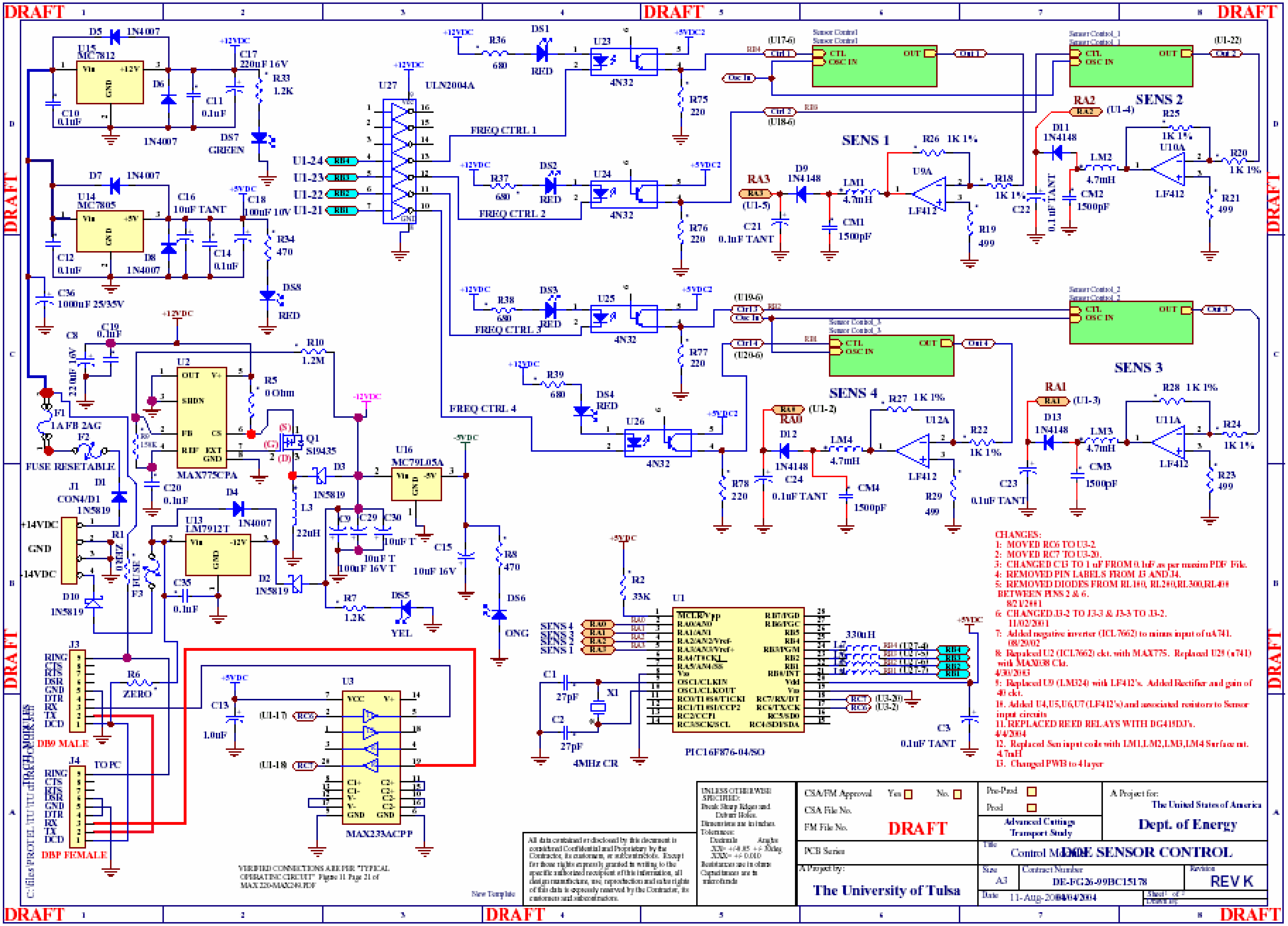

CHANGES:
1: MOVED RC6 TO U3-2
2: MOVED RC7 TO U3-20.
3: CHANGED C13 TO 1 uF FROM 0.1uF as per maxim PDF File.
4: REMOVED PIN LABELS FROM J3 AND J4.
5: REMOVED DIODES FROM RL100, RL200,RL300,RL400 BETWEEN PINS 2 & 6.
8/21/2001
6: CHANGED J3-2 TO J3-3 & J3-3 TO J3-2.
11/02/2001
7: Added negative inverter (ICL7662) to minus input of uA741.
08/29/02
8: Replaced U2 (ICL7662) ckt. with MAX775. Replaced U29 (u741) with MAX038 Ckt.
4/30/2003
9: Replaced U9 (LM324) with LF412's. Added Rectifier and gain of 40 ckt.
10. Added U4,U5,U6,U7 (LF412's) and associated resistors to Sensor input circuits
11. REPLACED REED RELAYS WITH DG418DJ's.
4/4/2004
12. Replaced Sen input coils with LM1,LM2,LM3,LM4 Surface mt. 4.7mH
13. Changed PWB to 4 layer

Fig. 10.21 Design of sensor control

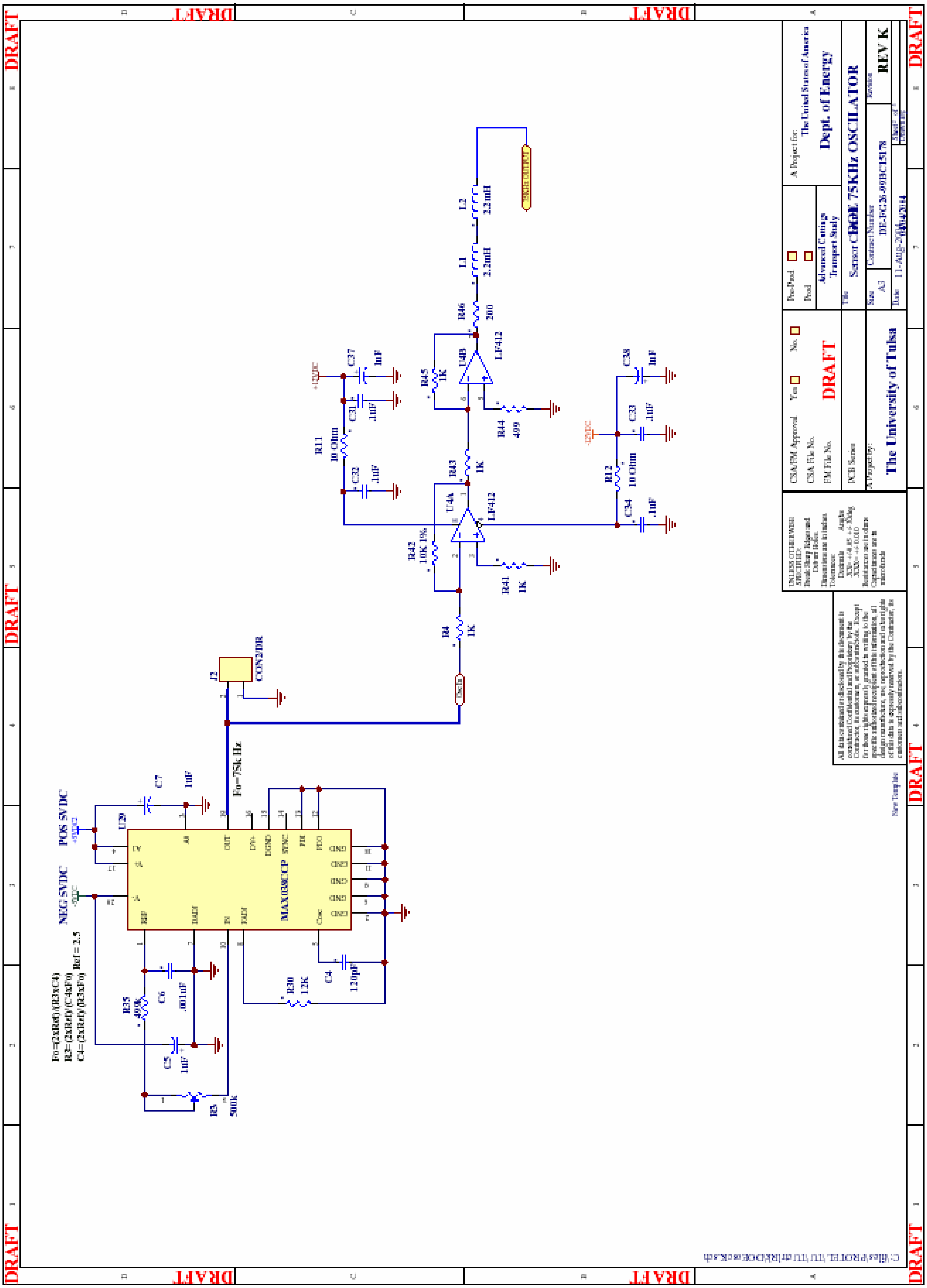

Fig. 10.22 75 KHz Oscillator Circuit

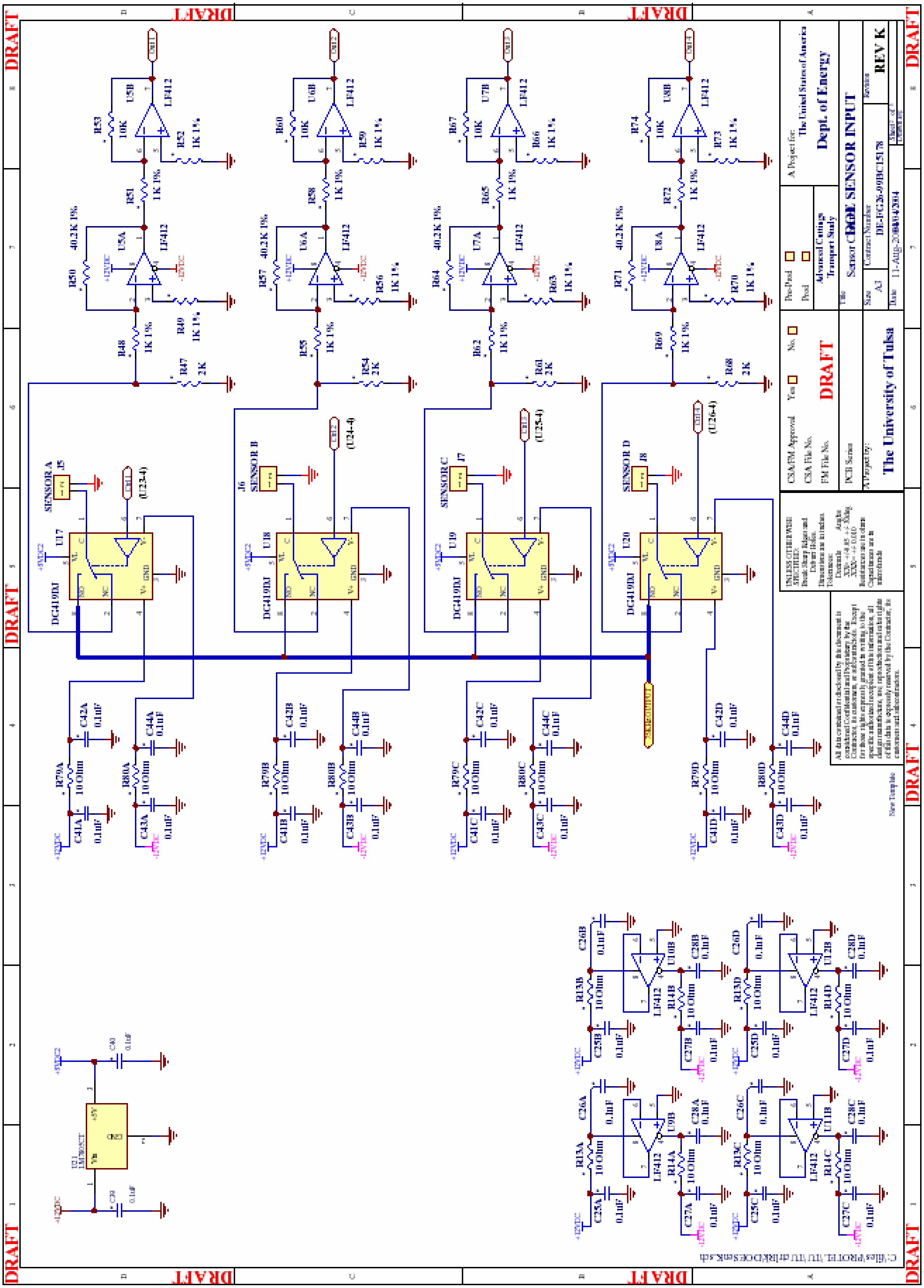

Fig. 10.23 Design of sensor block

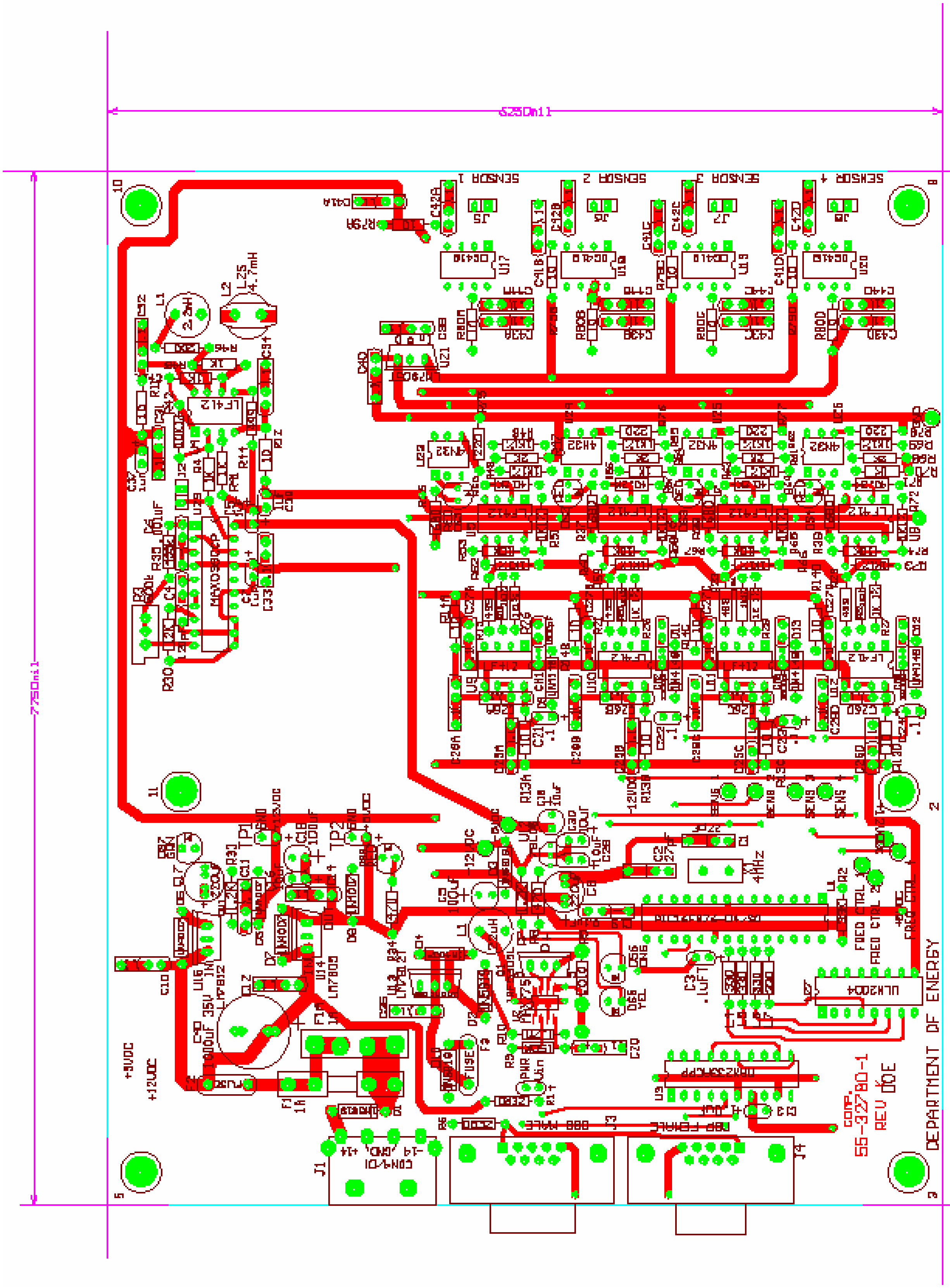

Fig. 10.24 Routing of the signal traces

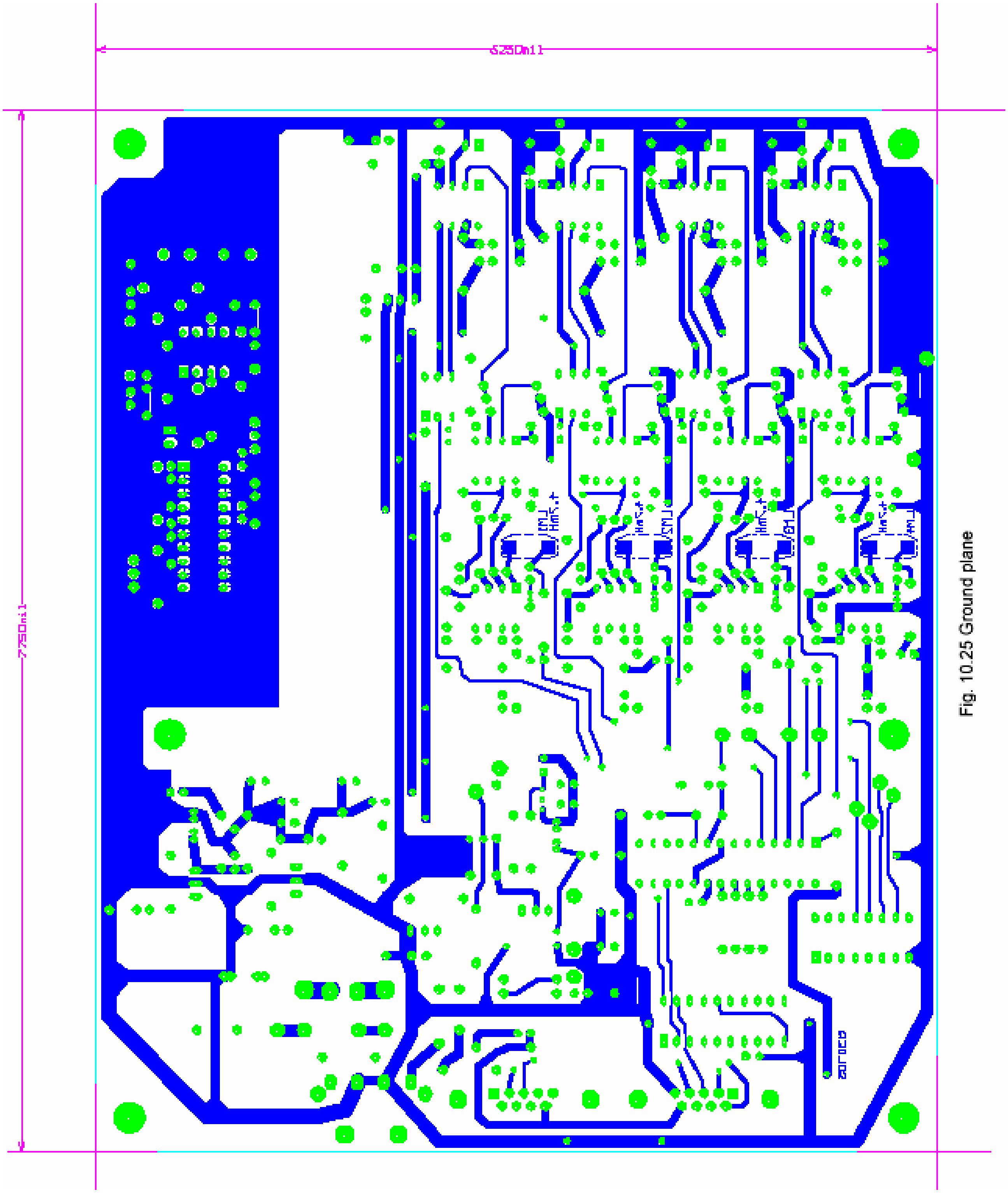

Fig. 10.25 Ground plane

11. Development of Instrumentation for Foam Bubble Characterization (Task 12)

11.1 INTRODUCTION

Bubbles (as foam or aerated fluid) will be moving at a high rate (in excess of 6 ft/s) in the drilling section of the ACTF, and may be very small (down to 10 mm). The bubble size and size distribution influence the fluid rheology and the ability of the fluid to transport cuttings. Bubbles in a shear field (flowing) may tend to be ellipsoidal which might alter both the rheology and transport characteristics. The objective of this task is to develop the methodology and apparatus needed to measure the bubble size, size distribution and shape during cuttings transport experiments. This task is divided into four subtasks:

Subtask 12.1. *Develop/test a microphotographic method for static conditions.* This task includes magnifying and capturing bubble images, measuring bubble sizes and shapes, and calculating the size distribution and various statistical parameters.

Subtask 12.2. *Develop/test a method for dynamic conditions.* This task develops the methods needed to apply the results of Subtask 12.1 to rapidly moving fluids, especially the method of “freezing” the motion of the bubbles. A dynamic testing facility was designed and constructed in conjunction with Task 11 for development and verification.

Subtask 12.3. *Develop simple, noninvasive methods for bubble characterization*. Added in year 3, this task aims at the development of simple, inexpensive and small-in-size methods for characterizing bubbles.

Subtask 12.4. *Provide technical assistance for installation on ACTF*. Techniques and methods developed under Subtask 12.2 and 3 are applied to the ACTF in this task.

11.2 PROJECT STATUS

11.2.1 STATIC BUBBLE CHARACTERIZATION

Bubble size in foams can vary over a wide range, depending on how the foam is prepared, the final system pressure and the chemical composition, but it is not uncommon to find bubbles with diameters down to 10 μm (0.01 mm). The minimum magnification to be able to analyze the bubble images is about 250X, but more may be needed, possibly as high as 400X. Initial magnification requirements did not include any allowance for “photographic “magnification that occurs when using a CCD attached to the microscope. The microscope needs a minimum working distance (distance from the object being photographed to the bottom of the objective lens) of 4 to 5 cm to allow for the thickness of the high-pressure glass window (~3/4 inch) and the window-retaining ring (~1/2 inch). This is illustrated in Fig. 11.1.

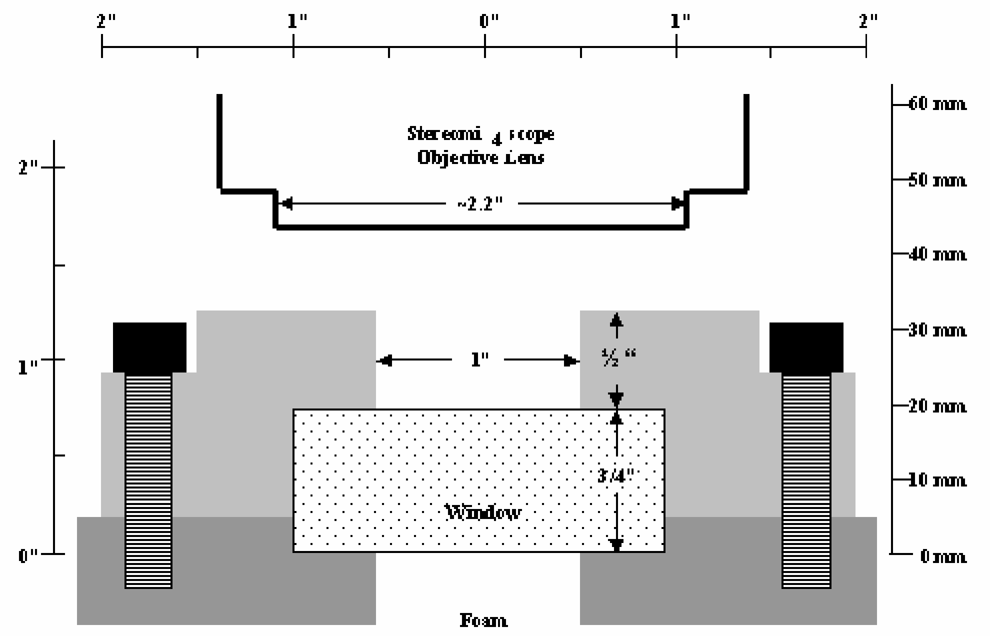

Fig. 11.1 Minimum working distance requirement and typical windowed high-pressure cell geometry

Stereomicroscopes typically have large working distances to view the surface features of large objects and can have maximum magnifications ranging from 225X to 450X. After evaluating several stereomicroscopes, we purchased a Nikon SMZ-800 stereomicroscope.

Illumination Method

An ambient pressure optical cell was constructed to evaluate different illumination methods and develop a feel for microscopic evaluation of foam. Figure 11.2 shows the schematic of this cell, which has an optical path length of 0.5”. In initial experiments with shaving cream, bubbles were easily seen using transmitted light. The layer of bubbles beneath those next to the window could be seen, but not easily. Figure 11.3 is a photo of foam taken through a microscope with a 35 mm camera. It is worthwhile to note that the second level bubbles are visible through the larger surface bubbles. The biggest drawback with using transmitted light is the loss of light intensity as the light passes through the bubbles (absorption by the liquid phase and scattering at the gas-liquid interface). If the illuminating light is directed onto the surface of the region being observed, the bubbles are almost indistinguishable (no contrast). This is the most common illumination method for microscopic studies of opaque samples and is shown in Figure 11.4, left side. If, however, the light is directed into the front surface of the bubbles, but somewhat remote from the viewing region, the bubbles become visible, though appear very different from transmitted illumination, also shown in Figure 11.4, right side. Figure 11.5 shows shaving cream illuminated in this way. The appearance is similar to transmission electron micrographs where the surface is gold-sputtered.

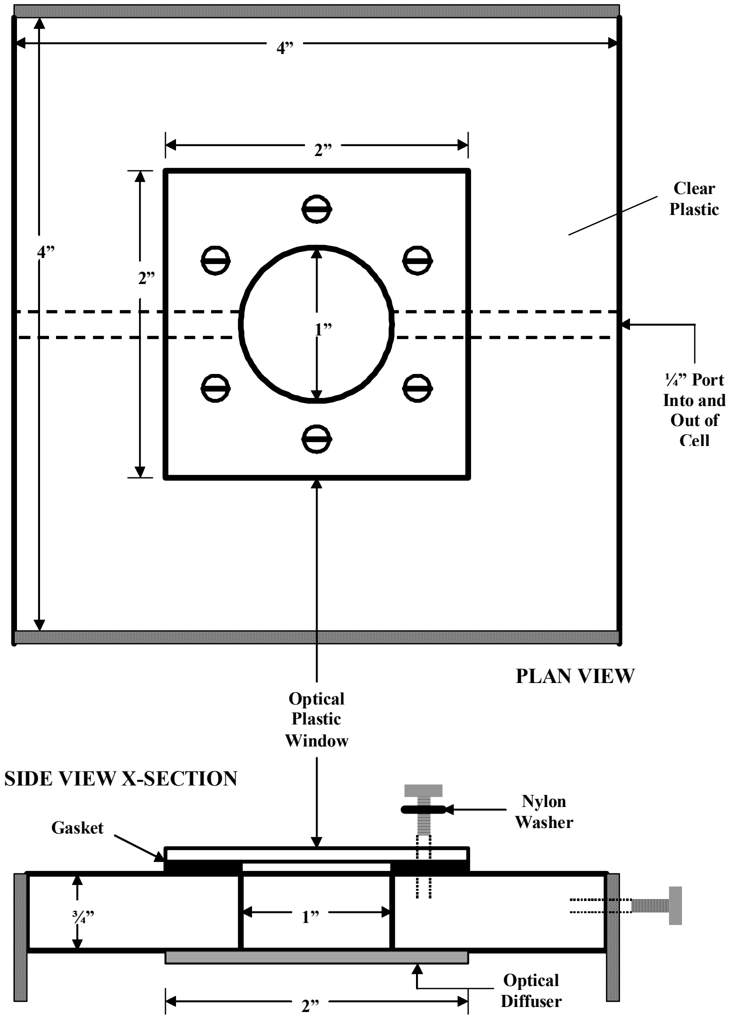

Fig. 11.2 Ambient pressure optical cell for microscope evaluation and illumination studies

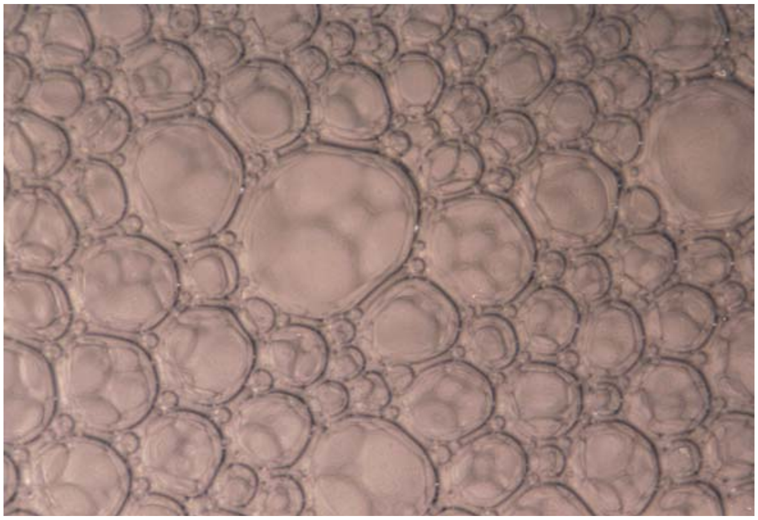

Fig. 11.3 Microphotograph of foamed drilling fluid using transmitted light

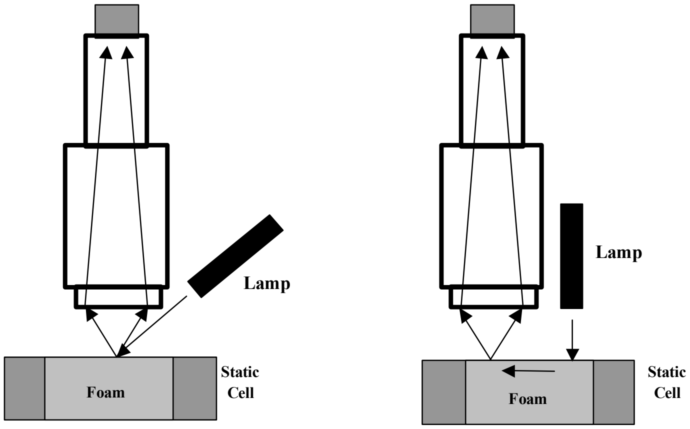

Fig. 11.4 Two methods for surface illumination

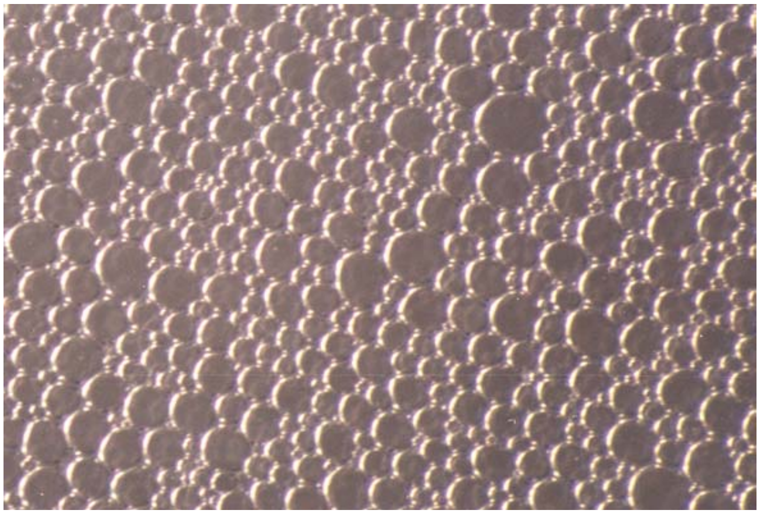

Fig. 11.5 Microphotograph of shaving cream illuminated indirectly from the front

Image Acquisition

There are basically two methods of capturing the bubble images for further processing: electronic, such as with a digital camera, and film. At the beginning of this project, digital cameras were expensive (~$5000) and lacked resolution and versatility. Digital cameras were not considered initially for capturing bubble images. Attaching a 35 mm camera to the microscope via a phototube was only marginally successful. Determining the appropriate light level using the built-in light meter was difficult at best. Several of the prints were not in sharp focus, most likely due do to vibration of the camera's focal-plane shutter when operating at the required ½ to 1/16 second. Manufacturers of the better grade of microscopes have coped with this problem by developing their own exposure meter and shutter system. Our experience with a 35 mm camera increased the attractiveness of CCD cameras, especially with the passage of time as they improved and prices began to drop. A CCD camera would offer some advantages over film photography for dynamic imaging:

- Almost unlimited imaging;
- No digitization requirement;
- Easy synchronization with pulsed light source;
- Electronic aperture control;
- Pseudo real-time imagining

During Year 2, we ordered and received a SMZ800 Nikon stereomicroscope along with two sets of eyepieces (X10 and X30) and two objectives (X1.5 and X2) that provide magnification from X15 to X378, and working distances of 50.5 mm (X1.5 objective) and 40 mm (X2.0 objective). These combinations allowed us to image bubbles down to 10 µm. The microscope was ordered with a boom stand to facilitate placing it directly in front of the view port window of flow cells. We have purchased a conventional microscope illumination source for examining static samples (150 watt halogen lamp equipped with a fiber optic cable).

11.2.2 DYNAMIC BUBBLE CHARACTERIZATION

Light Source

Since fluids containing microscopic bubbles might be flowing at 6 ft/s or greater, the motion of the bubbles must be “frozen” to image. In ordinary photography, the shutter serves this purpose. However, the speed of mechanical shutters is too slow. To freeze a 0.01 mm diameter bubble moving at 6 ft/s, the shutter speed must be ~0.3 µs. The simplest method is to use a pulsed light source. Figure 11.6 gives the relation between bubble size, fluid velocity and shutter speed or flash duration for 5% blur (5% blur means that the bubble can move 5% of its diameter while the shutter is open or the flash is on).

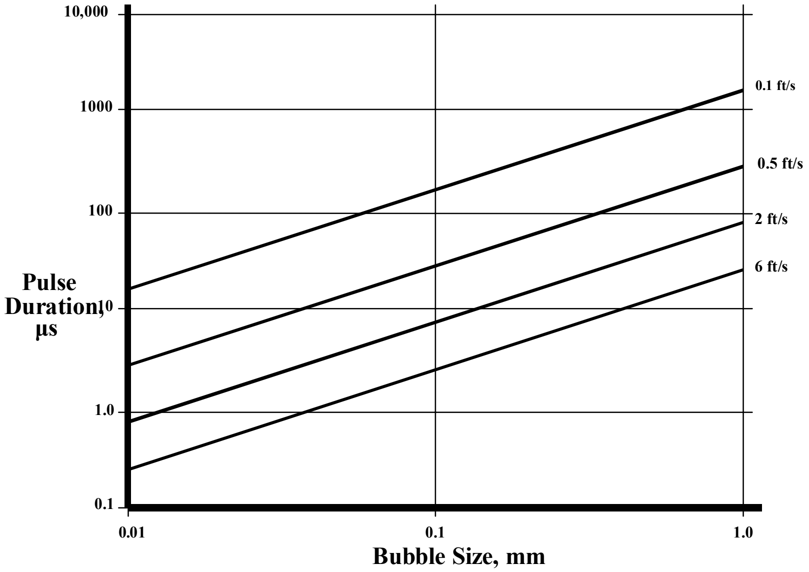

Fig. 11.6 Bubble size versus light pulse duration (shutter) for various fluid velocities

Figure 11.7 shows the timing sequence using a pulsed light source. Commercially available xenon strobes have flash durations longer than 7-10 μs. Gas discharge lamps with flash durations down to 4 ns are known, but their light intensity is very low. Lasers, operating in the visible or ultraviolet, having pulse widths shorter than 0.1 μs, are common. If an ultraviolet laser is used, the light can be converted to visible light using a laser dye. One question at this stage of the project was what light intensity would be required if a pulsed light source was used?

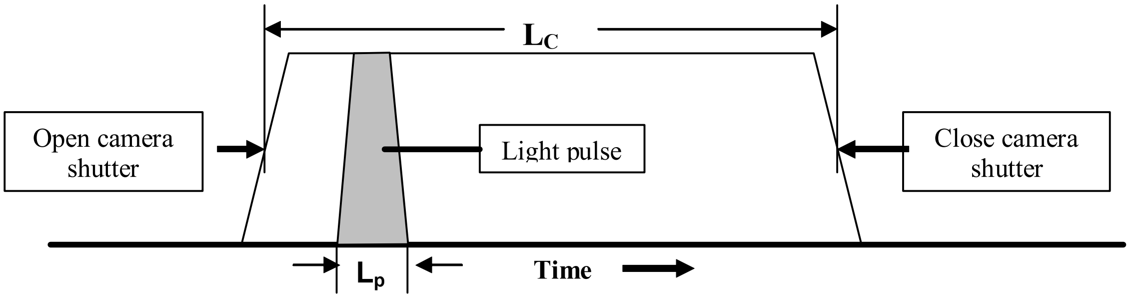

Fig. 11.7 Relative timing for opening a camera shutter, the opening duration (L_c), and the width (L_p) of the pulsed light source

During Year 2, we examined the usefulness of a laser as a microphotographic light source and continued to explore the availability of short-duration pulsed flash lamps.

Laser. Bubbles (shaving cream) illuminated with light from a 1 mW He-Ne laser revealed a problem with laser light source – specular reflection. Under a microscope, this phenomenon appears as “black bugs” running around in the viewing region, making visualization very difficult. This effect and the low average power of pulsed lasers (within our price range) posed problems for using a laser as a light source for imaging.

Pulsed gas discharge lamp. We located and purchased a short-duration xenon flash system from Oriel during Year 2. The flash has a 1.6 µs pulse width. Based on a 1.6 s pulse width, Fig. 11.6 gives us the smallest bubble we will be able to image, assuming that 5% blur (5% bubble movement during the light pulse) as a function of the fluid velocity.

We purchased a black and white CCD (Panasonic GP-MF130P/E), a frame grabber and a flash timing unit (VarioFlash) from The Image Source. The CCD has variable electronic shutter speeds from 1/100s to 1/96,000s and a frame capture rate of 30/s. Although these short shutter speeds may be of use later, the image exposure time will be controlled by the xenon flash because (1) the xenon flash is faster (1.6 µs), and (2) using the CCD to control the shutter speed would require an extremely high-powered (intense) continuous light source (expensive). The VarioFlash unit can provide a delayed trigger to the xenon flash to ensure that the flash occurs while the CCD is in an “acquire” mode.

During the quarter ending October 2001 (Year 3), low-quality, low-pressure foam was generated in the Dynamic Testing Facility (DTF). Although electronic images were captured, no bubble characterization was attempted at this time. We used both transmitted light and reflected light; however, residual cutting oil from the construction of the DTF coated the optical windows making transmitted light imaging particularly difficult.

During the April 2002 quarter (Year 3), we realized that the static mixer of the ACTF did not seem to impart sufficient energy to form fine-textured foam. As viewed through the sight glass cell, there seemed to be a liquid phase and bubbles in the foam on top of this liquid phase were large. As an alternate method of foam generation, an inline ball valve was partially closed while the Moyno pump was circulating fluid to provide a pressure drop. Visual observation through the sight glass cell showed that only uniform foam was flowing and that the bubble size was very small. Foam quality calculated from the fraction of water (with surfactant) removed from the system agreed with the foam quality calculated for a sample removed from the loop after adjusting for the change in pressure. For a permanent solution, we realized that a needle valve with a rather large flow coefficient was needed in a leg parallel to the static mixer. Although the static mixer is not useful for foam generation, it would be helpful for mixing chemicals “on-the-fly” such as foam breaker, friction reducer, corrosion inhibitor, etc.

During the July 2002 quarter (Year 3), microscopic images were obtained of foam generated in a blender and the DTF. Foam from the blender was injected into the atmospheric visualization cell shown in Fig. 11.2. Bubbles measured soon after injection (~ 1 minute 15 seconds) ranged from 60 μm to 500 μm diameter. Foam generated in the DTF and injected into this cell were as small as 40 μm but a few were up to four times this size, after adjusting for the drop in pressure. Bubble size depends on the shear rate (needle valve opening and flow rate). Whenever bubbles are examined with the visualization cell, the bubbles rapidly grow with time. Images of bubbles captured through the view port in the DTF circumvent this problem so long as the fluid passes through the needle valve. The bubble size varies between 25 μm and 100 μm at loop pressure, depending on the number of turns the needle valve is open and the flow rate. It seems apparent that in the time required to remove the foam from the DTF and inject it into the visualization cell (~75 s) the bubble size increases considerably.

The platform constructed to hold the microscope and CCD camera was attached to the DTF superstructure. Minor vibrations are amplified considerably by the microscope boom stand, causing some imaging problems. During the October 2002 (Year 4) quarter, a freestanding microscope bench is constructed to decouple the microscope from the DTF to reduce vibration. The picture quality on the video monitor or captured by the frame grabber was considerably poorer than that viewed through the microscope itself. We began looking into the possibility of acquiring a microscope-mounted digital camera to improve the image quality.

Residence time. There are several considerations when developing correlations to the average bubble size of foam. For a given surfactant formulation, the average bubble size is determined by the shear rate, the time at this shear rate and the length of time following this high shear until the bubble size is measured. On the DTF, these are:

- The needle valve opening that generates the foam and the volumetric flow rate (shear rate);
- The length of time required for the fluid to pass through the needle valve time (time at shear) – a very short time;
- The residence time of the loop;
- The equilibrium time.

Multiple passes through the needle valve and the residence time tend to produce a steady state bubble size distribution. In this work, we attempt to run the tests long enough so that the foam is in equilibrium (or steady state). This means that the bubbles are continually draining and coalescing, and periodically being reformed as the fluid passes through the needle valve. The residence time in the loop determines how long the foam has to drain and coalesce between subsequent exposures to high shear of the needle valve. The residence time can be calculated as follows:

$$R_H = \frac{V_H}{F_H} = \frac{V_H}{F_L\left[1 + Q_L(P_L/P_H - 1)\right]} \tag{11.1}$$

$$R_L = \frac{V_L}{F_L} \tag{11.2}$$

$$R_T = R_H + R_L \tag{11.3}$$

Where

F = Flow Rate
Q = Foam Quality
P = Pressure
V = Volume
R = Residence time

And the subscripts are defined as:
L = Low pressure section
H = High pressure section
T = Total

Note that V_L is the volumetric flow rate of the Moyno pump. Figure 11.8 shows a much simplified schematic of the DTF loop for ease of understanding the above equations.

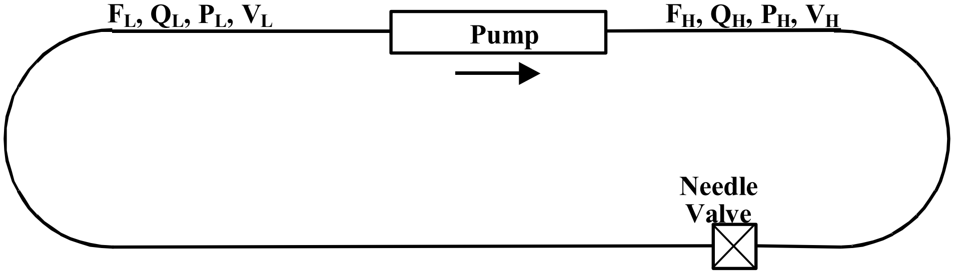

Fig. 11.8 Simplified schematic of the DTF flow loop

Typical residence times vary from 30 to 60 s although shorter and long times are possible.

Foam Quality Measurement. Prior to the April 2003 quarter (Year 4), the foam quality was measured by withdrawing a foam sample from the pressurized loop into a graduated cylinder, allowing it to collapse, and measuring the resulting liquid volume, compensating for bubble expansion due to the drop in pressure. This technique has a few problems: (1) As the foam is withdrawn from the loop, large bubbles are formed in the withdrawal process, changing the foam quality. (2) As the foam quality or shear rate increases, the bubble size tends to decrease, increasing the time required for the foam to collapse. To circumvent these problems, a 150 ml stainless cell was purchased and valves installed at each end. After weighing the empty cell and cell filled with water, we are able to calculate the cell volume. To measure foam quality, the cell is first completely filled with water and attached to a port on the DTF. Then the water in the cell is slowly displaced by foam. This process allows the foam to remain at essentially loop pressure, preventing flashing. Once all the water is displaced, some additional foam is allowed to slowly flow out of the cell to displace foam that was at the foam-water interface. Weighing the cell filled with foam give us the weight of the water-surfactant mixture in the cell, which allows us to calculate the foam quality. Repeated tests produce foam qualities within ±0.1. The addition of 1% surfactant and 0.1% corrosion inhibitor result in only minor changes in the fluid specific gravity taken to be the specific gravity of pure water and can be ignored. These changes produce less than ±0.01 change in foam quality. Since this stainless cell and associated valves are pressure rated to 1800 psi, the apparatus is also useful on the ACTF loop. Figure 11.9 is a photo of this apparatus for measuring foam quality at system pressure.

Fig. 11.9 Apparatus for measuring foam quality under system pressure

During the July 2003 quarter (Year 4), a Hitachi KP-F120CL progressive scan digital camera was purchased and installed (October 2003 quarter) on the Nikon microscope attached to the DTF. This camera has a high pixel density (24,100 pixels/mm^2) for high resolution images, and high quantum efficiency for improved performance under low light conditions that exist with microscopic imaging.

In the summer of 2003, a stop-flow technique was developed that will allow us to capture bubble images without the need for ultra fast shutter speeds or microsecond flash systems. This technique will be discussed further under the ACTF Bubble Characterization Cart development.

11.3 CONSTRUCTION AND OPERATION OF THE DYNAMIC TESTING FACILITY

In order to develop bubble characterization techniques, and test instrumentation for cuttings tomography under dynamic conditions, a facility referred to as the Dynamic Testing Facility (DTF) was designed during Year 1 and completed during Year 2. Figure 11.10 is a schematic of the DTF upon nearing completion at the end of the third quarter (April 2001) of Year 2.

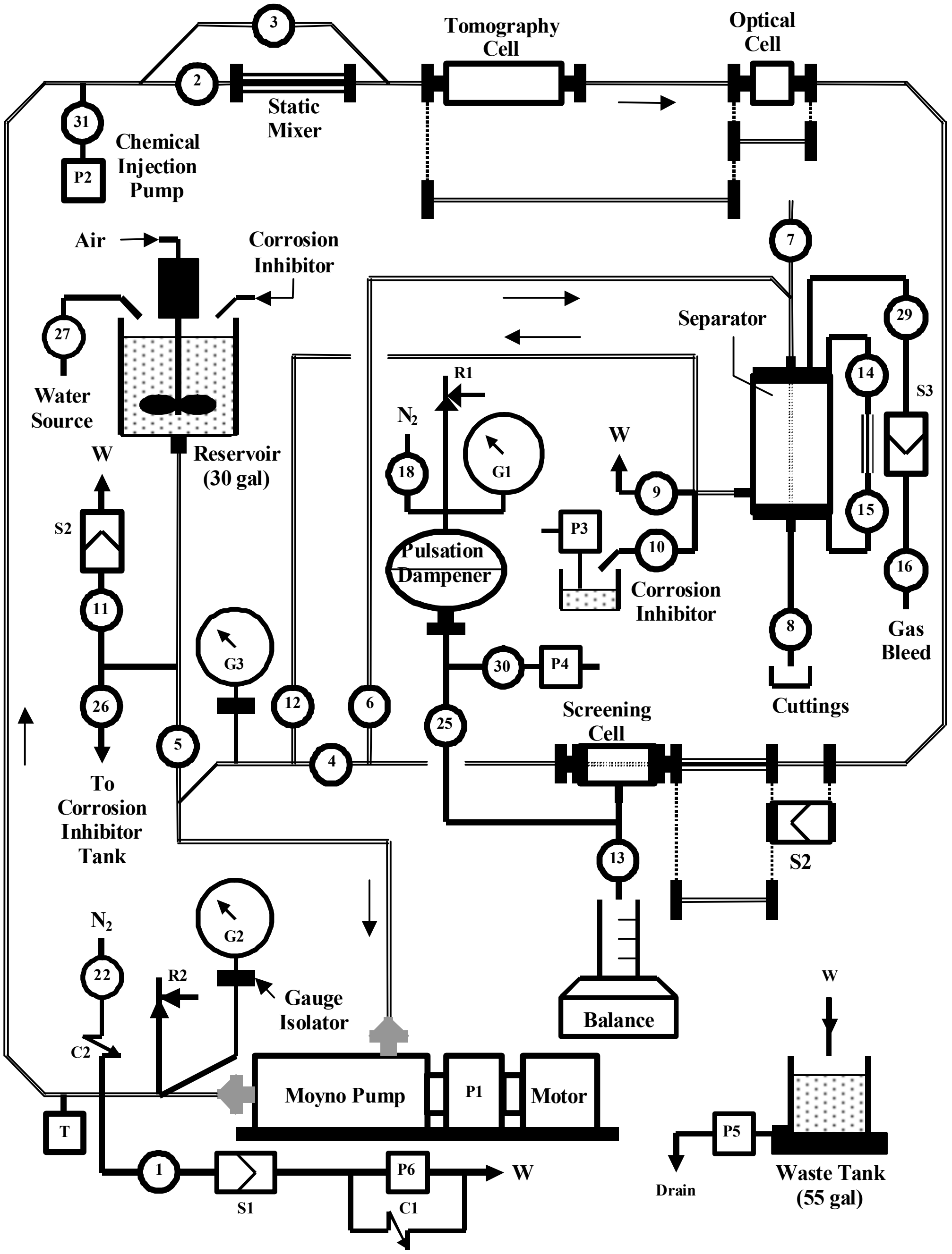

Fig. 11.10 Schematic of DTF (April 2001)

The DTF was constructed on a 16’ x 2-½’ skid with a Unistrut cage for supporting the pipe and other components. To better understand the DTF, it is broken into functional subsystems and described below.

Main Loop. The main loop is a closed system of 1-1/2” diameter steel pipe (schedule 40 or better) with a progressive cavity pump (Moyno) circulating the fluid (liquid or foam with/without cuttings) at rates from 2 to 23 gal/min at an operating pressure of 150 psi. The main loop is equipped with an optical cell for bubble imaging. A 6-foot section now occupied by 1-1/2” steel pipe has been reserved for verifying cuttings tomography under dynamic conditions. Although the loop is designed to operate at ambient temperature, a type K thermocouple monitors the system temperature. An in-line static mixer helps produce foam and/or mix chemicals that may be injected into the loop. The static mixer can be bypassed if desired. The original plan included a short, clear section of pipe in the loop to allow the experimenter to see the circulating fluid. This was not installed until later. A cell referred to as a Screening Cell was designed so that fluid could be removed while also removing cuttings. This was anticipated to be particularly important with foam experiments. Fig. 11.11 is a drawing of the Screening Cell.

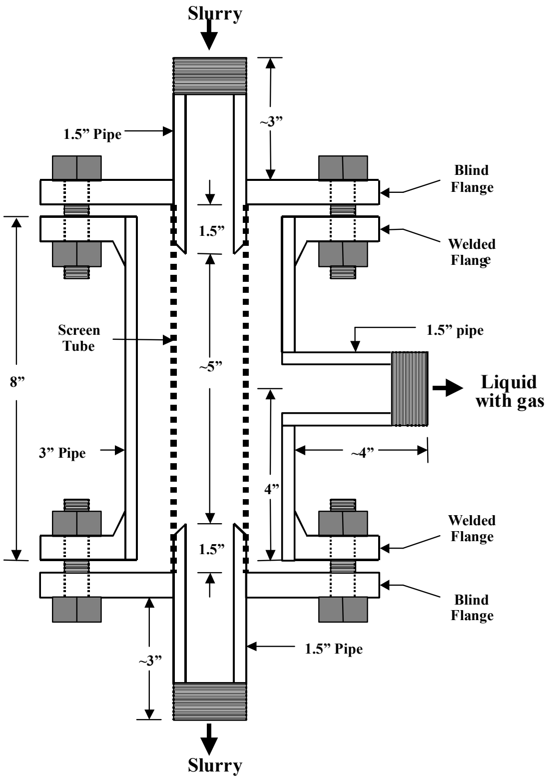

Fig. 11.11 Design of the DTF screening cell for fluid removal

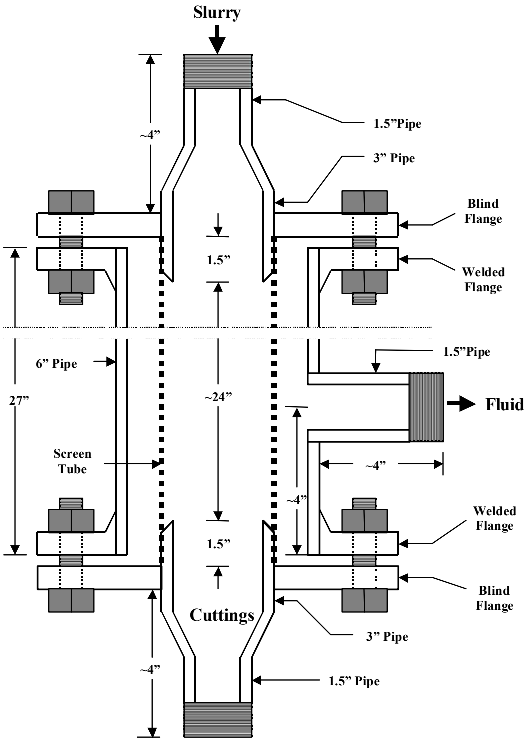

Fig. 11.12 Design of cuttings separator for separating liquid, cuttings and gas

Separator. Once an experiment has been completed, the fluid is routed through a separator, which will separate the cuttings, liquid and gas. Figure 11.12 is a drawing of the separator. We can monitor the gas-liquid level with a sight glass along side of the separator. Once depressurized, the cuttings can be withdrawn from the base of the separator. If needed, they can also be washed out from the top of the separator with water. Liquid from the separator can be directed to either a 55-gal waste tank or 30-gal corrosion inhibitor tank.

Mixing Subsystem. A standard garden hose connected to piping near the Moyno intake will direct water to the top of, and down into, the 30-gal mixing tank. A spray nozzle at the end of the water line serves to wash down the sides of the tank. An air-powered mixer mounted above the 30-gal mixing tank can mix water, surfactant (and other chemicals except foam breaker) and cuttings, which are gravity-fed into the Moyno pump. The air to the mixer motor passes through a shut-off valve, pressure regulator, regulator valve and an oiler. Unused fluid in the mixing tank can be drained directly to either the corrosion inhibitor tank or waste tank. An in-line strainer will remove any suspended cuttings.

Pressure Relief Subsystem. The pressure relief subsystem consisting of a relief valve (cracks at ~150 psi) and 1-1/2” steel piping directs any release to the 55-gal waste tank. A steel tee attached to the end of the release line (inside the waste tank) prevents any recoil during any high-pressure gas/liquid release.

Corrosion Inhibitor Subsystem. When not in use, the main loop is filled with corrosion inhibitor. While operating the DTF, the corrosion inhibitor is transferred to a 30 gal tank. Once an experiment has been completed, the corrosion inhibitor is pumped into the mixing tank and circulated throughout the main loop. Besides the 30 gal tank, this system consists of a small pump and plumbing to transfer the corrosion inhibitor to the mixing tank.

Sump Drain. A valve has been placed on the discharge side of the Moyno pump at the lowest point of the DTF to allow all fluid to be removed from the main loop. Once open, fluid will either pass directly to the waste tank or corrosion inhibitor tank. If the fluid in the main loop is pressurized, it will pass through a check valve. Otherwise a small pump will transfer the fluid to the appropriate tank. An in-line strainer will remove any residual cuttings. A 4-foot riser loop at the waste tank serves as a relief “valve” to prevent over pressurization.

Nitrogen Manifold. This manifold allows pressurized nitrogen to be routed to the main loop (foam formation) or to the pulsation dampener. Calibrated needle valves control the rate of nitrogen delivery. This manifold was constructed after April 2001.

110 Volt Electrical Subsystem. Small pumps, a thermocouple readout, light sources, etc., receive their power through a pair of power strips (located at each end of the DTF) and four switched outlets for equipment without on-off switches.

Bladder Accumulator. A one gal Hydril bladder accumulator pressurizes the main loop if non-energized fluid is to be used. It will also serve as a pressure compensator to counter minor changes in system pressure. A high-pressure hose connects the Hydril with the nitrogen manifold. The bladder accumulator was installed after April 2001.

Chemical Injection Pump. This is a medium-pressure pump for injecting chemicals directly into the main loop while the DTF is in operation. Although an injection port existed in April 2001, the injection pump was purchased and installed in Year 3.

In addition to the above, two instrumentation platforms were constructed to support the microscope and the illumination sources near the optical cell.
All fluid transfer subsystems are constructed of PVC rated to 150 psi or greater.

Several subsequent modifications and improvements to the DTF are presented in Table 11.1

Table 11. 1 Modifications and Improvements to the DTF

No	Modifications	Completed
1	Installation of an air bleed line on liquid side of bladder accumulator	April 2002 (Year 3)
2	Fabrication of a mixer shaft stabilizer	April 2002 (Year 3)
3	Fabrication of a cover for the mixing tank	April 2002 (Year 3)
4	Installation of a clear protective tube around the separator sight glass	April 2002 (Year 3)
5	Order and installation of a stainless steel pump for on-the-fly chemical injection	April 2002 (Year 3)
6	Construction of a glass liquid level indicator for the mixing tank	July 2002 (Year 3)
7	Installation of a needle valve in parallel with the static mixer for foam generation under high shear conditions	July 2002 (Year 3)
8	Calibration of the Moyno RPM indicator to estimate flow rate	August 2002 (Year 4)
9	Installation of a digital indicator on Moyno pump shaft calibrated to read directly in GPM	October 2002 (Year 4)
10	Order and installation of a 1-1/2” clear high-pressure glass section and construction of a Lexan safety shield	January 2003 (Year 4)
11	Replace Screening cell with 1-1/2” pipe tee to reduce dead volume	October 2003 (Year 4)
12	Install coarse and fine metering valves near the intake of the Moyno pump for controlled release of fluid from the loop	October 2003 (Year 4)
13	Calibration of the nitrogen manifold needle valves	October 2003 (Year 5)
14	Construction of a drain system to collect waste fluid from various parts of the DTF for disposal	October 2003 (Year 5)
15	Installation of a 1-1/2” magnetic flow meter	January 2004 (Year 5)
16	Installation of a ½” magnetic flow meter and 3/8” stainless plumbing for operating devices external to the DTF	January 2004 (Year 5)

Figure 11.13 is a photo of the DTF as it appeared near the end of Year 4. Some of the refinements listed above were not incorporated as of this date. The schematic of the DTF as of April 2004 is shown in Fig. 11.14. Most of the symbols used are shown in Fig. 11.15; the remainders are given below.

CI: Designates flow to or from the Corrosion Inhibitor Tank
W: Indicates flow to the 55 gal Waste Tank

PD:	Photo diode
Sight Cell	In-line cell constructed of a short length of 1-1/2” high-pressure glass tubing
RS300	An In-line, flow-through, high temperature and pressure viscometer (Thermo-Haake)
Drain	A system of ¾” PVC pipe that collects all waste fluids generated by the DTF

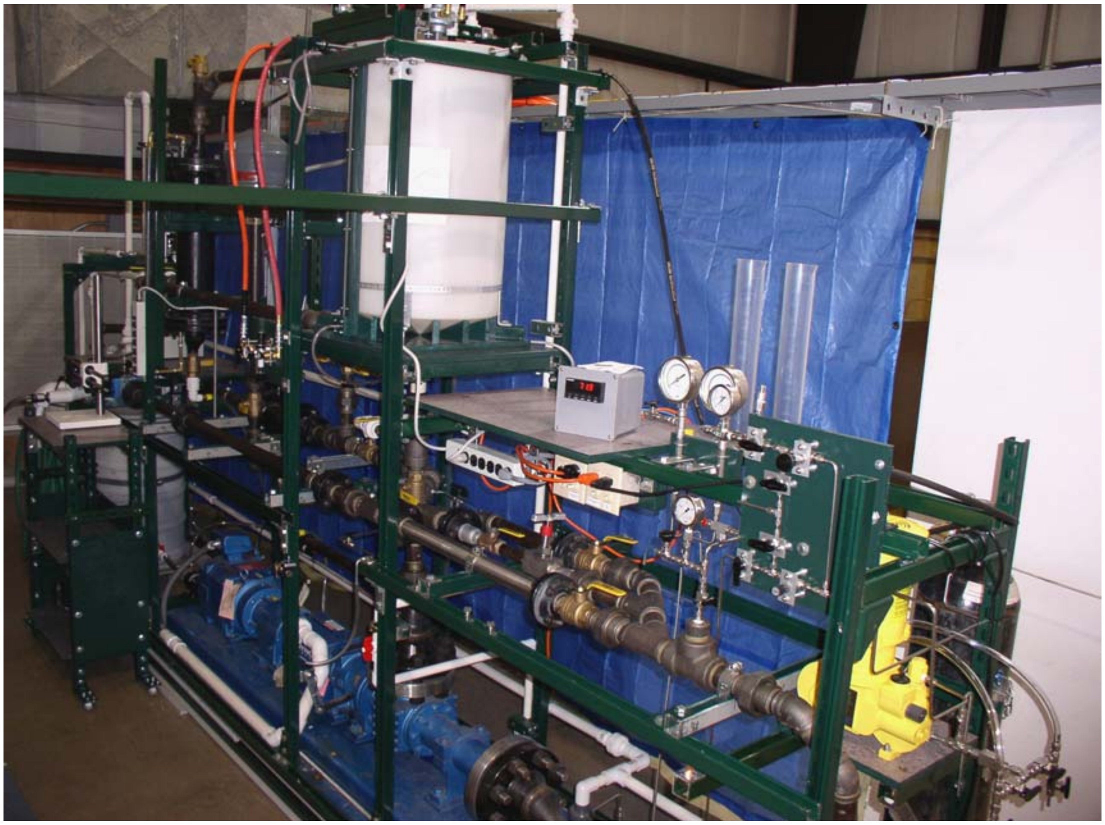

Fig. 11.13 Dynamic Testing Facility (April 2003)

Figure 11.15 shows the nitrogen manifold, which supplies nitrogen to the DTF for foam generation. Nitrogen is injected at the high-pressure end of the Moyno pump. The Nitrogen Manifold also supplies gas to the Bladder Accumulator.

Figure 11.16 is the chemical injection system. This system consists of a stainless pump and two possible reservoirs for injecting chemicals, such as shale inhibitors, polymers, corrosion inhibitors, foam breakers, etc. These chemicals are injected just ahead of the static mixer. The chemical pump can inject liquid chemicals under any loop pressure.

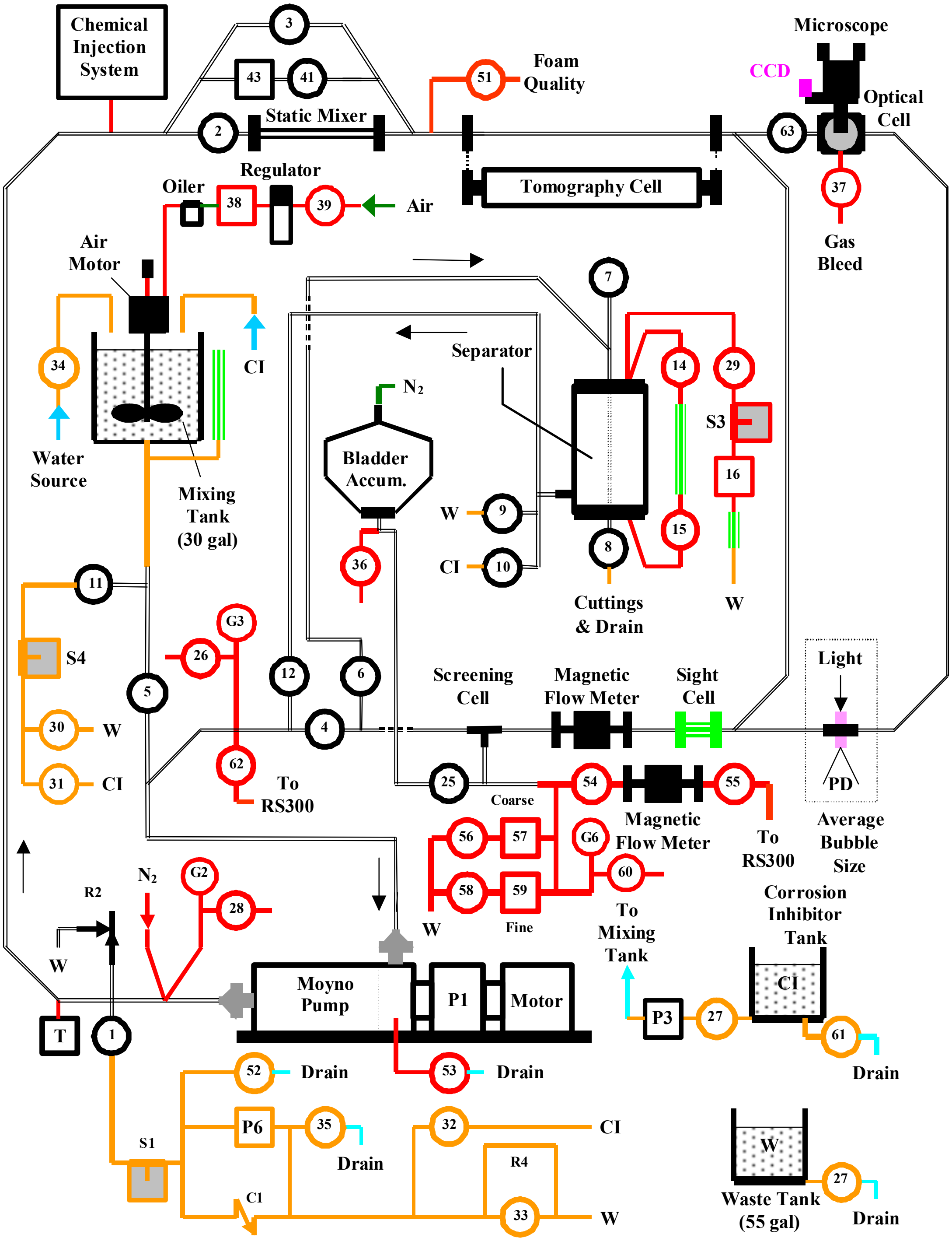

Fig. 11.14 Schematic of DTF (April 2004)

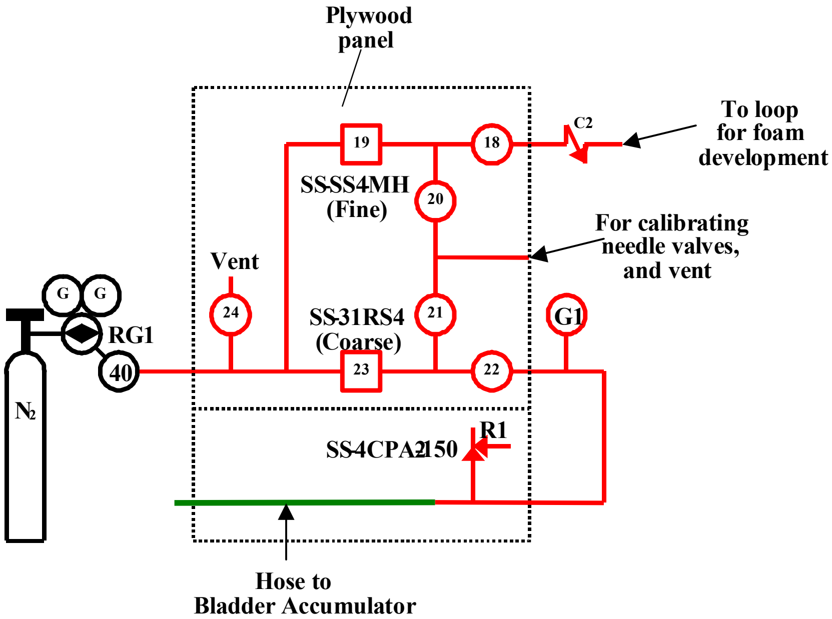

Fig. 11.15 Nitrogen manifold for the DTF

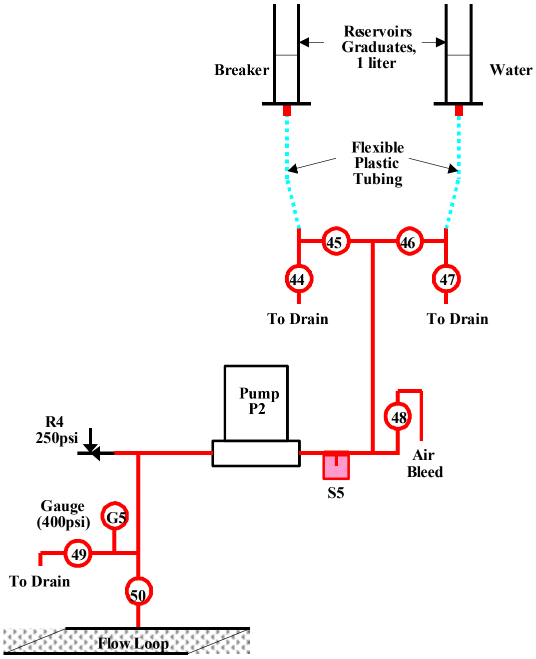

Fig. 11.16 Chemical injection system attached to the DTF

The key to the symbols and colors used in Figs. 11.14, 11.15 and 11.16 is given in Fig. 11.17 below.

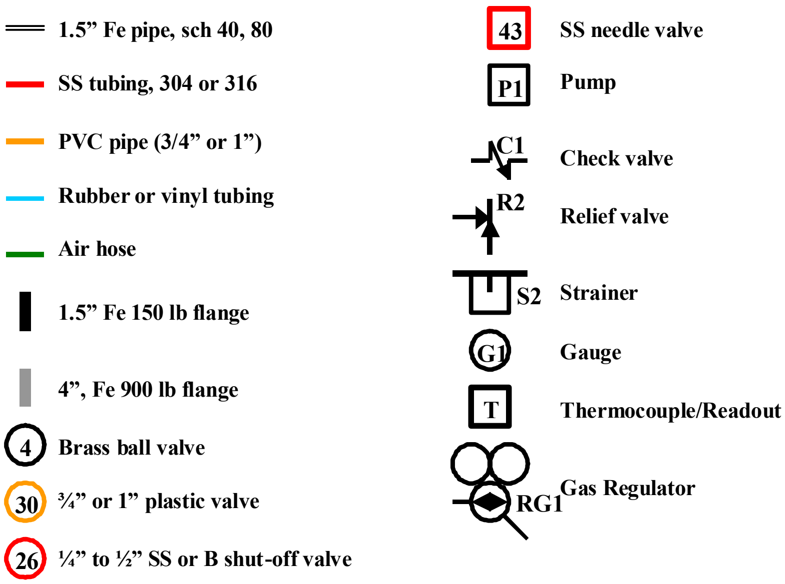

Fig. 11.17 Key to Figs. 11.14, 11.15 and 11.16

Improvements in foam generation. Modifications to improve the method of foam generation were begun during the last quarter of Year 3 and completed January 2003 of Year 4. Prior to these modifications, foam was generated by periodically removing foamy liquid followed by injection of nitrogen with measurement of foam quality to monitor progress. This was a time consuming process. Attempts to speed up this process by removing fluid or injection of gas too rapidly resulted in total collapse of the foam. To help understand the new foam development process described below, a much simplified schematic of the DTF has been included (see Fig. 11.18 below).

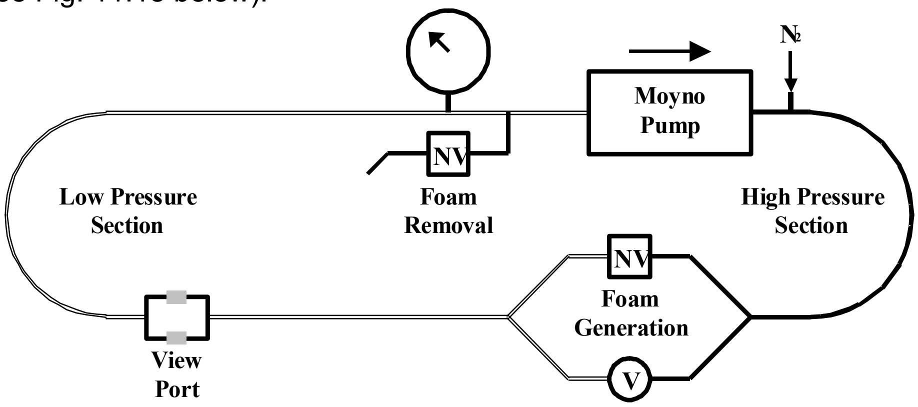

Fig. 11.18 Simplified schematic of DTF to illustrate foam generation method

The new foam generation method begins by introducing surfactant solution into the loop until liquid begins to appear in either the view port window or glass tubing cell. This will be 20 to 30% of the total loop volume and ensures that the pump will not be running dry. Next, nitrogen is injected into the loop until the desired operating pressure is attained (60 psi is typical). The time required to attain this pressure allows us to calculate the exact gas-liquid ratio. Figure 11.19 illustrates the Excel program that simplifies the calculation of gas-liquid ratio or “foam” quality.

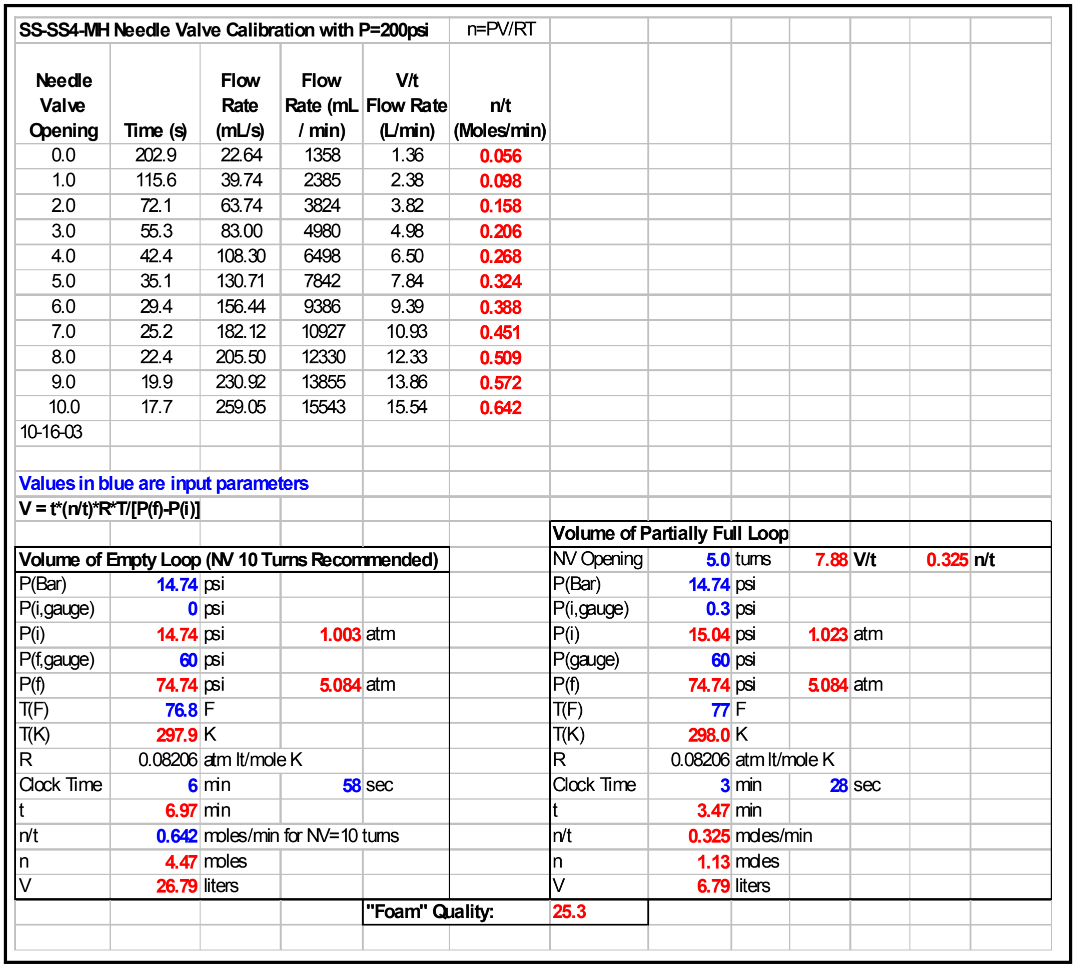

SS-SS4-MH Needle Valve Calibration with P=200psi					n=PV/RT
Needle Valve Opening	Time (s)	Flow Rate (mL/s)	Flow Rate (mL / min)	V/t Flow Rate (L/min)	n/t (Moles/min)
0.0	202.9	22.64	1358	1.36	0.056
1.0	115.6	39.74	2385	2.38	0.098
2.0	72.1	63.74	3824	3.82	0.158
3.0	55.3	83.00	4980	4.98	0.206
4.0	42.4	108.30	6498	6.50	0.268
5.0	35.1	130.71	7842	7.84	0.324
6.0	29.4	156.44	9386	9.39	0.388
7.0	25.2	182.12	10927	10.93	0.451
8.0	22.4	205.50	12330	12.33	0.509
9.0	19.9	230.92	13855	13.86	0.572
10.0	17.7	259.05	15543	15.54	0.642
10-16-03					

Values in blue are input parameters

V = t*(n/t)*R*T/[P(f)-P(i)]

Volume of Empty Loop (NV 10 Turns Recommended)				
P(Bar)	14.74	psi		
P(i,gauge)	0	psi		
P(i)	14.74	psi	1.003	atm
P(f,gauge)	60	psi		
P(f)	74.74	psi	5.084	atm
T(F)	76.8	F		
T(K)	297.9	K		
R	0.08206	atm lt/mole K		
Clock Time	6	min	58	sec
t	6.97	min		
n/t	0.642	moles/min for NV=10 turns		
n	4.47	moles		
V	26.79	liters		

Volume of Partially Full Loop						
NV Opening	5.0	turns	7.88	V/t	0.325	n/t
P(Bar)	14.74	psi				
P(i,gauge)	0.3	psi				
P(i)	15.04	psi	1.023	atm		
P(gauge)	60	psi				
P(f)	74.74	psi	5.084	atm		
T(F)	77	F				
T(K)	298.0	K				
R	0.08206	atm lt/mole K				
Clock Time	3	min	28	sec		
t	3.47	min				
n/t	0.325	moles/min				
n	1.13	moles				
V	6.79	liters				

"Foam" Quality: 25.3

Fig. 11.19 Calculation of initial "foam" quality in DTF for foam preparation

At this point, the Moyno pump is turned on to generate a low quality "foam". Figure 11.20 shows an Excel spreadsheet to assist in the foam generation process. Listed below are the input parameters and a brief description of each.

<u>Fraction of flow to replace with gas at P.</u> This technique replaces foam being withdrawn with injected nitrogen. To prevent starving the Moyno pump and reducing the chance of foam collapse at high foam qualities, the fraction of foam being replaced with gas should not be too great. Limiting the amount of gas being input at higher foam qualities also helps the integration of the new gas into the foam (reduces the chance of gas slugging). Probably 0.1 or less is acceptable.

<u>System pressure.</u> Normally, one would like to operate at a predetermined pressure, such as 60 psi. If one pressurizes the DTF to 60 psi and then closes the bypass valve (labeled "V" in Fig. 11.18), a pressure drop will develop across the foam generation needle valve so that there will now be a high pressure section and a low pressure section. What was once 60 psi may now be 55 psi in the low pressure section and 65 psi in the high pressure section. So if one wants to perform experiments in the low pressure section at 60 psi, additional nitrogen must be added to increase the pressure from 55 to 60 psi. The high-pressure section pressure will also increase to say 70 psi. We have therefore increased the average system

pressure from 60 psi to 65 psi and this increased pressure is entered into the spreadsheet, Fig. 11.20. The average pressure is actually measured by temporarily opening the bypass valve since the high-pressure and low-pressure sections of the DTF do not have identical volumes.

Initial foam quality. This value comes from the spreadsheet in Fig. 11.19 and represents the initial gas/liquid ratio in the DTF as foam generation begins.

Moyno “RPM”. This is a number that is proportional to the pump RPM and comes from the variable frequency drive. Although the approximate volumetric flow rate is known, it is more convenient to use the Moyno “RPM”.

Barometric pressure. Although changes in the barometric pressure can be included, these changes do not have much effect at higher pressures.

Desired final foam quality. Enter the final foam quality you would like to achieve. Depending on the desired foam quality, this program will under predict the foam quality by as much as 5%. We are working on corrections that should reduce this error considerably.

Data at the lower right and the adjacent plot illustrate how the foam quality will change with time. Initially the foam quality changes relatively rapidly because the foam being withdrawn contains more liquid than the higher foam qualities. Once the time to achieve a specified foam quality is attained, the quality should be measured for verification. If it is lower than desired, this process can be repeated. This time will be short since the foam quality should be close to that desired.

As mentioned, the system pressure should be the average pressure. Unfortunately, the system pressure changes as the foam quality increases. Figure 11.21 shows how the pressure drop across the foam generation needle valve varies as the foam quality increases for a particular needle valve setting. Since the pressure in the low-pressure section is held constant, the system pressure must change somewhat. Although one could automate this technique to account for changes in the average system pressure, a simple first-order correction should provide sufficient accuracy without added expense or complexity. Maintaining a constant pressure in the DTF is currently performed manually although this function could readily be automated if desired.

Stop Flow Technique. The stop-flow technique was developed to primarily circumvent the problem of capturing microphotographic images of bubbles while flowing. As mentioned, this would require either cameras having a very fast shutter speed and extremely intense light, or a high intensity flash lamp with a short pulse width. With the latter case, timing between the flash lamp and flash would be critical. The stop-flow technique briefly stops the flow through the windowed cell to allow imaging. One characteristic of the method is that the main fluid flow is not stopped. With the DTF, the flow is diverted. In principle, stopping the flow for a few seconds will not significantly increase the residence time and therefore not alter the size distribution of the foam bubbles. For foams studied to date, this condition is easily met. To accommodate the concept with the DTF, a second parallel leg was constructed to allow the windowed cell to be bypassed by manually closing valve 63 (see Fig. 11.14).

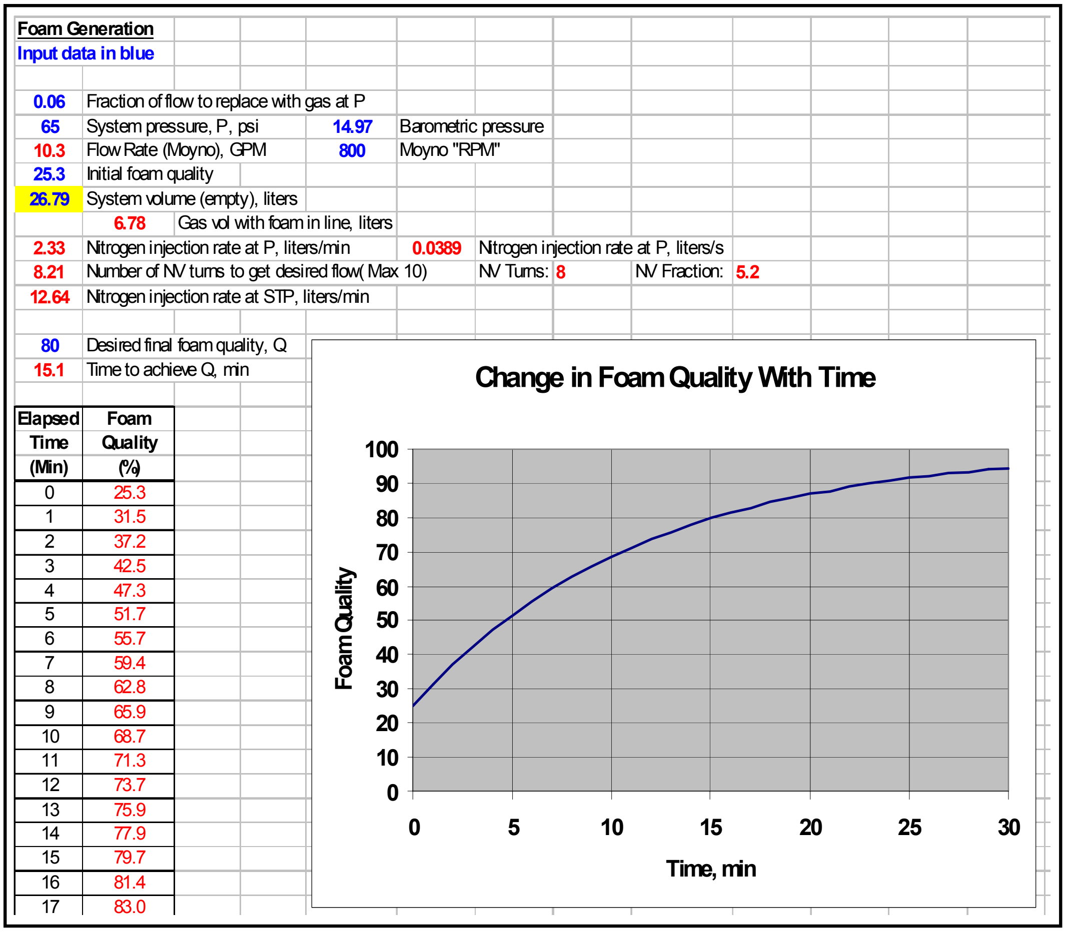

Foam Generation

Input data in blue

0.06	Fraction of flow to replace with gas at P		
65	System pressure, P, psi	14.97	Barometric pressure
10.3	Flow Rate (Moyno), GPM	800	Moyno "RPM"
25.3	Initial foam quality		
26.79	System volume (empty), liters		
6.78	Gas vol with foam in line, liters		
2.33	Nitrogen injection rate at P, liters/min	0.0389	Nitrogen injection rate at P, liters/s
8.21	Number of NV turns to get desired flow(Max 10)	NV Turns: 8	NV Fraction: 5.2
12.64	Nitrogen injection rate at STP, liters/min		
80	Desired final foam quality, Q		
15.1	Time to achieve Q, min		

Elapsed Time (Min)	Foam Quality (%)
0	25.3
1	31.5
2	37.2
3	42.5
4	47.3
5	51.7
6	55.7
7	59.4
8	62.8
9	65.9
10	68.7
11	71.3
12	73.7
13	75.9
14	77.9
15	79.7
16	81.4
17	83.0

Fig. 11.20 Foam generation in the DTF

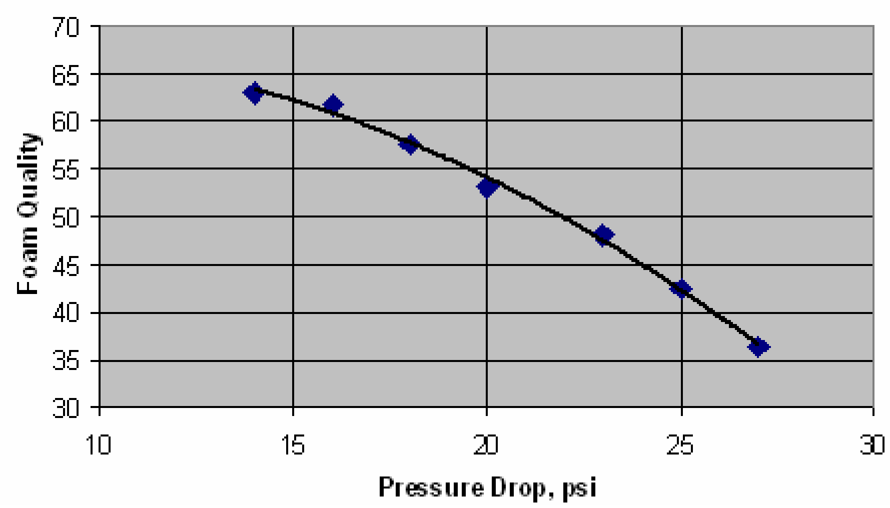

Fig. 11.21 Change in pressure drop across needle valve as a function of foam quality

Corrosion and Microbial Considerations. During disassembly of the DTF, considerable deposition of corrosion products were noticed on the windows of the optical cell and average bubble size electro-optical prototype. Tests were designed to check for the deposition of corrosion products in the presence of pipe dope, cutting oil residue and corrosion inhibitor. Microscope slides were placed at an angle inside 1-1/2" diameter by 2" long sections of pipe to examine the deposition on the top and under side of the slides as corrosion occurs. Deposition/corrosion in water served as a reference. Figure 11.22 shows the typical setup.

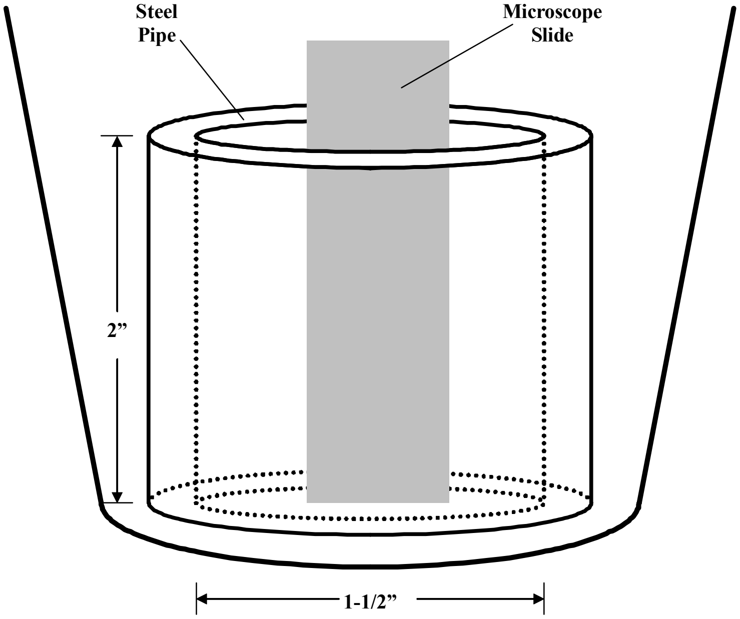

Fig. 11.22 Microscope slide placed inside pipe section for corrosion test

These tests indicated that the primary problem could be attributed to the deposition of corrosion products. Iron oxide even deposited on the under side of the microscope slides. We found that "Iron Out", a commercial form of $NaHSO_3$, removes oxidation products from glass windows far better than acids, even HNO_3. Fe^{+3} is reduced to Fe^{+2}, which is soluble up to a pH of 7. The corrosion inhibitor currently in use in the DTF and ACTF is an iron sequestering agent. Tests with this corrosion inhibitor and short sections of 1-1/2" steel pipe exposed to the air show that the solution darkens as corrosion progresses until all the corrosion inhibitor is consumed. At this point, the steel pipe will begin to rust. Glass will remain free of corrosion products until the corrosion inhibitor is consumed. Additionally, the corrosion inhibitor (0.1 to 0.2%) promotes bacterial growth. Corrosion inhibitor stored in a 30 gal plastic drum and exposed to the air exhibits extensive bacterial growth. In an effort to reduce the corrosion rate and retard bacterial growth, corrosion tests were set up using 1% surfactant with 0.1% corrosion inhibitor in a 0.1 molar phosphate buffer adjusted to a pH of 10.5 - 9. After five days exposure, the steel pipe in an unbuffered solution showed extensive oxidation but the steel pipe in the buffered solution showed none. Also the color of the buffered solution was unchanged from its original light yellow color. Tests for bacterial growth were admittedly crude but indicated that pH 10.5 - 9 did not support growth of the bacteria previously found in the 30 gal drum, even after inoculation.

11.4 ACTF BUBBLE CHARACTERIZATION CART

The idea of flowing a small quantity of foam from the primary ACTF for bubble analysis occurred during the last quarter of Year 4. Under this scenario, optical bubble characterization would be made on a small stream of foam under the same temperature and pressure (except for a small pressure drop) as in the ACTF at the point of extraction. A schematic of the ACTF Bubble Characterization Cart is shown in Fig. 11.23. Below is a description of the operational details of the Cart.

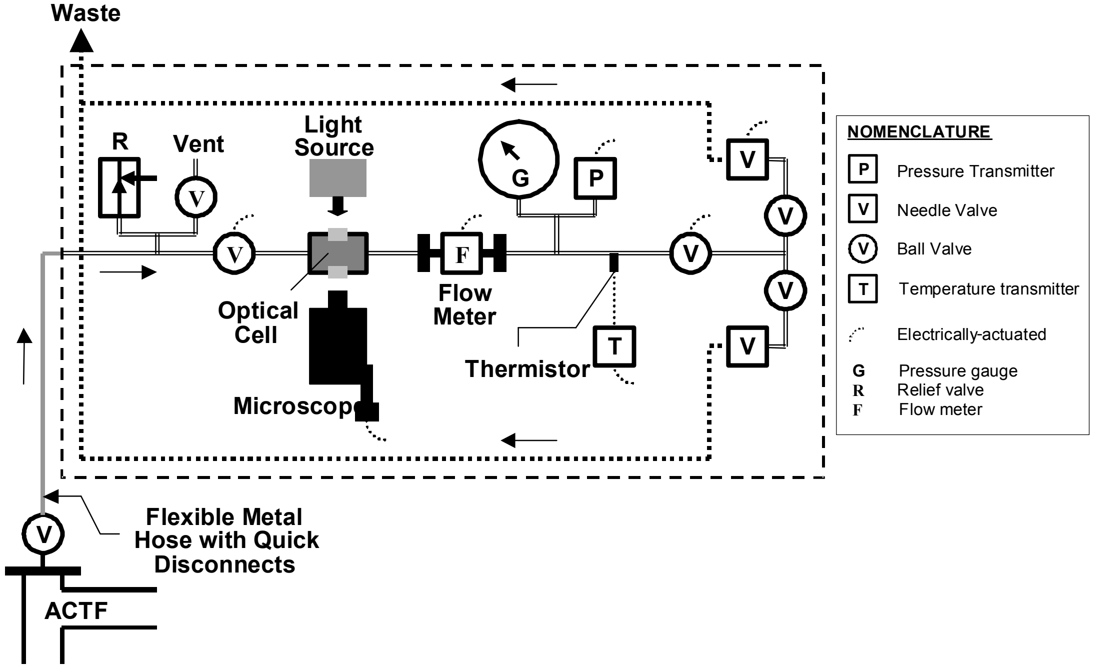

Fig. 11.23 Schematic of ACTF Bubble Characterization Cart

The flow rate is sufficiently rapid to give a relatively short residence time between the ACTF and the visualization cell (5-10s). A microscope equipped with a digital camera is mounted over the view port to capture foam images. This is the same type microscope and digital camera as used on the DTF. Light from either a fiber optic source or a ring light provides illumination for imaging. Temperature, pressure and flow rate are measured and transmitted to a computer (not shown in Fig. 11.23), which wirelessly transmits data to the control room for display, analysis and storage. Bubble images are also transmitted wirelessly. The flow rate is controlled manually by needle valve 4 or from the control room by an electrically-actuated needle, valve 2. Closing ball valve 1, also electrically-actuated, momentarily stops the flow, allowing microscopic bubble images to be captured.

Figure 11.24 is a photo of the Bubble Characterization Cart, without the top or protective side panels. The flow direction is from left to right. The optical cell is directly beneath the microscope on the fluid flow platform. The computer, monitor and data acquisition system are below the fluid flow platform. Note that the Cart is mounted on 6” wheels for easy relocation.

Fig. 11.24 Bubble Characterization Cart

Figure 11.25 shows a side view x-section of the windowed cell. Connections to the cell are made with ½" NPT fittings that have been drilled out so that the ½" tubing butts up against the flow channel to minimize dead volume and flow disruptions

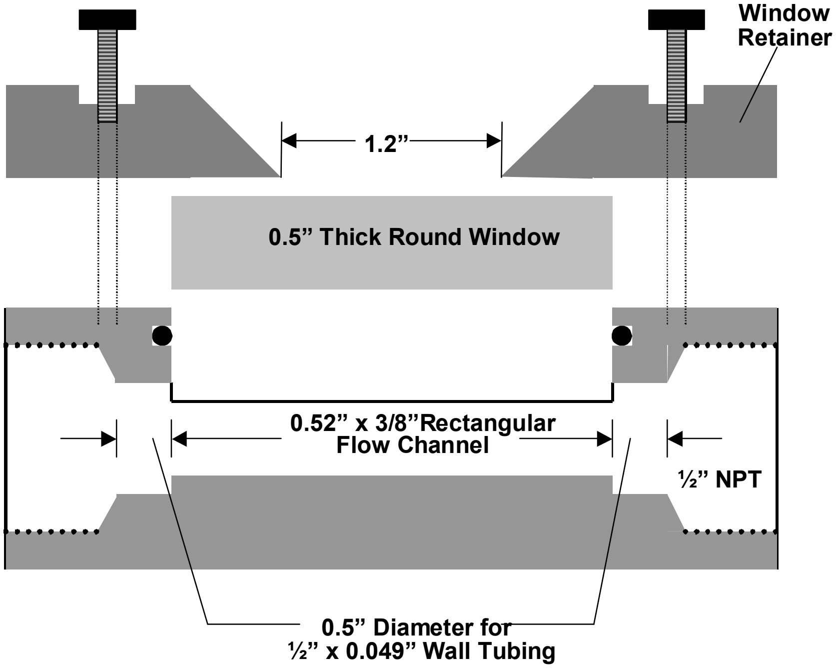

Fig. 11.24 Side view of x-section of ACTF windowed cell, with window and window retainer removed

Figure 11.26 illustrates the optical considerations used in designing the windowed cell to be used on the Cart.

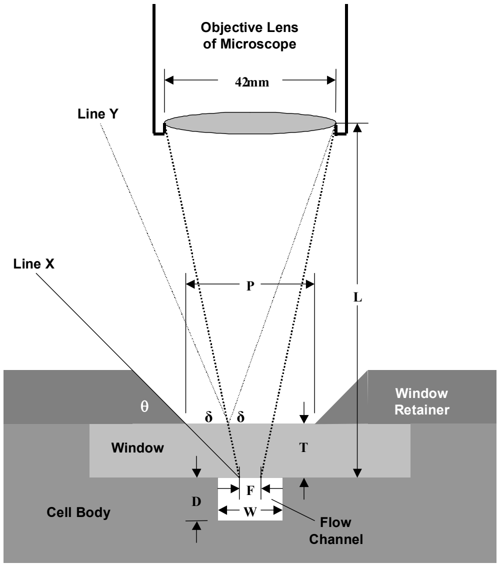

Fig. 11.26 Optical considerations for stop-flow cell for ACTF, DTF and Foam Generator-Viscometer

Fig. 11.27 Windowed cell designed & constructed for the ACTF Bubble Characterization Cart

Below is an explanation of the various letters and symbols used in Fig. 11.26.

F: Field of view of the microscope which is either approximately 3 or 5 mm depending on the objective lens.
L: Working distance or the distance from the bottom of the objective lens to the focal plane, and is either 50.5 or 84 mm, depending on the objective lens.
P: Diameter of the exposed portion of the window; about 1.2” for the ACTF cell.
W: Width of the flow channel; 0.52” for the ACTF cell.
D: Depth of the flow channel; 3/8” for the ACTF cell.
T: Window thickness; 0.5” for the ACTF cell
θ: Angle of the window retainer, 45°.
δ: Maximum angle of light that will not result in light being directly reflected into the objective lens.

Any light source must be located between Line X and Line Y. Optical cells offer the following advantages over conventional windowed cells:

- No dead area to flow where the window is mounted;
- Minimal changes in cross sectional area as fluid flows through the cell;
- Much better illumination angle for improved microphotography.

The cells can also be used in the Foam Generator-Viscometer. Figure 11.27 is a close-up of the windowed cell. The open area on either side of the flow channel allows light to enter at an angle through the ½” thick window. The 45° bevel around the window also helps increase the illumination.

11.5 NOVEL TECHNIQUES FOR BUBBLE CHARACTERIZATION

During Year 2, we realized the need for inexpensive techniques packaged in small devices that could measure foam properties such as foam quality and average bubble size.

11.5.1 FOAM QUALITY MEASUREMENT

If light reflects off an interface, such as glass-air or glass-water, the intensity of reflected light depends on the index of refraction of the materials forming the interface (along with the angle of incidence, light polarization, wavelength, etc.). Therefore, if we pass light through a glass window into a foam, the light reflected off the second surface (glass-foam interface) will depend on the amount of air in the foam. The higher the foam quality (more air) the more light will be reflected from this interface. This assumes that the bubbles of the foam are smaller than the light beam. Cuttings should have minimal effect on this measurement, providing we are not under the cuttings bed. Placing these devices around the circumference of the casing would provide us with a measure of segregation (air-foam-water). A fitting equipped with a small window should provide sufficient contact with the fluid, and a laser or light emitting diode would probably be the best light sources.

Tests measuring the reflected light intensity off the second surface of a glass cell filled with air, water or foam indicated that the reflected light intensity with foam was between the other two, as predicted.

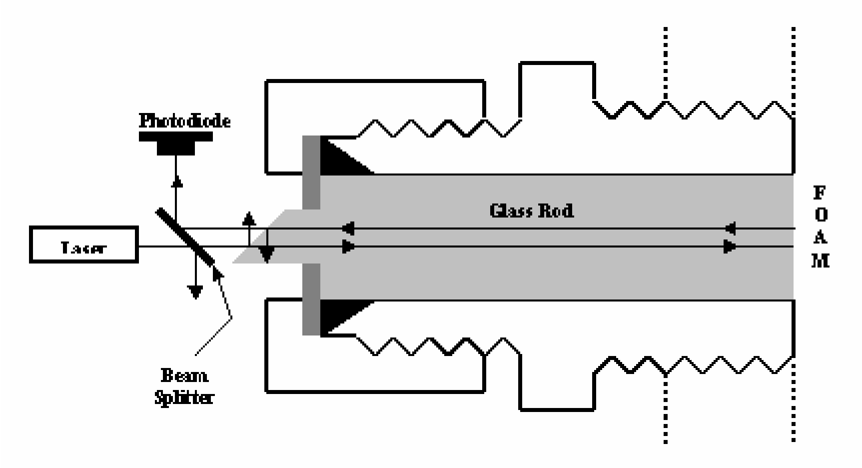

Fig. 11.28 Device for determining foam quality

One concept for this device involves transmitting laser light through a prism to a window adjacent the foam. The light exiting the prism will be directed at an angle to the window. The second surface reflected light from the window will be captured by the prism and directed to a photo diode. Both 90° (90°, 45°, 45°) and equilateral (60°, 60°, 60°) prisms are available off-the-shelf. A 90° prism allows reflected light to return parallel to the incident light, defeating one of the purposes of using a prism (separation of front and second surface reflected light). Unfortunately the light entering an equilateral prism is totally internally reflected (as we need to use it). With the correct angle, a prism should give the desired results, but it will be a special order. Also, the spacing between the prism and the glass-foam interface of the glass window will be critical. Since conceiving the idea of using a prism as a means of directing light onto and retrieving a signal from the foam-glass interface, we have developed a better method. The purpose of using a prism was to allow one to separate the first and second surface reflected light. By using a glass rod with one end cut at some angle other than 90°, only the reflection from the glass-foam interface will be measured by the photodiode. This concept is illustrated in Fig. 11.28. It will require a shoulder to be ground onto the rod. However, once constructed, it should be much easier to use.

11.5.2 FOAM BUBBLE SIZE MEASUREMENT

If light passes through foam, the transmitted light intensity is related to the average bubble size and the foam thickness. Fig. 11.29 illustrates this relationship. It is based on a simple parallel plate model of scattering. Bubble sizes are in µm.

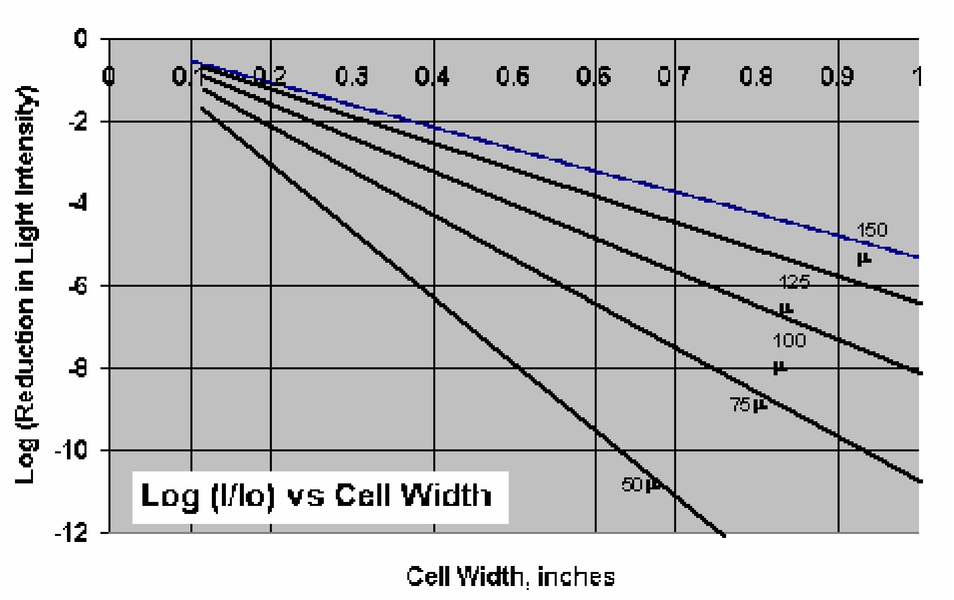

Fig. 11.29 Reduction in light intensity as a function of path length and bubble size

Cubes constructed of glass and clear plastic were constructed to measure the light attenuation by foam generated in a blender. There were two conclusions from this study:

1. One percent surfactant alone does not create sufficiently stable foam to allow accurate light attenuation measurements. Further studies are needed on either dynamic foam or stabilized foam.
2. As the optical path length increases the transmitted light intensity drops off very rapidly. Three inches of foam prevent any measurable light from being measured.

Figure 11.30 shows a schematic representation of this device. The light source depends on the path length across which the light must pass. For some applications, a light emitting diode is satisfactory. A prototype device was constructed using a 2000#, 1-1/2" pipe cross, two 3/8" NPT brass fittings, a pair of 10 mm windows, a photodiode and light from a fiber optic microscope illuminator. This cell was then installed into the DTF. The test data with dynamic foam confirmed that as the bubble size decreases, the signal decreases. As anticipated, the light intensity transmitted across the pipe also depends on the foam quality.

Figure 11.31 is a photo of prototype Average Bubble Size device for use with the foam generator-viscometer. It uses a light-emitting diode as a light source and a photo diode for a detector.

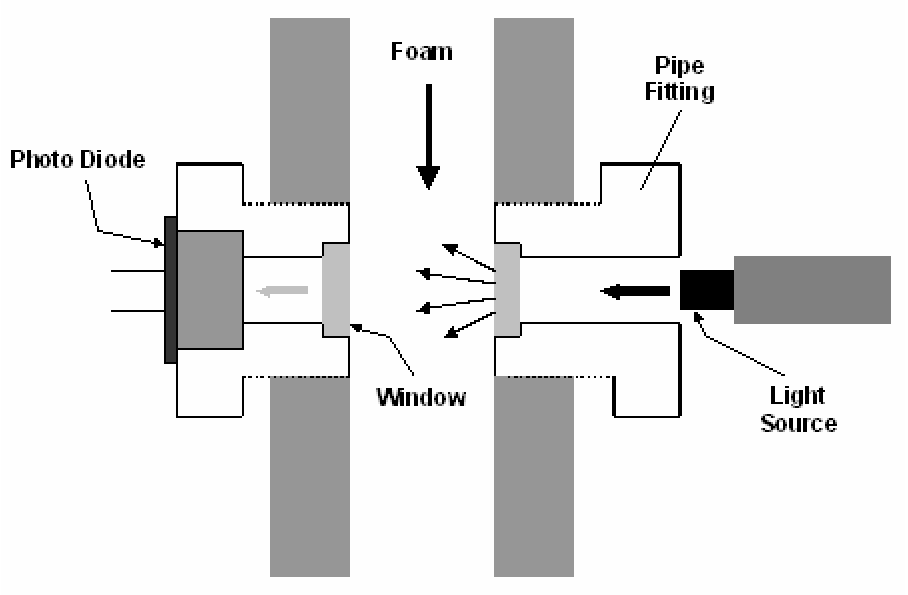

Fig. 11.30 Schematic of an Average Bubble Size device

Fig. 11.31 Average bubble size device for use with the Foam Generator-Viscometer

The next step will be to construct an improved electronic package to measure lower light intensities and liberalize the electronic signal output over a wider dynamic range. Alternate methods are being considered to compensate for the low light transmission by foam. One involves installing the light source and photo diode on a chord rather than at the diameter. This concept may be particularly useful for the drilling section when a drill pipe is in use.

11.6 BUBBLE RECOGNITION AND ANALYSIS SOFTWARE

In order to incorporate foam as a drilling fluid in a cuttings transport model, the average bubble size and bubble size distribution of the foam must be measured under various conditions. This is accomplished by imaging the foam through a glass cell and subsequently analyzing the image with software. Back illumination is not possible as the foam absorbs the light entirely, allowing no light to reach the front surface. This results in inherent features of the images that make them difficult to analyze by standard means.

Beginning in Year 1, several imaging packages were considered and/or tested. These are: i) Adobe PhotoShop; ii) Blob Finder from MVTec; iii) Optimas; iv) Image-Pro; and v) National Institute of Health developed software for blood analysis. Various lighting techniques were examined to improve image quality to facilitate image processing, including single and multiple light sources, a variety of illumination angles and polarization. Front-surface illuminated bubble images have three basic problems (refer to Fig. 11.5):

- Bubbles are not completely surrounded by dark (or light) arcs;
- very poor contrast exists on some portion of the bubble images;
- Arcs from adjacent bubbles can fuse, causing software problems distinguishing one bubble from its neighbor;
- Light reflections off a bubble appear as white spots along the circumference of the bubble, breaking the dark arc needed for imaging;
- Images using transmitted light eliminate some of these problems but create others;
- Transmitted light intensity falls off exponentially with path length, making this method useful only on relatively thin samples;
- Second layer bubbles can be confusing (see Fig. 11.3);
- Transmitted light is considerably distorted near bubble edges (see Fig. 11.3).

11.6.1 TESTING OF PARTICLE 2.0

The testing procedure in this study is divided into two parts: i) detecting bubbles with the software; and ii) analyzing the program outputs through a graphical method using spreadsheet software to determine the bubble size distribution. The software capabilities were studied in two stages: hand-drawn shapes and real bubble images. Very simple shapes or images were first used. Upon collecting acceptable results, more complex images or shapes were then tested. During the bubble image tests, two problems were identified: i) incomplete circles or bubbles; and ii) common boundaries (side of bubble where it touches another bubble).

The software Particle 2.0 requires a user input (sensitivity parameter) before each segmentation process. The choice of the right sensitivity parameter for a given sample is critical, and the quality of the segmentation is based on the choice of the parameter. Figure 11.32 shows some results of segmenting a simple object; with an example of bad results (where the program identified 7 objects) and good results (where the program was able to identify the correct number of objects, counting the background as one object).

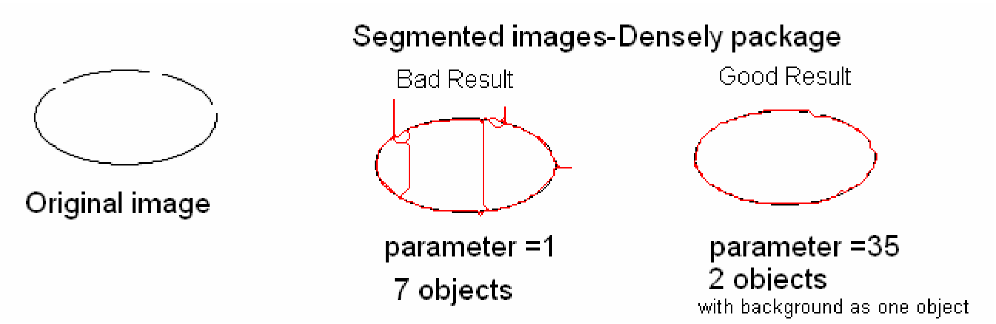

Fig. 11.32 Testing of the software with sample shaped object

In the following couple of cases (images), the relationship between the number of objects and the user input parameter was considered and the plots of number of objects vs. sensitivity parameters were also constructed:

Case 1: Figure 11.33 shows a simple irregularly shaped object with brakeage in the boundary to simulate the lighting effect in foam images. The software was able to process this image successfully. Results are shown Figs. 11.34 and 11.35.

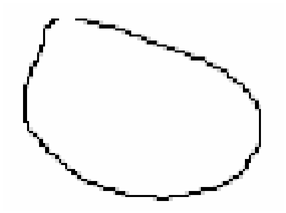

Fig. 11.33 Image used in Case 1

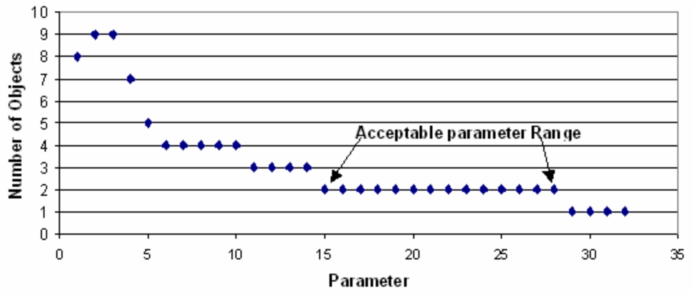

Fig. 11.34 Number of objects as a function of sensitivity parameter for Case 1

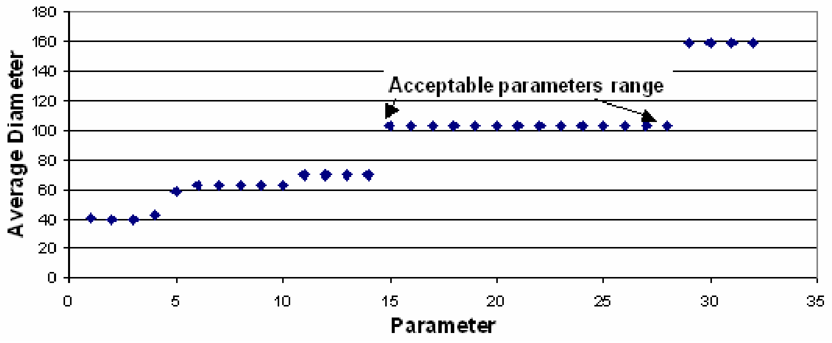

Fig. 11.35 Average bubble diameter as a function of sensitivity parameter for Case 1

Case 2: Figure 11.36, shows several elliptical-shaped objects, which were used to evaluate the ability of the software to identify bubbles or circles which have common boundaries. Results obtained from the Particle program are shown in Figs. 11.37 and 11.38.

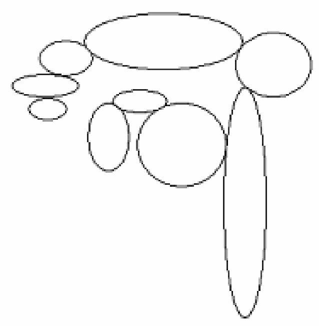

Fig. 11.36 Image used in Case 2

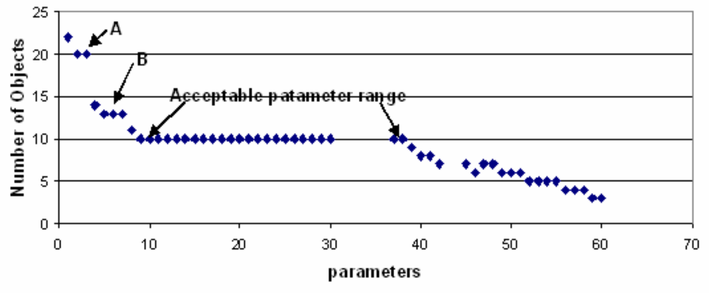

Fig. 11.37 Number of objects as a function of sensitivity parameter for Case 2

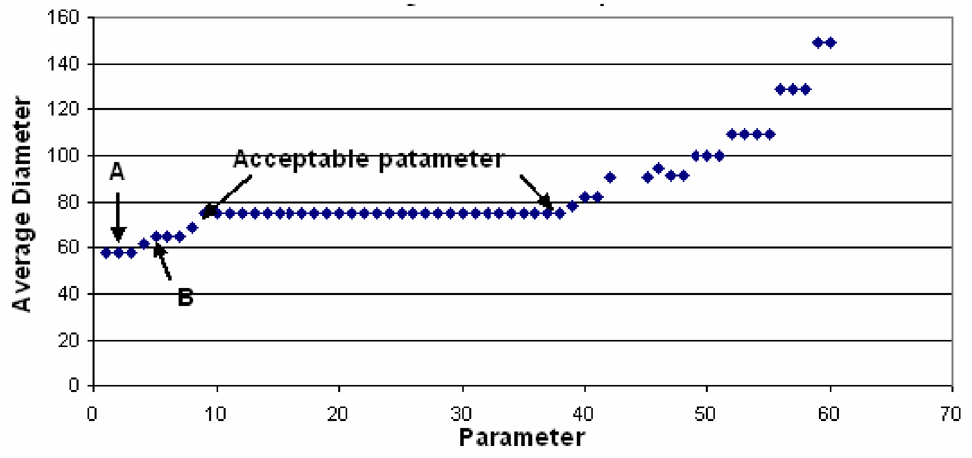

Fig. 11.38 Average bubble diameter as a function of sensitivity parameter for Case 2

<u>Case 3:</u> Figure 11.39, shows several irregularly-shaped objects (complex bubble-like image), which were used to evaluate the ability of the software to identify objects which have common boundaries. Results obtained from particle program are presented in Figs. 11.40 and 11.41.

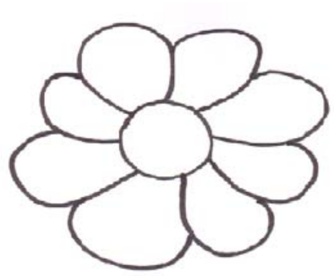

Fig. 11.39 Image used in Case 3

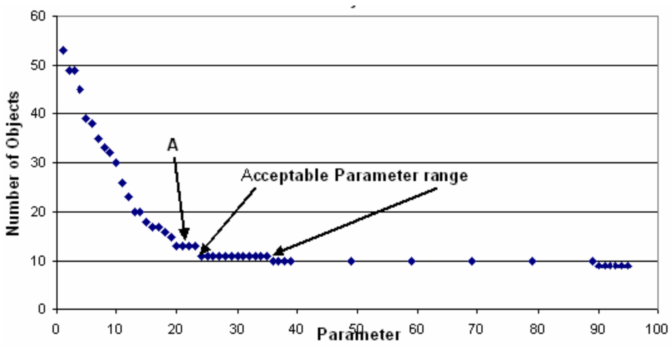

Fig. 11.40 Number of objects as a function of sensitivity parameter for Case 3

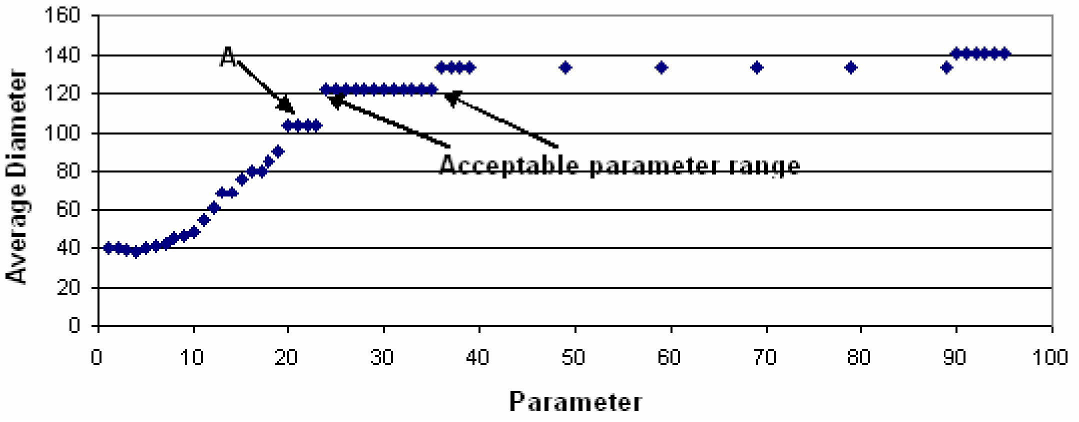

Fig. 11.41 Average bubble diameter as a function of sensitivity parameter for Case 3

In the three cases above, plots of number of objects vs. sensitivity parameter tend to have similar shapes. The number of objects decreases as the parameter value increases, levels for a couple of points, and then decreases again. The more objects in the image or the more complicated the image, the less likely for the curve to level out at the range of parameters that will give the correct or acceptable number of objects. The same thing can be said about the plots of average diameter vs. parameter. Average diameter is calculated by adding the diameters of all objects and then dividing by the number of objects. The values of the average diameter tend to increase as the parameter values increases. And as in the number of objects vs. sensitivity parameter plots, the curve of average diameter vs. parameter will level out for some points and then increases again. Finally a real bubble image was used to test this pattern.

<u>Case 4:</u> The bubble image (real bubble image) is shown in Fig. 11.42. A result obtained by processing the real image is presented in Figs 11.43 and 11.44. From Fig. 11.43, It can be seen that the number of objects decrease as the parameter entered to the program increases and that the curve levels out (number of objects will be constant at 46) exactly in the range of parameters that will give an acceptable segmentation.

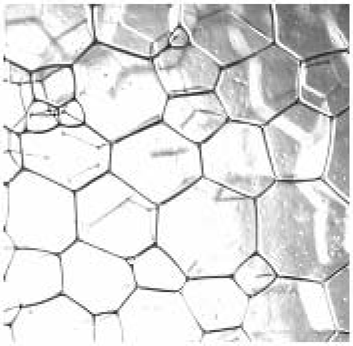

Fig. 11.42 Real bubble image used in Case 4

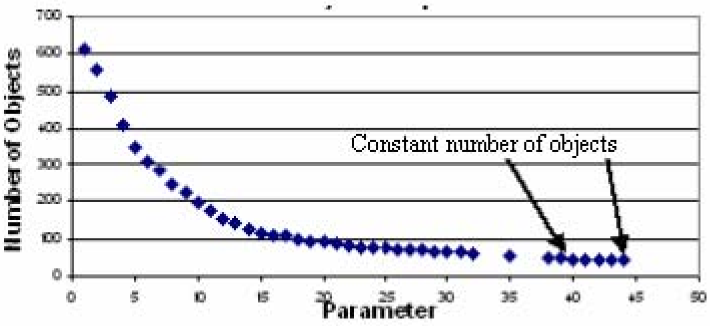

Fig. 11.43 Number of objects as a function of sensitivity parameter for Case 4

As seen in Fig. 11.44, the average diameter increases as the parameter value increases, and is only level at the expected parameter range (comparing Fig. 11.43 and 11.44). Therefore, either by using plots of number of objects vs. sensitivity parameter or plots of average diameter vs. sensitivity parameter, the range of sensitivity parameters that will give an acceptable value can be found. After determining the right sensitivity parameter, the results can be further filtered by eliminating the noise and the background effect from the results. The background might show in the results as an object with very large diameter. A real bubble image, with software segmentation is presented in Fig. 11.45. Bubble size distribution (cumulative) for the real bubble image, obtained using parameter value of 43, is shown in Fig. 11.46.

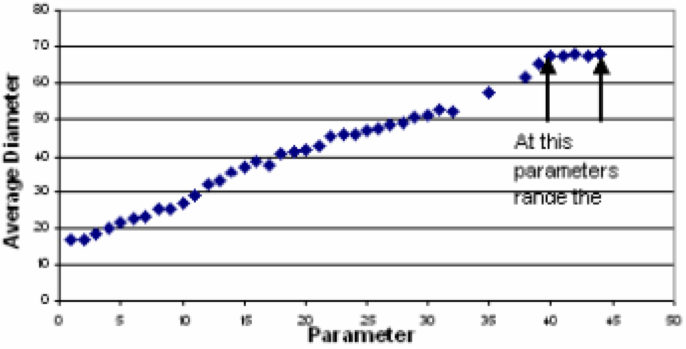

Fig. 11.44 Average bubble diameter as a function of sensitivity parameter for Case 4

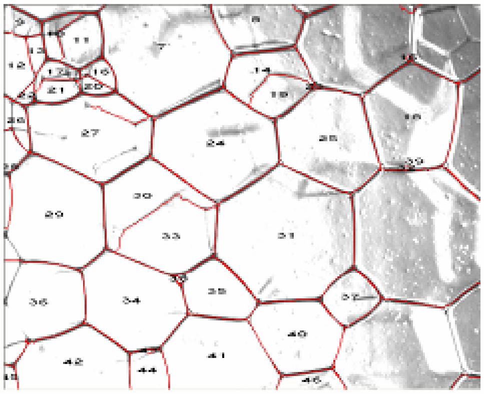

Fig. 11.45 Real bubble image after segmentation (sensitivity parameter = 43)

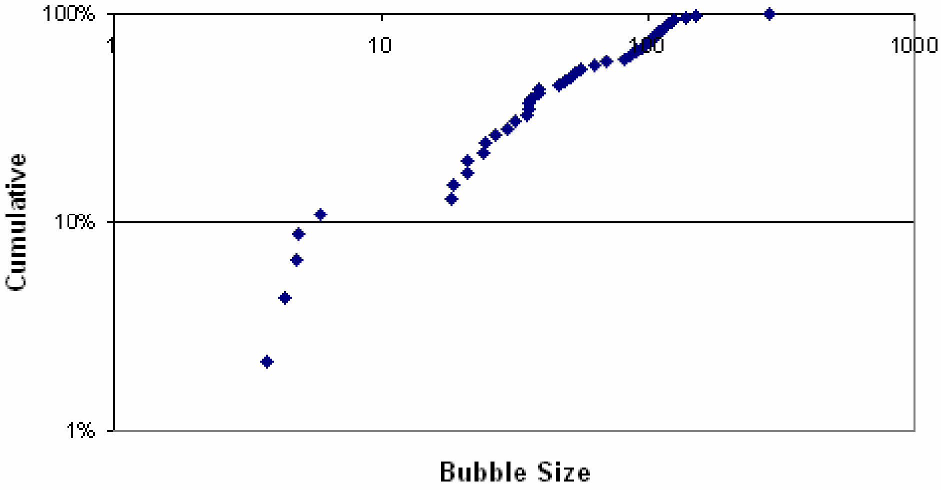

Fig. 11.46 Bubble size distribution (cumulative) for the real bubble image

11.6.2 CONCLUSIONS AND RECOMMENDATIONS

The Particle 2.0 software package can be used to analyze bubble images. The relationship between the sensitivity parameter and number of objects, and/or sensitivity parameter and average diameter can be used to identify the range of parameters that will give good or acceptable segmentation. Using results obtained with the parameter that gives a constant number of objects or constant average diameter, it is possible to plot the bubble size distribution and eliminate any noise. Conducting more tests on wet foam images is necessary since images used in this study are limited to dry foams.

11.7 MONITORING ON-LINE NON-INTRUSIVE MEASUREMENT SYSTEMS

Three on-line measurement systems, ultrasonic system, CCD camera system and the flow cart, will be installed on the ACTF flow loop. The Ultrasonic system will be used to measure local cuttings concentration. The on-line CCD camera system will be used to take pictures of the test section through view ports. The flow cart will be used to take real fluid sample from the test section and perform a detailed fluid characterization test.

11.7.1 ON-LINE VISION SYSTEM

The objectives of the on-line vision system are: i) to obtain dynamic bubble images from the cart system; and ii) to acquire real-time flow images using the CCD camera installed on the view-port. Images taken by the CCD camera will be transferred by the on-line computer to the control room during the experiments. A computer will be installed on the ACTF flow loop to control the CCD camera system and to communicate with a central computer in the control room. Dynamic bubble images obtained from the cart will be used for determining the bubble size distribution. It is well documented that foam texture has strong effects on foam rheology. Therefore, foam characterization is very import for cuttings transport.

A picture showing a setup of on-line system is shown in Fig. 11.47. The CCD camera (Hitachi KP F-120 CL progressive scan with 1.45M pixels, see Fig. 11.48) was installed close to the view port (Fig. 11.49) to capture real-time images. A camera link grabber (National Instruments PCI-1428) was installed on the in-line computer and connected to CCD camera through a 2-meter camera link cable. The camera link grabber was used to process the signals obtained by the CCD camera.

Fig. 11.47 On-line vision system

In order to obtain good quality images, light source is needed because the test section is completely dark during the tests. An adjustable light source was used in the system to provide the desired light. Two type of light source, a fiber light source (Fig. 11.50) and a ring light source (Fig. 11.51), were used and tested in the system to identify the best light source that can be used on the ACTF flow loop. Both light sources have their own light intensity controller. The ring light source has a controller that can be connected to a computer through RS-232C serial port. The in-line computer controls the intensity of the ring light through a RS-232 C port using a computer program. By carefully adjusting the light source through the controller, a sharp image of the test section can be obtained through the view port as shown in Fig. 11.52. When used on the flow loop to take real-time images, data can be stored on the in-line computer or transferred to the control room through a fast (108M) wireless network connection.

Fig. 11.48 CCD Camera together with Lens

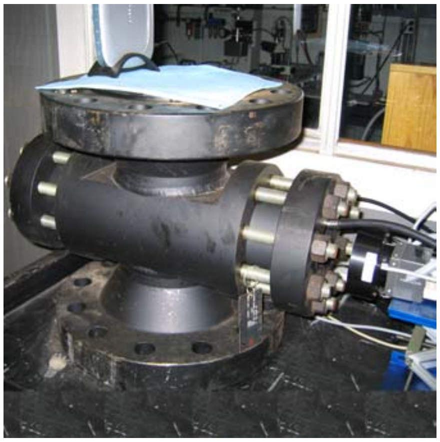

Fig. 11.49 View port

Computer codes have been implemented in C++ for capturing the image. Two operations can be performed through the program: 1) Snap a still image; 2) Grab continuous images (video). The program can acquire still images and/or the dynamic video during the test. A still image can be obtained whenever needed using the program developed in this phase. Recently, the image program has been used in the foam Generator/Viscometer test (Task 9b). Using the still images obtained by the program, bubble size distribution can be analyzed by Particle 2.0 (the software presented in Section 11.6). The program can record dynamic videos at the rate of 15 frames per second.

Fig. 11.50 Fiber light with the controller

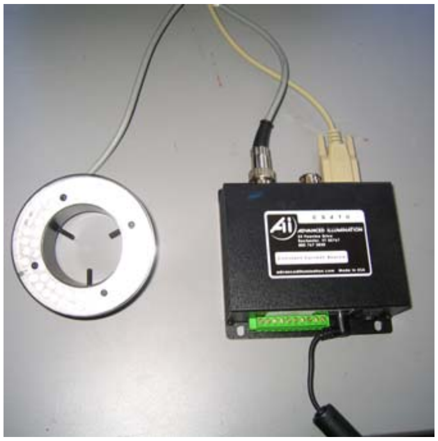

Fig. 11.51 Ring light and controller

Lab tests were conducted to check the on-line vision system. Sharp images were obtained through the CCD camera with the use of the ring light or the fiber light. Figure 11.53 shows the picture of CCD camera with both light sources (Fiber light and Ring light) installed. Preliminary results indicate that fiber light provides a better image while ring lights show reflection problems. During the lab tests, it was found that up to 15 frames per second can be achieved when grabbing continuous images. The “Client-Server” control system was tested in the lab. Tests results showed good response rate.

Fig. 11.52 Image of cuttings in the test section

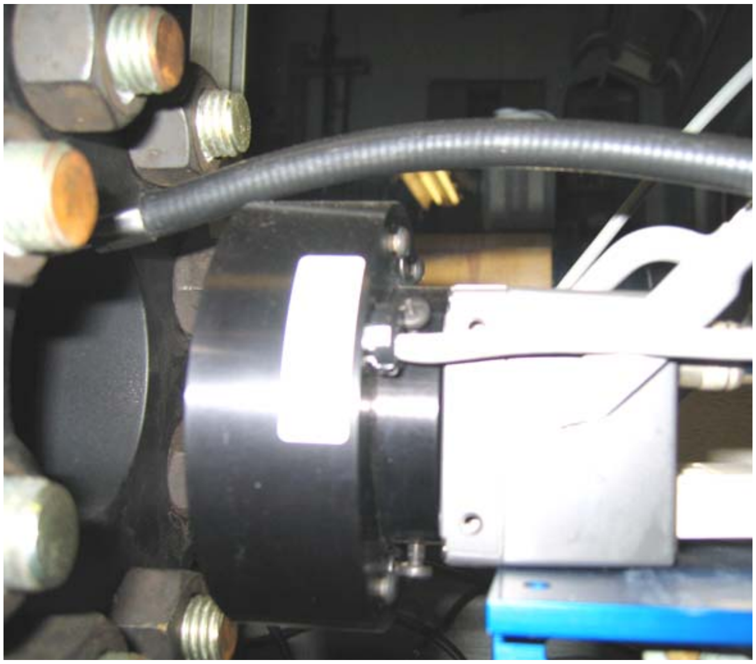

Fig. 11.53 CCD camera with fiber light and ring light installed

11.7.2 SYNCHRONIZATION OF ON-LINE MEASUREMENT SYSTEMS

Synchronization of sub systems (on-line vision system, Ultrasonic system and flow cart dynamic bubble characterization system) is very important to control and manipulate the streams of sampled data and images. In order to synchronize the sub systems, a distributed system with a “Client-Server” structure has been developed. All on-line sub systems are “linked” through a wireless network to communicate with the central computer. Initially, all sub systems listen to a “socket”. They will be blocked when there is no message available on that socket. The central computer located in the control room can trigger all the on-line sub systems when tests are started by broadcasting (sending) a message to them.

12. Study of Cuttings Transport with Foam under Elevated Pressure and Elevated Temperature Conditions (Task 13)

12.1 INTRODUCTION

This research task was not in the original proposal. It is a continuation of two other research tasks (Task #6 and Task #9) on foam rheology and cuttings transport. Literature survey, mathematical modeling, and preliminary rheology and cuttings transport tests are in their final stage. This task will extend beyond the 5-year DOE project timeline. It is scheduled to be completed in August, 2005.

Foam is a currently being used as drilling fluid in Underbalanced Drilling (UBD) because it provides downhole pressures that are less than formation pressures. Foam can also provide control of the Equivalent Circulating Density (ECD). Drilling with foam has such advantages as minimizing formation damage, increasing rate of penetration and preventing lost circulation etc. However, when compared with conventional incompressible fluids, such as water-based or oil-based drilling fluids, foams are significantly more complex. Foam is thermodynamically unstable; and its property changes with time. There is no general agreement in modeling foam rheology and little research has been done on foam rheology for practical downhole conditions.

Currently reliable data on cuttings transport with foam is unavailable. Little work has been done, and there is almost no publicly available knowledge on foam cuttings transport properties under practical down-hole conditions. A better understanding of foam cuttings transport characteristics may lead to advancements in the technology of underbalanced drilling with foams. In order to meet the increasing interest in foam drilling by the petroleum industry, the University of Tulsa ACTS/JIP proposed an extended research in this field.

The objectives of this project are: i) to investigate experimentally foam rheology under EPET conditions using pipe viscometers; ii) to determine experimentally volumetric requirements for effective cuttings transport with foam in horizontal wellbores without pipe rotation; iii) to develop a mechanistic cuttings-transport model; and iv) to verify the cuttings transport predictions of the model with experimental data. Table 12.1 presents the current status of the project.

Table 12.1 Project Status

Activities		**2002**	**2003**			**2004**	Status
		Fall	Spring	Summer	Fall	Spring	
Literature Review	Foam rheology	▨	▨	▨	▨	▨	95%
	Cuttings transport with foam	▨	▨	▨	▨	▨	95%
Laboratory Experiment	Lab testing of Bachman foam		▨	▨			100%
	Lab testing of Weatherford foam				▨	▨	95%
Flow-loop Experiment	Foam rheology tests				▨		15%
	Cuttings transport with foam tests				▨		2%
Mathematical Modeling	Mechanistic model development				▨	▨	70%
	Computer simulator					▨	20%

12.2 LABORATORY TEST WITH FOAM

Initially a foam system provided by Bachman Service Inc. was proposed in this study. However, due to short supply of Bachman surfactant and foam breaker, we finally decide to switch to a foam system provided by Weatherford Services. The formulation for foam cuttings transport experiment is: air, water, 0.1-0.3% liquid polymer (Weatherford KLEAN-VISH™) and 0.5-1% surfactant (Weatherford KLEAN-FOAM™). For breaking the foam, 0.3-0.6% defoamer (Weatherford WFT-DF-250) will be injected downstream of the annular test section. Although this foam system has been widely used in underbalanced drilling operations, it is new for ACTS project and TUDRP. Laboratory tests to characterize and evaluate this system were carried out before conducting flow loop tests. The lab test included evaluating properties of the foam system and liquid phase (water + 0.5% surfactant + liquid polymer). The surface tensions of the liquid Phase with respect to surfactant concentration, and the effect of polymer concentration on foam rheology and foam stability were investigated. Table 12.2 shows the rheological measurements of the liquid Phase with polymer concentration of 1 gal/100 bbl.

Table 12.2 Rheological Measurements of Base Liquid

Dial Reading						Rheological model
θ (3)	θ (6)	θ (100)	θ (200)	θ (300)	θ (600)	
0.2	0.3	2.0	3.5	5.0	9.0	$\tau=0.0128\gamma^{0.85}$

Foam stability tests were preformed with 100-ml liquid Phase samples (Water + 0.5% surfactant + varying quantities of liquid polymer). Foams were generated by a “high-speed mixer” (Multi-Mixer®) and a simple eight speed kitchen blender (Costerizer®). One minute foam generation time was used in both cases. The volumes of foams and half-life times were measured for different liquid polymer concentrations. Figures 12.1 and 12.2 present the half-life times and foam volumes as a function of polymer concentration for high-speed mixer and kitchen blender, respectively.

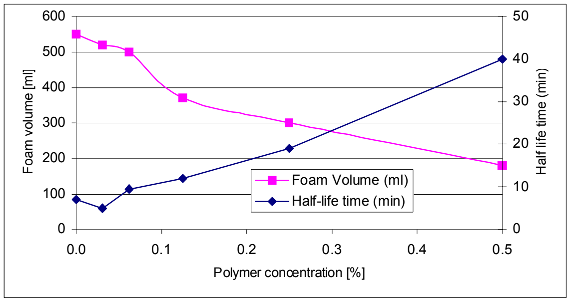

Fig. 12.1 Influence of polymer concentration on foam properties (high-speed mixer)

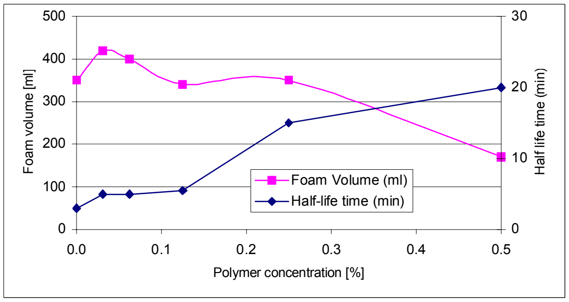

Fig. 12.2 Influence of polymer concentration on foam properties (kitchen Blender)

It can be seen that with the increase in liquid polymer concentration the half-life time increases while the amount of foam generated predominately decreases. At higher polymer concentration only low quality foams were generated. Figures 12.3 and 12.4 present foam qualities as a function of polymer concentration for the foam stability tests. It is worthwhile to note that low quality foams generated at higher polymer concentrations are more stable than high quality foams with less polymer concentration. This property of polymer-based foams can be very useful to control surface and bottomhole pressure during foam drilling. Foams generated using the high-speed mixer appear to more stable than foams generated by the kitchen blender. The volume or quality of the polymer-based foam generated at a given polymer concentration was approximately the same for both mixers. However, high-speed mixer produced a greater volume of foam than the kitchen blender.

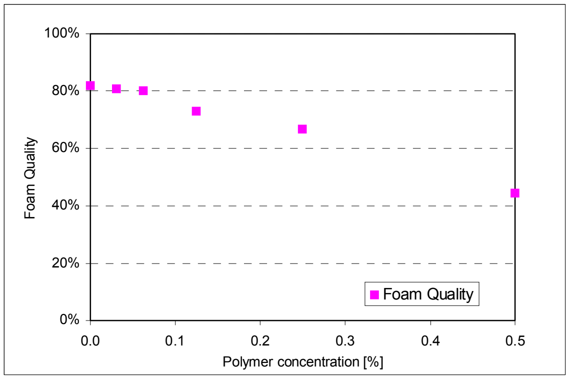

Fig. 12.3 Influence of polymer concentration on foam quality (high-speed mixer)

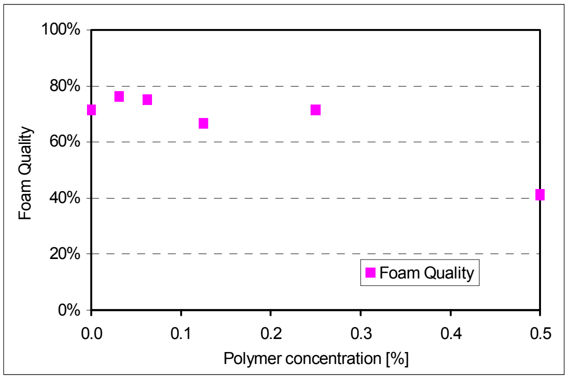

Fig. 12.4 Influence of polymer concentration on foam quality (Warren Blender)

Figure 12.5 shows the surface tension of the surfactant at room temperature. The surface tension was measured with the capillary method. Pure water surface tension at ambient conditions is 0.072 N/m, we found that while surface tension decreases dramatically up to 0.5% v/v surfactant, when the surfactant concentration is above 0.5%, there is little change of surface tension.

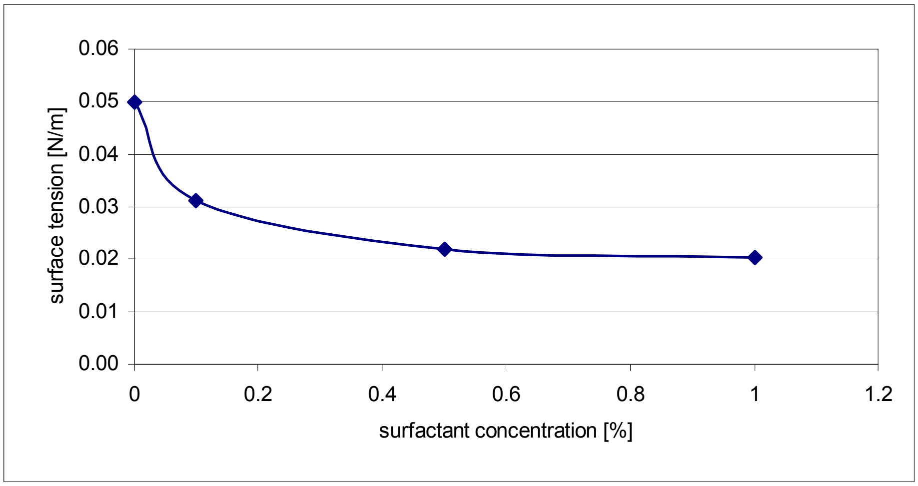

Fig. 12.5 Surface tension versus surfactant concentration

In addition, a laboratory test was conducted to check the possibility of injecting pre-mixed surfactant and polymer solutions into the flow loop upstream of the foam generator. In this experiment, surfactant solution was mixed with concentrated polymer solution (50% polymer). After mixing, a very thick gel formed, which was very difficult to pump was formed. Therefore, we decided to add the polymer solution directly into the 100-bbl water tank.

12.3 PRELIMINARY FOAM RHEOLOGY EXPERIMENT

12.3.1 FLOW LOOP SETUP

The Advanced Cuttings Transport Flow Loop is used for this experimental study. The test facility consists of i) pumping system; ii) compressed air system; iii) foam generation and breaking system; iv) heating and cooling system; v) cuttings injection and separation system; vi) measurement and data acquisition system; and vii) storage tanks. Figure 12.6 shows the schematic representation of the ACTS Flow Loop for foam experiments.

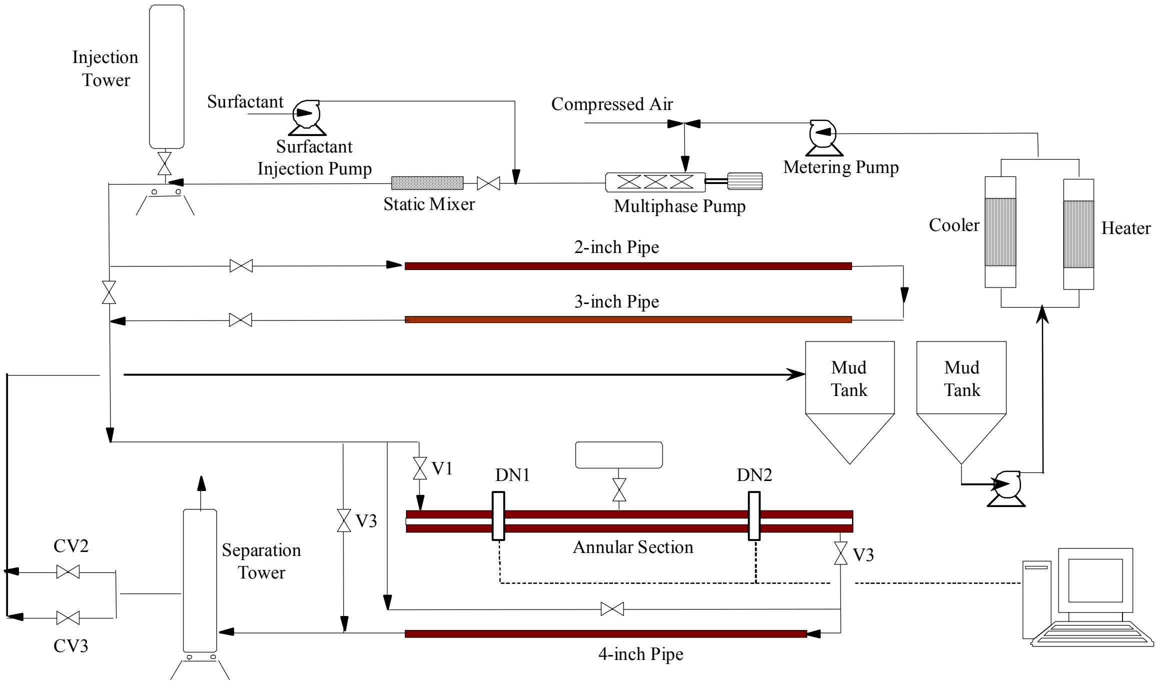

Fig. 12.6 Simplified schematics of the ACTF for foam test

Foam test begins by mixing liquid polymer and water in a 100-bbl water tank. A centrifugal pump delivers the polymer solution from this tank through a heat exchanger. After the heat exchanger the solution flows through a metering pump, which accurately feeds a desired amount of the solution to a multiphase pump. Compressed air at 200 psi is fed to the multiphase pump by an air compressor. The compressed air is mixed with the solution coming from the metering pump at the inlet of the multiphase pump. The multiphase pump can produce an additional pressure increase of up to 500 psi. A surfactant metering pump (Fig. 12.7) injects the surfactant at the outlet of the multiphase pump. The air-liquid mixture discharged from the multiphase pump flows through a Fisher valve and static mixer to generate foam. After the static mixer, foam flows through a 4-inch pipe, where the cuttings can be injected to the system.

Cuttings are not injected to the system during rheology tests. The foam from the 4-inch pipe flows through 2-inch and 3-inch rheology sections and the main test section (5.76”x3.5” annulus). On each of these sections view ports (Fig 6) are installed to offer online visual observation of the foam. The foam leaving the annulus flows through a 4-inch rheology section to a separation tower. Foam breaker is injected between the outlet of the 4” pipe and the separation tower using a defoamer injection pump. In the separation tower, foam separates into the liquid and gas phases; most of the gas phase is vented to the atmosphere while the liquid phase flows to a storage tank.

In order to conduct the cuttings transport test with foam, cuttings are injected when foam flows through the 4-inch the pipe, foam-cuttings mixture bypasses the 2” and 3” rheology sections and flows directly to the annular test section. Two gamma-ray densitometers measure the mixture density. Before a “steady state” is reached, some of the cuttings deposit in the test section. The foam carries undeposited cuttings to a separation tower via the 4-inch rheology section. Foam breaker is injected between the outlet of the 4” pipe and the separation tower using a defoamer injection pump. In this tower, the foam separates into the liquid and gas phases. Most of the gas phase is vented to the atmosphere. The separation tower has a screen with 0.06-inch (1.5 mm) hole size to remove cuttings from the liquid phase. Two backpressure valves (CV2 and CV3) down stream of the separation tower control the test section pressure. After the separation tower, the liquid phase returns to the storage tanks.

When the steady state condition is achieved, the quick closing valves V1 and V3 are closed to trap the foam-cuttings mixture inside the test section. The trapped foam is then allowed to expand into an expansion tank. The densitometer readings and foam expansion data are useful to determine the in-situ cuttings concentration.

Fig. 12.7 Surfactant injection metering pump

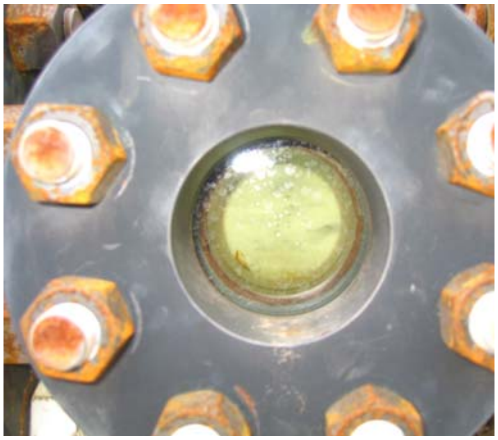

Fig. 12.8 View ports

12.3.2 FOAM RHEOLOGY EXPERIMENT RESULTS

Foam rheology tests were carried out to evaluate the rheological properties of the foam system, because this system is different from that used in Task 9. Rheology tests are needed to obtain the desired foam flow index, n, and consistency index, K, as well as foam rheology at different pressures, temperatures and qualities. After successful completion of the first trial foam test, two sets of rheological tests were conducted at different foam flow rates while keeping other parameters constant (100 psi, 70°F, 80% quality). Figures 12.9 and 12.10 present the wall shear stress as a function of Newtonian shear rate for polymeric foams with polymer concentrations of 0.025% and 0.075%, respectively. An interesting observation during these tests is that, in both cases, the wall shear stress in 2-inch pipe was lower than the 3-inch and 4-inch pipes.

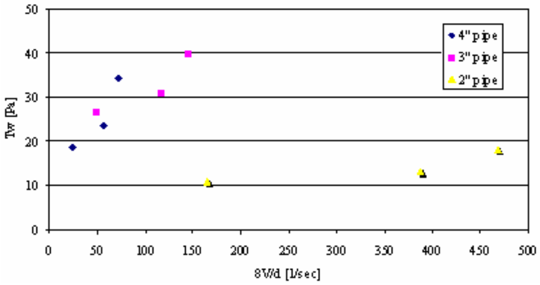

Fig. 12.9 Wall shear stress vs. Newtonian shear rate (0.025% polymer, and 0.83 % surfactant at 70°F, 100 psig, 80% quality)

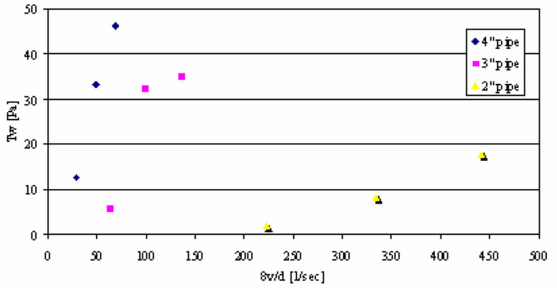

Fig. 12.9 Wall shear stress versus Newtonian shear rate (0.075% polymer, and 0.83 % surfactant at 70°F, 100 psig, 80% quality)

In order to find out what contributed to this unexpected phenomenon, extended preliminary tests were performed. The reason turned out to be the failure of a differential pressure transducer in the 2-inch pipe. A new pressure transducer has been installed and calibration tests were conducted with water at flow rates of 55 gpm and 100 gpm. Figure 12.11 shows the predicted and measured pressure drop versus flow rate in pipes and the annulus. Test data show that after the installation of the new 2-inch pressure transducer, the measured and predicted pressure losses are very close. We can also observe from Fig. 12.11 that for the 3" and 4" pipes and 5.76"x3.5" annulus the differential pressure transducers function properly, which means that except for the 2" pipe, the initial foam experimental data can still be used.

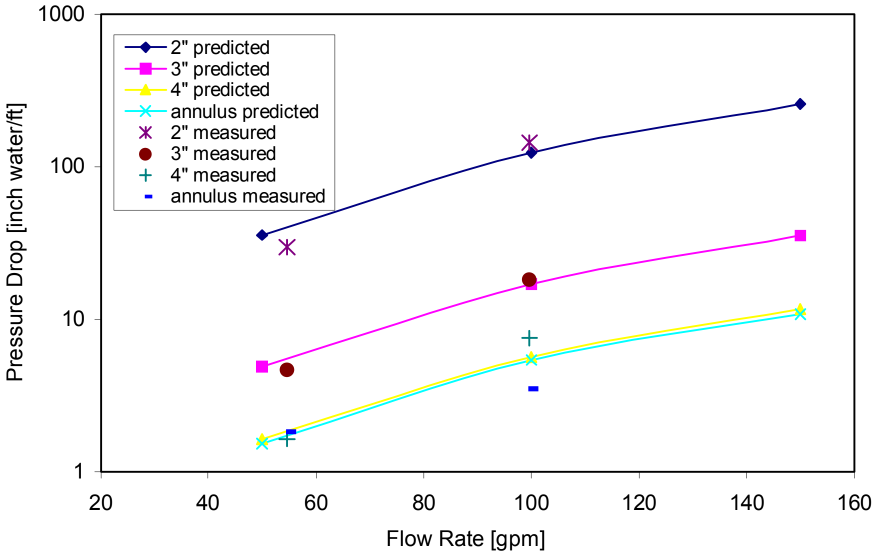

Fig. 12.11 Pressure drop in pipes and annulus versus water flow rate

As part of the trouble-shooting for the abnormal 2-inch pipe pressure drop, foam comparison tests were conducted. The primary purpose of this test was to check whether the low frictional pressure drop in the 2" pipe was due to the type of surfactant that was used. Two foam systems were tested under almost identical test conditions (i.e. 85 psi, 80 F, water injection rate 5.5 gpm and gas injection rate 72 SCFM). The only difference was the surfactant; one with Weatherford KLEAN-FOAM and the other one with Bachman F450. Although we finally ruled out the surfactant type as the explanation, some useful observations were made in these tests. Figures 12.12 and 12.13 show the measured pressure gradient using Bachman and Weatherford surfactant under identical conditions. In both experiments, foam was first generated with a static mixer and fully-opened Fisher valve; then a ball valve, located upstream of the static mixer, was gradually closed until the pressure loss across the ball valve reached 100 psi, in this way shear energy was added as previously done in Task 9. High pressure gradient before opening the ball valve indicated the generation of stable foam. However, when the ball valve was throttled to maintain the pressure gradient of 100 psi, low pressure drop was observed in both pipes and the annulus. One explanation for the reduction in pressure loss could be foam breakage while flowing through the opened Fisher valve.

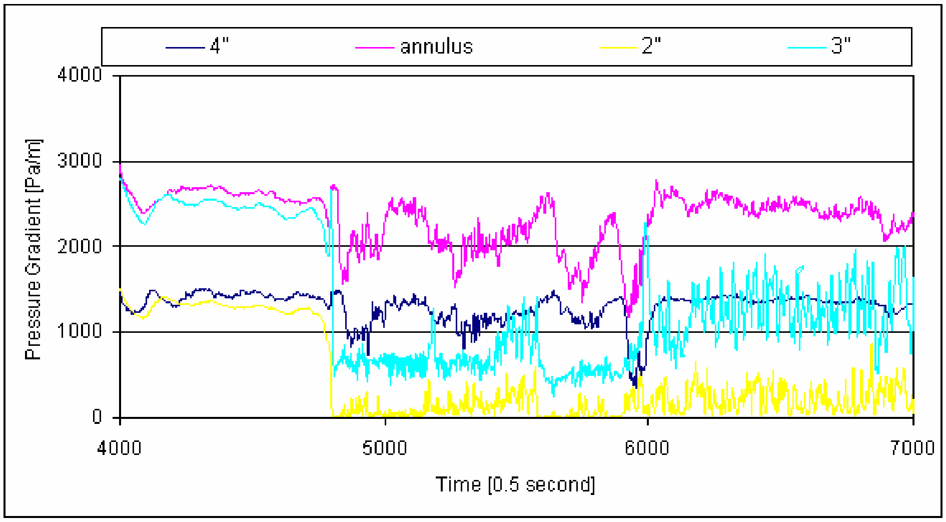

Fig. 12.13 Pressure gradient vs. time (Bachman foam, 1% Surfactant, 85 psi, 80°F, 5.5 gpm, 72 SCFM)

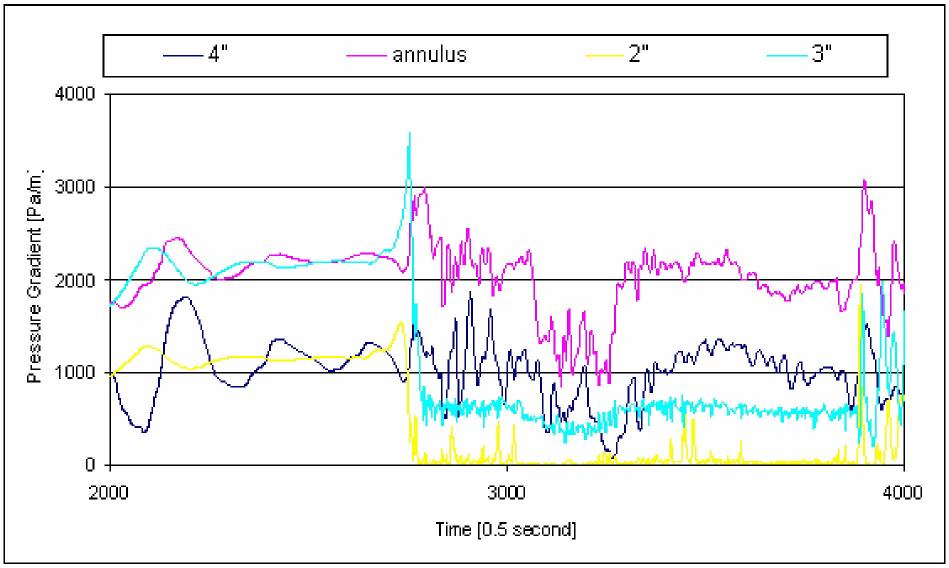

Fig. 12.13 Pressure Gradient vs. time (Weatherford Foam, 1% Surfactant, 85 psi, 80°F, 5.5 gpm, 72 SCFM)

In both tests, the pressure gradient in all the pipes and the annulus shows was comparable. In addition, from both figures we can observe that the 2-inch pipe pressure drop is lower than the other pipes in both test foams, this ruled out the hypothesis that a significant difference may exist between the two surfactants. In terms of foam generation method, both the Fisher valve and ball valve were used to generate foam on different occasions. It was found out that both of them can be used to generate stable foam. However, the Fisher valve is preferred because of its precise control of the foam generation process.

After the low pressure drop problem was solved, a preliminary foam rheology experiment was successfully conducted. The flow rates were 5.1 gpm, 9.3 gpm, 13.45 gpm for water injection and 45.7 scfm, 70.3 scfm, 108.29 scfm for air, which corresponds to 90% foam quality. Test pressure and temperature were 85 psi and 80°F, the ball valve was partially closed to add shear energy to generate stiff foam. In this experiment, the differential pressure across the ball valve was maintained around 35 psi; this value has not been optimized and will be standardized for future experiments. Test results are presented in Fig. 12.14; the 2-pipe pressure drop is higher than in 3-inch and 4-inch pipes. All the data points collapse into one curve. The data in Log-Log plot is also shown in Fig. 12.15, a Power-law rheological model was fitted in this case. Pressure losses in the 3-inch and 4-inch pipes appear to be very low. This could be due to instrument error because the differential pressure transmitters in the 3-inch and 4-inch pipes were maxed out during the test.

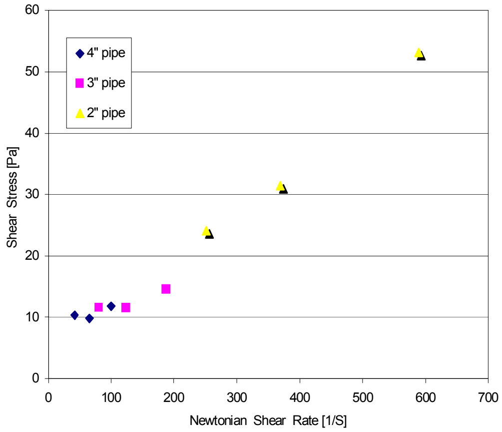

Fig. 12.14 Wall shear stress vs. Newtonian shear rate for 90% quality foam (Weatherford)

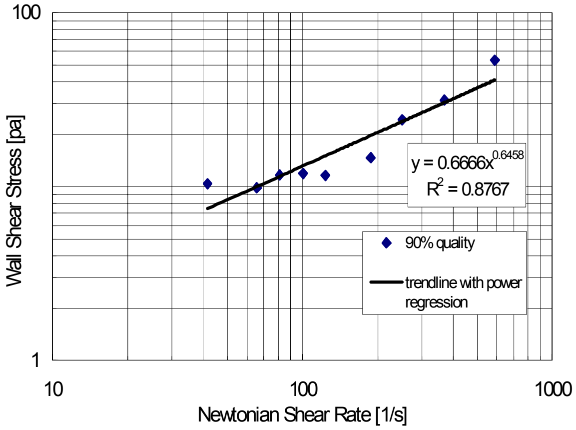

Fig. 12.15 Flow curve of 90% foam in log-log plot (Weatherford)

By the end of February, the test section of the flow loop was disassembled for installing the loop elevation system. Foam experiments will resume in August 2004. The plan is to determine the proper differential pressure drop across the foam generator, and then conduct all the foam rheology experiments. Cuttings experiments will follow the rheology tests.

12.4 PRELIMINARY CUTTINGS TRANSPORT EXPERIMENT WITH FOAM

A preliminary cuttings transport test with foam was conducted to evaluate: i) cuttings injection auger ii) densitometers response to foam flow and iii) cuttings carrying capacity of foam. Densitometer readings from this experiment are presented in Figs. 12.16 and 12.17. The test was subdivided into four test stages. These stages are:

Stage 1. Water flow, with densitometer readings of nearly 1.0;

Stage 2. Air-water flow, with the densitometer readings between 0.2 and 0.5;

Stage 3. Foam flow, during this period, the densitometer readings were nearly zero, which were also observed for all the other foam rheology tests;

Stage 4. Cuttings were being injected to the loop, the densitometers readings were between 0 and 0.15.

The reason why the densitometer readings become zero during foam flow is still not clear at this point. A detailed study of densitometer reading with respect to cuttings concentration will be done in the future.

Figure 12.17 shows the injection and collection of cuttings rates for this experiment, Cuttings injection began at about 15000 x 0.5 seconds. It can be seen that a nearly-constant injection rate (the slope of the curve) was maintained. This means that cuttings can be injected at a controlled way. Also, cuttings were transported without any blockage. Cuttings were visually observed through the view port installed in the annulus section.

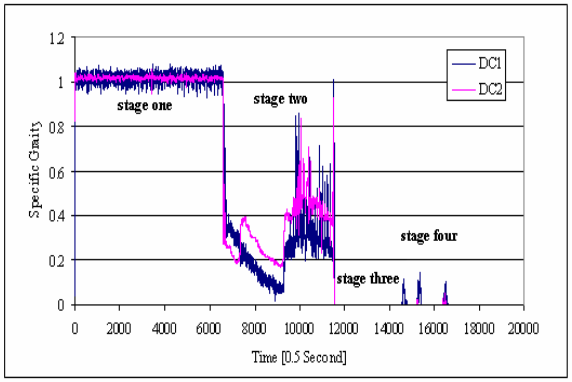

Fig. 12.16 Densitometer reading for foam cuttings transport test

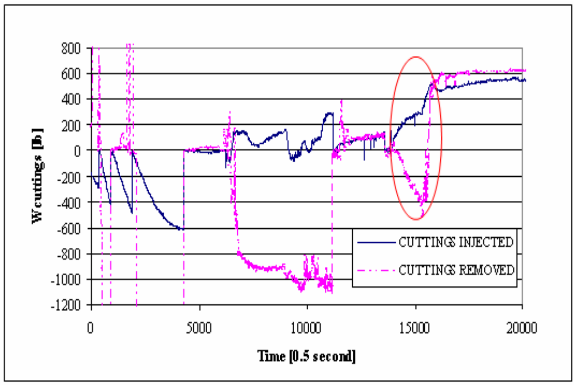

Fig. 12.17 Cutting injections and collection

As mentioned in Section 3.6, flexible hoses were installed to isolate the injection and separation towers from piping loads which were causing inconsistent load cells readings. Cuttings transport tests were conducted after the installation of the hoses. During these tests, load cell measurements were relatively stable; and they were in agreement with the readings of nuclear densitometers. In future, cuttings transport tests will not require flushing of cuttings to a container for manual weighing.

Prior to the cuttings transport tests, flow loop test with water was conducted to verify differential pressure transducers in the flow loop. Water flow rate was varied from 50 to 300 GPM and differential pressures were measured in the 2”, 3”, 4” and annulus section. The measured differential pressures are presented in Fig. 12.18 along with theoretical predictions for smooth pipe.

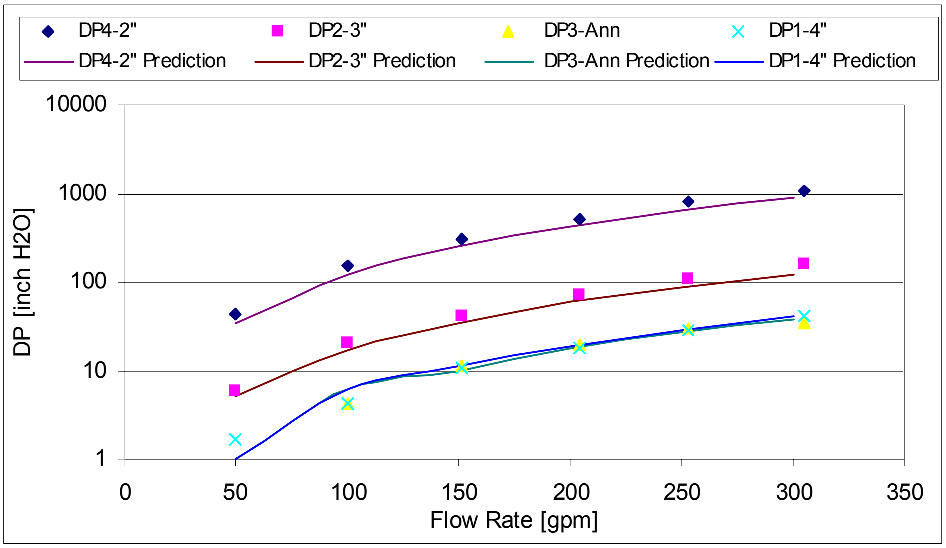

Fig. 12.18 Measured and predicted differential pressures versus flow rate

12.5 PREDICTING PRESSURE DROP USING CFD

An attempt was also made to use a computational fluid dynamics (CFD) package to model foam flow in pipes and annulus. This approach can be useful because foam is a non-Newtonian fluid and its rheology can be determined from flow loop experiments. CFD packages like FLUENT have the capability to model non-Newtonian fluid flow. Therefore, based on experimentally obtained rheological parameters and foam density, we can predict pressure drop in pipes and annuli, and compare the CFD predictions with experimental data.

The CFD package used in this study is FLUENT 6.0. It uses the finite-volume method to solve the governing equations of non-Newtonian flows. It provides the capability to use different physical models such as incompressible or compressible fluids, non-viscous or viscous flows, laminar or turbulent flow, etc. Geometry and grid generation is done using GAMBIT which is the preprocessor bundled with FLUENT.

The steps in using GAMBIT software to create geometry are as follows: i) creating the pipe and annulus geometry; ii) generating mesh; iii) defining boundary and continuum types; and iv) exporting mesh. The dimensions of the rheology sections and the annulus are given in Table 12.3. Figure 12.19 shows the mesh generated with Gambit for an annulus.

Table 12.3 Dimensions of Pipes and Annulus Used In CFD Modeling

Pipe diameter (in)	Pipe ID (in)	Length (ft)
2	1.918	52.75
3	2.900	52.75
4	3.826	66.50
Annulus (6 x 3.5)	5.761x 3.5	57.33

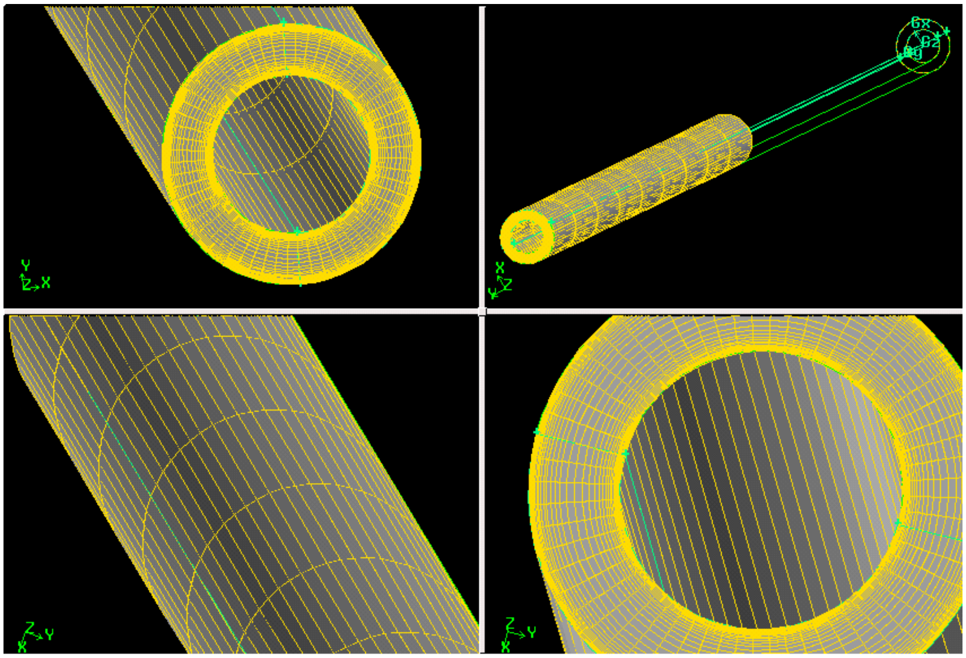

Fig. 12.19 Meshes generated for simulating annular flows

The main steps in FLUENT solver includes: i) reading the mesh file into FLUENT; ii) setting up solver properties such as viscosity, flow regime, flow material, operation conditions, boundary conditions; iii) setting solution schemes, initialization of flow field and convergence criteria; iv) solve; and v) post processing. As a first step to check the accuracy of CFD packages, water flow at 100 gpm was simulated in the 2”, 3” and 4” pipes, and 5.76” x 3.5” annulus. At this flow rate, the flow regimes in all geometries are turbulent flow. Figure 12.20 shows pressure drop in 4” pipe as a function pipe length. The simulated pressure drop in all pipes and annuli are shown in Table 12.4. It can be seen that the pressure drop predictions with CFD and the Fanning Equation are very close. Actually, when we compare them with measured data, they are also quite close.

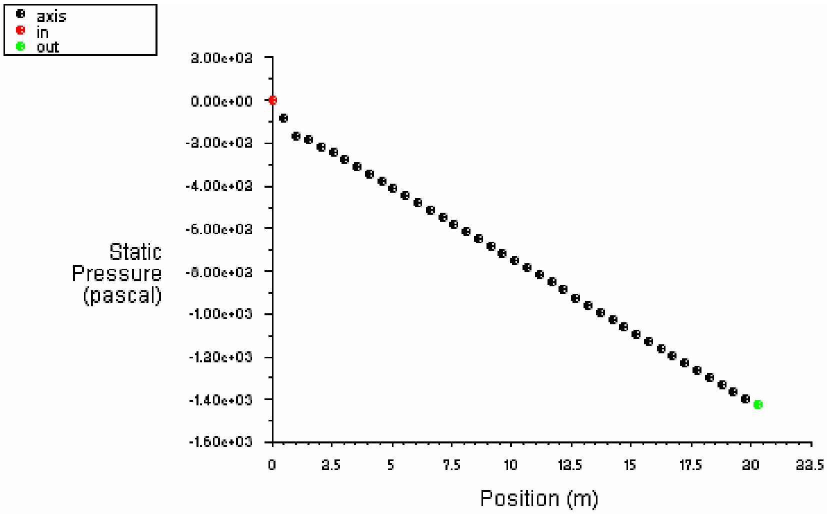

Fig. 12.20 Pressure drop prediction using FLUENT for water flow in 4-inch pipe at 100 gpm

Table 12.4 Comparisons of Pressure Drop for Water Flow

Pipe Size	CFD prediction [pa]	Fanning Eq. [pa]	Difference[%]
2”	32547	30807	5.6
3”	4598	4240	8.4
4”	1451	1415	2.5
5.76” x 3.5” annulus	1410	1350	4.4

Preliminary pressure drop predictions for foam flow in 2”, 3”, 4” pipes and 5.76” x 3.5” annulus were also carried out. Foam is assumed to be a Power-law fluid with $K = 0.3\ Pas^{0.5}$, $n = 0.5$, density of 200 kg/m^3; and flow velocity is fixed at 0.6096 m/s (2 ft/s). For all cases at this flow rate, the flow regimes in all geometries are expected to be laminar flow. The simulated and the exact solutions of pressure drop in all the pipes and annuli are shown in Table 12.5. The CFD predictions for foam flow are in good agreement with the exact values.

Table 12.5 Comparisons of Pressure Drop Predictions for Foam Flows

Pipe Section Size	CFD prediction [pa]	Analytical [pa]	Difference[%]
2”	3923	4430	11.4
3”	2071	2383	13.0
4”	1693	1588	6.6
5.76” x 3.5” annulus	3989	/	/

The CFD simulation of water and foam flows shows that it is possible to predict pressure drop with CFD software to simulate foam flows in pipes and annuli. In the future, User Defined Functions (UDF) can be added to the FLUENT package to predict more complicated scenarios; for example, by defining Equation of State, we can even predict pressure drop of foam flow in the whole wellbore. Moreover, the FLUENT package has the capability of tracking particles in non-Newtonian fluid flow. It is worthwhile exploring the possibilities of predicting cuttings concentration for foam flow in horizontal annuli.

13. Safety Program (Task 1S)

13.1 INTRODUCTION

This project was initiated during the fourth quarter of 2000 to assess the hazards associated with the Advanced Cuttings Transport Facility (ACTF) and develop an Action Plan to address problems discovered during this Hazards Review. A Hazards Review is an industry accepted method used to improve the overall safety characteristics and reduce the possibilities of accidents in the work place. Each individual component of the ACTF is examined as to the effect and consequences on safety, health, and the environment, of the component in all possible operational modes.

A Hazards Review can result in equipment modification, inspection and testing, documentation, personal protective equipment, personnel training, and/or emergency training. The hazards review process begins by selecting a review method. Next a team of qualified individuals must be formed. This team should include those knowledgeable in the review process and those familiar with the process to be reviewed. Prior to beginning the review, all available documentation needs to be gathered. This includes schematics, organized training, periodic inspections and testing results, design and construction documents, operating procedures, etc. Once the schematics have been verified and the operator of the equipment or process has reviewed its operation with the team, the Hazards Review begins. The review should continue uninterrupted until completed. After the findings and recommendations have been completed, a draft report is issued and reviewed by all team members, and the operator of the process or equipment. Following this review, any changes are incorporated and a final report issued. This completes the Hazard Review process. The operator then needs to develop an action plan to implement the recommendations from the Hazard Review. In our case, team members will participate in developing this plan.

The objective of this task is to identify problems (findings) that might result in injury, property damage or the release of environmentally damaging materials and provide recommendations to minimize them, and to develop an action plan based on these recommendations.

The “What if “ method was chosen for our Review because it is easy, straight forward, and widely used and accepted in industry. Each stage and each component of the ACTF is examined with a “What if” question as to what happens when that component is in different modes of operation. Next, the consequences of these operating modes are identified and listed. Safeguards are listed for those consequences that may result in injury, property damage or release of environmentally damaging material. If adequate safeguards do not exist, a finding is issued with a recommendation.

13.2 HAZARD REVIEW TEAM

Table 13.1 gives the membership for the Review Team and Work Team. The Work Team conducts the Hazard Review and the Review Team reviews the draft document generated by the Work Team and offers suggestions for modification and improvement. Other members may be added to the Review Team.

Table 13.1 Review Team and Work Team Members

Name	Affiliation	Review Team	Work Team
Leonard Volk	Chairman (TU)	X	X
John Ford	Nat’l Petr. Tech. Office (US DOE)	X	X
Don Harris	Microelectronics Technician (TU)	X	X
Dave Hensley	Consultant (Tulsa Tech. Center)	X	X
Stefan Miska	ACTS Co-PI (TU)	X	
Mark Pickell	ACTS Project Engineer (TU)	X	
Troy Reed	ACTS Principle Investigator (TU)	X	
Jim Sorem	Sr. Assoc. Dean Engineering (TU)	X	
Laurie St. Clair	Dir. Environmental, Health & Safety (TU)	X	X
Nicholas Takach	ACTS Co-Principle Investigator (TU)	X	
Mike Volk	Mgr. Research & Tech. Dev. (TU)	X	X

13.2.1 WORK TEAM MEETING (FEBRUARY 23, 2001)

The Work Team held their initial meeting February 23, 2001. Mark Pickell, ACTS Project Engineer, used existing schematics to lead the team through the operation of the facility. Bad weather prevented an on-site tour of the ACTF. It became apparent that we needed an updated schematic. The Team also expressed the need for a list of valves, their type and pressure rating as well as information on relief devices. Several safety-related scenarios were discussed with about 11 “What if” questions being asked.

Preliminary Hazard Review Activities

For review purposes, the ACTF was broken into the following subsystems:

- ACTF-1
- ACTF-2
- Diesel Tank
- Surge Tank
- Heater

Schematics for these systems were drawn to exclude “planned” modifications and obsolete (no longer existing) plumbing, and include all valves and other components present. The cuttings transport facility was somewhat arbitrarily broken into two parts so that the schematics could be maintained as readable as possible. The heater and surge tank are purchased equipment with built-in safeguards. Although external valves and other hardware can be accessed, manufacturing safety standards should be in place, and therefore these two subsystems were not reviewed. All components (shut-off valves, relief valves, gauges, flow meters, check valves and pumps) on these schematics have been identified and numbered. Numerous safety and operational improvements were noted are the time the drawings were made. These schematics appear in Fig. 13.1 below;

ACTF - 1

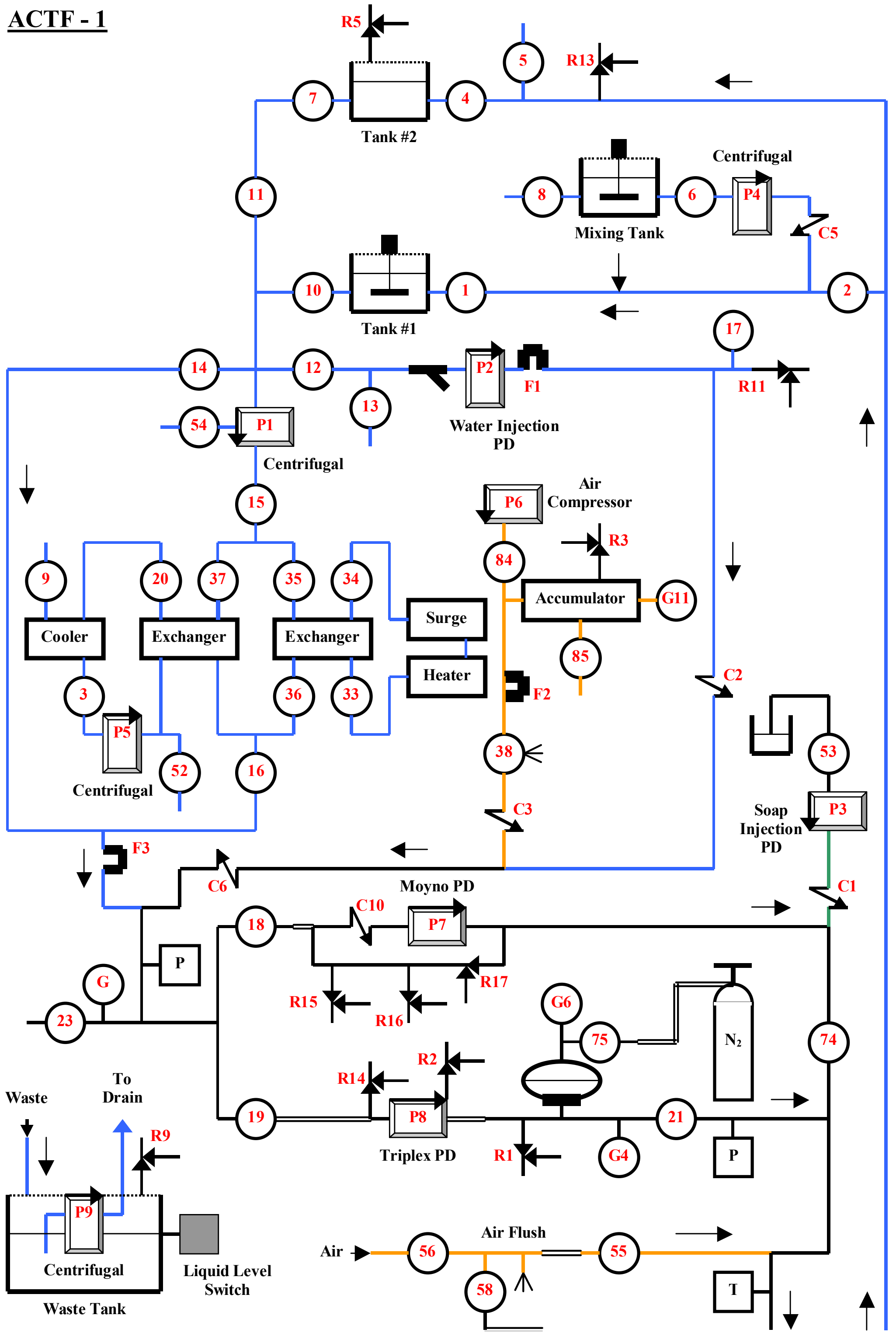

ACTF - 2

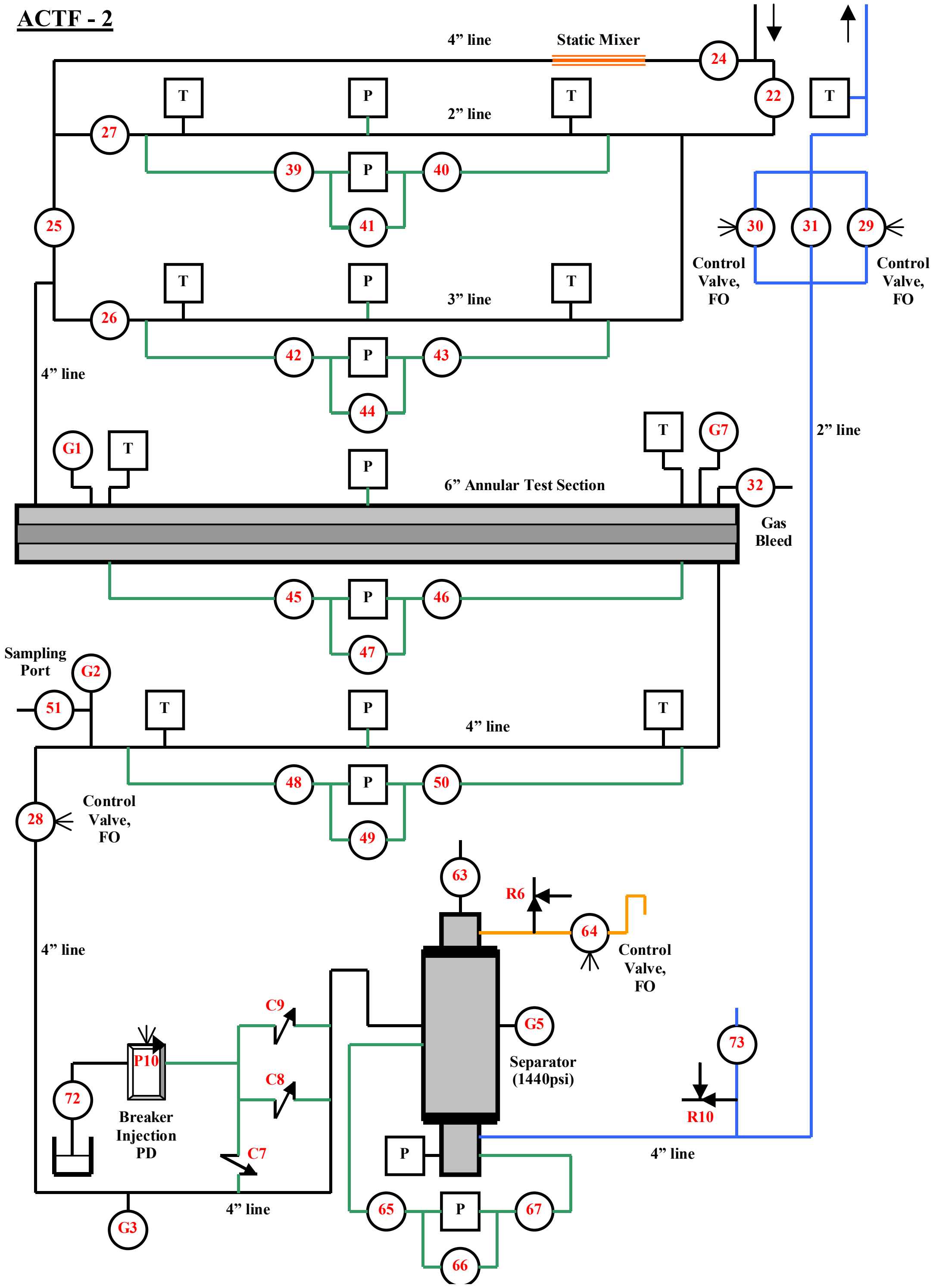
4” line
Static Mixer
24
22
T
T
P
T
2” line
27
39
P
40
41
25
30
31
29
Control Valve, FO
Control Valve, FO
T
P
T
3” line
26
42
P
43
44
4” line
2” line
G1
T
P
T
G7
6” Annular Test Section
32
Gas Bleed
45
P
46
47
Sampling Port
G2
51
T
P
4” line
T
48
P
50
49
28
Control Valve, FO
4” line
63
R6
64
Control Valve, FO
C9
C8
C7
P10
72
Breaker Injection PD
G5
Separator (1440psi)
73
R10
P
4” line
4” line
G3
65
P
67
66

DIESEL TANK

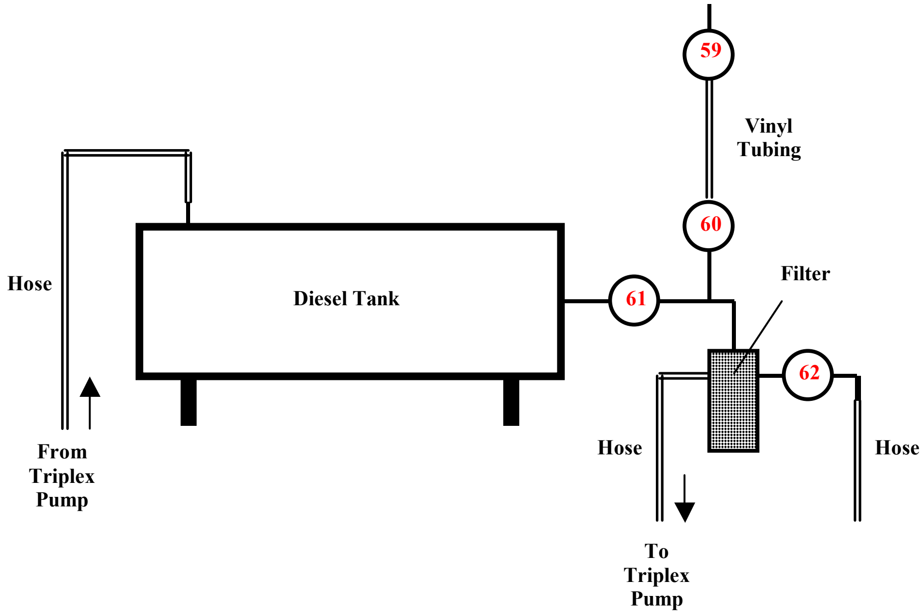

HEATER

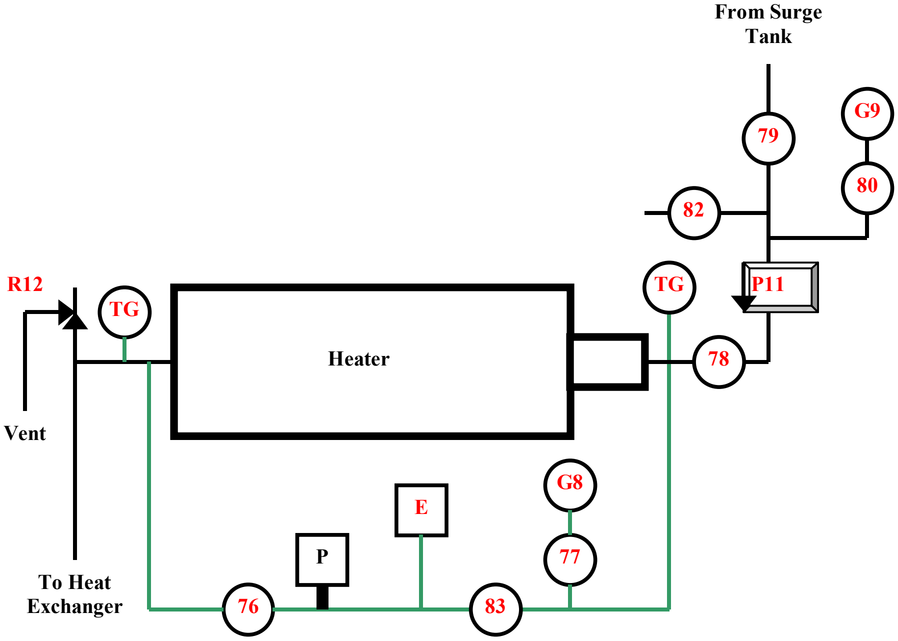

E: Electronic switch

SURGE TANK

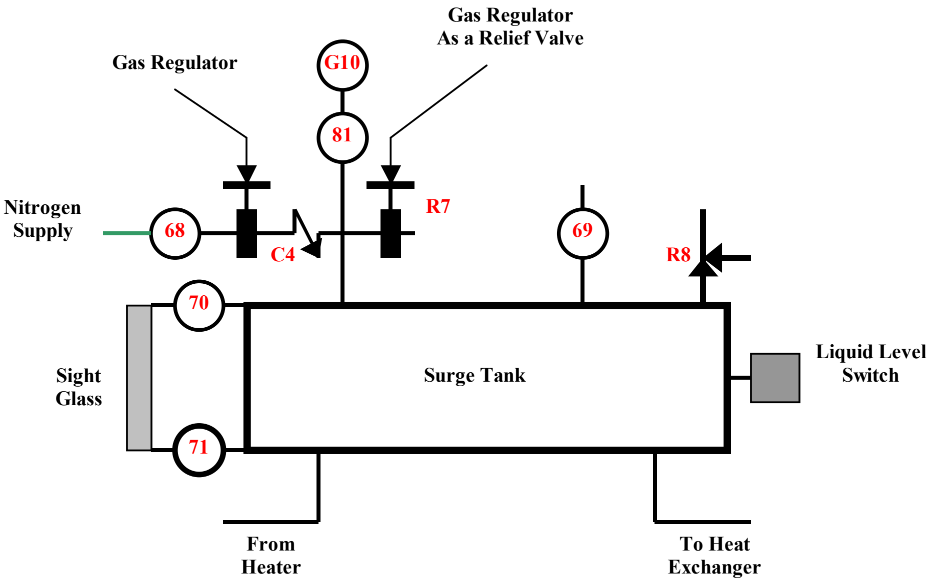

KEY

4	Valve
P	Pressure Transducer
T	Temperature Transducer
<	Air Quick Disconnect
| | |	Steel Pipe: Liquid, gas, both possible
|	Stainless Tubing
R3	Relief Valve
C2	Check Valve
‖	Flexible Hose
F2	Flow Meter
28 <	Pneumatically or electrically controlled valve
TG	Temperature Gauge
P2	Pump
G2	Pressure Gauge
FO	Valve - fails open when de-energized
FC	Valve - fails closed when de-energized

Fig. 13.1 ACTF schematics for the initial Hazards Review

Permanent brass tags have been attached to most components to aid in identification and developing operating procedures. A list of shut-off valves, relief valves, check valves, flow meters and pumps was compiled. This list includes the following:

Table 13.2 Properties of ACTF Components

Component	Type	Pressure Rating	Characteristics
Shut off valve	Globe, ball, control	Maximum	Size, material
Check valve		Maximum	Size, material
Relief valve	Shear pin, spring	Relief pressure	Maximum flow rate
Flow meter	Operating principle	Maximum	Flow rate range
Pump	Positive displacement & centrifugal	Maximum	Maximum flow rate

13.2.2 WORK TEAM MEETING (APRIL 30, 2001)

Laurie St. Clair and Mike Volk were unable to attend this meeting. Charles Alworth, a consultant with considerable background in piping design, electronic controls and law aided in our Review. Each member was provided with current schematics, a list of components and their properties and the “What if” table from our previous meeting. Mark Pickell began with an on-site review of the facility. Following a lengthy question and answer session, the Review Team began the formal Hazards Review. Review was completed by 2:30 PM.

13.2.3 HAZARDS REVIEW REPORT

The Hazard Review Team addressed 141 “What if” questions. The findings were broken down into several categories under three general headings.

1) Pertaining to equipment/piping/components

- No monitoring of “no flow” condition by pumps while operating
- Insufficient protective splash guard from relief valve discharge
- Improper hose for application
- Incorrect relief valve setting
- Air hoses not secured
- No reverse flow protection
- No relief protection
- No pressure bleed valve
- Improper direction of released fluid
- Flammable material too close to ignition source
- No secondary spill containment
- No placarding or labeling of containers or storage devices
- Tubing incompatible with contents
- No protection against mechanical breakage
- No automatic shut-off of fuel supply
- Inadequate protection against high volume gas release
- Inadequate number/location of fire extinguishers
- No protection barrier around facility

2) Pertaining to inspection & documentation

- No design documentation of piping or fittings
- No design documentation for relief valves
- No inspection procedures & documentation for relief valves
- No design documentation for hoses
- No inspection procedures & documentation for hoses
- Incomplete design documentation of component parts (valves, etc)
- No written operating procedure
- No inspection procedure & documentation for pipe corrosion

3) Pertaining to training

- No site-specific emergency action plan
- No specific lock-out, tag-out procedures
- No documented training procedure for operating personnel
- No documented safety training program

During the third quarter of 2003 (Year 4), a table labeled "Hazards Review Finding Status" was developed to track the progress in resolving the various Findings. Hazards review finding status updates on April 22, 2003 and July 1, 2004 are presented in Tables 13.3 and 13.4.

Table 13.3 Hazards Review Findings Status (4-22-03)

Finding	Occurrence	Type	Risk	Consequence	Status	Lead
No monitoring of "no flow" condition of pump while operating	1, 2, 3, 8, 9, 12, 15, 31, 37, 41, 98, 118, 119	O	1	2	20	ST
No design documentation for piping or fittings	7, 23, 24, 29	S			20	LV
No design documentation for relief valves	32, 96, 102	S			20	LV
No inspection documentation for relief valves	33, 97, 103	S			20	LV
Insufficient splash protection	39, 40, 48, 49, 110, 111	S	2	2	100	MP
Improper hose for application	42	S	2	2	100	MP
No design documentation for hose	43, 46, 55, 65, 121, 127	S			10	LV
No inspection procedure & documentation for hoses	44, 47, 56, 66, 122, 128	S	2	2	10	LV
Incorrect relief valve pressure setting	45, 95, 101	S	2	3	40	MP
No pressure bleed valve	58	S	1	2	100	ST

Finding	Occurrence	Type	Risk	Consequence	Status	Lead
Air hose not secured	59	S	1	3	100	MP
No reverse flow protection	60	O	1	2	10	ST
No relief protection	61	S	1	3	10	ST
Incomplete design documentation of components (valves, etc.)	67	S			90	LV
No written operating procedure	74, 76, 82, 84, 86, 88, 89, 91, 107, 109	S	3	3	0	MP
Improper direction of released fluid	85, 92	S	1	2	50	ST
Inadequate protection against high-volume gas release	113, 115	S	2	3	10	MP
Flammable material too close to ignition source	123	S	1	3	10	MP
No secondary spill containment	124	E	1	2	10	ST
No placarding or labeling of containers or equipment storing flammable or hazardous material	125, 134	S	1	2	50	MP
Tubing incompatible with contents	126	E	2	2	100	ST
No protection against mechanical breakage – diesel site tube	129	E	1	2	10	ST
No automatic shut-off of fuel supply	130	S	1	3	10	ST
Inadequate number/location of fire extinguishers	131	S	1	3	10	MP
No site-specific emergency action plan	132	S	1	3	10	LV
No specific lock-out, tag-out procedure	133	S	1	3	10	LV
No corrosion inspection procedure & documentation for corrosion	135	S	1	3	10	LV
No written operating procedure	137	S	2	3	0	MP
No documented training procedure for operating personnel	138	S	2	3	0	MP
No documented safety training program	139, 145-147	S	2	3	10	LV
No protecting barrier around facility	140	S	1	2	0	ST

Finding	Occurrence	Type	Risk	Consequence	Status	Lead
No hazard communication training	141	S	1	3	20	LV
No training or documentation on cleaning up small spills	142	S	1	1	10	LV
No MSD sheets available on site	143	S	1	3	20	LV

Table 13.4 Hazards Review Findings Status* (7-01-04)

Finding		Response	Completed
1	No monitoring of a “no flow” condition of pump while operating	Enabled alarms in LabView program to indicate a failure when flow level is at a zero flow condition	100%
2	No design documentation for piping or fittings	Drawings and Technical Documentation book completed	100%
3	No design documentation for relief valves	Document template completed. Data input in progress.	20%
4	No inspection documentation for relief valves	Document template completed. Data input in progress	20%
5	Insufficient splash protection	Splash guards installed	100%
6	Improper hose for application	Suction piping re-built & hose replaced	100%
7	No design documentation for hose	Drawings and Technical Documentation book completed	100%
8	No inspection procedure & documentation for hoses	Document template completed	10%
9	Incorrect relief valve pressure setting	Relief valve settings re-set	100%
10	No pressure bleed valve	A new valve was installed to allow the pressure to bleed into the process piping	100%
11	Air hose not secured	Air hose removed; hook-up for stainless steel tubing installed	100%
12	No Reverse flow protection	Changed piping configuration to eliminate the possibility of reverse flow	100%
13	No relief protection	This is a return line from the fuel supply on the low pressure diesel pump no relief is required	100%
14	Incomplete design documentation of components (valves, etc)	Drawings and Technical Documentation book completed	100%
15	No written operating procedure	Students now required to write operating procedures for their experiments	100%
16	Improper direction of released fluid	Installed deflection shield and directed air blast in a safe direction	100%

Finding		Response	Completed
17	Inadequate protection against high-volume gas release	Relief discharges piped beneath splash guards or elevated	100%
18	Flammable material too close to ignition source	New fuel tank installed	100%
19	No Secondary spill containment	Moved Diesel Tank into the confines of the containment trenches	100%
20	No placarding or labeling of containers or equipment storing flammable or hazardous material	Signage in place	100%
21	Tubing incompatible with contents	Removed from diesel tank	100%
22	No protection against mechanical breakage-diesel site tube	Removed from diesel tank	100%
23	No automatic shut off fuel supply	Moved Diesel Tank into the confines of the containment trenches	100%
24	Inadequate number / location of fire extinguishers	Three additional fire extinguishers have been purchased and received / awaiting installation	80%
25	No site-specific emergency action plan	Building Emergency Plan adopted; further review needed to be site specific for the test loop	80%
26	No specific lock-out, tag-out procedure	Lock-out, tag-out training courses completed by personnel	100%
27	No corrosion inspection procedure & documentation for corrosion	Ultrasonic thickness gage purchased and received / a regular and documented inspection schedule yet to be implemented	60%
28	No written operating procedure	Students now required to write operating procedures for their experiments	100%
29	No documented training procedure for operating personnel	Safety training documented and maintained	100%
30	No documented safety training program	Safety training documented and maintained	100%
31	No protecting barrier around facility	Was not feasible at the time of the original review. Current situation allows the installation of a barrier and other safety striping. Parts on order and will be complete 08-19-04.	50%
32	No hazard communication training	Hazard communication training courses completed by personnel; MSDS sheets on site	100%
33	No training or documentation on cleaning up small spills	Spill Prevention, Control, and Countermeasures (SPCC) Plan written	100%
34	No MSD sheets available on site	Safety Data Sheets now available on site	100%

* reported by Mark Pickell and Steve Turpin

Table 13.5 lists classes that would be beneficial to those working on the ACTF. Not everyone will need every class as noted in this table. Table 13.6 provides a brief description of these courses. Safety is an ongoing job. As the ACTF construction continues, safety issues are discussed and potential problems are addressed. Because of the ever-changing landscape, a formal hazard review should be conducted of plumbing, engineering and electrical aspects of the ACTF once Phase V construction has been completed.

Table 13.5 ACTS Training for ACTF, Mud Lab, DTF and Rheometer Room

Class	TU #	Frequency	Faculty	Students	Staff	ACTS Specific
Bloodborn Pathogens	12	Initial & Annual	Yes	Yes		No
Emergency Action Plan	1	Initial	Yes	Yes		Yes. Severe weather, fire, explosion, spills, etc.
Fall Protection	23	Initial	No	No	Yes	No
Forklift Safety	18	Initial & every 3 yr	No*	No*	Yes*	No
Hazard Communication - Lab	14	Initial & every 2 yr	Yes	Yes		Specific chemicals, hazards, MSDS locations
Hazard Communication – Non-Lab	13	Initial & Annual	Yes	Yes		Specific chemicals, hazards, MSDS locations
Personal Protective Equipment	20	Initial	Yes	Yes		Discuss specific hazards
Lock-Out/Tag-Out (Authorized)	15	Initial	No	No	Yes	No
Lock-Out/Tag-Out (Affected)	16	Initial	Yes	Yes		No
Permit Required – Confined Space			No	No	No	Discuss no entry allowed in storage tanks
Spill Control & Containment	4	Initial & Annual	No	No	Yes	Discuss responsibility of students, faculty for small & large spills

* If use a forklift

Table 13.6 Course Description

Course	Description
Blood born Pathogens	Discusses the diseases that can be transmitted by contact with body fluids due to rendering of first aid or other activities in the work place
Emergency Action Plan	Covers actions employees/students must take in the event of an emergency such as fire, tornado, etc. Covers the use of portable fire extinguishers and the ways to prevent fires in the work
Fall Protection	Covers the safe use of ladders and fall protection
Forklift Safety	Discusses the safety considerations to be observed when operating a forklift, how to read capacity charts and how to perform operator pre-operation checks and maintenance
Hazard Communication (Lab)	Includes the health and safety information concerning the proper use and possible deleterious effects of substances (chemicals) in the work area. Discusses use of MSDS. This course is designed for those working in a laboratory environment.
Hazard Communication (Non-Lab)	Same as above but for those whose work place is other than a chemical laboratory
Personal Protective Equipment	Covers the effects of noise in the work area and how to minimize it. Also addresses proper selection, use and care of items such as gloves, face shields, hearing protectors, safety glasses, aprons, coveralls, etc.
Lock-Out/Tag-Out (Authorized)	This course is designed for those authorized to lock or tag equipment as out of service, usually for repair.
Lock-Out/Tag-Out (Affected)	This covers the precautions workers must observe when equipment is tagged or locked out of service.
Spill Control & Containment	This course presents the general procedures for cleaning up chemical spills

14. Technology Transfer

Several activities have been conducted since July 14 1999 including: i) Advisory Board Meetings with ACTF-JIP member companies; ii) Oil and Gas conference presentations and journal publications; and iii) individual visits and presentations to oil and service companies.

14.1 ADVISORY BOARD MEETINGS

Since July 14, 1999 efforts have been spent continuously to increase the number of industry members supporting the ACTS projects. Table 14.1 presents a summary of ACTS-JIP members for the last 5 years.

Table 14.1 List of ACTS-JIP Members

	ACTS-JIP Members
Year 1	1) U.S DOE, 2) Chevron, 3) Halliburton, 4) Statoil, 5) JNOC, 6) Schlumberger, 7) BP-Amoco, 8) Baker-Hughes, 9) Intevep and 10) Petrobras
Year 2	1) U.S DOE, 2) Chevron, 3) Halliburton, 4) Statoil, 5) JNOC, 6) Schlumberger, 7) BP-Amoco, 8) Baker-Hughes, 9) Intevep, 10) Petrobras and 11) Weatherford.
Year 3	1) U.S DOE, 2) Chevron, 3) Halliburton, 4) Statoil, 5) JNOC, 6) Schlumberger, 7) BP-Amoco, 8) Baker-Hughes, 9) Intevep, 10) Petrobras, 11) Weatherford and 12) TotalFina-Elf.
Year 4	1) U.S DOE, 2) Chevron, 3) Halliburton, 4) Statoil, 5) Schlumberger, 6) BP-Amoco, 7) Baker-Hughes, 8) Intevep, 9) Petrobras, 10) Weatherford and 11) TotalFina-Elf.
Year 5	1) U.S DOE, 2) Chevron, 3) Halliburton, 4) Statoil, 5) Schlumberger, 6) BP-Amoco, 7) Baker-Hughes, 8) Intevep, 9) Petrobras, 10) Weatherford and 11) TotalFina-Elf.

The ACTS project had ten advisory board meetings. During these meetings, presentations were made to the industry members on the progress of flow loop development, research projects and ACTS budget. The research project proposals were evaluated by the industry members. Discussions were held and the industry members provided their input on various issues of the ACTS project. In addition to the members, several potential member companies and organization participated in the meetings, including: Unocal, Nabors Drilling, Hughes-Christensen, M-I Drilling Fluids, Tesco, SMF International, Bachman Services, ExxonMobil, ConocoPhillips, Anadarko Petroleum, Saudi Aramco, Environmental Drilling Technology, Oil and Gas Institute of Poland, Anadarko Petroleum, M-I Drilling, Precision Drilling and ASCOMETAL.

14.2 CONFERENCE PRESENTATIONS AND JOURNAL PUBLICATIONS

We participated in several SPE conferences and meetings and presented articles and posters. In total six articles were presented at different SPE meetings and one paper was published in a technical journal. Table 14.2 summarizes the publications.

Table 14.2 Summary of Publications

Task #	Title	Type
6	SPE 79856: Cuttings Transport with Foam in Horizontal & Highly-Inclined Wellbores	Conf. Paper
	SPE 78939: Analysis of Bed Height in Horizontal and Highly-Inclined Wellbores by Using Artificial Neural Networks	Conf. Paper
	SPE 65489: A Comparative Study of Hydraulic Models for Foam Drilling	Conf. Paper
	A comparative Study of Hydraulic Models for Foam Drilling Technology	J. Canadian Petroleum Tech.
7	SPE 74463: Minimum Air and Water Flow Rates Required for Effective Cuttings Transport in High Angle and Horizontal Wells	Conf. Paper
9	SPE 84175: Study of the Effects of Pressure and Temperature on the Rheology of Drilling Foams and Frictional Pressure Losses	Conf. Paper
	Study of the Effects of Pressure and Temperature on the Viscosity of Drilling Foams and Frictional Pressure Losses	SPE Drilling & Completion[a]
9b	Rheology of Aqueous Drilling Foam Using an In-line Rotational Viscometer	Conf. Paper[b]
10	SPE 89531: Experimental Study of Aerated Mud Flows under Horizontal Borehole Conditions	Conf. Paper[c]
	SPE 90038: Experimental Study and Modeling of Cuttings Transport With Aerated Fluids in Horizontal Wellbore at Simulated Downhole Conditions	Conf. Paper[d]
	SPE 92484: Hydraulics of Drilling with Aerated Muds under Borehole Conditions	Conf. Paper[d]

a: accepted for journal publication
b: abstract is submitted
c: being reviewed for journal publication
d: accepted for conference presentation

14.3 VISITS AND PRESENTATIONS TO OIL AND SERVICE COMPANY

For the last five years, several individual visits and presentations about the ACTS Project were made to oil and service companies (ACTS-JIP members and non-members). Overviews of research projects were presented to potential member companies. The responses from the companies were very positive.

Technical work groups were also established with the participation of ACTS-JIP members to discuss issues regarding ACTS flow loop construction. As part of the activities of the construction work group, we visited the Halliburton research center in Duncan, Oklahoma. In addition, we visited the Ohio State University (OSU) Multi-Phase Flow Technology Center, where they have been using Tri-Phase Moyno pumps to circulate air-liquid and solid mixtures. We had discussions with the OSU people regarding the performance of Tri-Phase Moyno pumps when circulating air/liquid/solid mixtures.

During year 2000, we were contacted by Gas Technology (formerly Gas Research Institute) to discuss the opportunities for developing flow-loop test programs that are complementary and mutually beneficial.

Since July 14, 1999, the ACTS facility has been visited many times by representatives of ACTS-JIP member companies. During these visits, technical presentations were made regarding the flow loop construction and research tasks. Member companies were strongly encouraged to provide input.